Federico Canova Luca Poletto *Editors*

Optical Technologies for Extreme-Ultraviolet and Soft X-ray Coherent Sources



Springer Series in Optical Sciences

Volume 197

Founded by

H.K.V. Lotsch

Editor-in-Chief

William T. Rhodes, Georgia Institute of Technology, Atlanta, USA

Editorial Board

Ali Adibi, Georgia Institute of Technology, Atlanta, USA

Theodor W. Hänsch, Max-Planck-Institut für Quantenoptik, Garching, Germany Ferenc Krausz, Ludwig-Maximilians-Universität München, Garching, Germany Barry R. Masters, Cambridge, USA

Katsumi Midorikawa, Saitama, Japan

Herbert Venghaus, Fraunhofer Institut für Nachrichtentechnik, Berlin, Germany Horst Weber, Technische Universität Berlin, Berlin, Germany

Harald Weinfurter, Ludwig-Maximilians-Universität München, München, Germany

Springer Series in Optical Sciences

The Springer Series in Optical Sciences, under the leadership of Editor-in-Chief William T. Rhodes, Georgia Institute of Technology, USA, provides an expanding selection of research monographs in all major areas of optics: lasers and quantum optics, ultrafast phenomena, optical spectroscopy techniques, optoelectronics, quantum information, information optics, applied laser technology, industrial applications, and other topics of contemporary interest.

With this broad coverage of topics, the series is of use to all research scientists and engineers who need up-to-date reference books.

The editors encourage prospective authors to correspond with them in advance of submitting a manuscript. Submission of manuscripts should be made to the Editor-in-Chief or one of the Editors. See also www.springer.com/series/624

More information about this series at http://www.springer.com/series/624

Federico Canova · Luca Poletto Editors

Optical Technologies for Extreme-Ultraviolet and Soft X-ray Coherent Sources



Editors
Federico Canova
Amplitude Technologies
Evry
France

Luca Poletto National Research Council Institute of Photonics and Nanotechnology Padova Italy

ISSN 0342-4111 ISSN 1556-1534 (electronic) Springer Series in Optical Sciences ISBN 978-3-662-47442-6 ISBN 978-3-662-47443-3 (eBook) DOI 10.1007/978-3-662-47443-3

Library of Congress Control Number: 2015943791

Springer Heidelberg New York Dordrecht London

© Springer-Verlag Berlin Heidelberg 2015

This work is subject to copyright. All rights are reserved by the Publisher, whether the whole or part of the material is concerned, specifically the rights of translation, reprinting, reuse of illustrations, recitation, broadcasting, reproduction on microfilms or in any other physical way, and transmission or information storage and retrieval, electronic adaptation, computer software, or by similar or dissimilar methodology now known or hereafter developed.

The use of general descriptive names, registered names, trademarks, service marks, etc. in this publication does not imply, even in the absence of a specific statement, that such names are exempt from the relevant protective laws and regulations and therefore free for general use.

The publisher, the authors and the editors are safe to assume that the advice and information in this book are believed to be true and accurate at the date of publication. Neither the publisher nor the authors or the editors give a warranty, express or implied, with respect to the material contained herein or for any errors or omissions that may have been made.

Printed on acid-free paper

Springer-Verlag GmbH Berlin Heidelberg is part of Springer Science+Business Media (www.springer.com)

Preface

The book will review the most recent achievements in optical technologies applied to photon handling and conditioning of extreme-ultraviolet (XUV) and soft X-ray coherent sources.

The developments in laser technology over the past 30 years led to the generation of coherent optical pulses as short as a few femtoseconds, providing a unique tool for high-resolution time-domain spectroscopy that revolutionized many areas of science from solid-state physics to biology. While femtosecond optical lasers offered unique insights into ultrafast dynamics, they are limited by the fact that the structural arrangement and motion of nuclei are not directly accessible from measured optical properties. This scientific gap has been filled by the availability of ultrafast coherent sources in the extreme-ultraviolet and X-ray spectral region, such as high-order laser harmonics and free-electron lasers.

High-order laser harmonics, that are produced by the interaction between a very intense ultrashort pulsed laser and a gas/solid target, exhibit high brightness, high degree of coherence, and high peak intensity. The combination of the use of advanced phase matching mechanisms and interaction geometries as well as intense ultrafast laser has made possible to obtain radiation down to the water window region (2.3–4.4 nm). Moreover, the radiation generated with the scheme of the high-order harmonics using few-optical-cycles laser pulses is presently the most advanced tool for the investigation of matter with attosecond resolution.

Synchrotron radiation has provided over the past 40 years an increase in flux and brilliance of more than ten orders of magnitude in the extreme-ultraviolet and X-ray spectral regions. The free-electron-laser sources generate spatially coherent XUV/X-ray radiation with characteristics similar to the light from conventional optical lasers, ultrashort time duration, and an additional increase of 6–8 orders of magnitude on the peak brilliance with respect to synchrotrons.

In order to investigate the properties of these laser-type sources as well as to exploit their new capabilities in terms of scientific return, the instrumentation that is used to handle, condition, and characterize the photon beam has a fundamental role. The development of optical technologies suitable for photon handling of coherent XUV/X-ray sources is a typical field where a strong collaboration between research

vi Preface

and industry is required to reach new exciting results. On one side, the impressive developments of lasers have opened the way to major improvements in terms of performance from the sources. On the other side, new optical techniques have been studied and demonstrated in order to exploit the full potentialities of coherent light in the XUV/X-ray, especially in terms of coherence preservation and temporal resolution. An increasing number of scientific and industrial partners are collaborating on the development of the applications based on next-generation light sources, and in the twenty-first century many secondary sources came out of the laboratory to be proposed as "machine" to perform experiments. The optical technologies described in this book represent the achievement of the scientific development and the beginning of the technological life of the coherent light sources.

The book is organized as follows.

Chapters 1 and 2 are focused on the two free-electron laser facilities that are presently in operation with photon emission in the extreme-ultraviolet region: FLASH in Germany and FERMI in Italy. Photon beam transport and diagnostic techniques on the two facilities are reviewed.

Chapters 3 and 4 review the techniques related to high-order laser harmonics to generate intense pulses in the femtosecond and attosecond timescale. Recent experimental progresses in the field of attosecond sources and on high-flux ultrafast sources are discussed.

Chapter 5 is focused on the use of high-order laser harmonics as seeding sources for free-electron lasers, joining the two techniques previously described, namely free-electron lasers and high-order laser harmonics, to obtain a coherent source with increased performance.

Chapter 6 reviews the diagnostic techniques to measure the pulse duration, that is an essential tool to assess the ultrafast time regime. The most important methods for temporal pulse characterization are discussed, with particular emphasis on attosecond pulses generated by high-order harmonics and on femtosecond soft X-ray pulses emitted by free-electron lasers.

Chapter 7 is focused on the metrology of the optical elements that are requested to handle the coherent photon beam. Particularly demanding are the requirements on optical elements for free-electron lasers, where an improvement of one order of magnitude in terms of figure error has been achieved with respect to the optics for third generation storage rings.

Chapters 8 and 9 review the main technologies used for photon handling, beam conditioning, spectral selection, and temporal shaping of ultrafast pulses, namely multilayer mirrors and reflection gratings.

Finally, as editors, we would like to thank all the authors for their appreciable contributions to the book.

Evry, France Padova, Italy Federico Canova Luca Poletto

Contents

1	The	Soft X-ray Free-Electron Laser FLASH at DESY	1
	E. Pl	önjes and K. Tiedtke	
	1.1	Introduction	1
	1.2	FLASH Machine	2
	1.3	Layout of the Facility	3
		1.3.1 Layout of the Optical System	5
		1.3.2 Characterization of the Optical System	9
	1.4	Characterization of the FEL Pulses	10
		1.4.1 Monitoring of the Intensity and Beam Position	11
		1.4.2 Monitoring of the Spectral Distribution	11
		1.4.3 Monitoring of the Temporal Properties	13
	1.5	Manipulation of the Photon Beam	14
		1.5.1 Reduction of Photon Pulse Energy	14
		1.5.2 Suppression of FEL Harmonics	14
		1.5.3 Single Pulse Selection	15
		1.5.4 Split and Delay Units	15
	1.6	Additional Light Sources for Advanced Multi-colour	
		Experiments	17
		1.6.1 Optical Laser System	17
		1.6.2 THz Beamline for Pump-Probe Experiments	18
	1.7	Near Future Perspectives	18
	Refe	ences	20
2	The	Soft X-ray Free-Electron Laser FERMI@Elettra	23
	Marc	o Zangrando, Nicola Mahne, Lorenzo Raimondi	
		Cristian Svetina	
	2.1	Introduction	23
	2.2	Diagnostics	26
		2.2.1 Beam Position Monitor	26
		2.2.2 Intensity Monitors	27
		2.2.3 Energy Spectrometer	27

viii Contents

		2.2.4 Transverse Distribution
		2.2.5 Transverse Coherence
	2.3	Manipulation
		2.3.1 Beam Defining Apertures
		2.3.2 Gas Absorber
		2.3.3 Split and Delay Line
		2.3.4 Focusing Mirrors
	2.4	Conclusions
		ences
	Keleit	SHCCS
3	Overv	view on Attosecond Sources
	France	esca Calegari, Giuseppe Sansone and Mauro Nisoli
	3.1	Introduction
	3.2	Ultrafast Laser Technologies for the Generation
		of Attosecond Pulses
		3.2.1 Pulse Compression Techniques 42
		3.2.2 Optical Parametric Amplification
		3.2.3 Carrier-Envelope Phase Stabilization
	3.3	High-Order Harmonic Generation
	- 10	3.3.1 Semiclassical Model
		3.3.2 Strong-Field Approximation 50
		3.3.3 Phase-Matching in High-Order Harmonic
		Generation
	3.4	Generation of Isolated Attosecond Pulses
	5.4	3.4.1 Spectral Gating
		3.4.2 Temporal Gating
	3.5	Spatial Gating
	3.6	Conclusions
		ences
	Keiere	sices00
4	Overv	view on HHG High-Flux Sources
	Willer	n Boutu, Mathieu Ducousso, Jean-François Hergott
	and H	amed Merdji
	4.1	Introduction
	4.2	Optimization of the Atomic Response 64
	4.3	Phase Matching
		4.3.1 Loose Focusing
		4.3.2 Quasi Phase Matching
		4.3.3 Artificial Tailoring of the Laser Pulses
	4.4	High Repetition Rate Sources
	4.5	Conclusion
	Refere	

Contents ix

	Seeding Free Electron Lasers with High Order Harmonics					
		n Gas				
Mar		nuelle Couprie and Luca Giannessi				
5.1						
5.2	Seedin	ng and Harmonic Generation, a Particular FEL				
	Config	guration				
	5.2.1	Oscillator				
	5.2.2	High Gain and Self Amplified Spontaneous				
		Emission				
	5.2.3	Seeding and Harmonic Generation				
5.3	HHG	Seeding and Harmonic Generation Process				
	5.3.1	Shot Noise and Comparison with Available				
		Seed Power				
	5.3.2	HHG Seeded FEL Dynamics				
5.4	Coupli	ing the Seed Source to the FEL				
	5.4.1	HHG Chamber Design for FEL Seeding				
	5.4.2	Spectral Tuning, Tuneability, Polarisation Matching,				
		Optical Transport and Synchronization				
5.5	Achiev	vements with HHG Seeding				
	5.5.1	Direct Seeding Mode				
	5.5.2	Cascaded FEL Configuration				
5.6	Conclu	usion				
Refe	erences					
		haracterization of Ultrashort Extreme-Ultraviolet				
		ray Pulses				
		etta, Matteo Negro, Salvatore Stagira and Caterina Vozzi				
6.1		rement of Attosecond Pulses				
	6.1.1	The Attosecond Streak Camera				
	6.1.2	Semiclassical Model for Attosecond Streaking				
	6.1.3	RABBIT: Measurement of Attosecond Pulse Trains				
	6.1.4	Isolated Attosecond Pulse Characterization:				
		Experimental Results				
	6.1.5	XUV Non-linear Optics				
6.2		oral Characterization of Pulses Generated by FELs				
	6.2.1	Autocorrelation of XUV FEL Pulses				
	6.2.2	Cross-Correlation Measurements Involving XUV				
		FEL Pulses				
6.3	Conclu	usions				
Refe	erences					

x Contents

7			rology—On the Inspection of Ultra-Precise	137
		-Optics. k Siewer		137
	7.1		iction	137
	7.1		Error and Micro-Roughness	137
	1.2	7.2.1	The Principle of Slope Measurement	141
		7.2.1		141
			On the Calibration of Slope Measuring Profiler	
	Dofo	7.2.3	Super Polished Mirrors for FEL Application	145 148
	Kele	iences		140
8			Airrors for Coherent Extreme-Ultraviolet	1.7.1
			ray Sources	151
			assin-Bouchet, Sébastien de Rossi	
		Franck D		
	8.1		ayer Mirrors for the XUV Spectral Range	152
		8.1.1	Multilayer Mirrors: Theory and Design	152
		8.1.2	Deposition and Characterization of Multilayers	154
		8.1.3	State-of-the-Art of Normal Incidence Multilayer	
			Mirrors	155
		8.1.4	Specificities of Multilayer Mirrors for Coherent	
			X-ray Sources	156
	8.2	Multila	ayer Mirrors for Picosecond and Femtosecond	
		Source	S	157
		8.2.1	High Reflectivity Mirrors	157
		8.2.2	High Selectivity Mirrors	158
		8.2.3	High Stability Mirrors	162
	8.3	Multila	ayer Mirrors for Attosecond Sources	163
		8.3.1	Specificities of the Attosecond Regime	163
		8.3.2	Design of Attosecond Mirrors	165
		8.3.3	Characterization of Attosecond Mirrors	166
	8.4	Conclu	ısion	170
	Refe			170
9	Grat	ings for	Ultrashort Coherent Pulses in the Extreme	
	Ultra	aviolet .		175
		Sekikaw	· 	
	9.1		action	175
	9.2		g for the Extreme Ultraviolet and Soft X-ray	177
		9.2.1	Absorption and Reflectance	177
		9.2.2	Grating	178
	9.3		Preserving Monochromator Using a Single Grating	182
	9.4		Delay Compensated Monochromator	183
		9.4.1	Compensation of Time Delay Introduced	
			by Diffraction	183

Contents xi

		9.4.2	Experimental Demonstration of a Time-Delay	
			Compensated Monochromator	184
		9.4.3	Future Applications	190
	9.5	Conclu	isions	191
	Refe	rences		192
Inc	lev			195

Contributors

Charles Bourassin-Bouchet Laboratoire Charles Fabry, Institut d'Optique, CNRS, University of Paris-Sud, Palaiseau Cedex, France

Willem Boutu Laboratoire Interactions, Dynamique et Lasers, CEA-Saclay, Gif-sur-Yvette Cédex, France

Francesca Calegari National Research Council of Italy, Institute of Photonics and Nanotechnologies (CNR-IFN), Milano, Italy

Marie-Emmanuelle Couprie Synchrotron SOLEIL, Gif-sur-Yvette Cedex, France

Sébastien de Rossi Laboratoire Charles Fabry, Institut d'Optique, CNRS, University of Paris-Sud, Palaiseau Cedex, France

Franck Delmotte Laboratoire Charles Fabry, Institut d'Optique, CNRS, University of Paris-Sud, Palaiseau Cedex, France

Michele Devetta Istituto di Fotonica e Nanotecnologie IFN-CNR & Physics Department, Politecnico di Milano, Milan, Italy

Mathieu Ducousso Laboratoire Interactions, Dynamique et Lasers, CEA-Saclay, Gif-sur-Yvette Cédex, France

Luca Giannessi ENEA C. R. Frascati, Frascati, Rome, Italy; Elettra-Sincrotrone Trieste, Basovizza, Italy

Jean-François Hergott Laboratoire Interactions, Dynamique et Lasers, CEA-Saclay, Gif-sur-Yvette Cédex, France

Nicola Mahne Elettra Sincrotrone Trieste, Trieste, Italy

Hamed Merdji Laboratoire Interactions, Dynamique et Lasers, CEA-Saclay, Gif-sur-Yvette Cédex, France

xiv Contributors

Matteo Negro Istituto di Fotonica e Nanotecnologie IFN-CNR & Physics Department, Politecnico di Milano, Milan, Italy

Mauro Nisoli Department of Physics, Politecnico di Milano and National Research Council of Italy Institute of Photonics and Nanotechnologies (CNR-IFN), Milano, Italy

E. Plönjes Deutsches Elektronen-Synchrotron, Hamburg, Germany

Lorenzo Raimondi Elettra Sincrotrone Trieste, Trieste, Italy

Giuseppe Sansone Department of Physics, Politecnico di Milano and National Research Council of Italy Institute of Photonics and Nanotechnologies (CNR-IFN), Milano, Italy

Taro Sekikawa Department of Applied Physics, Hokkaido University, Sapporo, Japan

Frank Siewert Helmholtz Zentrum Berlin—Elektronenspeicherring BESSY-II, Institut für Nanometer Optik und Technologie, Berlin, Germany

Salvatore Stagira Istituto di Fotonica e Nanotecnologie IFN-CNR & Physics Department, Politecnico di Milano, Milan, Italy

Cristian Svetina Elettra Sincrotrone Trieste, Trieste, Italy; University of Trieste, Graduate School of Nanotechnology, Trieste, Italy

K. Tiedtke Deutsches Elektronen-Synchrotron, Hamburg, Germany

Caterina Vozzi Istituto di Fotonica e Nanotecnologie IFN-CNR & Physics Department, Politecnico di Milano, Milan, Italy

Marco Zangrando IOM—CNR and Elettra Sincrotrone Trieste, Trieste, Italy

Chapter 1 The Soft X-ray Free-Electron Laser FLASH at DESY

E. Plönjes and K. Tiedtke

Abstract FLASH, the Free-electron LASer in Hamburg, is the world's first free electron laser for extremely bright and ultra-short pulses in the extreme ultraviolet and soft X-ray range. Efficient photon beam transport and diagnostics play an essential role in exploiting the features of this new generation of light sources in a large variety of user experiments. A detailed overview of the FLASH user facility is presented.

1.1 Introduction

Since 2005 the Free electron LASer in Hamburg (FLASH) has served as a user facility [1–3], providing highly intense, short-pulsed radiation. 80–6 nm was the design wavelength range, which FLASH and its photon beamlines were originally configured for. Based on user requests a tuning range from 47–6.9 nm was experimentally explored in the first phase. With the upgrade in 2009, the maximum electron energy has been increased from 750 MeV to 1.25 GeV extending the wavelength range down to 4.2 nm [4, 5].

Peak and average brilliance of FLASH exceed both, modern synchrotron facilities and laser plasma sources by many orders of magnitude. The soft X-ray output possesses unprecedented flux of about 10^{13} photons per pulse with pulse durations in the femtosecond range and a high level of coherence. Hence, combined with appropriate focusing optics, peak irradiance levels of more than 10^{16} W/cm² can be achieved.

Over the past decade FLASH has hosted many international groups who actively explore a diverse range of novel applications. These include fundamental studies on atoms, ions, molecules and clusters, creation and characterization of warm dense matter, diffraction imaging of nanoparticles, spectroscopy of bulk solids and

1

E. Plönjes (⋈) · K. Tiedtke

Deutsches Elektronen-Synchrotron, Notkestraße 85, D-22603 Hamburg, Germany

e-mail: elke.ploenjes@desy.de

K. Tiedtke

e-mail: kai.tiedtke@desy.de

© Springer-Verlag Berlin Heidelberg 2015
F. Canova and L. Poletto (eds.), *Optical Technologies for Extreme-Ultraviolet and Soft X-ray Coherent Sources*, Springer Series in Optical Sciences 197, DOI 10.1007/978-3-662-47443-3_1

surfaces, investigation of surface reactions and spin dynamics, and the development of advanced photon diagnostics and experimental techniques (see http://www.photon-science.desy.de/facilities/flash/ and references therein).

1.2 FLASH Machine

FLASH is a single-pass free electron laser (FEL) lasing in the soft X-ray regime. The generation of soft X-ray laser radiation is based on the so called self-amplified spontaneous emission (SASE) process [6]. The 1.25 GeV superconducting linear accelerator is described in detail by Ackermann et al. [1] and references therein.

In short, a photo-injector generates very high quality electron bunch trains which are accelerated to relativistic energies of up to 1.25 GeV. They produce laser-like soft X-ray radiation during a single pass through a 30 m long undulator, a periodic magnetic structure. In the undulator, the electron bunches undergo a sinusoidal motion and emit synchrotron radiation. The radiation moves faster than the electron bunch and interacts with electrons farther up. This leads to a charge density modulation within the bunch with a period corresponding to the fundamental in the wavelength spectrum of the undulator. This well-defined periodicity in the emitting bunch enhances the power and coherence of the radiation field exponentially while the electron bunch travels once through the long undulator without the need for a resonator.

Figure 1.1 depicts the electron bunch and the resulting photon pulse pattern of FLASH at a repetition rate of 10 Hz. Table 1.1 summarizes the performance of FLASH achieved since 2009.

The exponential amplification process in a SASE FEL starts from spontaneous emission (shot noise) in the electron bunch. Therefore, the SASE FEL radiation itself is of stochastic nature and individual radiation pulses differ in their intensity,

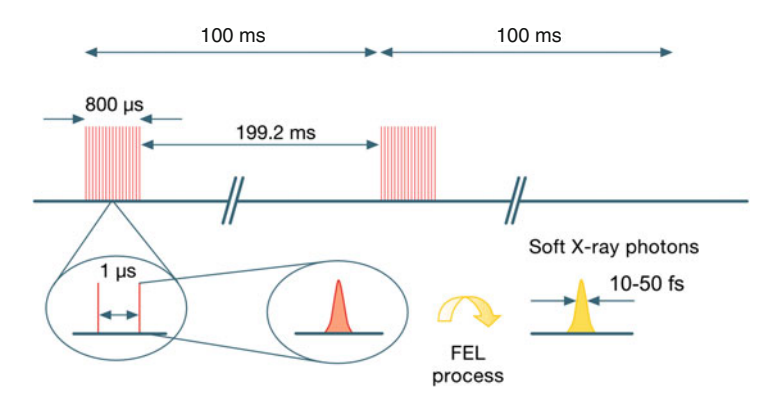


Fig. 1.1 Electron bunch and resulting photon bunch time pattern of FLASH with $10\,\text{Hz}$ repetition rate and up to 800 bunches in a $800\,\mu\text{s}$ -long bunch train. Electron/photon bunch separation within a train can be set to 1, 2, 10, or $100\,\mu\text{s}$

Parameters of FLASH					
Wavelength range fundamental (measured)	4.2–47 nm				
Higher harmonics	3rd ∼ 1.4 nm				
Pulse energy average	10–250 μJ				
Peak power	Several GW				
Pulse duration (FWHM)	10–300 fs				
Spectral width (FWHM)	0.5–1 %				
Angular divergence (FWHM)	$90 \pm 10 \mu rad^a$				
Peak brilliance	10 ²⁹ –10 ³⁰ photons/sec/mrad ² /mm ² /0.1 % bw				

Table 1.1 Performance of FLASH

temporal structure, and spectral distribution. As a consequence, exploitation of the unique properties of the FEL radiation requires suitable pulse-resolved diagnostic tools. Online determination of important photon beam parameters, such as intensity, spectral distribution, and temporal structure are mandatory for most user experiments. This requires diagnostics tools which operate in parallel to the user experiments and in a non-destructive way. To fulfill these demands, new diagnostics concepts, such as online spectrometers and intensity monitors, have been developed for FLASH.

1.3 Layout of the Facility

The layout of the FLASH facility takes essential aspects which are unique to SASE X-ray free electron lasers into account. First, in contrast to synchrotrons, FELs are single-pass machines which can serve only one user at a time. Despite this fact, the FLASH beam is delivered to five experimental stations with different characteristics described in detail below. The photon beam can be switched from one station to the other very quickly, thus making very efficient use of the 24-h operation of FLASH. Second, due to the strong absorption of vacuum-ultraviolet and soft X-ray radiation in any material, particularly also in air, a windowless ultra-high vacuum and particle free system has been designed encompassing the FEL, the photon beam transport and the experimental stations, altogether 330 m. The photon beam transport system, which is approximately 75 m long from the undulator to the endstations, includes only grazing incidence optics which cover the wavelength range of FLASH described in Table 1.1. Finally, due to the stochastic nature of the SASE process, FLASH fluctuates significantly from pulse to pulse in its photon beam parameters and user experiments require photon diagnostics which are capable of resolving each individual pulse within a pulse train at all beamlines.

Figure 1.2 shows the layout of the user facility. The FEL, a THz and a synchrotron radiation beamline (see Sect. 1.6) enter into the hall from the bottom of the schematic. The FLASH beam is delivered directly to the beamlines BL1–BL3 which differ in

^aSASE in saturation@30 nm

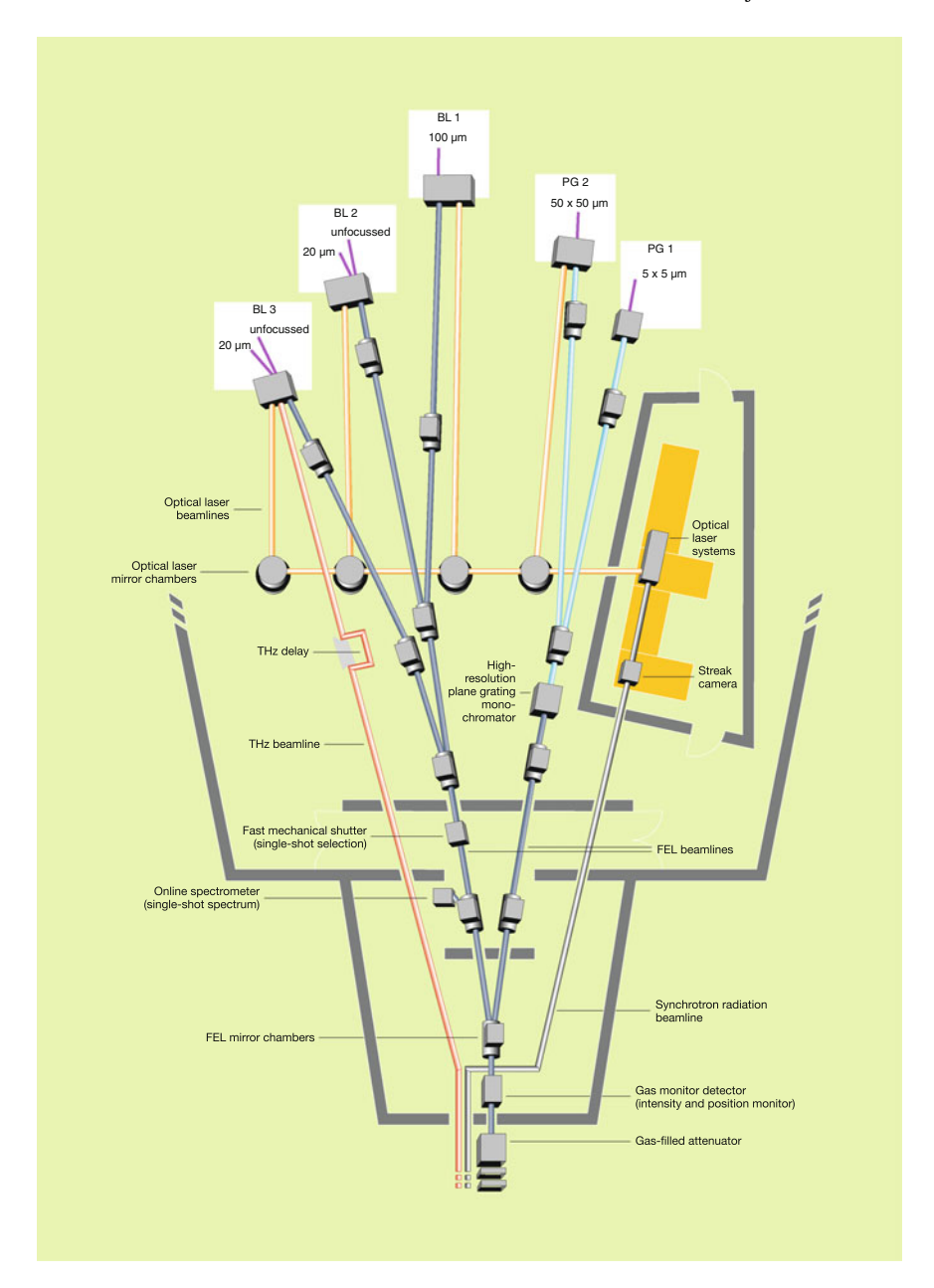


Fig. 1.2 Schematic view of the experimental hall. Beamlines are highlighted by a colour code: 'direct' FEL beam in *dark blue*, monochromatised FEL beam in *light blue*, optical laser in *orange* and THz radiation in *red*. Different experimental stations are named 'BL' in case of direct FEL beam or 'PG' for the monochromatised FEL beam. Approximate focal sizes are given next to the station name

their focusing optics and offer different beam manipulation tools. The beamlines PG1 and PG2 comprise of a high-resolution monochromator allowing the selection of an even narrower spectrum from the FEL pulse.

Before and during the separation of beamlines the FEL radiation passes through a set of photon diagnostics and beam manipulation tools, such as a set of four gasmonitor detectors (GMD) for intensity and beam position determination (Sect. 1.4), an attenuation system based on gas absorption (Sect. 1.5), a set of filters and a fast shutter. The BL beamlines are equipped with a variable-line-spacing spectrograph as well as a detector system based on photoelectron and -ion spectroscopy (Sect. 1.4) for online determination of the FLASH wavelength spectrum in parallel to the user experiments. Due to the strong interest in ultra-fast time resolved studies, the facility provides two additional light sources for femtosecond time-resolved pump-and-probe experiments. A femtosecond optical laser synchronized to the FEL (Sect. 1.6) is situated in a laser hutch depicted in Fig. 1.2 and distributed to the end stations in a separate beamline system. A THz source is generated by a dedicated undulator through which the FLASH electron beam passes subsequent to the XUV undulators.

1.3.1 Layout of the Optical System

The FEL beam is distributed to the five endstations by moving one or two plane mirrors between in and out positions. Most of the beamline system and some of the photon diagnostics have been designed for the originally envisaged wavelength range of 6–80 nm. Downstream of the first pair of mirrors, which creates a beam offset to separate potential Bremsstrahlung from FEL radiation, the beam can be distributed in two different branches: the 'direct' or the 'monochromator' branch. In the beamline design, particularly when choosing the focusing optics, a large number of different user chambers had to be taken into account. This required a compromise between necessary focal length and reachable focal spot size.

1.3.1.1 Grazing Incidence Optics

Again, in the choice of optics, the large wavelength range and a high flexibility for different user applications had to be taken into account. Thus, grazing incidence optics were chosen for the general layout of the facility. To provide high degrees of reflectivity, avoid the risk of damage due to the high peak powers, and minimize deformation of the mirrors by long bunch trains, very shallow incidence angles of 2° and 3° are used. A total mirror length of 500 mm has been chosen based on a 6σ acceptance for a beam diameter of 3–5 mm (FWHM). The beam divergence strongly depends on wavelength and for the longer wavelength ≥ 30 nm a 6σ acceptance of the optics cannot be expected any more.

The mirrors are silicon (plane) or zerodur (focusing) substrates with high-density carbon coatings. A state of the art low surface roughness amounts to less than 3 Å over the full mirror length for the plane mirrors and less than 5 Å for the focusing optics. Carbon coatings have been chosen because of their nearly constant high reflectivity between 94 and 96% in the originally anticipated spectral range of the FLASH fundamental of 6–80 nm. The first pair of mirrors, which directs the beam to BL2 has an additional nickel coating and thus allows experiments the carbon K-edge.

1.3.1.2 Multi-layer Optics

In addition to the general endstation layout, users can bring their own focusing optics as part of their experimental chambers. For this purpose, at beamlines BL2 and BL3 (see below) the grazing incidence focusing optics can be retracted, allowing users either to conduct experiments in the non-focused beam with typically 5–10 mm FWHM beam size or to install their own optics. A variety of configurations have been used in past experimental runs. Back-reflecting spherical multilayer mirrors have been used to cover a large range of irradiation conditions from ~ 10 mm in the non-focused beam down to $\sim 2 \,\mu m$ [7] or for THz-XUV pump-probe setups (see Sect. 1.6.2). Extremely small foci down to $\leq 1 \,\mu m$ have been achieved using off-axis parabolas for warm dense matter studies [8] and other special optics are used for coherent diffraction imaging (see [9] and references therein).

1.3.1.3 Beamlines

BL1, BL2 and BL3 utilize the direct SASE FEL beam. The three end-stations offer different focusing schemes leading to more or less intensely collimated FEL beams. BL1 was originally been equipped with a toroidal mirror (f = 10 m) providing a focal spot size of $\sim\!100\,\mu\text{m}$. Since the vast majority of user experiments require smaller foci than BL1 can offer, this endstation is currently newly equipped with a permanent endstation—the CAMP chamber [10]—which will include a Kirkpatrick-Baez system. This new endstation will be available to users from the middle of 2014.

At BL2 and BL3 ellipsoidal mirrors with focal length $f=2\,m$ generate focal sizes of $\sim\!20\text{--}30\,\mu\text{m}$. As described in detail above, at both beamlines the focusing optics can be retracted to install other types of optics.

For the second branch a high-resolution plane grating monochromator has been built by the University of Hamburg in collaboration with DESY [11, 12] to enable high resolution spectroscopy at beamlines PG1 and PG2. Although the photon pulses of FLASH already offer a narrow inherent bandwidth of $\sim 1\,\%$, many scientific areas require even further monochromatised radiation. Examples are the spectroscopy of highly charged ions [13], measurements of higher-order intensity correlation functions [14], or time-resolved pump-probe X-ray photoelectron spectroscopy [15]. Figures 1.3 and 1.4 depict the calculated photon flux behind the PG beamlines and the resolving power, respectively.

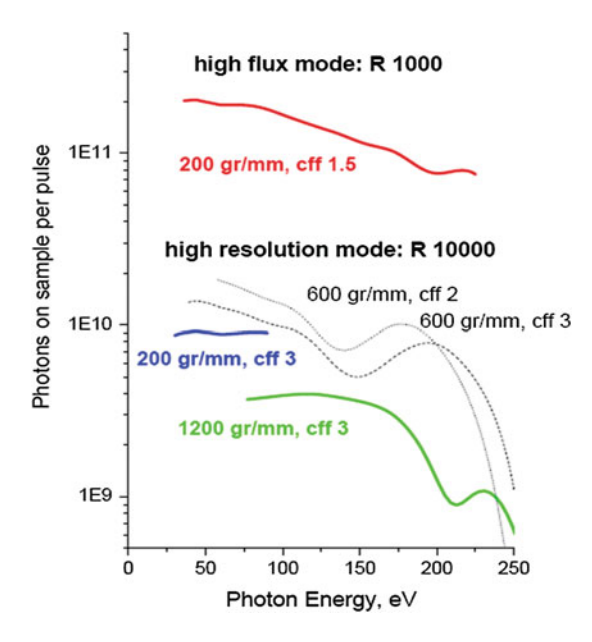


Fig. 1.3 Calculated photon flux behind the monochromator assuming $100\,\mu J$ pulse energy at the undulator exit

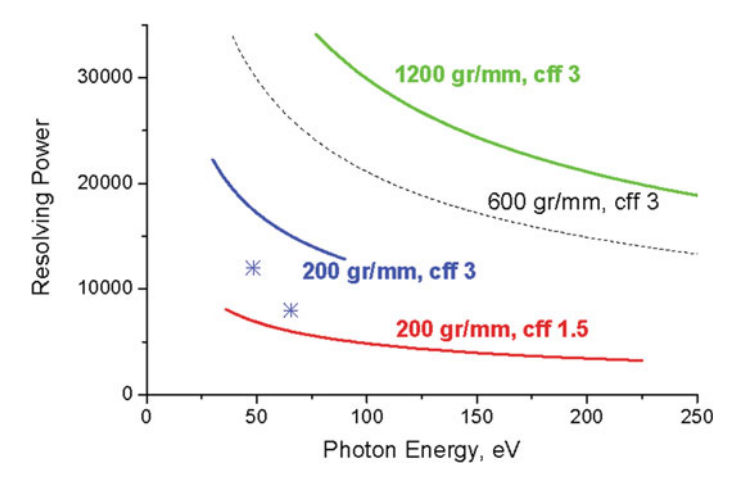


Fig. 1.4 Calculated (*lines*) and measured (*stars*) resolving power. Exit slit set to $20\,\mu m$ for a constant fixed focus cff = 3 and $35\,\mu m$ for cff = 1.5

PG1 is equipped with a permanently installed high-resolution double VUV-Raman spectrometer which can be used to study various samples with different techniques, such as resonant inelastic X-ray scattering (RIXS) to probe low-energy elementary (charge, spin, orbital and lattice) excitations in complex solids. The spectrometer employs a double monochromator setup which—along with enhanced stray light

	BL1	BL2	BL3	PG1	PG2
Monochromatisation	_	_	_	Yes	Yes
Optical elements	4	3(2)	5(4)	8	6
Focusing	Toroidal	Ellipsoidal (none)	Ellipsoidal (none)	KB ^a	Toroidal
Focus size approx. (µm FWHM)	100	20	20	5	50
Distance undulator end-focus (m)	76	73	72.2	75.2	72.5
Distance last flange-focus (m)	1.281	0.636	0.637	0.758	0.758
Transmission @13.5 nm (%)	65 ^b	64±4	59±6	_	64 ^c

 Table 1.2 Technical specifications of the FLASH beamlines

rejection—allows high energy resolution measurements close to the Rayleigh line. During the first commissioning phase an instrument resolution of 30 meV has been confirmed [16, 17]. The ultimate resolution of below 10 meV should be reached after the commissioning of an improved Kirkpatrick-Baez (KB) focusing optic generating a FEL focal spot of 5 μm (vertically) at the sample position. PG2, on the other hand, is a general purpose monochromator beamline, where users provide their own experimental chambers. The spot size at PG2 is presently about 50 μm depending on wavelength and monochromator settings.

In Table 1.2 the most relevant information on the FLASH beamlines is summarized.

1.3.1.4 Fast Switching Mirror

Switching of beamlines is typically performed between user shifts every 12 or 24 h. The procedure takes several minutes with an accuracy of the position reproducibility in the μm range. However, not all user experiments require a 10 Hz repetition rate of the photon pulse trains. Provided that both user groups require the same FEL parameters, the laser beam could in principle be shared between two beamlines by using a fast switching mirror capable of shifting between pulse trains. Such a system has been developed at FLASH [18] and installed for switching between beamlines BL2 and BL3. It can move the FEL between the two beamlines with a frequency of up to 2.5 Hz and is coupled to the fast shutter (Sect. 1.5) to provide an appropriate FLASH pulse repetition rate. A major design challenge is posed for and met by the system in the repetition accuracy for the mechanical movement. At the reversal points, an accuracy in position of a few μm and in angle of about 1 arcsec is required, because the user endstations are typically 15–20 m downstream of the switching mirror.

^aKirkpatrick-Baez

^bCalculated

 $^{^{\}rm c}\sim64\,\%$ for the zeroth order diffration of the 200 lines mm⁻¹

1.3.1.5 Experimental Endstations

Up to 2013, FLASH user groups have typically brought their own experimental setups to the beamtimes. In the near future with the addition of FLASH2 (Sect. 1.7) and thus a higher number of available beamlines, several user endstations will be permanently installed. All beamlines end with an interconnection point, which consists of a differential pumping unit interfacing the ultra-high vacuum of FLASH to the user experiments. The latter may be operated with pressures up to 10^{-5} mbar. The experimental area is typically $3.4\,\mathrm{m}^2$ and contains provisions for connection to FLASH signals such as trigger, time stamp, photon diagnostics, the FLASH data acquisition system as well as vacuum control and interlock and gas systems [3].

1.3.2 Characterization of the Optical System

1.3.2.1 Damage of Optical Components

At a free electron laser, high peak powers could potentially render an (costly) optical component useless within fractions of a second [19]. The research of various damage mechanisms caused by this kind of sources is therefore an active field [20, 21]. The empirical data for damage thresholds that exist are often very specific to a certain (synchrotron) beamline and are thus unique in flux and operating wavelength. For these reasons, materials for optics and their coatings employed at X-ray free electron lasers around the world have begun to be studied in a more systematic fashion [21, 22], notably the low Z materials B₄C and SiC [23].

Damage to optical elements at a FEL can be thought of as direct and in-direct: direct damage could be ablation cratering of the surface, distortion due to the heatload caused by the pulse, etc. In-direct damage mechanisms are more subtle and include damage to multilayers by diffusion or chemical modification of surfaces and layers or changes to the refractive index. Careful monitoring of the beamline performance is thus important and the methods described in Sect. 1.3.2.2 inherently give information that can be used to diagnose the optics.

1.3.2.2 Advanced Beamline Alignment Techniques and Determination of Coherence Properties

For alignment of the FLASH beamlines and focusing optics, wave-front sensors are regularly employed. First, a wave-front sensor by Imagine Optic [24] was used. Meanwhile, two very compact sensors, which include alignment mechanics directly in the system, were developed and extensively tested in a collaboration of DESY and *Laser Laboratorium Göttingen (LLG)* for beamline characterization and optimization both at FLASH [25] and FERMI [26]. They can also be employed by user groups in their experimental setups. The Hartmann-type sensors are largely independent

of wavelength in the soft X-ray region and capable of measuring the wave-front of individual FEL pulses. They proved a valuable tool for observing the FEL beam quality as well as the performance of optical elements, such as metal filter foils or the gas attenuator.

In a Hartmann sensor the incoming photon beam is divided into a large number of sub-rays by a pinhole array and monitored in intensity and position on a CCD camera. The incident wave-front is determined by comparing the CCD image to that of a perfect spherical wave generated behind a pinhole for calibration. Ray tracing in upstream direction based on the measured wave-fronts is used to determine focal spot size and position.

In SASE FELs such as FLASH an influence of the stochastic nature of the beam generation process on the degree of spatial coherence is to be expected. Techniques to measure it are necessary and currently under investigation. In particular, 2nd order correlations should be considered for partially coherent sources to achieve reliable beam propagation and in the design of complex optical systems. Several experiments have been carried out so far based on an evaluation of two-beam interference patterns similar to Young's double slit experiment [27–29]. Alternatively, phase space tomography i.e. the reconstruction of the Wigner distribution function from selected two-dimensional intensity profiles along the beam caustic behind a focusing optic, has recently been carried out at FLASH with promising results (see [30, 31] and reference therein). This technique delivers in principle a complete beam characterization including wave-front, propagation and spatial coherence. However, unlike Hartmann wave-front measurements and techniques based on Young's double slit experiment, the Wigner-reconstruction gives only average results and no single pulse information.

1.4 Characterization of the FEL Pulses

Inside the FLASH tunnel a set of photon diagnostics is installed mainly for use by operators during setup of SASE. The FEL beam passes two diagnostic units equipped with apertures ranging between 0.5 and 15 mm and Ce:YAG screens for visualization of the XUV radiation which are located 20 and 25 m behind the last undulator segment. Centering the FEL beam with respect to these apertures ensures an accurate propagation of the photon beam across all beamlines towards the experiments. For fast intensity measurements an MCP tool and one of the GMD detector pairs (see below) are located inside the tunnel, as well as a grating spectrometer [32] and an OPIS (see below) for wavelength calibration.

At the same time, most user experiments need online information about important photon beam parameters, such as intensity, spectral distribution, and temporal structure. Due to the pulse-to-pulse fluctuations of FLASH, photon diagnostics need to be capable of resolving each individual pulse within a pulse train. This requires diagnostic tools which operate in parallel to the experiments in a non-destructive way.

1.4.1 Monitoring of the Intensity and Beam Position

A precise knowledge of the pulse energy of each individual FEL pulse is naturally essential for almost all user experiments. Depending on the operating conditions of the FEL, the average energy per bunch is typically in the range of $10-250\,\mu\mathrm{J}$ as shown in Table 1.1. Intensity monitors have to cover the full spectral range from 4.2 and below to 80 nm as well as the extended dynamic range from spontaneous undulator radiation to SASE in saturation. To accomplish these requirements a state-of-the-art gas monitor detector has been developed [33, 34] to perform a non-invasive measurement of the intensity of each individual pulse within a pulse train.

Four gas monitor detectors, which are also used to determine the beam position of FLASH for each pulse, are positioned in the FEL beamlines. A set of two GMDs is located at the end of the accelerator tunnel and a second one at the beginning of the experimental hall. Between these two sets of GMDs a 15 m long gas filled attenuator is positioned as described in Sect. 1.5. When an FEL pulse passes through the ionization chamber of a GMD detector, the gas inside is ionized, and an electric field accelerates the ions upwards and the electrons downwards to be detected by Faraday cups. The absolute number of photons in each shot can be deduced with an accuracy of 10% from the resulting electron and ion currents. Furthermore, the FEL pulse passes between two split electrode plates, allowing the pulse-resolved determination of the horizontal and vertical position of the beam. The gas in the ionization chamber has a very low pressure of about 10^{-6} mbar, and it is nearly transparent to the FEL pulse that proceeds unaltered to the experimental stations.

1.4.2 Monitoring of the Spectral Distribution

Some user experiments require pulse-to-pulse knowledge of the spectral distribution of individual FEL pulses to interpret their data. Still, they may not want to use the PG beamline, because of temporal broadening of the pulse or a reduction of photon flux. Three options have been developed for this purpose at FLASH, a variable-line-spacing (VLS) grating spectrometer integrated into the BL beamline branch, an online photoionization spectrometer (OPIS) located in the photon diagnostic section in the FLASH tunnel and a mobile compact spectrometer which can be setup at the endstation or behind user experiments [35].

1.4.2.1 High Precision Online VLS Grating Spectrometer

A variable line spacing (VLS) grating spectrometer installed at the non-monochromatised BL-beamline branch allows to parasitically measure the spectral distribution of the FEL pulses. The optical design of the spectrometer has been carried out in a collaboration of DESY, *Scientific Answers and Solutions* (SAS) in Madison and the *Council for the Central Laboratory of the Research Councils* (CCLRC) in

Daresbury [36]. Making use of two interchangeable plane VLS diffraction gratings the spectrometer covers the wavelength range from 6 to 60 nm. Shorter wavelengths can be reached using second order light. The main vacuum vessel which houses the optics as well as the mechanics for the movement of the gratings have been designed in a joint project of *Helmholtzzentrum Berlin (HZB)* and DESY.

The major fraction of the radiation, \sim 85–99% depending on wavelength and grating, is reflected in zeroth order to the experimental station, while only a small fraction is dispersed in first order and used for the online measurement of the spectral distribution. In the current setup, the dispersed radiation is focused on a detector unit containing a Ce:YAG single crystal screen which is imaged by an intensified CCD camera with an effective pixel size of 12 μ m. The gated camera is able to record single shot spectra with a repetition rate of 10 Hz. Up to now, the instrument has reached a resolving power of 1000 at 25 nm FEL wavelength. In the near future, the gated CCD camera will be complimented by a fast line detector for spectral analysis of pulse trains. Alternatively, a mirror with both, carbon or nickel coating can be moved in place of the gratings if no information of the spectral distribution is requested or if the intensity on the sample is very critical.

1.4.2.2 Online Photoionization Spectrometer

Wavelength measurements with the online photoionization spectrometer (OPIS) are based on photoionization processes of gas targets such as rare gases or small molecules like N_2 or O_2 [37–39]. Since binding energies and photoionization cross sections are precisely known from literature they can be used as a basis for wavelength determination.

An ion spectrometer is used to measure the intensities of different charge states of the created photo-ions. Since the partial cross sections of the different charge states evolve differently with increasing photon energy, the ratios of their corresponding intensities are a unique measure of the photon wavelength in a certain wavelength interval. Literature data of partial cross sections for the different charge states of various rare gases cover basically the full wavelength range of FLASH. The ion spectrometer has two major advantages. The signal intensity is high since the extraction fields collect all ions created by the radiation and it is insensitive against beam position changes.

In electron time-of-flight spectra, the arrival times of the photo-electrons reflect directly their kinetic energy. The electron binding energies of the orbitals from which the photo-electrons are emitted are the only information needed for wavelength determination. Hence, with only a few well known constant quantities the FEL wavelength can be derived over the full wavelength range. This is the main advantage compared to the ion method described above. In addition, more detailed spectral information such as higher harmonics content or the number of FEL modes [3] can, in principle, be deduced as well. On the other hand, the electron signal intensity is lower compared to the ion spectrometer due to limited acceptance angles and it is sensitive to external magnetic and electric fields.

The OPIS device contains a set of time-of-flight spectrometers for detection of photo-ions and photo-electrons, respectively. Since ion and electron signals are measured using fast digitizers, traces of full bunch trains of FLASH can be recorded and it is possible to monitor the spectral distribution resolved for each micro bunch. In addition, the spectrometer is in principle not limited in wavelength range and typical gas target pressures are in the range of 10^{-7} hPa which allow a photon transmission to the user experiment of essentially $100\,\%$. These advantages make OPIS a promising complement to the existing grating spectrometers.

1.4.2.3 Compact Spectrometer

In collaboration with the *CNR-Institute of Photonics and Nanotechnologies* in Padova, a compact and portable spectrometer has been built for real time monitoring of the high-order harmonic contents of the FEL radiation [35]. This spectrometer can be installed at beamline ends or behind user experiments to determine the fundamental and high-order harmonic contents in single-shot operation mode. Its design is based on two flat-field grazing-incidence gratings combined with a EUV-enhanced CCD. The spectrometer covers the spectral range from 1.7 to 40 nm (720–30 eV).

1.4.3 Monitoring of the Temporal Properties

The temporal properties of the photon beam are a key measure of the performance of FELs. The pulse *length* is required to estimate the integral power at the experiment; the pulse *profile* determines the "quality" of the pulse in terms of length and height of the ideal pedestal shape; the pulse *jitter* is a random fluctuation in the arrival time of a pulse and needs to be correlated to another timing event. Thus, for pump-probe experiments it is obviously a crucial parameter. Since the temporal properties of a SASE FEL are going to change on a pulse by pulse basis by an amount that will cause difficulty for many experiments, there is a general need for temporal online diagnostics.

Such tools for the whole parameter range of FLASH are not a straightforward choice since they require intricate setups often with external laser sources. At FLASH, they are currently under intensive development. A choice of techniques like cross-correlation with an optical laser, intensity auto-correlation, reflectivity modulation of a semiconductor by a FEL pulse or the utilization of phase-correlated terahertz radiation has been tested and at this time each has shown their pros and cons. For details see [40] and references therein.

1.5 Manipulation of the Photon Beam

The photon beam can be manipulated by changing FLASH machine parameters. Within the pulse trains, the bunch repetition rate can be varied from single pulse to 1 MHz with up to 800 bunches (see Fig. 1.1), while a wavelength range from 4.2 to 47 nm is available at FLASH with the current machine parameters. Moreover, several options to modify beam properties are incorporated into the beamlines while the machine parameters are kept fixed. These are reduction of the intensity by a gas attenuator, suppression of harmonics using filter foils, and pulse picking with a fast shutter. Users can directly access these beamline components through the control system interface. Finally, two split-and-delay units, one at BL2 and the other at PG2, allow XUV-XUV pump-probe techniques both in the direct FLASH beam and in the monochromatic beam.

1.5.1 Reduction of Photon Pulse Energy

Research on the interaction of intense photon beams with matter benefits strongly from the possibility to vary the FEL intensity continuously over a large range. For this purpose, a gas filled attenuator is installed at FLASH, which gives the option to reduce the photon pulse energy by absorption in various gases. This technique leaves the other beam characteristics unchanged in contrast to changing machine parameters [41].

The attenuator is a windowless 15 m long gas-filled tube which is installed between the FLASH machine tunnel and the experimental hall. Two pairs of GMD in front of and behind the attenuator monitor the transmission of light. The attenuator is operated with either rare gases or nitrogen. Nitrogen covers an attenuation range of about four orders of magnitude in the spectral range of 19–60 nm. Between 19 and 9 nm and for shorter wavelengths Xenon and Krypton are used. Both sides of the attenuator are terminated by differential pumping stages to preserve the beamline vacuum. Within minutes to tens of minutes the transmission can be reduced by orders of magnitude and re-established to 100 %. Wave-front measurements have demonstrated that this attenuation technique does not degrade the coherence properties of the beam.

1.5.2 Suppression of FEL Harmonics

Spectrally, the FLASH photon beam consists of a strong fundamental and, to a much lesser degree, of higher harmonics [1, 42]. Certain experiments desire the suppression of the harmonic content, for example to distinguish between multi-photon and single photon processes due to harmonics. On the other hand, suppression of the fundamental and transmission of selected higher harmonics offers the opportunity

Filter	Thickness [Å]	Calc. transmission at 7 nm	Calc. transmission at 13.7 nm	Calc. transmission at 27.3 nm
Al	1000/1980	0.111/0.013	0.063/0.004	0.804/0.651
Si	2210/4190	0.017/4.5E-4	0.687/0.491	0.465/0.235
Zr	2000/2870	0.486/0.354	0.490/0.359	3.0E-8/<1E-10
Nb	1970/3840	0.398/0.166	0.369/0.143	<1E-10/<1E-10
Si ₃ N ₄	3500/5000	0.002/1.2E-4	0.047/0.013	2.2E-5/2.2E-7
C/Al/C	2512/5025/2511	8.3E-6	3.8E-8	5.8E-7

Table 1.3 Calculated transmission of various filter foils for three selected wavelengths of FLASH [43]

For the calculation an additional coverage of a 20 Å oxide layer was assumed for the filters

to perform experiments at considerably higher photon energies. Also, a very quick reduction of the photon intensity for equipment tests is possible. Both, the BL and the PG branch have filter wheels with a variety of different metal foil filters. All filters are produced as self-supporting films without mesh support on frames with $10\,\mathrm{mm}$ diameter apertures. Table 1.3 summarizes the properties of the filters installed typically in the units.

1.5.3 Single Pulse Selection

A rotating fast bunch train shutter, shown in Fig. 1.5, has been developed at DESY for selection of individual photon bunch trains, repetition rates of below 10 Hz, or, in case of one bunch operation, single pulses of FLASH. The shutter contains an aluminum or glassy carbon disk which has six equidistant slits each providing a beam aperture of 20 mm. The disk rotation in vacuum is generated by a special magnetic rotary feed-through combined with a DC-motor outside of the vacuum system. The feed-through couples the rotation of the motor to the disk inside the vacuum without using bellows, mechanical or fluidic couplings. The rotating shutter can be operated through the FLASH control system [44].

1.5.4 Split and Delay Units

At BL2, a grazing incidence split-and-delay unit, which was developed and built in a collaboration of *HZB*, *Universität Münster* and DESY, is incorporated into the beamline to facilitate XUV-XUV pump-probe experiments. The device consists of eight mirrors under 6° grazing incidence which are positioned in a tubular ultrahigh vacuum (UHV) chamber with a length of 1800 mm and a diameter of 500 mm.

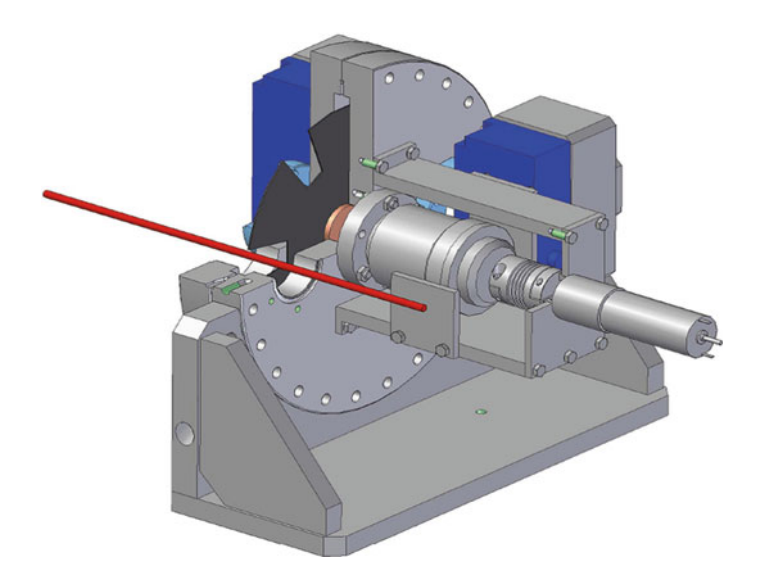


Fig. 1.5 The fast shutter is able to select a single pulses or pulse trains out of the generic 10 Hz repetition rate of the FLASH machine

The entire instrument can be shifted under vacuum to open a clear path through it, in case BL2 is to be used without the autocorrelator.

The FEL beam is split into two parts geometrically on the edge of the first mirror. One half passes a fixed length beam path, while two mirrors are positioned on a parallelogram-based delay stage in the other arm. A delay of -5 to $+20\,\mathrm{ps}$ can be realized in this instrument with a 1 fs stability/reproducibility. Finally, both beams are recombined at the focus of BL2. The precision of the translation of the delay stage allows interference experiments, autocorrelation measurements of the pulse length of the femtosecond FEL pulses and pump-probe experiments at the user endstation. A detailed technical description can be found in [28, 45] and references therein.

At the plane grating monochromator beamline PG2, a Mach-Zehnder type autocorrelator has been developed by the *Universität Hamburg* and implemented as a XUV split-and-delay line. The device is able to split the pulses and delay them up to ± 5.1 ps with a stability in the 200 attosecond range. Both delay arms include an intensity monitor system to measure the beam splitting ratio online. A filter unit in the arms of the delay-line allows a choice of harmonics, as described above, and thus two-colour XUV-XUV pump-probe experiments [46].

The device allows studies of ultra-fast XUV induced dynamics in a site-selective way and it can again be used to monitor the temporal coherence properties of FLASH. In particular, at the monochromator beamline PG2 temporal coherence properties can be measured energy resolved at the expense of lengthening the pulses.

1.6 Additional Light Sources for Advanced Multi-colour Experiments

The femtosecond pulses of FELs make studies of ultra-short processes a particularly attractive area of research at these facilities. More than half of the user experiments use the various options of pump-probe techniques at FLASH. In addition to the split-and-delay units which open up XUV-XUV pump-probe measurements, the FLASH facility offers two additional light sources in combination with the FEL for two-colour pump-probe experiments: a highly advanced optical laser system and a THz radiation source.

1.6.1 Optical Laser System

The optical laser system and the associated infrastructure in the FLASH experimental hall fulfill exceptional requirements [47]. To offer very flexible research opportunities, a complex laser system was built delivering either femtosecond pulses down to 60 fs duration with the macro pulse structure of the FEL (see Fig. 1.1) and moderate pulse energies of $50\,\mu J$ (pulse train option) or a few hundred times more intense pulses at $10\,Hz$ repetition rate (mJ-option).

The system is reliable for long-term measurements, highly automated, and remotely controllable from the experiment. Advanced techniques for the synchronization of the optical laser to FLASH are in place. A synchronization scheme with long-term stability is used. It is based on a length-stabilized fiber-distributed optical reference signal with sub-10 fs (rms) timing jitter employing a balanced optical cross-correlator [48].

The pulse train option delivers ultra-short pulses with the same time structure as FLASH. The system was built in collaboration with the Max-Born-Institute in Berlin and consists of three modular sub-systems. The pump laser, a slightly modified copy of the photo cathode laser of the FLASH accelerator, is a Nd:YLF based burst mode laser which was optimized to produce pulse trains of up to 600 pulses with a spacing of 1 µs between individual laser pulses. The pulse trains are produced with 10 Hz, thus delivering up to 6000 pulses per second. A Ti:Sapphire oscillator is used to provide ultra-short ($\sim 20 \, \text{fs}$, 3 nJ per pulse, 108 MHz repetition rate, synchronized to the FEL) pulses. These femtosecond pulses are subsequently amplified by the second harmonic of the Nd:YLF laser in an optical parametric amplifier (OPA). As a result \sim 60 fs (FWHM) near infrared laser pulses at a wavelength of around 800 nm and a pulse energy of up to $50\,\mu J$ with the pulse train structure of the FEL can be produced. This laser is particularly suited for high repetition rate experiments such as pumpprobe experiments in solids (e.g. magnetization dynamics) which yield low count rates for single pulses and thus need a high number of pulses to acquire sufficient signal.

The mJ-option on the other hand is suited for experiments which need a more intense laser pulse. The same Ti:Sapphire oscillator pulses are this time amplified by a commercial amplifier based on a chirped pulse amplification (CPA) setup including a regenerative as well as a 2-pass amplifier (Hidra 25 by Coherent). The maximum laser output amounts up to 20 mJ at 60 fs pulse duration (15 mJ, at the experimental station).

Since the user endstations are up to 20 m distance away from the laser hutch, the optical laser is distributed in a separate dedicated beamline system to four of the experimental stations, namely BL1-BL3, and PG2 as seen in Fig. 1.2 [3].

1.6.2 THz Beamline for Pump-Probe Experiments

As a second option for pump-probe experiments, a planar electromagnetic undulator with 9 full periods producing THz radiation was installed 5 m downstream of the FLASH undulator [49]. It generates THz pulses from 10–330 μm , i.e. 30–0.9 THz, in wavelength and 300 fs–10 ps in pulse duration. The soft X-ray and THz pulses are synchronized on a femtosecond scale since they are emitted by the same electron bunch.

The two pulses are separated and transported in dedicated beamlines to be recombined at endstation BL3 for two-colour pump probe experiments. In its dedicated 65 m long beamline the THz beam is refocused repeatedly owing to its large divergence. As a result, the XUV beamline to BL3, which includes only grazing incidence optics, is 4 m shorter than the THz beamline. Thus, this path difference has to be compensated by redirecting the XUV beam using appropriate multi-layer mirrors in back reflection geometry to achieve zero delay. Following this coarse timing overlap, an optical delay line in the THz beamline compensates path differences in order to match the timing of both pulses or delay them in a controlled way.

1.7 Near Future Perspectives

Since 2005, the FLASH user facility has been steadily improved, the wavelength range enlarged and new diagnostic tools have been added. The user time at the facility is highly overbooked and possibilities to extend it with the existing FLASH facility are limited. Thus, a major upgrade to expand the facility and double the user capacity is under way. In the FLASHII project, a new tunnel and experimental hall are added to the existing facility as shown in Fig. 1.6 [50, 51]. They will house a new undulator line FLASH2 with up to seven photon beamlines and reserve capacity for a third undulator line FLASH3 as well as other upgrades and extensions. In the future, a seeding scheme will be added to FLASH2 as an alternative to SASE to improve the beam quality.

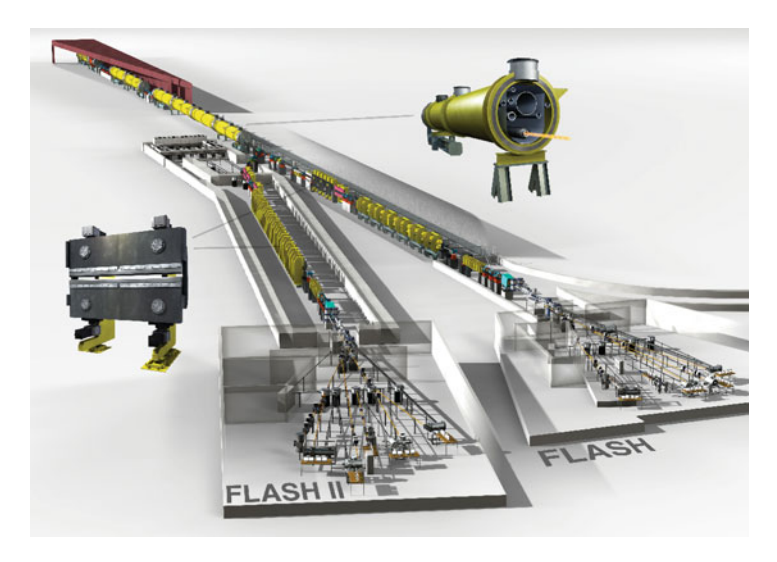


Fig. 1.6 Layout of the FLASH facility including FLASH1 and FLASH2

FLASHII uses to a large extent the existing facility and infrastructure. Modifications needed to the present accelerator which will now drive both undulator lines are minor. Behind the last accelerating module, the beam is switched between the original undulator line now called FLASH1 and the new variable gap undulator line FLASH2. The bunch train can be divided into two bursts, one going straight to FLASH1, the second being kicked to FLASH2. Thus, the electron beam is delivered for both lines with a 10 Hz repetition rate each while varying pulse repetition options are possible. Since FLASH1 has a fixed-gap undulator, the desired FLASH1 wavelength determines the accelerator parameters and the FLASH2 undulator gap is then tuned to the desired wavelength at FLASH2 in a second step.

Similarly to FLASH1, photon diagnostics are positioned in the new FLASHII tunnel behind the dump magnet as well as at the front of the experimental hall. However, contrary to FLASH1, the first two deflecting mirrors are also in the tunnel and radiation shielding will not be necessary inside the new experimental hall. The new hall will allow space for up to seven beamlines [52, 53]. All diagnostic and beam manipulation tools described above, as well as an optical pump-probe laser system and a THz source based on a dedicated undulator will be included into the FLASH2 facility.

Acknowledgments The authors are indebted to all collaboration partners and the FLASH team at DESY for their contributions.

References

- 1. W. Ackermann et al., Nat. Photonics 1, 336–342 (2007)
- 2. V. Ayvazyan et al., Eur. Phys. J. D 37, 297–303 (2006)
- 3. K. Tiedtke et al., New J. Phys. 11, 023029 (2009)
- 4. S. Schreiber, in *Proceeding of FEL2011*, Shanghai, pp. 164–165 (2011)
- 5. S. Schreiber, in *Proceedings of FEL2011*, Shanghai, pp. 267–270 (2011)
- E.L. Saldin, E.A. Schneidmiller, M. Yurkov, *The Physics of Free Electron Lasers*. (Springer, Berlin-Heidelberg, 2000)
- 7. A.A. Sorokin et al., Phys. Rev. Lett. **99**, 213002 (2007)
- 8. A.J. Nelson et al., Opt. Express 17, 18271–18278 (2009)
- 9. S. Bajt et al., Photon science (2012), http://photon-science.desy.de/annual_report/
- 10. L. Strüder et al., NIM A 614, 483-96 (2010)
- 11. M. Martins et al., Rev. Sci. Instr. 77, 115108 (2006)
- 12. M. Wellhöfer et al., J. Opt. A. 9, 749 (2007)
- 13. S.W. Epp et al., Phys. Rev. Lett. 98, 183001 (2007)
- 14. A. Singer et al., Phys. Rev. Lett. 111, 034802 (2013)
- 15. S. Hellmann et al., New J. Phys. 14, 013062 (2012)
- 16. N. Gerasimova et al., J. Mod. Opt. 58, 1480 (2011)
- A. Rusydi, M. Rübhausen et al., Screening enhanced hole pairing in Spin = 1/2 two-leg ladder compounds unravelled by high-resolution resonant inelastic X-ray scattering at FLASH (in preparation)
- 18. S. Pauliuk et al., in *Proceedings of EPAC08*, Genoa, pp. 124–26 (2008)
- 19. A.R. Khorsand et al., Opt. Express 18, 700–712 (2010)
- 20. J. Kuba et al., NIM A **507**, 475–78 (2003)
- 21. S.P. Hau-Riege et al., Appl. Phys. Lett. 93, 201105 (2008)
- 22. S.P. Hau-Riege et al., Phys. Rev. E 76, 046403 (2007)
- 23. S.P. Hau-Riege et al., Opt. Express 18, 23933–38 (2010)
- 24. M. Kuhlmann et al., in *Proceedings of FEL 2006*, Berlin, pp. 794–797 (2006)
- 25. B. Flöter et al., NIM A **635**, S108–S111 (2011)
- 26. L. Raimondi et al., in *Proceedings of SPIE Optics* + *Photonics*, San Diego (2013)
- 27. A. Singer et al., Phys. Rev. Lett. 101, 254801 (2008)
- 28. R. Mitzner et al., Opt. Express **16**, 19909–19 (2008)
- 29. R. Ischebeck et al., NIM A 507, 175–180 (2003)
- 30. T. Mey et al., in *Proceedings of SPIE*, vol. 8778, 87780H1-8 (2013)
- 31. B. Schäfer et al., in *Proceedings of SPIE*, vol. 8778, 877810-10 (2013)
- 32. L. Poletto et al., in *Proceedings of SPIE*, vol. 5534, p. 37 (2004)
- 33. M. Richter et al., Appl. Phys. Lett. 83, 2970 (2003)
- 34. K. Tiedtke et al., J. Appl. Phys. 103, 094511 (2008)
- 35. F. Frassetto et al., NIM A 635, S94–S98 (2011)
- 36. G. Brenner et al., NIM A **635**, S99–S103 (2011)
- 37. P. Juranic et al., JINST 4, P09011 (2009)
- 38. M. Wellhöfer et al., JINST 3, P02003 (2008)
- 39. M. Braune, G. Brenner, S. Dziarzhytski, K. Tiedtke, Cross-calibration measurements for online wavelength monitoring at FLASH (in preparation)
- 40. S. Düsterer et al., Phys. Rev. STAB 17, 120702 (2014)
- 41. U. Hahn, K. Tiedtke, in AIP Conference Proceedings, vol. 879, pp. 276–282 (2007)
- 42. S. Düsterer et al., Opt. Lett. 31, 1750-2 (2006)
- 43. B.L. Henke, E.M. Gullikson, J.C. Davis (1992) Atomic Data Nuclear Data Tables 54 181, CXRO website, http://henke.lbl.gov/optical_constants/
- 44. S. Toleikis et al., Photon science (2009), http://photon-science.desy.de/annual_report/
- 45. M. Wöstmann et al., J. Phys. B: At. Mol. Opt. Phys. 46, Special Issue: Frontiers of FEL Science 164005 (2013)

- 46. F. Sorgenfrei et al., Rev. Sci. Instrum **81**, 043107–7 (2010)
- 47. H. Redlin et al., NIM A 635, S88-S93 (2012)
- 48. S. Schulz et al., in *Proceedings of SPIE*, vol. 8778, 87780R1-9 (2013)
- 49. M. Gensch et al., Infrared Phys. Techn. 51, 423-25 (2008)
- 50. B. Faatz et al., NIM A **635**, S2–S5 (2011)
- 51. K. Honkavaara et al., in *Proceedings of FEL2012*, Nara, pp. 381–84 (2012)
- 52. M. Kuhlmann et al., in *Proceedings of SPIE*, vol. 8778, 87781A1-7 (2013)
- 53. E. Plönjes et al., in *Proceedings of FEL2013*, New York (2013)

Chapter 2 The Soft X-ray Free-Electron Laser FERMI@Elettra

Marco Zangrando, Nicola Mahne, Lorenzo Raimondi and Cristian Svetina

Abstract FERMI, the Italian free electron laser (FEL) user facility, delivers high-intensity ultra-short photon pulses in the 100–4 nm range. A diagnostic section called PADReS (Photon Analysis, Delivery, and Reduction System) follows the two undulator chains, giving informations about the photon beam intensity, transverse distribution and coherence, pointing, and energy spectrum. All these quantities are available during the experiments as they are obtained in a non-invasive way on a shot-to-shot basis. The radiation intensity can also be controlled by means of a gas absorber. Moreover, it is possible to split and delay part of the beam to perform auto-correlation measurements determining the pulse length and temporal coherence, as well as to perform pump-probe experiments. Finally, active optics-based systems refocus the photon beam into the endstations.

2.1 Introduction

FERMI, the Italian seeded FEL user facility at Elettra—Sincrotrone Trieste (Italy), has been designed to produce high-quality ultra-short photon pulses in the EUV and soft-X-ray spectral range. Being currently in operation, it has been running for users' operations since the end of 2011, and the first users started to perform experiments

M. Zangrando (⊠)

IOM—CNR and Elettra Sincrotrone Trieste, S.S. 14 km 163.5, 34149 Trieste, Italy

 $e\hbox{-mail:}\ marco.zangrando@elettra.eu$

N. Mahne \cdot L. Raimondi \cdot C. Svetina

Elettra Sincrotrone Trieste, S.S. 14 km 163.5, 34149 Trieste, Italy

e-mail: nicola.mahne@elettra.eu

L. Raimondi

e-mail: lorenzo.raimondi@elettra.eu

C. Svetina

University of Trieste, Graduate School of Nanotechnology, Piazzale Europa 1, 34127 Trieste, Italy e-mail: cristian.svetina@elettra.eu

© Springer-Verlag Berlin Heidelberg 2015

F. Canova and L. Poletto (eds.), Optical Technologies for

Extreme-Ultraviolet and Soft X-ray Coherent Sources, Springer Series

in Optical Sciences 197, DOI 10.1007/978-3-662-47443-3_2

24 M. Zangrando et al.

	P	F		
Parameter	FEL-1	FEL-2	FEL-1 (to date)	FEL-2 (to date)
e-beam energy (GeV)	0.9-1.5		0.9–1.5	
Bunch charge (nC)	0.5-0.8		0.5-0.8	
Peak current (A)	500-800		500-800	
Repetition rate (Hz)	10/50		10	
Wavelength (nm)	100-20	20–4	100-20 ^a	14.4–4
Pulse length FWHM (fs)	30–100	≤100	95 (estimated)	t.b.d.
Bandwidth rms (meV)	20–40	20–40	20 ^b	~60°
Polarization	Variable	Variable	LH-LV-RC-LC	LH-LV-RC-LC
Energy/pulse (μJ)	≥100	≤100a	30–200	100 ^c
Power fluctuations (%)	~25	≥50	10 ^b	50°
Central λ fluct. (meV)	Within BW	Within BW	~3 ^b	~30°
Pointing fluct. (µrad)	≤5	≤5	In specs	In specs
Source size FWHM (µm)	290	140	t.b.d.	t.b.d.
Divergence rms (µrad)	$1.25 \times \lambda$ (nm)	$1.5 \times \lambda$ (nm)	In specs	In specs

Table 2.1 FERMI machine and photon beam parameters

in 2012. The parameters of the machine as well as those of the emitted photon beam are reported in Table 2.1.

The FEL generation is alternated in two parallel undulator chains that share the electron beam produced by a common linear accelerat [1, 2]. The first undulator line (FEL-1) nominally produces coherent radiation in the spectral range from 100 to 20 nm, while the second line (FEL-2) covers the spectral range between 20 and 4 nm (14.4–4 nm actually verified to date). In both cases the wavelength can be tuned continuously on selected energy ranges by operating on the seed laser wavelength. Both undulator chains are based on the high-gain harmonic generation (HGHG) scheme [3] and represent the first high-gain FELs to be operated with APPLE-II radiators [4], providing full control of the FEL polarization state. In particular, they allow the production of on-axis, coherent harmonic emission with both planar and circular polarization [5].

As the HGHG seeding scheme is based on the use of an external UV laser (the seed) that drives the emission of coherent radiation from the undulator chains, the coherence properties of the FEL radiation are directly inherited from the seeding source. This leads to improved longitudinal coherence and stability as compared to existing FEL facilities operating in the same spectral range and typically based on a self-amplified spontaneous emission scheme. In particular, under optimized conditions FERMI can produce FEL pulses close to the Fourier time-bandwidth limit, as confirmed by first results [1]. The use of nonlinear harmonic emission [6],

t.b.d. To be determined

^aWith some limitations depending on the specific working range

^bMeasured at 32.5 nm

^cMeasured at 10.8 nm

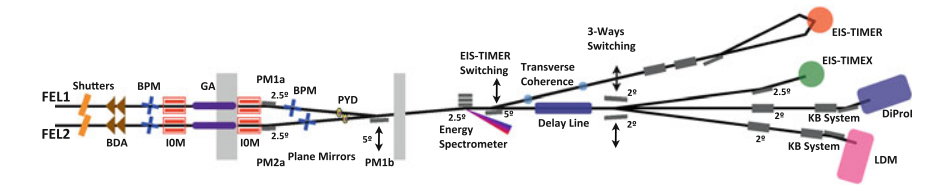


Fig. 2.1 Layout of PADReS. The system is installed after the undulators, and it is devoted to carry the photon beam to the endstations. It includes beam diagnostics and manipulation systems that are described in the text

finally, will further extend the tuning range of FERMI up to a photon energies of $\sim 1\,\mathrm{keV}$.

The spent electron beam, after the undulators, is then sent to the beam dump while the emitted radiation propagates for \sim 15 m to the front-end sections of PADReS (Photon Analysis Delivery and REduction System) [7–9]. The layout of the system is reported in Fig. 2.1.

Each FEL line has a dedicated front-end hosting a shutter, a Beam-Defining Aperture (BDA), and a Beam Position Monitor (BPM). Then, for both FEL lines a differential pumping section, hosting an Intensity Monitor (I0M), ends into a Gas Absorber (GA) section [10]. A following differential pumping section including a second I0M links the GA to the subsequent plane mirror chamber (PM1a for FEL-1 and PM2a for FEL-2). These mirrors deviate the photon beam with respect to the initial undulator trajectory in order to fulfill radiation safety restrictions. As a by-product, in this way it is possible to merge the FEL-1 and FEL-2 optical paths into a common transport system towards the Experimental Hall (EH). A third plane mirror (PM1b) can then be used (for FEL-1; for FEL-2 it is not necessary) to send the beam to the PRESTO (Pulse Resolved Energy Spectrometer: Transparent and Online) that is the first element of PADReS installed in EH. PRESTO covers the wavelength ranges of both FELs with two variable line spacing (VLS) diffraction gratings, sending the non-diffracted beam (0-order) to the beamlines, and using the diffracted part to determine the pulse spectral characteristics [11, 12].

All the above-mentioned diagnostics work non-invasively shot-to-shot, and give pulse-resolved information (tagged by the bunch number). An additional diagnostic dedicated to transverse coherence measurements (not pulse-resolved and invasive) is installed along one of the beamlines.

After PRESTO two switching mirror chambers hosting plane mirrors give the possibility to select one of the four endstations available: EIS-TIMER, EIS-TIMEX, DiProI, and LDM. Before reaching the endstations (except for EIS-TIMER) the photon beam passes through a split-and-delay section where, after a wavefront splitting, the resulting two half-beams are delayed one respect to the other up to tens of ps or ns, depending on the optical configuration selected. At the end, each beamline uses a dedicated refocusing section to focus the photon beam down to several μm onto the samples.

26 M. Zangrando et al.

2.2 Diagnostics

Most of the elements of PADReS are devoted to serve as diagnostic tools during the routine activity of the facility. All the users involved in these activities (machine physicists, people taking care of the transport system, experimentalists) have access to a set of photon beam parameters tagged by the bunch number, and carrying all the available informations about the single pulse. If possible, every diagnostic works online and shot-to-shot, providing information without perturbing the photon beam that is delivered to the endstations.

2.2.1 Beam Position Monitor

The BPMs collect the drain current generated on four metallic blades intercepting the tails of the FERMI photon beam transverse intensity distribution. The four blades are electrically insulated and made of copper, and they are tilted by 20° to avoid ablation. In Fig. 2.2 the mechanical assembly of the BPM is reported.

Being the photon beam transverse distribution Gaussian in both transverse directions, it is possible to calculate precisely its centroid in the space. The spatial resolution is determined by the resolution in measuring the currents generated on the blades (10^{-6} for the picoammeters used at FERMI) and by the minimum mechanical step of the motors controlling the travel of the blades ($1\,\mu$ m in this case). Since a

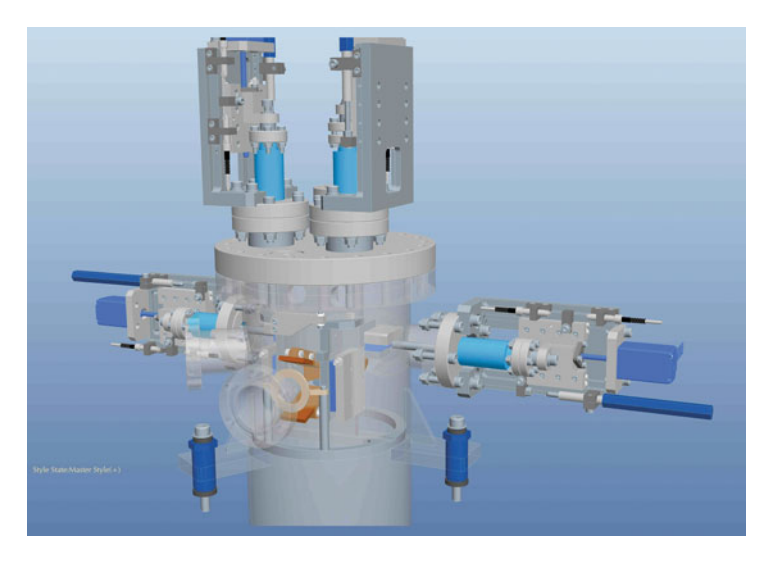


Fig. 2.2 Mechanical drawing of the BPM. The incoming beam enters the BPM vacuum chamber through the flange visible in the forefront. The *tilted brown* plates intercept the tails of the photon beam distribution in the four directions *up*, *down*, *left*, and *right*

transverse displacement of $1\,\mu m$ on the tails of the distribution ($\geq 3\sigma$ from the center) introduces a relative variation of the electrical current as low as 3×10^{-6} , which is already detectable by the picoammeters, the spatial resolution can be conservatively set to $1.5\,\mu m$ rms. Moreover, by the concurrent readings of the second BPM positioned about 9 m after, it is possible to deter-mine the angular movement of the photon beam shot-by-shot with sub- μ rad precision.

2.2.2 Intensity Monitors

Different ways of detecting the photon beam intensity have been implemented at FERMI. In particular, both non-invasive and invasive methods have been used during the machine commissioning to determine the generated number of photon per pulse, often performing cross-check measurements among the different detectors. The adopted solutions span from gas-based monitors, to calibrated photodiodes, to integrated signal from the energy spectrometer, to bolometers and other devices used in the endstations.

The most used diagnostics during normal operation are the gas-based intensity monitors, as they are available online and give shot-to-shot informations. They are simple iom chambers based on the atomic photoionization of a rare gas at low particle density in the range of $10^{11} \, \mathrm{cm}^{-3}$, corresponding to a pressure of $\sim 10^{-5} \, \mathrm{mbar}$. The monitors are practically transparent thanks to the low pressure used for the rare gas, and they do not suffer from saturation effects. Additionally, they do not depend on the beam position fluctuations and they can be used on the whole wavelength range. Finally they can be calibrated providing the absolute number of photons per single pulse. In Fig. 2.3 a mechanical sketch of the IOM as well as a typical intensity acquisition over about 15 min are reported.

The calibration has been carried out using a diagnostic composed by a photodiode (IRD SXUV100), and a 500 μm -thick Ce:YAG fluorescent screen coated with 200 nm of aluminum (to cut the seed laser radiation). This diagnostic has been implemented into PADReS after prior calibration on the BEAR beamline at the Elettra synchrotron radiation facility [13]. Moreover, it has been cross-checked with respect to a calibrated bolometer installed in the experimental hall (ForTech HTS High Speed Thermal detector) with concordant results.

2.2.3 Energy Spectrometer

The energy spectrometer PRESTO, positioned on the common optical path toward the endstations, is equipped with two variable-line-spacing plane gratings, designed to cover (in first order of diffraction) the 100–24 and 27–6.7 nm ranges respectively. An additional plane mirror is also mounted to maximize the throughput, if necessary. The parameters of the optics and the optical characterization of the instrument are



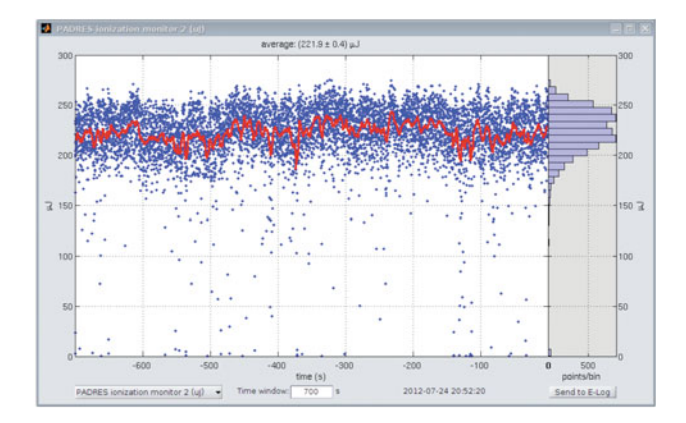


Fig. 2.3 *Left* mechanical drawing of the IOM. The arrow represents the incoming beam, and the two plates forming the ion chamber condenser are visible. *Right* typical behavior of the intensity (in μ J) versus time (in s) as recorded by the intensity monitors through the control system. In this case a time frame of 1000s is recorded at 52.18 nm, giving indications about the absolute intensity and the FEL emission stability

described in detail in [11, 12], while a mechanical representation of the instrument is reported in Fig. 2.4.

The ES is designed to work online and shot-to-shot, delivering $\sim 97\,\%$ of the radiation in 0-order to the following beamlines, while horizontally focusing the diffracted part onto a Ce:YAG crystal, then imaged by a visible-light CCD camera (Hamamatsu C8800-01C high-resolution, 1000×1000 , 12-bit). A double analysis is thus possible from the recorded images: in the vertical direction they represent the (vertical) intensity distribution of the FEL emission, while horizontally they reproduce the spectral distribution of the emitted photon beam. These informations are immediately available during the operations, and have proven to be essential during the entire machine commissioning.

Single-shot spectra have been routinely obtained in the first order of diffraction for all the wavelengths emitted by FEL1 and FEL2, from 65 to 7 nm (up to date). Moreover higher orders of diffraction can be (and were) successfully used to cover broader wavelength ranges than those restricted to the first orders (of both gratings).

By the measurement of the bandwidths at different wavelengths it has been possible to verify that the FERMI FEL emission is close to the transform limit. For example at 43.3 nm the measured single-shot FEL bandwidth was 33.8 meV, while the pulse length was estimated to be \sim 61.2 fs FWHM (seed laser pulse length FWHM, divided by the square root of the seed laser harmonic number: \sim 150 fs $/\sqrt{6}$, at 43.3 nm) [14]. Assuming a Gaussian pulse, the FEL pulse was found to be $1.12\times$ -transform limited, and similar values were found for different wavelengths in the FEL1 emission range.

The spectral stability of the FEL emission in time can also be monitored by the ES, as reported in Fig. 2.5 for a 12 h-long shift at 52 nm. The average measured bandwidth (FWHM) was 27.8 meV, and the maximum deviation of the peak position in energy

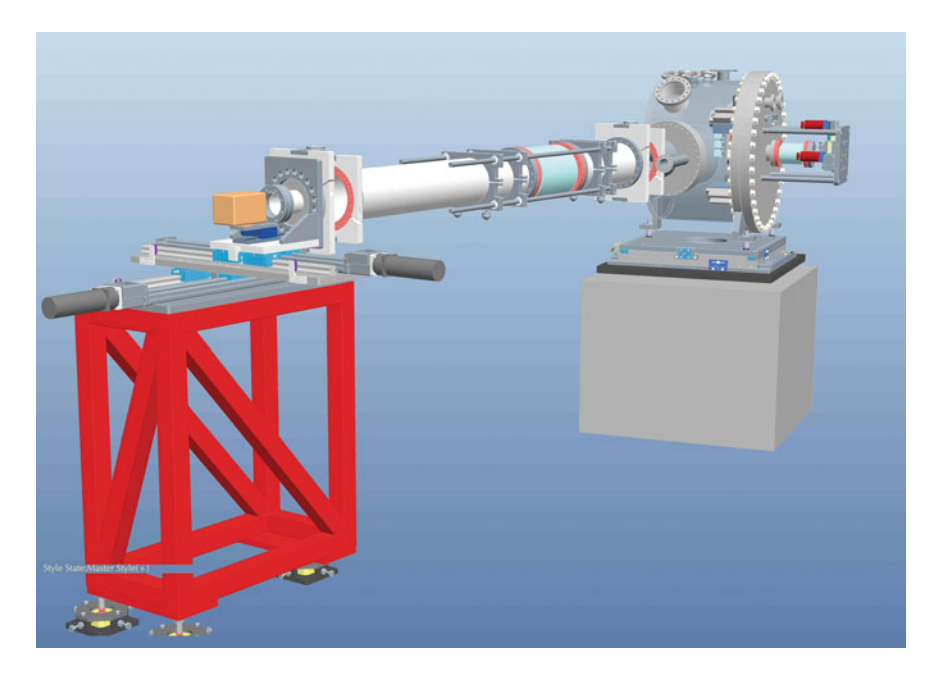


Fig. 2.4 Mechanical drawing of PRESTO, the energy spectrometer. The vacuum chamber, visible on the right side, is endowed with two exit flanges: one for the 0-order reflected radiation, and one for the diffracted radiation. The latter is followed by an adjustable vacuum pipe connecting the main chamber with the movable detector housing, visible on the left side of the figure

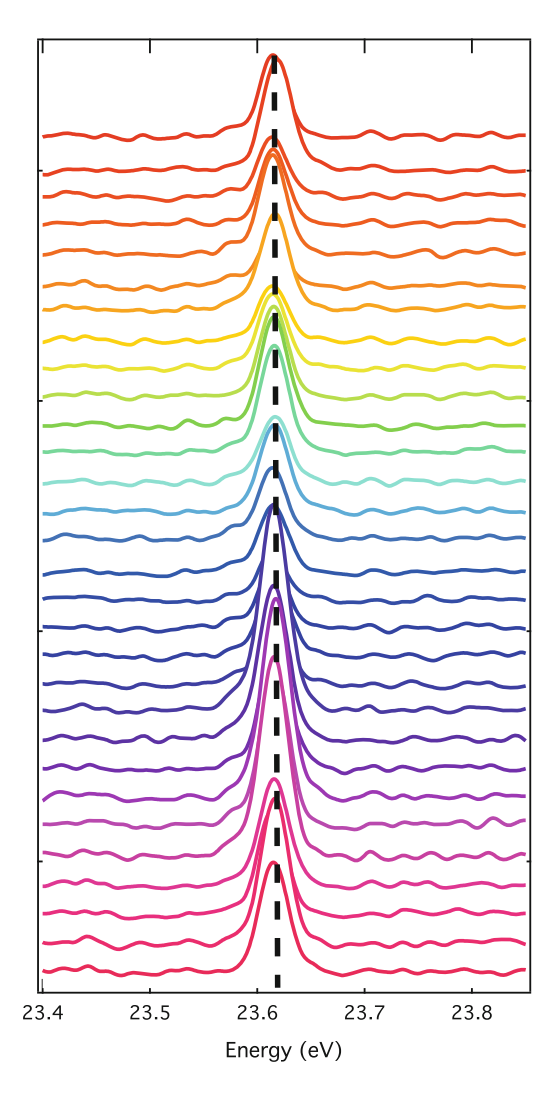
was 5.5 meV, well within the bandwidth itself. Moreover, on shorter timescales, such as minutes, the FEL spectral stability (wavelength and bandwidth) further increases. For instance at 32.46 nm (38.19 eV) 500 consecutive shots (corresponding to 50 s) have shown an emission energy deviation of 1.1 meV rms, leading to a fluctuation of $\sim 3 \times 10^{-5}$ rms on the wavelength. For the same set of spectra, on the other side, the bandwidth, which was measured to be 22.5 meV rms, fluctuated within 3 % rms.

Another possible important measurement deals with the determination of the third harmonic of the FEL emission. As an example, working at 65 nm as the fundamental wavelength it was possible to characterize the third harmonic at 21.7 nm by proper tuning of the ES. The results showed that the intensity of the third harmonic (0.6% of the intensity of the fundamental) and the bandwidth (3× that of the fundamental) are in good agreement with the expectations.

2.2.4 Transverse Distribution

The determination of the transverse spatial distribution of the photon beam has revealed to be crucial for the proper optimization of the machine parameters. The 30 M. Zangrando et al.

Fig. 2.5 Single-shot spectra acquired at an emission wavelength of 52 nm during a 12 h dayshift. The coordinate of the y-axis is the intensity in arbitrary units, while the spectra taken during the shift are vertically displaced for clarity. The vertical dashed line represents a guide for the eye



measurement of the absolute intensity only, in fact, does not guarantee that the machine optimization follows the right path, especially when getting to medium-high intensities (e.g., $0.1-10\,\mathrm{s}\,\mu\mathrm{J}$). In the case of FERMI, for instance, the contribution of photons emitted off-axis can be non-negligible with respect to the central TEM $_{00}$ mode emission, but the gas-based intensity monitors cannot distinguish between on- and off-axis photons. As a consequence, the additional help of some diagnostic devoted to the spatial transverse distribution is mandatory. The solutions chosen at FERMI are two: simple Ce:YAG fluorescent screens and the energy spectrometer.

Several Ce:YAG screens are installed along the photon beam transport (typically after each optical element, when possible). They are insertable into the beam and are

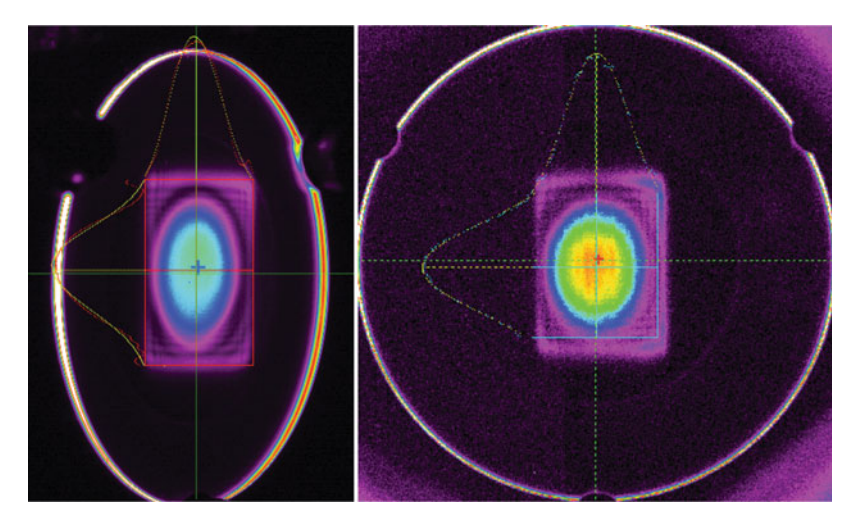


Fig. 2.6 *Left* photon beam profile on a Ce:YAG screen positioned in the safety hutch at the beginning of the experimental hall. The *oval shape*, though the beam hits perpendicularly the screen, is due to the angle of view of the camera. *Right* photon beam profile on a Ce:YAG screen located in the experimental hall. The slightly elongated image in the vertical direction is due to the fact that the screen is inserted into the beam at a 45° incidence angle, while the camera looks perpendicularly to the screen itself

imaged by visible CCD cameras. They are, of course, invasive, and cannot be used during normal operations when the beam should arrive to the endstations. Nonetheless they have been intensively used during the machine commissioning, and they are still used during every beamtime to monitor the FEL emission behavior and to optimize it when needed. In Fig. 2.6 two examples of spot profiles onto YAG screens along the transport system are reported.

On the other side, in order to monitor the transverse distribution online and shot to shot, it is possible to use the energy spectrometer, namely the 2D image produced by the diffraction grating onto a Ce:YAG screen imaged by a CCD camera. As a matter of fact, the spectrometer uses a set of plane gratings (with variable line spacing) to focus shot to shot a small fraction of the photons contained in a single pulse, while the rest of the photons travel unperturbed to the endstations. Consequently, the planar shape of each grating assures that the diffracted photons are focused only in the horizontal direction by the VLS grooves. In the vertical direction, on the contrary, the gratings behave as pure plane mirrors, leading to a distribution on the CCD camera that is simply reproducing the transverse photon beam distribution in the vertical direction (see Fig. 2.7). In this way it is always possible to monitor and record at least the vertical transverse distribution of each single pulse, on an online and shot-to-shot basis.

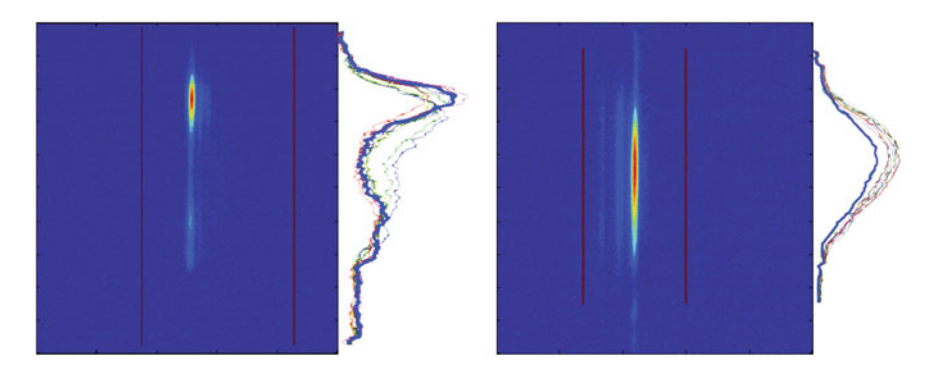


Fig. 2.7 *Left* FEL emission with off-axis components imaged by the spectrometer CCD camera. The *vertical* profile clearly shows how the vertical distribution of the photon beam is markedly off-axis. *Right* FEL emission in standard optimized conditions. The *vertical* profile shows the expected centered Gaussian-like shape

2.2.5 Transverse Coherence

As mentioned, the FEL emission of FERMI is based on the HGHG scheme, in which the seed laser imprints its properties onto the electron beam. In particular, due to the high degree of coherence of the seed laser, a very good transverse coherence is expected for the photon beam. Different transverse profiles of the FEL emission at 32.5 nm were measured on YAG screens placed \sim 52 and \sim 72 m after the last radiator exit. They have confirmed a photon beam very close to be a diffractionlimited Gaussian. In addition, the good degree of transverse coherence has been demonstrated by using a Young's double-slits setup [15] installed in the experimental hall (see Fig. 2.1). This setup consists of a set of vertical slits (with different separation and width) laser-cut into a copper foil (placed at \sim 64 m from the last radiator exit) mounted 8.5 m before a YAG screen collecting the interference patterns (see Fig. 2.8). Preliminary data analysis shows a coherence factor of ~90 %, measured at a 0.8 mmslit separation corresponding to $\sim 0.3\sigma$), reducing to $\sim 50\%$ at a 2 mm-separation $(\sim 0.7\sigma)$. It is of course evident that such a setup to measure the coherence properties of the photon beam cannot be operated online as it is invasive and, moreover, it requires long times both for the alignment and the acquisition.

2.3 Manipulation

PADReS includes, besides the true diagnostics, also a set of instruments and installations whose task is to give the possibility to manipulate the photon beam. In this way it is then possible for the user to modify controllably some parameters (e.g., the intensity), to isolate some portions of the beam (e.g., to get rid of unwanted lateral

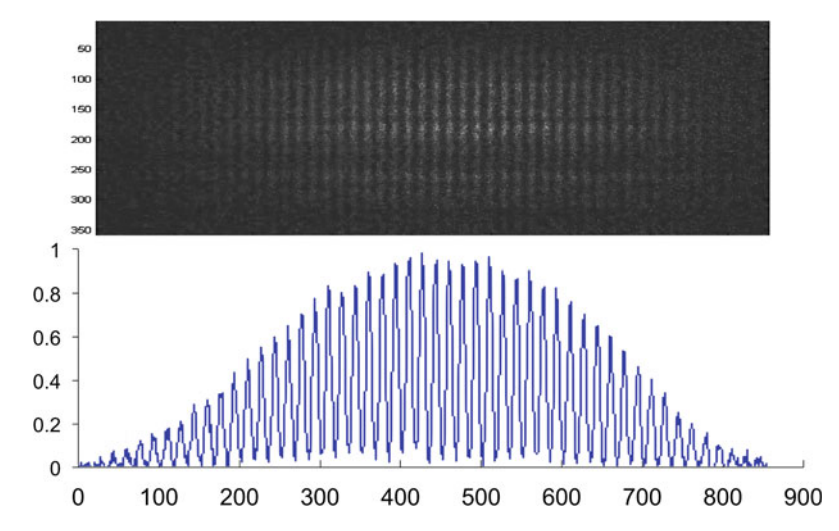


Fig. 2.8 Image and projection of the interference pattern recorded on the second YAG screen when the FEL beam propagates through two $20\,\mu\text{m}$ slits, separated by 0.8 mm, placed about 8.5 m before the screen. The coordinate of the *x*-axis is the pixel number referred to the CCD camera imaging the YAG screen where the interference pattern is imaged

off-axis structures), to introduce a delayed part of the beam itself, to modify the optical properties of the beam so to refocus or collimate it, and so on.

2.3.1 Beam Defining Apertures

The BDAs define the acceptance angle of the incoming photon beam, and particular care has been used in designing them, due to the very high peak power (or fluence) characterizing the FEL photon beam impinging on these elements (\sim 40 mJ/cm² for FEL1 at 20 nm, and \sim 400 mJ/cm² for FEL2 at 5 nm).

They are formed by two copper trunks of pyramid, with a central aperture of each trunk being $20 \times 20 \, \text{mm}^2$ (see Fig. 2.9). The trunks are moved one with respect to the other in order to select the effective aperture, and a complete closure of the total aperture is possible. The central aperture itself, which corresponds to an angular acceptance of 0.6 mrad for FEL-1 and 0.8 mrad for FEL-2, can be moved by $\pm 12.5 \, \text{mm}$ around the ideal axis in order to give the possibility to explore also off-axis emission structures of the FEL. The pyramidal shape has been selected so to guarantee a grazing incidence angle of the radiation on the trunks, avoiding possible radiation damage [7].

34 M. Zangrando et al.

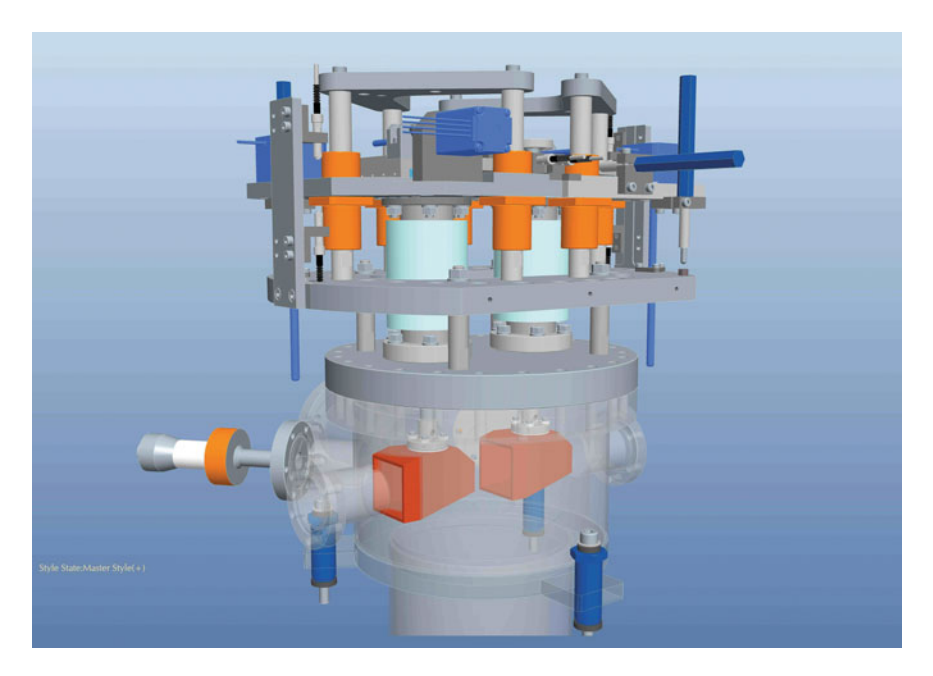


Fig. 2.9 Mechanical drawing of the beam defining apertures setup. The two trunks of pyramid are clearly visible inside the vacuum chamber. Each of them is moved in the two directions perpendicular to the direction of propagation of the photon beam

2.3.2 Gas Absorber

The high peak power of the pulses delivered by the FELs require the possibility to actively control the photon beam intensity over several orders of magnitude, for different reasons such as sample alignment or fluence-dependent studies. In order to accomplish this task, a 5.5 m-long pipe (positioned between the two I0Ms of each FEL) can be filled by a properly selected gas (different gases are used to cover the entire wavelength range) in order to achieve a reduction factor of 10^{-4} for every wavelength emitted by the machine. The gas pressure can be dosed in the range 10^{-7} to 0.1 mbar, having two differentially-pumped sections (before and after the GA itself) to maintain the ultra high vacuum level in the other systems along the photon beam transport paths [10].

In order to monitor the effective damping factor achieved at a certain gas pressure within the GA, the ratio of the I0M2 and I0M1 intensities is recorded online during the experiments. In Fig. 2.10 the typical behavior of the I0M2/I0M1 ratio versus the pressure inside the GA is reported (in this case for 32.5 nm, using N_2).

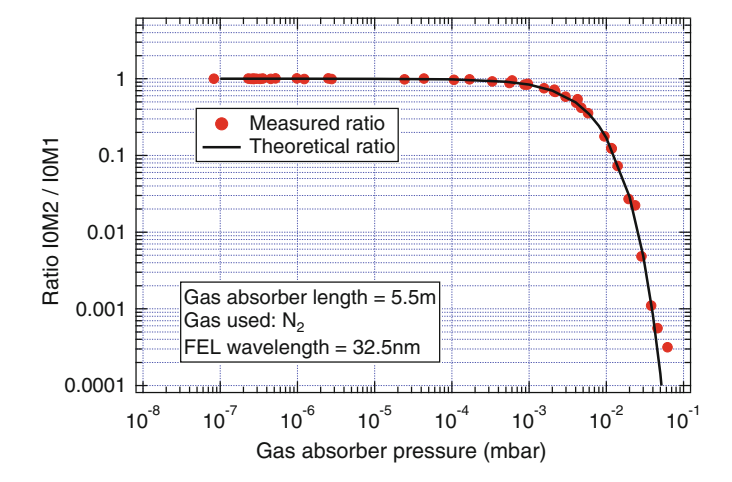


Fig. 2.10 Ratio of the photon beam intensities measured by I0M2 and I0M1 plotted versus the N_2 pressure inside the GA (in mbar). The data refer to a 32.5 nm-wavelength photon beam. The theoretical values, as calculated by the CXRO toolset, are also reported

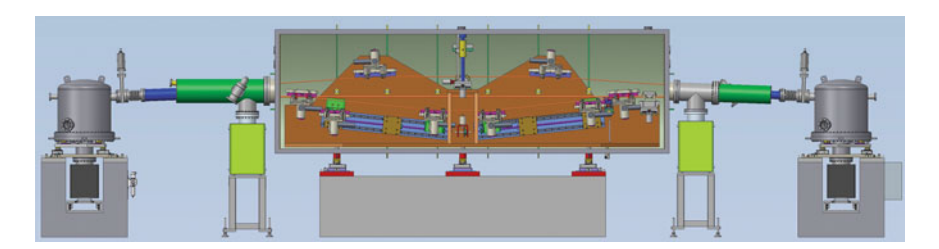


Fig. 2.11 Mechanical drawing of the split and delay line as seen from a side. The two satellite vacuum chambers host the mirrors in charge of splitting and recombining the photon beam, which in the middle follows the two different optical paths

2.3.3 Split and Delay Line

The split and delay line that will be installed at FERMI is based on the wavefront splitting operated by a knife-edge mirror working at grazing incidence angle that splits the beam in two semi-beams. These semi-beams travel different optical paths and are subsequently recombined by a mirror similar to the splitting one, and sent forward on the same optical travel to the endstations. One of the two optical paths is variable by moving concordantly two mirrors along two mechanical guides. In this way it is possible to introduce a temporal delay ranging from -2 to ~ 30 ps. All the optics used to create the two optical paths are plane mirrors working at grazing incidence angles of 2° or 3° (see Fig. 2.11).

36 M. Zangrando et al.

The delay range set by the grazing plane mirrors can be further increased by introducing additional differences in the two main optical paths. This can be done using, on each path, a dedicated small delay line based on 4 multilayer-coated optics working at 45°-incidence angle that introduces an additional travel of tens of centimeters. By the proper choice of the dimensions of these delay lines, and even implementing the possibility to control the delay in one of the two, it is possible to extend the delay range up to 1.3 ns. The drawback in using the multilayer-based optics is that, differently from when using only grazing incidence mirrors, only some wavelengths are allowed, due to the typical narrow-band reflectivity of the multilayer optics themselves.

2.3.4 Focusing Mirrors

The photon radiation, as emitted from the undulators, apart from passing through plane mirrors as described before, is not focused until the very last vacuum chambers before the endstations, and this is true for all the different branchlines. The distances of the endstations from the effective photon sources (FEL-1 and -2) are about $97 \pm 4 \,\mathrm{m}$. In order to reduce as much as possible the achievable spot sizes, the demagnification factors (e.g., the ratio between the distances [source–refocusing optic] and [refocusing optic–focus]) should be kept quite high, meaning that the distances between the refocusing optics and the focal points are of the order of 1.5 m. These high demagnifications pose some constrains on the choice of the shape to be adopted for the refocusing mirrors.

At FERMI, when there was the indication to use just one single optic to refocus the radiation, avoiding additional reflections and consequently additional intensity losses, an ellipsoidal shape was selected. As known, the elliptical shape is nearly aberration-free when working with the photon source and the photon focus positioned in the two focii of the ellipse itself. This can be generalized in three dimensions using an ellipsoidal shape. This kind of shape is very demanding in terms of manufacturing as it is requested to produce a portion of the ellipsoid very far from the central part located in the middle between the two focii, keeping the optical quality very good (e.g., slope error rms $\leq 1\,\mu$ rad in this case). This kind of optic has been chosen for the EIS-TIMEX endstation where the interest is specifically directed to the highest fluence achievable (smallest spot).

On the other hand, two other endstations (DiProI and LDM) are more interested in the full control of the spot size in different conditions. In particular, they use an active-optics Kirkpatrick-Baez (KB) refocusing system [16] that focuses the radiation independently in the horizontal and vertical plane. Each of these systems is endowed by two thin plane mirrors (thickness = $10 \, \text{mm}$; optical surface dimensions $400 \times 40 \, \text{mm}^2$) that are bent through mechanical pushers acting on clamps holding them in place and acting on the shorter edges of the mirrors (see Fig. 2.12). With this solution several advantages can be obtained: the two focusing planes are decoupled (easier alignment on the sample), the mirror parameters can be adjusted in order to

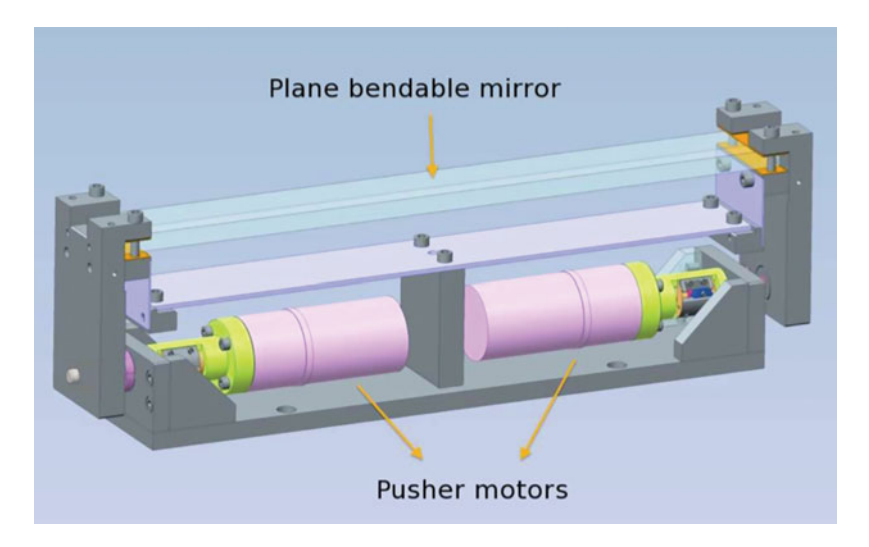


Fig. 2.12 Holder of one of the KB mirrors used to refocus the radiation in the endstations. Just two mechanical pushers are enough to deform the mirror to the required shapes

optimally focus the two different FEL sources (adaptivity), the surface quality can be the highest possible as the mirrors are manufactured in the plane shape and then curved (spot quality).

Different techniques can be used to determine and characterize the spot dimensions, and several campaigns of measurements have been carried out at FERMI on this topic. A rough estimation of the spot size can be made using Ce:YAG and/or phosphor fluorescent screens placed in the focal plane. This kind of techniques suffers heavily from the damaging induced almost immediately on the used substrates by the highly intense FEL radiation, even in single shot mode (reaching power densisties as high as 10^{15} – 10^{16} W/cm²). Nonetheless, with this type of diagnostics it is possible to determine a higher value for the spot size in the 30– $50\,\mu$ m range. Most of the limitations come from mainly two problems: some saturation effect due to the screen materials (phosphor or YAG) in the image acquisition, and a spot broadening due to the non-homogeneity of the screen surfaces after few FEL shots.

Consequently, if a smaller spot is needed by the experimentalists, then additional tools should be used. In particular, the single-shot damaging of a selected substrate (like PMMA or bare silicon) can be used to analyze in more detailed, and with higher spatial resolution, the spot size and shape. With this technique features as small as few μm can be resolved, leading to a proper determination (and optimization) of the spot size. The drawback of this kind of post-mortem analysis is the time consumption: the damaged samples, most of the times, need to be taken out from the vacuum chambers and then analyzed with proper microscopes (AFM, Nomarski, etc.).

In order to avoid these dead times, another way to precisely measure the spot size, and to optimize it, is the use of a wavefront Hartmann sensor [17]. This diagnostic

38

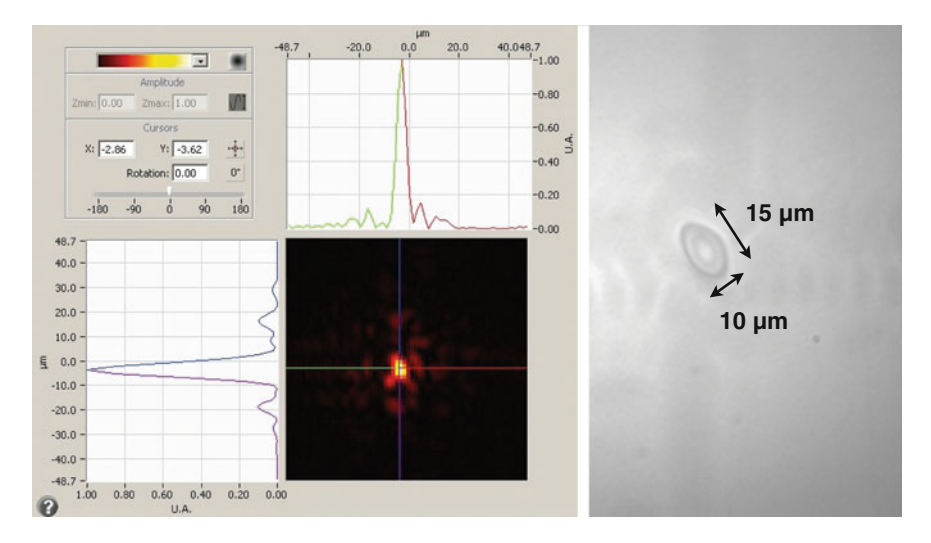


Fig. 2.13 Left reconstruction of the spot shape and size with the wavefront sensor software, analyzing data taken with a radiation of 32.5 nm. The estimated spot size FWHM is $5 \times 8 \, \mu \text{m}^2$. Right single shot indentation of a PMMA substrate in the same conditions as in the left pane. The dimensions refer to the "whole peak" widths

consists of an array of pinholes (typically, \sim 80 μ m-pinholes distributed in 2D with a pitch of $\sim 250 \,\mu$ m) that splits the incoming wavefront into several individual beams that are imaged by a CCD camera (typical field of view of $\sim 10 \times 10 \,\mathrm{mm}^2$). From the analysis of the image, namely taking into account the deviations of each single beam with respect to a reference position, it is possible to reconstruct the wavefront hitting the pinhole array. This instrument can be placed conveniently extra-focus by some tens of cm, so to be used online and without any interference with a possible experiment going on in the focal region. With this diagnostic it is then possible, and it has been done at FERMI, to determine the spot sizes with sub µm-resolution, leading also to the ideal optimization of the bendable mirrors used in the KB systems. In Fig. 2.13 it is reported (Left) the reconstruction of the spot at 32.5 nm via the wavefront sensor software controlling the instrument. With this tool it has been possible to reduce the final spot sizes down to a value ($5 \times 8 \,\mu\text{m}^2$ FWHM) close to the diffraction limit of the equivalent optical system, being also close to the mechanical limit of the system itself. To confirm these results, in the same optical configuration it has been also damaged a PMMA substrate in single shot mode, analyzing subsequently the indentations on the surface. A typical result is shown in the right pane of the same Fig. 2.13, where the "whole peak" widths of the pulse are indicated.

2.4 Conclusions

New generation lightsources like the free electron lasers currently represent the state of the art in terms of the emission of ultra-intense ultra-short light pulses in the extended x-rays range (EUV to hard x-rays). These facilities are spreading world-wide, having some of them already operative, and others in the design or realization phases. In most of the cases the target is to serve a fast-growing community of users, providing them the tools to perform new and innovative experiments. Besides the machine physics and physicists needed to achieve the goal of having stable, reliable, and reproducible sources, another target is to have the possibility of actually monitor and characterize the produced radiation. In order to do that, more and more efforts are spent to realize diagnostics and instruments capable of accurately determine the photon beam parameters, ideally without perturbing the beam itself.

In this chapter the diagnostics and the photon beam manipulation systems of FERMI (PADReS) have been presented and discussed. Whenever possible, they are operated online giving shot-to-shot informations about each single pulse that is then delivered to the endstations. Currently, PADReS is operative on FEL-1 and FEL-2, and it is used by both machine physicists and endstation experimentalists to determine, improve, and exploit the photon beam properties.

References

- E. Allaria, R. Appio, L. Badano, W.A. Barletta, S. Bassanese, S.G. Biedron, A. Borga, E. Busetto, D. Castronovo, P. Cinquegrana, S. Cleva, D. Cocco, M. Cornacchia, P. Craievich, I. Cudin, G. D'Auria, M. Dal Forno, M.B. Danailov, R. De Monte, G. De Ninno, P. Delgiusto, A. Demidovich, S. Di Mitri, B. Diviacco, A. Fabris, R. Fabris, W.M. Fawley, M. Ferianis, E. Ferrari, S. Ferry, L. Froehlich, P. Furlan, G. Gaio, F. Gelmetti, L. Giannessi, M. Giannini, R. Gobessi, R. Ivanov, E. Karantzoulis, M. Lonza, A. Lutman, B. Mahieu, M. Milloch, S.V. Milton, M. Musardo, I. Nikolov, S. Noè, F. Parmigiani, G. Penco, M. Petronio, L. Pivetta, M. Predonzani, F. Rossi, L. Rumiz, A. Salom, C. Scafuri, C. Serpico, P. Sigalotti, S. Spampinati, C. Spezzani, M. Svandrlik, C. Svetina, S. Tazzari, M. Trovò, R. Umer, A. Vascotto, M. Veronese, R. Visintini, M. Zaccaria, D. Zangrando, M. Zangrando, Nat. Phot. 6, 699 (2012)
- E. Allaria, D. Castronovo, P. Cinquegrana, P. Craievich, M. Dal Forno, M.B. Danailov, G. D'Auria, A. Demidovich, G. De Ninno, S. Di Mitri, B. Diviacco, W.M. Fawley, M. Ferianis, E. Ferrari, L. Froehlich, G. Gaio, D. Gauthier, L. Giannessi, R. Ivanov, B. Mahieu, N. Mahne, I. Nikolov, F. Parmigiani, G. Penco, L. Raimondi, C. Scafuri, C. Serpico, P. Sigalotti, S. Spampinati, C. Spezzani, M. Svandrlik, C. Svetina, M. Trovò, M. Veronese, D. Zangrando, M. Zangrando, Nat. Phot. 7, 913 (2013)
- 3. L.H. Yu, Phys. Rev. A 44, 5178 (1991)
- 4. S. Sasaki, Nucl. Instrum. Methods A 347, 83 (1994)
- C. Spezzani, E. Allaria, M. Coreno, B. Diviacco, E. Ferrari, G. Geloni, E. Karantzoulis, B. Mahieu, M. Vento, G. De Ninno, Phys. Rev. Lett. 107, 084801 (2011)
- R. Bonifacio, L. De Salvo Souza, P. Pierini, E.T. Scharlemann, Nucl. Instrum. Methods A 296, 787 (1990)
- M. Zangrando, A. Abrami, D. Bacescu, I. Cudin, C. Fava, F. Frassetto, A. Galimberti, R. Godnig, D. Giuressi, L. Poletto, L. Rumiz, R. Sergo, C. Svetina, D. Cocco, Rev. Sci. Instrum. 80, 113110 (2009)

40 M. Zangrando et al.

8. D. Cocco, A. Abrami, A. Bianco, I. Cudin, C. Fava, D. Giuressi, R. Godnig, F. Parmigiani, L. Rumiz, R. Sergo, C. Svetina, M. Zangrando, in *Proceedings SPIE*, vol. 7361, 736106 (2009)

- 9. M. Zangrando, I. Cudin, C. Fava, S. Gerusina, R. Gobessi, R. Godnig, L. Rumiz, C. Svetina, F. Parmigiani, D. Cocco, in *Proceedings SPIE*, vol. 8078, 80780I (2011)
- L. Rumiz, D. Cocco, C. Fava, S. Gerusina, R. Gobessi, E. Mazzucco, F. Zudini, M. Zangrando, in *Proceedings IPAC*, vol. 2011, 1530 (2011)
- C. Svetina, A. Abrami, I. Cudin, C. Fava, S. Gerusina, R. Gobessi, L. Rumiz, G. Sostero, M. Zangrando, D. Cocco, in *Proceedings SPIE*, vol. 8139, 81390J (2011)
- 12. C. Svetina, D. Cocco, N. Mahne, L. Raimondi, F. Parmigiani, M. Zangrando, in preparation (2013)
- S. Nannarone, F. Borgatti, A. DeLuisa, B.P. Doyle, G.C. Gazzadi, A. Giglia, P. Finetti, N. Mahne, L. Pasquali, M. Pedio, G. Selvaggi, G. Naletto, M.G. Pelizzo, G. Tondello, in AIP Conference Proceedings, vol. 705, 450 (2004)
- 14. D. Ratner, A. Fry, G. Stupakov, W. White, Phys. Rev. ST Accel. Beams 15, 030702 (2012)
- 15. J.W. Goodman, Statistical Optics (Wiley-Interscience, New York, 1985)
- 16. P. Kirkpatrick, A.V. Baez, Appl. J. Opt. Soc. Am. 38, 766 (1948)
- B. Flöter, P. Juranić, S. Kapitzki, B. Keitel, K. Mann, E. Plönjes, B. Schäfer, K. Tiedtke, New J. Phys. 12, 083015 (2010)

Chapter 3 Overview on Attosecond Sources

Francesca Calegari, Giuseppe Sansone and Mauro Nisoli

Abstract In the last decade dramatic progress has been achieved in the field of attosecond technology, due to breakthroughs in ultrafast laser science and to the introduction of novel experimental techniques for the characterization and application of extreme ultraviolet attosecond pulses, produced by high-order harmonic generation in noble gases. This chapter will review recent experimental progress in the field of attosecond sources.

3.1 Introduction

High-order harmonic generation (HHG) in gases is a widely used technique for the generation of attosecond pulses. In the last decade extreme-ultraviolet (XUV) attosecond pulses have been employed for the investigation of ultrafast electron dynamics in atoms, molecules and solids [1, 2]. Attosecond science is now a well-established research field, which offers formidable tools for the investigation and control of fundamental atomic and sub-atomic electron processes. Novel experimental approaches have been proposed and implemented in order to achieve time-resolved imaging of electronic and molecular structures. In this contest, the exploitation of the recollision physics, in combination with optical science, offers the possibility to observe, with sub-Angstrom resolution, atomic and molecular orbitals [3].

F. Calegari (⊠)

National Research Council of Italy, Institute of Photonics and Nanotechnologies (CNR-IFN), L. da Vinci 32, 20133 Milano, Italy e-mail: francesca.calegari@polimi.it

G. Sansone · M. Nisoli Department of Physics, Politecnico di Milano and National Research Council of Italy Institute of Photonics and Nanotechnologies (CNR-IFN), Piazza L. da Vinci 32, 20133 Milano, Italy

e-mail: giuseppe.sansone@polimi.it

M. Nisoli e-mail: mauro.nisoli@polimi.it In this chapter we will review recent experimental progress in the field of attosecond sources. Section 3.2 briefly describes various techniques for the generation of few-optical-cycle pulses with high-peak-power, required for the production of attosecond pulses. Section 3.3 presents a description of the physical processes at the basis of HHG and attosecond pulse generation, together with an overview of the theoretical model used for the numerical simulation of the XUV generation process. Various techniques used to confine the harmonic generation process to a single event are described in Sect. 3.4.

3.2 Ultrafast Laser Technologies for the Generation of Attosecond Pulses

Ultrashort laser pulses with stabilized carrier envelope phase (CEP) are a fundamental prerequisite for the generation of attosecond pulses. A typical Ti:sapphire laser system based on chirped pulse amplification (CPA) routinely delivers 20 fs, 800 nm, CEP-stabilized pulses at the multi-millijoule level. Shortening the pulse duration to sub-10 fs requires a post-compression stage. In order to improve the photon flux of the attosecond sources, efforts have been made to increase the energy of the broadband driving pulses and different approaches for post-compression have been developed. A promising alternative for the generation of ultrashort laser pulses is offered by the optical parametric chirped pulse amplification (OPCPA) technique, which combines optical parametric amplification and CPA in order to obtain few-optical cycle pulses with peak power up to the petawatt level.

3.2.1 Pulse Compression Techniques

The most common technique for pulse compression of high-energy femtosecond pulses is based on propagation in a gas-filled hollow-core fiber (HCF) in combination with ultrabroadband dispersion compensation. This method requires a long interaction length (~1 m) and peak intensity below 10¹⁴ W/cm² to avoid ionization. The first demonstration of this compression technique was achieved in 1996: 10 fs, 0.24 mJ pulses were obtained starting from 140 fs, 0.66 mJ input pulses [4]. To date, sub-5 fs durations associated with pulse energies close to 1 mJ are available in many laboratories. The peak intensity of the input pulses is limited by self focusing and plasma generation. Both processes can occur near the entrance of the fiber, thus giving rise to filamentation which degrades the spatial beam quality and results in a less efficient coupling into the fiber. In order to overcome this problem and boost the output energy beyond the millijoule level, several strategies have been adopted. In 2005 Suda and co-authors [5] proposed and demonstrated a method to compress multi-mJ pulses based on the use of an HCF with pressure gradient.

In this configuration, the gas cell of the HCF is divided in two parts: the first cell is evacuated in order to avoid nonlinear processes at the fiber entrance, and the second cell is filled with a continuous flow of noble gas. Pressure gradient in combination with chirped pulses was implemented in 2010 in order to obtain 5 fs, 5 mJ pulses [6]. The use of circularly polarized light was also proposed to reduce ionization at the fiber entrance and an increase of 30% in the throughput compared to the linearly polarized light was demonstrated [7]. A progress in scaling this post-compression technique to higher peak intensities (>10¹⁵ W/cm²) has been recently obtained by using spectral broadening induced by gas ionization in an HCF filled with helium at low gas pressure (a few millibars). The experiment was performed by using 70 mJ, 40 fs input pulses, the hole setup was maintained under vacuum to avoid ionization outside the HCF and He gas was injected through a hole in the capillary well. In this configuration an output pulse energy of 13.7 mJ and a pulse duration of 11.4 fs were obtained [8].

Recently Wirth et al. proposed and demonstrated a more sophisticated approach to obtain almost single-cycle pulses [9]. The idea is to generate a coherent supercontinuum (ranging from 330 to 1100 nm) by using a gas-filled HCF and to separately compress different spectral regions by using properly designed dispersive chirped mirrors. By using this light field synthesizer a complete control of the electric field on the sub-cycle temporal scale has been demonstrated.

3.2.2 Optical Parametric Amplification

CPA based Ti:sapphire laser systems are currently the most common sources for driving the HHG process. Although CPA scheme in combination with postcompression techniques allows one to obtain few-optical cycle pulses in the millijoule range, these laser sources have a few limitations including frequency tunability in a narrow range around 800 nm, power scalability in the post-compression step and demand for active electronic stabilization of CEP using two separate feedback loops. A different approach for the generation of few-optical cycle, high-peak power pulses with stable CEP is based on optical parametric amplification (OPA) [10]. Several schemes have been developed for the generation of near infrared (IR) pulses. In the OPA process the pump beam (angular frequency ω_p) generates the idler beam at ω_i and transfer energy to the signal (seed) beam at ω_s which is amplified. Energy conservation requires that $\omega_i = \omega_p - \omega_s$ and momentum conservation leads to the phase-matching condition: $\Delta \mathbf{k} = \mathbf{k}_p - \mathbf{k}_i - \mathbf{k}_s = 0$, where \mathbf{k}_p , \mathbf{k}_i and \mathbf{k}_s are the wave vectors of pump, idler and signal. If signal and idler have parallel polarizations phase matching is achieved in Type I configuration, on the other hand Type II phase matching requires that signal or idler is polarized parallel to the pump beam. In near-IR OPA Type I phase matching is generally used for broadband amplification, while Type II phase matching allows tunability of the central wavelength over a broad range. The group velocity mismatch (GVM) between pump and signal or idler limits the maximum interaction length and thus the amplification, and the GVM

between idler and signal limits the phase matching bandwidth. To overcome this last problem and to obtain a broadband amplification, a non collinear configuration can be adopted (NOPA).

 β -Barium Borate (BBO) is the most common uniaxial crystal employed for OPA in the near-IR and, because of the availability of large pump energies from CPA Ti:sapphire systems, a pumping wavelength of 800 nm is often used. A scheme for the generation of high-energy, CEP-stabilized few-optical cycle pulses in the near-IR has been proposed and demonstrated in 2007 [11]. In this approach a CEP-stable seed is produced by difference frequency generation (DFG) between different components of a supercontinuum obtained by optical filamentation of 800 nm pulses in a gas cell. The energy of the near-IR pulses produced by DFG is boosted with two OPA stages operated around degeneracy and with a broadband gain in the near-IR. Starting from a CPA-based Ti:sapphire laser system (60 fs, 10 mJ, 800 nm, 10 Hz), the generation of 1.2 mJ, 17 fs, CEP-stable pulses with a carrier wavelength tunable between 1.3 and 1.7 μ m has been demonstrated. In principle this approach can be scaled to the multi-mJ level by increasing the pumping energy and the number of OPA stages, thus reaching the terawatt (TW) level in the near-IR.

Higher peak intensities can only be achieved by integrating CPA and OPA in an optical parametric chirped pulse amplification (OPCPA) technique, which combines the advantages of both amplification methods [12–15]. In a typical OPCPA design a broadband seed is stretched to a temporal duration in the 10–100 ps range. Parametric amplification occurs in a nonlinear crystal with a quasi-monochromatic high-energy pump pulse and the subsequent compression of the amplified pulse leads to a peak power up to the PW level. OPA is an instantaneous process which requires seed and pump pulses to have similar durations and to be simultaneously present in the nonlinear crystal. The direct consequence of the first requirement is the demand for pump lasers with temporal durations much shorter compared to pump lasers used for Ti:sapphire systems, thus custom pump lasers operating in the 10–100 ps range have been developed. Moreover a temporal synchronization between the two pulses with sub-ps accuracy is required. The pump-seed synchronization can be achieved either by using the same laser (output of a broadband Ti:sapphire oscillator) as a seed for the OPCPA and for the pump laser [16, 17] or by using electronic stabilization with active feedback loops [18, 19].

This amplification scheme is a valuable alternative to the conventional CPA scheme (combined with a post compression stage) to obtain powerful few-optical cycle pulses for the generation of bright attosecond pulses.

Broadband amplification in the near-IR and mid-IR has been demonstrated by using KTA or KTP crystals pumped by Nd:YLF (1053 nm) or Nd:YAG (1064 nm) lasers. Few-optical cycle, 8 mJ pulses at 3.9 μ m carrier wavelength have been generated by using a KTA based OPCPA in combination with a CPA femtosecond laser in an hybrid configuration [20]. The front end of the system is a Yb:CaF₂ CPA amplifier followed by a cascade of three KTP based OPAs producing 65 μ J, 1460 nm seed pulses for a two-stages OPCPA. The near-IR seed pulse is stretched by a negative dispersion grating pair and subsequently amplified up to 0.5 mJ with a first OPCPA stage based on a 10 mm long KTA crystal and pumped by 50 mJ, 1064 nm pulses.

The amplified signal is used to seed a second OPCPA stage pumped by 175 mJ pulses and producing uncompressed 22 mJ, 1.46 μ m (signal) and 13 mJ, 3.9 μ m (idler) pulses. After compression the 3.9 μ m pulses have a temporal duration of about 80 fs. Using this powerful source in the mid-IR to drive the HHG process, the generation of bright, coherent radiation with photon energies above 1 keV has been obtained [21].

Waveform synthesis based on the coherent combination of two CEP-stable, few-optical cycle pulses obtained from a near-infrared (NIR) OPCPA and a short-wavelength infrared (SWIR) OPCPA has been demonstrated [22]. The generated optical waveform has a non-sinusoidal temporal shape, a two-octave spanning spectrum and an energy of $15~\mu J$ at a repetition rate of 1~kHz.

A further step in the development of waveform controlled, few-optical cycle pulses with PW peak power for the generation of bright attosecond pulses is represented by the petawatt field synthesizer (PFS). This laser source based on OPCPA technology is currently under construction and it is designed to deliver 5 fs pulses with an energy of 3 J at a repetition rate of 10 Hz [23].

3.2.3 Carrier-Envelope Phase Stabilization

The electric field of a laser pulse can be written as:

$$E(t) = E_0(t)\cos(\omega_0 t + \phi) \tag{3.1}$$

where $E_0(t)$ is the envelope, ω_0 is the carrier frequency and ϕ is the CEP, which is defined as the offset between the maximum of the envelope and the maximum of the carrier wave. Stable and reproducible attosecond pulse generation trough HHG with few-optical cycle pulses requires CEP stabilization. CEP stability can be obtained with active or passive methods: in the first case electronic feedback loops are required, while in the second case CEP fluctuations are automatically cancelled with the DFG process, all-optically.

Active stabilization of Ti:sapphire laser system based on CPA is achieved with two feedback loops: a fast-loop to phase-stabilize the laser pulses at the output of the oscillator and a slow-loop to compensate for CEP fluctuations introduced by the amplification process [24–26].

In a conventional Ti:sapphire oscillator the absolute phase changes from pulse to pulse. Indeed, each time the pulse travels in the cavity through the active medium a mismatch between the group velocity and the phase velocity occurs, so that a systematic pulse-to-pulse CEP slippage $\Delta\phi$ is present at the output of the cavity. In this picture consecutive pulses should be characterized by a constant $\Delta\phi$, however energy fluctuations of the pump laser translate into additional CEP fluctuations by means of the nonlinear Kerr effect inside the rod. Conventionally, in the fast-loop, CEP control is achieved in three steps: (i) measurement of $\Delta\phi$; (ii) stabilization of $\Delta\phi$ using an electronic feedback on an acousto-optic modulator (AOM), which

adjusts the oscillator pump power; (iii) selection of pulses every $2\pi/\Delta\phi$ round trips, sharing the same CEP for amplification.

The CEP variation $\Delta\phi$ can be derived from the corresponding carrier envelope offset frequency $\nu_{ceo} = \nu_{rep} \Delta\phi/2\pi$, where ν_{rep} is the repetition rate. Indeed, ν_{ceo} can be obtained by measuring the heterodyne beat note signal resulting from the interference between the fundamental f and the second harmonic 2f components of the frequency comb corresponding to the mode-locked pulse train. If the output of the oscillator is not octave-spanning, spectral broadening can be achieved by Self Phase Modulation (SPM) in a photonic crystal fiber (PCF) [27]. A monolithic scheme for CEP stabilization has also been demonstrated: the output of a Ti:sapphire oscillator is tightly focused in a periodically poled magnesium-oxide-doped lithium niobate (PP-MgO:LN) crystal to induce SPM and DFG in the near-IR. In the region of spectral overlap between the broadened fundamental and the DFG signal an interferometric beat note is produced and CEP locking can be obtained [28]. Compared to the conventional f-2f approach, this method obviates the need for coupling in a PCF, splitting a portion of the laser for CEP control, and recombining the spectral components with an interferometer.

A different method for CEP stabilization of a free-running femtosecond oscillator has been recently demonstrated [29]. In this approach an acousto-optic frequency shifter (AOFS) for comb synthesis is used to split the output of the oscillator in zero-order (30–40%) and first-order (60–70%) beams by diffraction. The first-order is used for applications while the zero-order serves to measure the carrier envelope offset frequency. The measured ν_{ceo} is sent to the AOFS in order to shift the first-order beam to zero offset, thus cancelling the phase fluctuations for each pulse. Compared to other active methods, this scheme does not require complicated electronics and can be applied to any type of mode-locked laser.

Due to pump energy fluctuations which are responsible for refractive index changes in the active medium of the amplifier, a slow CEP drift is introduced by the amplification [30]. For this reason most of the CPA systems with CEP control are equipped with a second feedback known as slow-loop [31]. CEP drift is detected with a collinear f-2f in which an octave spanning continua is generated by SPM in a sapphire plate [32] and second harmonic generation (SHG) is subsequently performed in a BBO crystal. The spectral fringes generated in the green portion of the spectrum are recorded with a spectrometer and $\Delta \phi$ can be extracted by Fourier processing the data [33]. The slow feedback loop can be used to control the AOM in the oscillator cavity or the position of glass wedges situated before the amplifier. An efficient control of CEP in a CPA laser system featuring an acousto-optic programmable dispersive filter (AOPDF) has been also demonstrated [34].

Passive CEP stabilization, pioneered by Baltuška et al. [35], is based on the process of DFG, in which two pulses with frequencies ω_1 and ω_3 are combined in a second order nonlinear crystal to produce the difference frequency $\omega_2 = \omega_3 - \omega_1$. If the two pulses are coming from the same laser source, they share the same CEP except for constant contributions due to propagation ($\phi_1 = \phi + c_1$ and $\phi_3 = \phi + c_3$), and the phase of the DF pulse results:

$$\phi_2 = \phi_3 - \phi_1 - \pi/2 = c_3 - c_1 - \pi/2 = const. \tag{3.2}$$

If ϕ is a random phase coming from the source DFG always cancel it, thus leaving the constant CEP value $c_3-c_1-\pi/2$. CEP stabilization can be achieved with OPA: if pump and signal are coming from the same laser source, then idler (DF between pump and signal) is phase-stable. Passive CEP stabilization of the idler pulse has been demonstrated by using OPAs pumped with either 800 or 400 nm pulses [35–37]. Phase stabilization through DFG between pulses coming from two different OPAs and sharing the same CEP has been also demonstrated [38]. These schemes suffer from the drawback that the two pulses undergoing DFG travel distinct optical paths, so that fluctuations in the path length difference result in CEP fluctuations. This limitation can be overcome by performing DFG between different spectral components of a single ultrabroadband pulse [28, 39]. With this approach the two spectral components are automatically synchronized and the delay-induced CEP jitter is eliminated. This scheme has been successfully used for CEP-stable seeding of OPAs and OPCPAs [11, 40, 41].

3.3 High-Order Harmonic Generation

The advances in laser technology described in the previous section have contributed to the rapid evolution of the attosecond research field. In this section we will briefly describe the basic physical processes leading to the production of attosecond pulses by high-order harmonic generation in gases and the theoretical models used to investigate these processes.

3.3.1 Semiclassical Model

High-order harmonic generation in gases can be understood in the framework of the semiclassical model introduced by Kulander et al. [42] and Corkum [43]. When a femtosecond laser pulse is focused onto a gas target, with peak intensity in the range between 10^{13} and 10^{15} W/cm², the Coulomb potential experienced by the outer shell electrons is strongly modified by the laser field. A potential barrier is generated, through which an electron can tunnel. As a first approximation we can assume that the freed electron appears in the continuum with velocity $\mathbf{v} = 0$. Assuming a monochromatic driving field, linearly polarized in the x direction, $\mathbf{E}(t) = E_0 \cos(\omega_0 t) \mathbf{u}_x$, where ω_0 is the angular frequency of the fundamental radiation ($\omega_0 = 2\pi/T_0$, T_0 is the optical period), the equation of motion of the electron after ionization is

$$\frac{dv}{dt} = -\frac{e}{m}E(t),\tag{3.3}$$

where m and -e are the electron mass and charge, respectively. This equation of motion can be easily integrated, thus giving the velocity of the electron after ionization:

$$v(t) = -\frac{eE_0}{m\omega_0} [\sin(\omega_0 t) - \sin(\omega_0 t')], \tag{3.4}$$

where t' is the tunnel ionization instant, and the electron position:

$$x(t) = \frac{eE_0}{m\omega_0^2} [\cos(\omega_0 t) - \cos(\omega_0 t') + \omega_0 (t - t') \sin(\omega_0 t')], \tag{3.5}$$

where we have assumed that the initial position of the electron after ionization is x(t') = 0. In the case of linear polarization, the electron can return to the parent ion and recombine to the ground state, with emission of photons with energy given by the following expression:

$$\hbar\omega(t) = I_p + \frac{1}{2}mv^2(t) = I_p + 2U_p[\sin(\omega_0 t) - \sin(\omega_0 t')]^2,$$
 (3.6)

where I_p is the ionization potential of the atom and $U_p = e^2 E_0^2 / 4m\omega_0^2$ is the ponderomotive energy. Figure 3.1 shows a graphical illustration of the physical processes giving rise to high-order harmonic generation. The recombination instant can be calculated by solving the equation x(t) = 0, which does not have analytical solutions.

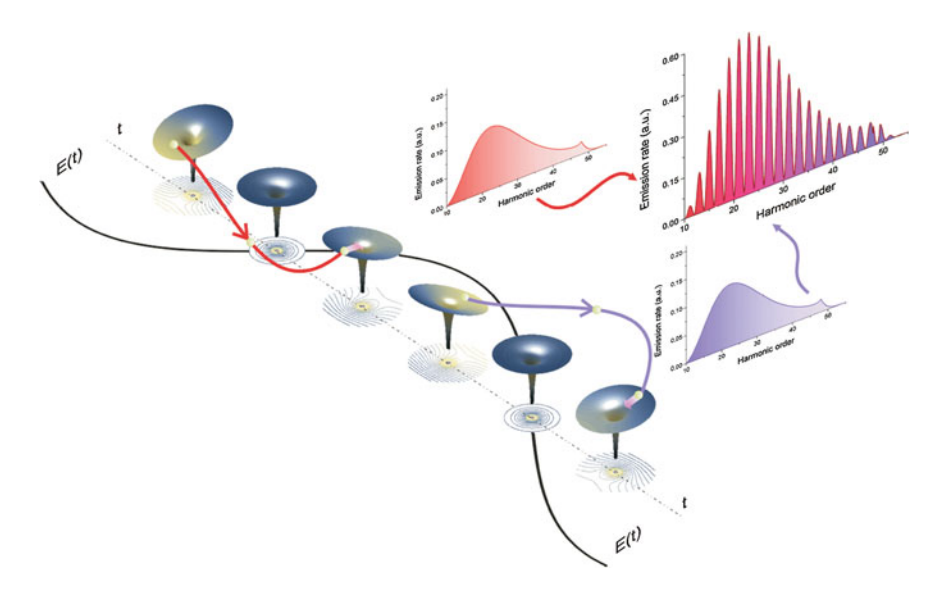


Fig. 3.1 Graphical illustration of the semiclassical, three-step model. Since the process is periodically repeated each half-optical cycle of the driving radiation, the generated XUV spectrum is composed by the odd harmonics of the fundamental frequency ω_0

It is possible to show that the freed electron can return to the parent ion if $0 \le \omega_0 t' \le 80^\circ$ or $180^\circ \le \omega_0 t' \le 260^\circ$. The numerical solution of equation x(t) = 0 can be fitted by the following function [44]:

$$\omega_0 t = \frac{\pi}{2} - 3\sin^{-1}\left(\frac{2}{\pi}\omega_0 t' - 1\right),\tag{3.7}$$

By using the previous expression in (3.6) it is possible to obtain a simple expression for the energy of the emitted photons

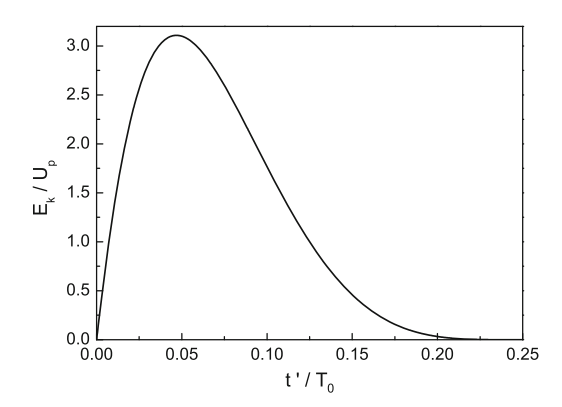
$$\hbar\omega(t) = I_p + 2U_p \left\{ \cos\left[3\sin^{-1}\left(\frac{2}{\pi}\omega_0 t' - 1\right)\right] - \sin(\omega_0 t') \right\}^2$$
 (3.8)

Figure 3.2 shows the kinetic energy of the returning electron, normalized to the ponderomotive energy, as a function of $t'/T_0 = \omega_0 t'/2\pi$. The electron released at a particular instant $t' < 0.05T_0$ has the same kinetic energy of an electron emitted at $t' > 0.05T_0$. Since shorter ionization times, t', correspond to longer recombination times, t (see 3.7), it is common to group the trajectories described by the electrons between tunnel ionization and recombination in two classes. The *long* trajectories are the paths followed by the electrons ionized at $t' < 0.05T_0$, while the *short* paths correspond to the trajectories described by the electrons ionized at $t' > 0.05T_0$. In the case of the short trajectories, the corresponding recombination time, t is $0.25T_0 < t < 0.7T_0$. For the long trajectories $0.7T_0 < t < T_0$.

The maximum energy of the photons emitted by recombination of the returning electrons is given by $\hbar\omega_{max}=I_p+3.17U_p$ (cutoff law). Since $U_p \propto I_0\lambda_0^2$, where I_0 is the peak intensity of the driving pulse and λ_0 the excitation wavelength, the cutoff frequency can be extended by increasing the excitation intensity and by increasing the wavelength. On the other hand the driving intensity is limited by the saturation intensity, which leads to complete ionization of the ground state.

The processes at the basis of the semiclassical, three-step model (i.e., tunnel ionization, acceleration in the laser electric field and recombination) are repeated

Fig. 3.2 Kinetic energy of the returning electron, normalized to the ponderomotive energy, as a function of $t'/T_0 = \omega_0 t'/2\pi$, calculated using the approximated expression (3.8)



every half optical cycle of the driving radiation, so that a train of extreme-ultraviolet pulses, separated by $T_0/2$, are generated.

Since the instantaneous angular frequency of the XUV pulses is a function of time, as shown by (3.6), the attosecond pulses present an intrinsic chirp, $C = d\omega/dt$ [45]. The XUV pulses generated by the short trajectories exhibit a positive (almost linear) chirp, while the pulses generated by the long ones are negatively chirped. As it will be discussed in Sect. 3.3.3, the short electron trajectories can be experimentally selected, thus generating trains of attosecond pulses characterized by a linear and positive chirp, which can be properly compensated by suitable techniques.

3.3.2 Strong-Field Approximation

A more accurate physical description of the single-atom response has been presented by Lewenstein et al. in 1994 [46]. Considering a single atom in a classical electromagnetic field, the Schrödinger equation can be solved using the following approximations: (i) single active electron approximation: the atom is treated as a hydrogen-like system and multiple ionization is neglected; (ii) strong field approximation (SFA): the electron in the continuum is treated as a free particle moving in the electric field, i.e. the influence of the Coulomb potential is completely neglected; (iii) only the ground state and the continuum are considered, the influence of the other bound states of the atom is completely neglected. The expectation value of the dipole moment of the atom, which represents the source of the harmonic emission, is given by (in atomic units)

$$\langle \mathbf{r}(t) \rangle = \langle \psi(\mathbf{r}, t) | \mathbf{r} | \psi(\mathbf{r}, t) \rangle,$$
 (3.9)

where $|\psi(\mathbf{r},t)\rangle$ is the time dependent wavefunction of the system, which can be written as a superposition of the ground state wavefunction, $|0\rangle e^{iI_pt}$, and of the continuum wavefunction, which corresponds to the electron wave packet moving in the continuum after tunnel ionization:

$$|\psi(\mathbf{r},t)\rangle = e^{iI_p t} \left[a(t)|0\rangle + \int d^3 \mathbf{v} b(\mathbf{v},t)|\mathbf{v}\rangle \right],$$
 (3.10)

where a(t) is the amplitude of the ground state wavefunction and b(v, t) are the amplitudes of the continuum states. Using the SFA it is possible to obtain a simple expression for the dipole moment (3.9):

$$\langle \mathbf{r}(t) \rangle = i \int_0^t dt' \int d^3 \mathbf{p} a^*(t) \mathbf{d}^* [\mathbf{p} + \mathbf{A}(t)] e^{-iS(\mathbf{p},t,t')} a(t') \mathbf{E}(t') \mathbf{d} [\mathbf{p} + \mathbf{A}(t')], \quad (3.11)$$

where: **A** and **E** are the vector potential and electric field of the driving radiation, **p** is the canonical momentum defined as $\mathbf{p} = \mathbf{v}(t) - \mathbf{A}(t)$, $\mathbf{d}[\mathbf{p} + \mathbf{A}(t')]$ and $\mathbf{d}^*[\mathbf{p} + \mathbf{A}(t)]$ are

the expectation values of the dipole transition moment between the ground state an a state in the continuum characterized by velocity $\mathbf{p} + \mathbf{A}(t')$ and $\mathbf{p} + \mathbf{A}(t)$ respectively; $S(\mathbf{p}, t, t')$ is the quasi-classical action, which gives the phase accumulated by the electron wavefunction during the propagation in the continuum:

$$S(\mathbf{p}, t, t') = \int_{t'}^{t} dt'' \left\{ \frac{[\mathbf{p} + \mathbf{A}(t'')]^2}{2} + I_p \right\},$$
(3.12)

Equation (3.11) has a simple physical interpretation in complete agreement with the three-step quasi-classical model. The dipole moment is given by the contribution of all the electrons emitted in the continuum at an instant t' with momentum \mathbf{p} with a probability given by the term $\mathbf{E}(t')\mathbf{d}[\mathbf{p}+\mathbf{A}(t')]$; the electron is then accelerated by the electric field and acquires a phase factor $e^{-iS(\mathbf{p},t,t')}$, and finally recombines with the parent ion at an instant t with probability $\mathbf{d}^*[\mathbf{p}+\mathbf{A}(t)]$. In the spirit of Feynman's quantum paths approach [47], each electron trajectory has to be considered and integrations over the momentum space $d^3\mathbf{p}$ and over the ionization instants dt' are required. It is important to observe that the various electron trajectories (quantum paths) do not contribute in the same way to the electric dipole moment: due to the fast oscillating phase term, all the contributions tend to cancel out apart for those corresponding to the stationary points of the classical action:

$$\nabla_{\mathbf{p}} S(\mathbf{p}, t, t') = 0, \tag{3.13}$$

In this way the dipole moment can be written as a coherent superposition of only a few electron quantum paths, which are the complex trajectories followed by the electrons from the ionization instant to the recombination with the parent ion. Using the saddle-point method, the Fourier transform of the dipole moment, $x(\omega)$ (assuming a driving field polarized along the x-axis), can be written as a coherent superposition of the contributions from the different electron quantum paths corresponding to the complex saddle-point solutions (\mathbf{p}_s , t_s , t_s'), where \mathbf{p}_s is the stationary value of the momentum acquired by an electron which is set free at time t_s' and recombines with the parent ion at time t_s . The sum over the relevant quantum paths can be decomposed in two terms related to the short and long quantum paths. The Fourier transform of the dipole moment can be written as [48]:

$$x(\omega) = \sum_{s \in short} |x_s(\omega)| \exp[i\Phi_s(\omega)] + \sum_{s \in long} |x_s(\omega)| \exp[i\Phi_s(\omega)], \quad (3.14)$$

where the first sum takes into accounts the contributions of the short quantum paths, while the second one considers the long quantum paths. $\Phi_s(\omega)$ is the phase of the complex function $x_s(\omega)$.

3.3.3 Phase-Matching in High-Order Harmonic Generation

So far we have discussed the single atom response of the generating medium: XUV radiation is produced by many atoms, with a typical conversion efficiency of the order of 10^{-5} – 10^{-6} . As all nonlinear processes, high conversion efficiency in harmonic generation requires phase-matching of the harmonic field with the driving polarization, i.e. the phase difference between the generated field and the driving polarization has to be minimized over the generating medium in order to have an efficient energy transfer. In the case of plane waves and low order harmonics this gives rise to the phase-matching condition on the wave vectors: $\Delta \mathbf{k} = \mathbf{k}_q - q \mathbf{k}_0 = 0$, where \mathbf{k}_0 and \mathbf{k}_q are the wave vectors of the fundamental and qth harmonic beams, respectively. The corresponding coherence length, defined as the propagation length at which the phase mismatch between harmonic and fundamental radiation is equal to π , is given by $L_{coh} = \pi/|\Delta \mathbf{k}|$. For high harmonic orders the phase variation of the driving polarization is much more important than that of the induced field, therefore efficient harmonic generation requires the minimization of the phase variation of the driving polarization. The analysis of phase matching conditions in HHG is complicated by the presence of the dipole phase term $S(\mathbf{p}, t, t')$ in (3.11). It has been shown that, in the adiabatic case, this term can be approximated as $S \approx U_p \tau$ [47], where $\tau = t - t'$ represents the time spent by the electron in the continuum between tunnel ionization and recombination, and depends on the considered quantum path and on the laser intensity (and therefore on the position of the nonlinear medium with respect to the focus position of the fundamental beam). This intrinsic phase introduces an additional dispersion term proportional to the gradient of the laser intensity. The generation of an electron plasma also influences the phase matching mechanism because of the introduction of a time dependent refractive index affecting the propagation of the driving pulse. Such dispersion term tends to speed up the fundamental phase velocity with respect to the harmonic radiation, thus reducing the coherence length. Since shorter wavelengths are generated in the presence of a higher free electron density, the phase mismatch rapidly increases with harmonic order. Finally, due to focusing, the laser beam experiences a geometric phase shift called Gouy phase shift, which limits the coherence length corresponding to the qth harmonic to $L_g = \pi z_0/q$, where z_0 is the Rayleigh range. All these terms contribute to the phase of the driving and harmonic pulses determining complex phase-matching mechanisms. In particular, in the longitudinal direction, the dipole phase term, $U_p\tau$, is symmetric with respect to the laser focus, and competes with the antisymmetric Guoy phase. Depending on the geometrical conditions, the contribution of one trajectory can be enhanced and the others reduced [49]. For example, when the laser beam is focused before the nonlinear medium, the phase variation induced by focusing is small and the selected trajectory is the one with the slowest phase variation (short trajectory). When the nonlinear medium is located around the position of the laser focus the contribution of the long paths increases. Moreover, it has been demonstrated that the harmonic emission due to the long paths is characterized by a larger divergence with respect to that due to the short paths, therefore it is possible to isolate the contributions of the

short and long quantum paths simply adjusting the position of the nonlinear medium with respect to the laser focus and by spatial filtering.

Note that, due to the high photon energy the harmonic radiation can excite core electrons and ionize valence electrons along its propagation in the gas medium and can be reabsorbed. For this reason the conversion efficiency saturates after the absorption length $L_{abs} = 1/\sigma \rho$, where σ is the absorption cross section and ρ is the gas density [50]. A rule of thumb for the optimization of the harmonic conversion efficiency is given by two conditions: $L_{med} > 3L_{abs}$ (where L_{med} is the medium length) and $L_{coh} > 5L_{abs}$ [50]. In the case of a short medium, the first condition is generally not fulfilled and the emission is limited by the medium length; in the case of long media, both conditions can be fulfilled simultaneously. By controlling the laser aperture, length, pressure and position of the gas medium, harmonic energies in the microjoule range have been reached, thus opening new perspectives for the applications of harmonic radiation. In this case the harmonic radiation is intense enough to induce nonlinear optical processes in the XUV spectral range.

3.4 Generation of Isolated Attosecond Pulses

As shown in Sect. 3.3, trains of attosecond pulses can be generated using multi-cycle driving IR pulses. Several techniques have been implemented over the last decade in order to isolate a single attosecond pulse out of these trains. All these strategies can be understood and schematized in terms of "gating" of the harmonic radiation or of the harmonic generation process. Even though some techniques are based on the combination of different gating mechanisms, the principles of operation can be divided in spectral, temporal and spatial gating.

3.4.1 Spectral Gating

The first experimental generation and characterization of isolated pulse were based on few-cycle driving pulses [51]. Using these driving fields, a short train of attosecond pulses (typically \sim 3–4 pulses) is produced. It is fundamental to observe that for these pulses the optical period T_0 is comparable with the duration of the pulse envelope (usually defined as the full-width at half maximum of the intensity profile τ), leading to strong variations of the maximum electric field strength between consecutive oscillations of the electric field. As the harmonic generation process is driven by the electric field waveform, variations of the timing between the carrier-wave oscillation and the pulse envelope determine a different electric field evolution, and, in general, a different harmonic spectrum. The timing between the optical field oscillation and the pulse envelope is usually described in terms of the CEP φ . The generation of a reproducible harmonic spectrum and of isolated attosecond pulse relies on the availability of driving pulses with a well-defined and reproducible CEP, i.e. with a stable CEP.

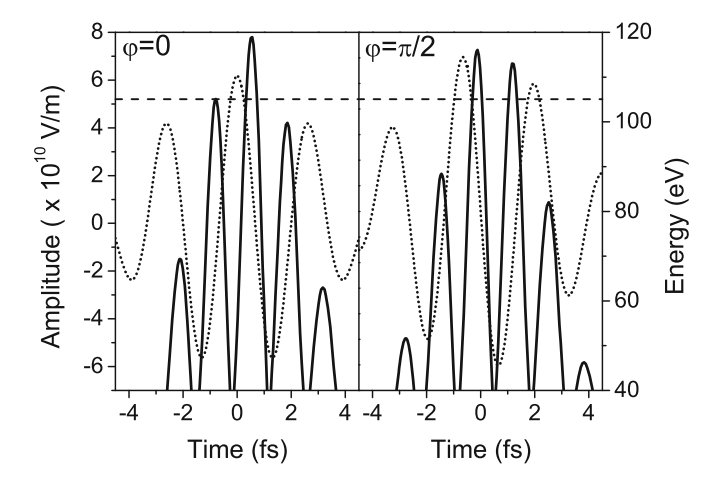


Fig. 3.3 Electric field (dotted line) of a \cos^2 -shaped, 5 fs 800 nm wavelength pulse with an amplitude of $E_0 = 6.17 \times 10^{10}$ V/m for the CEPs $\varphi = 0$ (left panel) and $\varphi = \pi/2$ (right panel). Energy of the emitted XUV photon according to the three-step model (full line) for the two CEPs. In the spectral region above the dashed vertical line (>105 eV) an isolated and two attosecond pulses are obtained for the CEPs $\varphi = 0$ and $\varphi = \pi/2$, respectively

As already discussed in Sect. 3.3 the XUV photon energy spectral distribution of a single attosecond pulse in the train depends on the energy acquired by the released electron wave packet and, therefore, on the strength of the electric field during the motion in the continuum. As a consequence, the attosecond pulses emitted at the center of the driving field present a higher photon energies with respect to the ones emitted on the leading and trailing edges of the pulse, as shown in Fig. 3.3. As the CEP influences the maximum electric field strength of few-cycle pulses, cosine-like $(\varphi = 0)$ and sine-like $(\varphi = \pi/2)$ lead to different photon energy spectral distributions, as shown in Figs. 3.3a and 3.3b, respectively. In particular, it is clear that the highest energy part (cut-off) of the harmonic spectrum is confined only in the central attosecond pulse for the cosine-like pulse, and in the two central adjacent attosecond pulses for the sine-like pulse. Using a suitable spectral filter, only the highest photon energies can be selected thus leading to the selection of an isolated attosecond pulses. This method for the generation of isolated attosecond pulses was first proposed by Christov et al. [52] and experimentally demonstrated by Hentschel et al. [51]. In this first experimental demonstration CEP-unstable few-cycle pulses were used; however later theoretical analysis [53] demonstrated that in the experimental conditions reported in [51] efficient generation of harmonic radiation could occur only for those CEPs leading to an isolated attosecond XUV pulse, thus confirming the main experimental conclusions. Further experiments using CEP-stabilized pulses have reported the generation and characterization of isolated attosecond pulses [54], selecting only the highest energy range of the harmonic radiation.

Recent advances in the generation of supercontinuum extending from the infrared to the ultraviolet region have been reported [9]. These pulse comprises only a single

complete oscillation of the electric field. For theses pulses, efficient harmonic generation can occur only for the central half optical cycle oscillation, thus leading to the generation of an isolated attosecond pulse for each CEP [9].

3.4.2 Temporal Gating

3.4.2.1 Polarization Gating

Since the first experiments, it was clear that the HHG process efficiency strongly depends on the polarization state of the driving pulse [55]. From the three-step model, it is straightforward that the recombination process can occur only if the electron revisits the position of the parent ion, thus requiring a linearly polarized driving field. For a circularly polarized driving field, the electron acquires a transverse momentum and does not revisit the original position during its motion in the continuum, thus inhibiting the HHG process. Measurements of the HHG efficiency on the ellipticity of the driving field indicate that the harmonic yield is reduced by a factor of $\simeq 2$ for an ellipticity ε_{th} of 0.13 [55]. Taking advantage of this property, Corkum et al. [56] proposed a method for the generation of isolated attosecond pulses based on the combination of two perpendicularly polarized pulses with frequencies ω_1 and ω_2 slightly detuned $((\omega_1 - \omega_2) \ll (\omega_1 + \omega_2)/2)$. Due to the coherent superposition of the two fields, the polarization state changes through the pulse being circularly polarized on the edges and linearly polarized at the center. For such a pulse, HHG is efficient only in the central temporal window whose duration depends on the duration of the two pulses and on the frequency differences between the two components. Tcherbakoff et al. [57] implemented this original idea using a single-color driving pulse and two birefringent plates. The first one splits the incoming beam in two replica with perpendicular polarization, that, propagating through the birefringent material acquire delay T_d given by the thickness of the first plate and by the difference of the group velocities between the ordinary and extraordinary axes. The second plate is a zero-order quarter wave plate oriented parallel to the incoming polarization direction that transforms the linear polarization of the leading and trailing edge in counterrotating circular polarization, and the circular polarization of the central part in linear. The final intensity envelope and polarization state of the pulse at the output of the second plate is shown in Fig. 3.4.

The final field can be also decomposed in two linearly polarized components: a driving and a gating field polarized along perpendicular directions as shown in Fig. 3.4b. At the center of the gating the gating field is zero and the pulse is linearly polarized. At the edges, the driving and gating fields have similar amplitude (and present a phase difference of $\pi/2$) thus leading to circular polarization. The duration of the central temporal gate δt_g where HHG can occur can be estimated as [58]:

$$\delta t_g = 0.3 \frac{\varepsilon_{thr} \tau_p^2}{T_d} \tag{3.15}$$

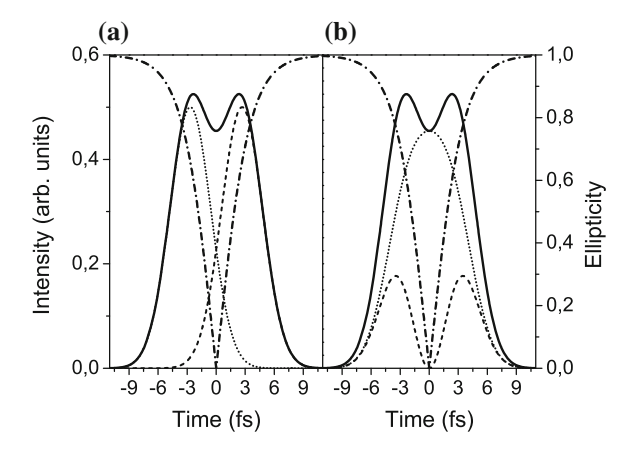


Fig. 3.4 a Intensity of the driving field at the output of the two birefringent plates (*solid line*). Absolute value of the ellipticity of the final electric field (*dash-dotted line*). The field can be decomposed in the composition of two delayed pulses with circular polarization (*dash and dotted lines*) (a) or of two linearly polarized pulses; a driving field (*dotted line*) and a gating field (*dashed line*) (b)

where T_d is the temporal delay between the two pulses introduced by the first plate and τ_p is the duration of the incoming pulse. When the temporal gate is shorter than half-optical-cycle, a single attosecond pulse can be generated. This technique has been used for the generation of XUV continua [59] and for the first complete characterization of isolated attosecond pulses [60], using few-cycle pulses. An advantage of this technique is the possibility to generate XUV continua also in the plateau region of the harmonic spectrum and not only in the cut-off region.

The polarization gating (PG) technique requires few-cycle pulses in order to generate efficiently isolated attosecond pulses. For longer pulses, the condition $\delta t_g < T_0$ requires larger delay between the two perpendicularly polarized components of the incoming beam after the first plate, determining a low intensity of the electric field in the central temporal gate and, therefore, a low efficiency of the harmonic process. A solution of this problem has been implemented combining the polarization gating technique with a two-color scheme in a technique dubbed double optical gating (DOG).

3.4.2.2 Double Optical Gating and Generalized Double Optical Gating

This approach is based on the use of a weak second harmonic field added to the fundamental field in order to relax the requirement about the duration of the temporal gate [61]. The combination of the fundamental and its second harmonic resemble the two-color scheme discussed in Sect. 3.4.1. Also in this case the constructive and destructive interference effect enhance the electric field in one semi-cycle while decreasing the total field in the two adjacent ones. For this reason the condition for

the generation of an isolated attosecond pulse in the double optical gating requires a time window shorter than the full optical cycle $\delta t_g < T_0$, rather than the half-optical cycle as in the polarization gating scheme. In this configuration, longer pulses or smaller delays can be used with an increase in the harmonic generation efficiency as demonstrated in [62] were pulses as short as 12 fs were used to generate an isolated attosecond pulse.

In the implementation of the PG and DOG techniques, pulses from an hollow fiber compressor were used. Isolated attosecond pulses using driving pulses obtained without post-compression were demonstrated using a generalization of the DOG technique [63]. This scheme can be understood considering the driving and gating field introduced in the description of the polarization gating technique and shown in Fig. 3.4b. A possibility for reducing the duration of the time window is to reduce the amplitude of the driving field; in this way the variation from linear to circular polarization occurs on a shorter time window while the edges of the pulses are elliptically polarized as shown in Fig. 3.5. Also in this case HHG is strongly reduced on the leading and trailing edges of the pulse. The attenuation of the electric field of driving field can be accomplished exploiting the dependence on the angle of incidence for the transmission of a thin plate as schematically shown in Fig. 3.6. The first quartz plate (QP1) splits the incoming beam in two perpendicularly polarized replica with a delay T_d . The Brewster plate reduces by reflection the energy of the driving component. The transmission for this component can be controlled by varying the angle of the Brewster plate. The second quartz plate and the BBO crystal acts as a quarter wave plate. In addition a second harmonic field parallel to the driving field is generated in the BBO to relax the requirement on the duration of the time gate. In this approach, therefore, part of the driving beam energy is rejected for obtaining a

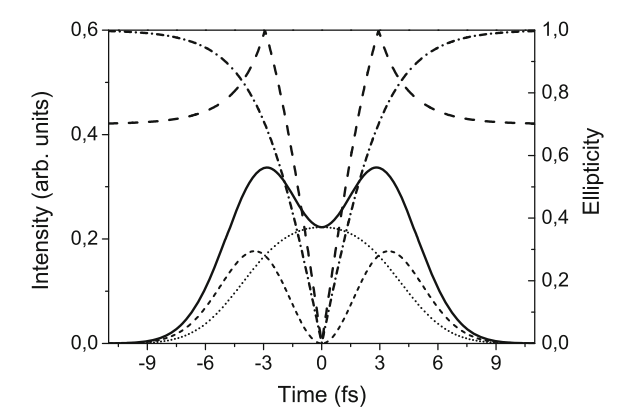


Fig. 3.5 Intensity of the driving field at the output of the two birefringent plates and of the Brewsterangle plate (*solid line*). The field can be decomposed in the sum of two linearly polarized pulses: a driving field (*dotted line*) and a gating field (*thin dashed line*). Absolute value of the ellipticity of the final electric field (*thick dashed line*). For comparison the absolute value of the ellipticity without Brewster-angle plate is shown (*dash-dotted line*)

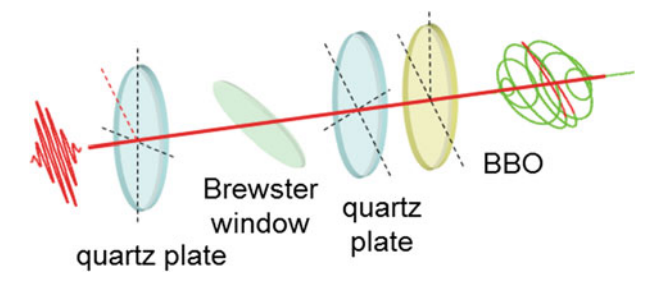


Fig. 3.6 Optics used for the implementation of the GDOG: quartz plates (QP1 and QP2), Brewsterangle plate (BW) and second harmonic crystal (BBO)

shorter time gate. Using this scheme, isolated attosecond pulses were demonstrated using CEP-stable and CEP-unstable laser systems [64].

3.4.2.3 Interferometric Gating

Similar to the previous technique, the interferometric gating has been realized and implemented for many cycle high-energetic pulses [65]. The manipulation of the polarization state of the driving pulse is achieved by using a series of interferometers and birefringent plates for rotating the polarization of the incoming beams. This scheme resembles the first part of the GDOG scheme were the driving field is attenuated with respect to the gating one, in order to reduce the duration of the gating window. This scheme allows one to handle pulses with high energy (up to few hundreds of millijoules and even Joule) [65]. Recently a compact, collinear version of this scheme has been created and used for the generation of XUV continua [66]. This technique is scalable to high energy pulses, the main limitation being the self-phase modulation occurring in the plates at high intensities.

3.5 Spatial Gating

Recently Vincenti and Quéré [67] introduced a new method for the generation of isolated attosecond pulses based on the dependence of the emission direction of attosecond pulses generated in gases or in plasma on the wave front rotation of the driving IR pulse. This scheme is based on the exploitation of spatio-temporal coupling occurring in ultrashort pulses, i.e. the dependence of the spatial properties of a pulse on its temporal profile and vice versa. These effects are usually considered as detrimental because they limit the maximum intensity that can be achieved at the focus; in particular pulse-front tilt is a spatio-temporal effect that can affect ultrashort pulses delivered by amplified laser systems as the result of a small misalignment of

the a dispersive element in a grating or prism compressor. This effect can be described according to the relation:

$$E(x,t) = E_0 \exp\left(-2\left[\frac{t - \xi x}{\tau}\right]^2 - 2\frac{x^2}{w^2} + i\omega t\right)$$
 (3.16)

where τ is the pulse duration, w the beam diameter before focusing, ξ the pulse-front tilt parameter and ω the laser frequency. In the absence of pulse-front tilt, $\xi=0$. From (3.16), it turns out that the maxima of the field in the (x,t) plane are tilted with respect to the wave front. Upon focusing with an optic of focal length f, different frequencies are focused in different transverse position thus leading to a reduction of the maximum achievable intensity. In terms of wave fronts, this condition corresponds to a wave front rotation in time with a speed given by the relation:

$$v_r = \frac{w^2}{f\tau^2} \frac{\xi}{1 + (w\xi/\tau)^2}$$
 (3.17)

This effects can be used to produced isolated attosecond pulses. Ultrashort pulses with negligible pulse-front tilt are usually implemented for HHG in gases or in plasma, in order to obtain the maximize the intensity in the interaction point. In this condition a train of attosecond pulses propagating in the same direction are generated. The interference in the far field of these pulses determines the harmonic structure observed in the spectral domain. On the other hand, for ultrashort pulses presenting a non negligible pulse-front tilt, each attosecond pulse is emitted in a slightly different direction corresponding to the instantaneous direction of propagation of the driving field at the instant of generation. In the far field, therefore, it is possible to separate consecutive attosecond pulses emitted with a time distance Δ_t , thus obtaining a continuous XUV spectrum, assuming that the angular separation of two consecutive attosecond pulses $\Delta \beta = v_r \Delta_t$ is larger than the divergence θ_n of the XUV pulses: $\theta_n < \Delta \beta$. This condition limits the maximum pulse duration and the minimum wave-front rotation that can be used for generation of isolated attosecond pulses. As isolated attosecond pulses are emitted in different directions, the effect is indicated as attosecond lighthouse.

This scheme should be applicable for the generation of isolated attosecond pulses from gas and solid targets. The first experimental demonstration of the validity of this approach has been demonstrated using CEP-controlled few-cycle light pulses at 800 nm wavelength used to drive harmonic generation on solid targets [68]. Optimal pulse compression was achieved by adjusting the thickness of two fused silica wedges in the beam path before the interaction region. Upon tilting one of the two wedges, a controllable pulse front tilt was introduced in the ultrashort pulse. Upon increasing the pulse front tilt the XUV beam splits into well separated beams, each corresponding to an isolated attosecond pulse.

F. Calegari et al.

3.6 Conclusions

Attosecond pulses are powerful tools for the investigation of important ultrafast processes in atoms, molecules and solids, where the electron dynamics play a crucial role. In this chapter we have reported on recent advances in laser technology relevant for the generation of attosecond pulses. Particular attention has been devoted to the hollow-fiber compression technique and to the development of high-energy parametric sources with stable carrier-envelope phase. Various techniques for the generation of attosecond pulses have been discussed, with particular emphasis on the production of isolated sub-femtosecond pulses.

Acknowledgments We acknowledge financial support from the European Research Council under the European Community's Seventh Framework Programme (FP7/2007–2013)/ERC grant agreement n. 227355—ELYCHE, from the Italian Ministry of Research (FIRB-IDEAS RBID08CRXK) and from MC-RTN ATTOFEL (FP7-238362).

References

- 1. F. Krausz, M. Ivanov, Rev. Mod. Phys. 81, 163 (2009)
- 2. M. Nisoli, G. Sansone, Prog. Quantum Electron. 33, 17 (2009)
- J. Itatani, J. Levesque, D. Zeidler, H. Niikura, H. Pépin, J.C. Kieffer, P.B. Corkum, D.M. Villeneuve, Nature 432, 867 (2004)
- 4. M. Nisoli, S. De Silvestri, O. Svelto, Appl. Phys. Lett. 68, 2793 (1996)
- 5. A. Suda, M. Hatayama, K. Nagasaka, K. Midorikawa, Appl. Phys. Lett. 86, 111116 (2005)
- 6. S. Bohman, A. Suda, T. Kanai, S. Yamaguchi, K. Midorikawa, Opt. Lett. 35, 1887 (2010)
- X. Chen, A. Jullien, A. Malvache, L. Canova, A. Borot, A. Trisorio, C.G. Durfee, R. Lopez-Martens, Opt. Lett. 34, 1588 (2009)
- 8. C.F. Dutin, A. Dubrouil, S. Petit, E. Mével, E. Constant, D. Descamps, Opt. Lett. 253, 15 (2010)
- A. Wirth, MTh Hassan, I. Grguraš, J. Gagnon, A. Moulet, T.T. Luu, S. Pabst, R. Santra, Z.A. Alahmed, A.M. Azzeer, V.S. Yakovlev, V. Pervak, F. Krausz, E. Goulielmakis, Science 334, 195 (2011)
- 10. G. Cerullo, S. De Silvestri, Rev. Sci. Instrum. 74, 1 (2003)
- C. Vozzi, F. Calegari, E. Benedetti, S. Gasilov, G. Sansone, G. Cerullo, M. Nisoli, S. De Silvestri, S. Stagira, Opt. Lett. 32, 2957 (2007)
- 12. A. Pirskarskas, A. Stabinis, A. Yankauskas, Sov. Phys. Usp. 29, 869 (1986)
- 13. A. Dubietis, G. Jonušauskas, A. Piskarskas, Opt. Commun. 88, 437 (1992)
- 14. I.N. Ross, P. Matousek, M. Towrie, A.J. Langley, J.L. Collier, Opt. Commun. 144, 125 (1997)
- 15. S. Witte, K.S.E. Eikema, IEEE J. Sel. Top. Quantum Electron. 18, 296 (2012)
- N. Ishii, C.Y. Teisset, T. Fuji, S. Kohler, K. Schmid, L. Veisz, A. Baltuška, F. Krausz, IEEE J. Sel. Top. Quantum Electron. 12, 173 (2006)
- 17. C.Y. Teisset, N. Ishii, T. Fuji, T. Metzger, S. Kohler, R. Holzwarth, A. Baltuška, A. Zheltikov, F. Krausz, Opt. Express 13, 6550 (2005)
- 18. R.T. Zinkstok, S. Witte, W. Hogervorst, K.S.E. Eikema, Opt. Lett. 30, 78 (2005)
- 19. J.V. Rudd, R.J. Law, T.S. Luk, S.M. Cameron, Opt. Lett. 30, 1974 (2005)
- G. Andriukaitis, T. Baličunas, S. Ališauskas, A. Pugžlys, A. Baltuška, T. Popmintchev, M. Chen, M.M. Murnane, H.C. Kapteyn, Opt. Lett. 36, 2755 (2011)
- T. Popmintchev, M.C. Chen, D. Popmintchev, P. Arpin, S. Brown, S. Ališauskas, G. Andriukaitis, T. Balčiunas, O. Mücke, A. Pugzlys, A. Baltuška, B. Shim, S.E. Schrauth, A. Gaeta, C. Hernndez-Garca, L. Plaja, A. Becker, A. Jaron-Becker, M.M. Murnane, H.C. Kapteyn, Science 336, 1287 (2012)

- 22. S.-W. Huang, G. Cirmi, J. Moses, K.-H. Hong, S. Bhardwaj, J.R. Birge, L.-J. Chen, E. Li, B.J. Eggleton, G. Cerullo, F.X. Kärtner, Nature Phot. 5, 475 (2011)
- Z. Major, S.A. Trushin, I. Ahmad, M. Siebold, C. Wandt, S. Klingebiel, T.-J. Wang, J.A. Fülöp,
 A. Henig, S. Kruber, R. Weingartner, A. Popp, J. Osterhoff, R. Hörlein, J. Hein, V. Pervak, A. Apolonski, F. Krausz, S. Karsch, Laser Rev. 37, 431 (2009)
- 24. S.T. Cundiff, J. Phys. D: Appl. Phys. **35**, 43 (2002)
- F.W. Helbing, G. Steinmeyer, U. Keller, R.S. Windeler, J. Stenger, H.R. Telle, Opt. Lett. 27, 194 (2002)
- A. Baltuška, T. Udem, M. Uiberacker, M. Hentschel, E. Goulielmakis, Ch. Gohle, R. Holzwarth,
 V.S. Yakovlev, A. Scrinzi, T.W. Hänsch, F. Krausz, Nature 421, 611 (2003)
- 27. J.M. Dudley, G. Genty, S. Coen, Rev. Mod. Phys. 78, 1135 (2006)
- 28. T. Fuji, J. Rauschenberger, A. Apolonski, V.S. Yakovlev, G. Tempea, T. Udem, C. Gohle, T.W. Hänsch, W. Lehnert, M. Scherer, F. Krausz, Opt. Lett. 30, 332 (2005)
- S. Koke, C. Grebing, H. Frei, A. Anderson, A. Assion, Günter Steinmeyer. Nature Phot. 4, 462 (2010)
- A. Baltuška, M. Uiberacker, E. Goulielmakis, R. Kienberger, V. Yakovlev, T. Udem, T. Hänsch, F. Krausz, IEEE J. Sel. Top. Quantum Electron. 9, 972 (2003)
- M. Kakehata, H. Takada, Y. Kobayashi, K. Torizuka, Y. Fujihira, T. Homma, H. Takahashi, Opt. Lett. 26, 1436 (2001)
- 32. A. Brodeur, S.L. Chin, J. Opt. Soc. Am. B 16, 637 (1999)
- 33. M. Takeda, H. Ina, S. Kobayashi, J. Opt. Soc. Am. B 72, 156 (1982)
- L. Canova, X. Chen, A. Trisorio, A. Jullien, A. Assion, G. Tempea, N. Forget, T. Oksenhendler, R. Lopez-Martens, Opt. Lett. 34, 1333 (2009)
- 35. A. Baltuška, T. Fuji, T. Kobayashi, Phys. Rev. Lett. 88, 133901 (2002)
- 36. X. Fang, T. Kobayashi, Opt. Lett. 29, 1282 (2004)
- 37. S. Adachi, P. Kumbhakar, T. Kobayashi, Opt. Lett. 29, 1150 (2004)
- 38. C. Manzoni, G. Cerullo, S. De Silvestri, Opt. Lett. **29**, 2668 (2004)
- 39. T. Fuji, A. Apolonski, F. Krausz, Opt. Lett. 29, 632 (2004)
- C. Manzoni, C. Vozzi, E. Benedetti, G. Sansone, S. Stagira, O. Svelto, S. De Silvestri, M. Nisoli, G. Cerullo, Opt. Lett. 31, 963 (2006)
- 41. T. Fuji, N. Ishii, C.Y. Teisset, X. Gu, T. Metzger, A. Baltuška, N. Forget, D. Kaplan, A. Galvanauskas, F. Krausz, Opt. Lett. 31, 1103 (2006)
- 42. K.C. Kulander, K.J. Schafer, J.L. Krause, *Super-Intense Laser-Atom Physics*, vol. 316, NATO Advanced Study Institute, Series B: Physics (Plenum, New York, 1993), p. 95
- 43. P.B. Corkum, Phys. Rev. Lett. 71, 1994 (1993)
- 44. Z. Chang, Fundamentals of Attosecond Optics (CRS Press, Taylor and Francis Group, 2011)
- Y. Mairesse, A. de Bohan, L.J. Frasinski, H. Merdji, L.C. Dinu, P. Monchicourt, P. Breger, M. Kovačev, R. Taïeb, B. Carré, H.G. Muller, P. Agostini, P. Salières, Science 302, 1540 (2003)
- M. Lewenstein, P.H Balcou, M.Y. Ivanov, A. L'Huillier, P.B. Corkum, Phys. Rev. A 49, 2117 (1994)
- P. Salières, B. Carré, L. Le Déroff, F. Grasbon, G.G. Paulus, H. Walther, R. Kopold, W. Becker,
 D.B. Miloševic, A. Sanpera, M. Lewenstein, Science 292, 902 (2001)
- 48. G. Sansone, C. Vozzi, S. Stagira, M. Nisoli, Phys. Rev. A 70, 013411 (2004)
- M. Bellini, C. Lynga, A. Tozzi, M.B. Gaarde, T.W. Hänsch, A. LHuillier, C.-G. Wahlström, Phys. Rev. Lett. 81, 297 (1998)
- E. Constant, D. Garzella, P. Breger, E. Mével, Ch. Dorrer, C. Le Blanc, F. Salin, P. Agostini, Phys. Rev. Lett. 82, 1668 (1999)
- M. Hentschel, R. Kienberger, C. Spielmann, G.A. Reider, N. Milosevic, T. Brabec, P. Corkum, U. Heinzmann, M. Drescher, F. Krausz, Nature 414, 509 (2001)
- 52. I.P. Christov, M.M. Murnane, H.C. Kapteyn, Phys. Rev. Lett. 78, 1251 (1997)
- 53. M.B. Gaarde, K.J. Schafer, Opt. Lett. **31**, 3188 (2006)
- R. Kienberger, M. Hentschel, M. Uiberacker, C. Spielmann, M. Kitzler, A. Scrinzi, M. Wieland, T. Westerwalbesloh, U. Kleineberg, U. Heinzmann, M. Drescher, F. Krausz, Science 297, 1144 (2002)

F. Calegari et al.

- 55. N.H. Burnett, C. Kan, P.B. Corkum, Phys. Rev. A **51**, R3418 (1995)
- 56. P.B. Corkum, N.H. Burnett, M.Y. Ivanov, Opt. Lett. 19, 1870 (1994)
- O. Tcherbakoff, E. Mével, D. Descamps, J. Plumridge, E. Constant, Phys. Rev. A 68, 043804 (2003)
- 58. V. Strelkov, A. Zaïr, O. Tcherbakoff, R. Lopez-Martens, E. Cormier, E. Mével, E. Constant, J. Phys. B 38, L161 (2005)
- 59. I.J. Sola, E. Mével, L. Elouga, E. Constant, V. Strelkov, L. Poletto, P. Villoresi, E. Benedetti, J.P. Caumes, S. Stagira, C. Vozzi, G. Sansone, M. Nisoli, Nature Phys. 2, 319 (2006)
- G. Sansone, E. Benedetti, F. Calegari, C. Vozzi, L. Avaldi, R. Flammini, L. Poletto, P. Villoresi,
 C. Altucci, R. Velotta, S. Stagira, S. De Silvestri, M. Nisoli, Science 314, 443 (2006)
- 61. Z. Chang, Phys. Rev. A **76**, 051403(R) (2007)
- H. Mashiko, S. Gilbertson, C.Q. Li, S.D. Khan, M.M. Shakya, E. Moon, Z.H. Chang, Phys. Rev. Lett. 100, 103906 (2008)
- X.M. Feng, S. Gilbertson, H. Mashiko, H. Wang, S.D. Khan, M. Chini, Y. Wu, K. Zhao,
 Z. Chang, Phys. Rev. Lett. 103, 183901 (2009)
- 64. S. Gilbertson, S.D. Khan, Y. Wu, M. Chini, Z. Chang, Phys. Rev. Lett. 105, 093902 (2010)
- P. Tzallas, E. Skantzakis, C. Kalpouzos, E.P. Benis, G.D. Tsakiris, D. Charalambidis, Nature Phys. 3, 846 (2007)
- G. Kolliopoulos, P.A. Carpeggiani, D. Rompotis, D. Charalambidis, P. Tzallas, Rev. Sci. Instrum. 83 (2012)
- 67. H. Vincenti, F. Quéré, Phys. Rev. Lett. 108, 113904 (2012)
- J.A. Wheeler, A. Borot, S. Monchoce, H. Vincenti, A. Ricci, A. Malvache, R. Lopez-Martens,
 F. Quéré, Nature Phot. 6, 828 (2012)
- D. Herrmann, L. Veisz, R. Tautz, F. Tavella, K. Schmid, V. Pervak, F. Krausz, Opt. Lett. 34, 2459 (2009)
- J.M. Mikhailova, A. Buck, A. Borot, K. Schmid, C. Sears, G.D. Tsakiris, F. Krausz, L. Veisz, Opt. Lett. 36, 3145 (2011)

Chapter 4 Overview on HHG High-Flux Sources

Willem Boutu, Mathieu Ducousso, Jean-François Hergott and Hamed Merdji

Abstract High order laser harmonic generation is a relatively recent and promising source of intense coherent radiation in the extreme ultraviolet and soft X-ray domains. The process, due to the highly non linear interaction between an intense and ultrashort laser pulse and a gas medium, has a relatively low efficiency at the single atom level. However, progresses in laser technology and a better understanding of the macroscopic construction of the harmonic field have enabled high flux sources. In this chapter, we will review the last developments that allow the publication of the first demonstrations of photon demanding experiments in solid state physics and non linear optics. Control and shaping of the fundamental laser field have led to an increase of the conversion efficiency of several orders of magnitude. Microjoule level emissions have been obtained on high power lasers thanks to phase matching and quasi phase matching schemes. We will also mention very high repetition rate laser systems that produce photon flux per second of the same order of magnitude than those obtained with lower repetition rate and higher energy level.

4.1 Introduction

With the rapid development of always more powerful laser systems, high-order harmonic generation (HHG) of intense laser pulses interacting with atomic gases has known impressive advances. Two decades of theoretical and experimental works

W. Boutu (⋈) · M. Ducousso · J.-F. Hergott · H. Merdji

Laboratoire Interactions, Dynamique et Lasers, CEA-Saclay, 91191

Gif-sur-Yvette Cédex, France e-mail: willem.boutu@cea.fr

M. Ducousso

e-mail: mathieu.ducousso@safran.fr

J.-F. Hergott

e-mail: jean-francois.hergott@cea.fr

H. Merdji

e-mail: hamed.merdji@cea.fr

© Springer-Verlag Berlin Heidelberg 2015 F. Canova and L. Poletto (eds.), *Optical Technologies for Extreme-Ultraviolet and Soft X-ray Coherent Sources*, Springer Series in Optical Sciences 197, DOI 10.1007/978-3-662-47443-3_4

have allowed pushing the radiation towards promising characteristics. The covered spectral range now extends from 100 nm (12 eV) [1, 2] to a few nanometers (the keV range), thus including the water window that allows imaging of biological samples (2.34–4.4 nm; 530–280 eV) [3, 4]. Exhaustive studies have characterized the XUV emission, both in the spatial and temporal domains, and have demonstrated control over crucial properties, such as spatial coherence [5, 6], beam quality [7] or temporal coherence [8, 9]. A growing number of time resolved experiments have been performed using HHG pulses either as a probing tool to follow ultrafast phenomena or as a energetic pump to trigger them. Applications to ultrafast dynamics in atomic and molecular systems, solid state and plasma physics are a non exhaustive list of such examples. However, some areas are not yet fully accessible to researchers, because of the limited number of XUV photons available. The first implementations of photon demanding experiments were possible after extensive beamline optimizations, such as multiphoton ionization of atoms and molecules in the gas phase [10-12] or single shot coherent diffractive imaging [13–15]. High order harmonic generation from plasma mirrors is a promising source of intense XUV radiation [16, 17]. As there is no limitation in the laser intensity producing the radiation, powerful emission can be achieved using the multiterawatt lasers that are nowadays available. However, very few applications using those sources have been published yet, as there are still in a characterization stage (for instance, no temporal characterization of the emission has been performed yet). For this reason, the following chapter will be limited to HHG from gases.

The low conversion efficiency is due to the combination of two factors: first the weak atomic response to the laser field and, second, phase mismatches between fundamental and harmonic fields during the macroscopic construction of the field. To increase the harmonic photon flux, one can compensate one or the other, as will be explained in the first two sections. A third section will review a new promising geometry, HHG from a multi-kHz fiber laser sources, that already reached integrated flux per second similar to high power laser based sources.

4.2 Optimization of the Atomic Response

High order laser harmonic generation is a highly nonlinear coherent process resulting from the interaction between an intense ultrashort pulse and a gas medium, usually a rare gas. In the spectral domain, the emission has a discrete structure consisting of odd harmonic orders of the fundamental wavelength. The spectrum can be divided in two areas: the plateau region, where the amplitude of the consecutive orders is constant, followed by the cutoff, where their amplitudes drop very fast. The position of the cutoff depends on several parameters. The maximum photon energy can be written as:

$$h\nu_{max} = I_p + 3.17U_p (4.1)$$

Here, I_p is the gas ionization potential and U_p , scaling as $I_{laser}\lambda^2$, the ponderomotive energy. One could in principle reach arbitrarily high photon energies simply by increasing the driving laser intensity. In practice, however, one observes that above the saturation intensity the large fraction of plasma prevents emission of HHG at higher photon energies. This is due to two effects. First, the plasma induces defocusing of the laser, effectively decreasing the laser intensity. Second, the conversion efficiency is low due to the large spectral dispersion in the plasma and the resulting phase mismatch between the laser and the soft X-rays. According to (4.1), using higher ionization potential leads to shorter wavelengths. However, lighter atoms also have a smaller ionization cross-section, reducing the overall efficiency. Looking closely at the HHG mechanism gives hints of ways to enhance the atomic response.

HHG can be explained by the semi-classical three-step model [18]. Close to each maxima of the laser field, an electron is tunnel ionized. It is subsequently accelerated by the electric field, and reverse direction with the field to come back at the core ion vicinity, with the possibility for recombination. The recolliding electrons follow trajectories that can be sorted into two main families, the so-called short and long ones. Experimentally, the short one is usually selected, because of the properties of the photons it generates (coherence, conversion efficiency, divergence). This can be experimentally achieved by putting the generating medium after the focal spot or by using a small aperture in the XUV beampath [19–21].

The ionization step is limited in time around the field maxima because of the high intensity dependence of tunnel ionization. Short trajectories electrons, being emitted close to field zero crossings, are more sensitive to this effect. The addition of a second electro-magnetic field, helping the ionization step, allows increasing the number of released electrons. This second field is used to change the ionization step to a single photon process and/or to choose the time at which the ionization happens by varying the relative phase between the two fields. Moreover, it offers additional control over the free electron trajectories, increasing for instance the energy gained by the free electron from the laser field, or limiting the lateral spreading of the electron wavepacket. This fine control of the generating field can lead to an enhancement of the produced XUV radiation under some specific conditions.

Several demonstrations using the fundamental field together with its second harmonic, generated in a crystal, have been published (see e.g. [22–24]). Both parallel and orthogonal polarization directions have been tested, the latter being more efficient according to [23] (they achieved $0.6\,\mu$ J at harmonic order 38 (21.6 nm)). Contrary to the weak perturbative second harmonic field used in single attosecond pulse experiments, the fundamental and harmonic fields are of comparable intensities. Watanabe and coworkers observed a close to one order of magnitude enhancement for harmonic orders 27–31 using the third harmonic from a crystal [25]. The third harmonic field can also be produced in a gas cell put before the HHG cell. This technique recently led to an enhancement factor between two and five at harmonic order 41 (19.5 nm) between the seeded and unseeded cases, depending on the generation intensity, leading to the generation of 20 nJ [26].

Higher harmonic orders can also be used. Two main configurations have been proposed. In the first case, the booster beam can be generated in a first cell, before the main one (see e.g. [27]). In the second one a gas mixture is used as the generation medium: lower order harmonics from an heavy gas are used to boost HHG from a lighter gas (e.g. [28]). The first case allows for the optimization of both generation stages independently, while the second configuration is easier to align. As an illustration of the latter case, harmonics 11–23 from xenon were used to boost harmonics from helium, and a gain of more than three orders of magnitude was observed at harmonic 27 (29.6 nm).

One has to keep in mind that quantifying the enhancement factor is not an easy task. In principle, one should find the optimum sets of HHG parameters for both the seeded and unseeded cases, which can be totally different (in focal length, gas specie, medium length and pressure, laser intensity ...). Moreover, a gain in harmonic signal does not necessarily translate as a gain in frequency conversion efficiency. Measuring HHG efficiency implies measuring the exact number of emitted photons at the source level, which in turn means that the detector has to be calibrated, and that the spectral transmission or reflectivity of the different optical components and filters (used to remove the fundamental laser and select harmonic orders) also need to be measured and calibrated.

4.3 Phase Matching

In addition to the single atom response, the macroscopic coherent construction of the harmonic field has to be optimized. It relies on the balance between three terms: phase matching, absorption and coherence. The different contributions to phase matching can be written as:

$$\mathbf{k}_{q} = q\mathbf{k}_{1} + \Delta\mathbf{k}_{geo} + \Delta\mathbf{k}_{atom} + \Delta\mathbf{k}_{elec} + \Delta\mathbf{k}_{ion} + \alpha_{i}\nabla I_{laser}$$
(4.2)

where k_1 and k_q are the fundamental and harmonic wave vectors. The successive terms stand for the effect of the focusing (Gouy phase), the dispersion from the neutral atoms/free electrons/ions in the gas medium and the dipole phase, with α_i depending on the electron trajectory considered and I_{laser} the laser intensity. Balcou et al. derived from (4.2) conditions for effective phase matching [19]. When the gas medium is at focus, the last term of (4.2) is equal to zero and phase matching is not possible. When the medium is after the focus, on-axis phase matching is possible, while before focus the phase matching happens only off axis.

The effect of the ions on the phase matching, which is as we saw critical, can be reduced using very short laser pulse duration. For long pulse duration, total ionization of the medium is reached before the maximum of the pulse envelope, and the harmonic emission saturates. For shorter pulses, the ionization onset comes later in the envelope, close to its maximum. The saturation intensity value is consequently increased, and the position of the cutoff is shifted towards higher harmonic orders, while plateau harmonics keep the same intensity [29, 30].

The choice over the optimum HHG experimental geometry can be reduced to a discussion over three typical lengths: the medium length L_{med} , the coherence length L_{coh} and the absorption length L_{abs} . L_{coh} represents the length over which the nonlinear polarization and the harmonic field get dephased by π , and L_{abs} is the distance over which the XUV radiation is reabsorbed by the generating medium ($L_{abs} = 1/(\sigma \rho)$ with σ the ionization cross section and ρ the atomic density). Constant and coworkers showed that the following conditions had to be fulfilled [31]:

$$L_{med} > 3L_{abs} \tag{4.3}$$

$$L_{coh} > 5L_{abs} \tag{4.4}$$

4.3.1 Loose Focusing

Equations (4.3) and (4.4) need to be fulfilled at each point throughout the medium, which in turn implies that the laser wavefront and intensity are optimized and slowly varying along the propagation axis. This leads to the so—called loose focusing geometry, where the beam is focused with a long focal length lens into a long and homogeneous medium such as a long gas jet [32], a gas cell [33, 34], a gas filled hollow core fiber [31]. Long focal lenses create large focal spots, which in turn allows coupling more laser energy for the same saturation intensities and enlarges the generation volume in the radial direction. When phase matching is obtained, the number of harmonic photons will scale with the increase of the laser energy and generation volume. Figures 4.1 and 4.2 illustrate the scaling effect from numerical simulations and experimental data, respectively. The expected scaling laws are not followed in most cases, for various reasons. In Fig. 4.1a, the number of photons decreases for long media due to reabsorption of the harmonics and refraction effects on the fundamental field that

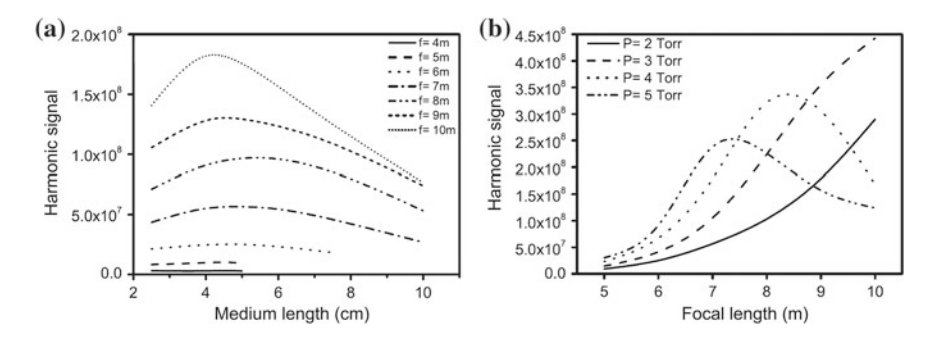


Fig. 4.1 Scaling effect of the harmonic photon number. **a** Variation of the number of photons (H25) as a function of the argon cell length for different focal lengths. **b** Variation of the number of photons (H25) as a function of the focal length for different argon pressure. In both cases, the authors considered argon and an IR intensity of 2×10^{14} W/cm². From [34]

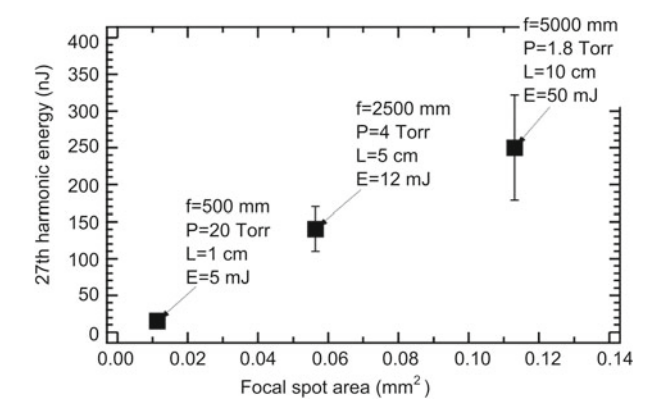
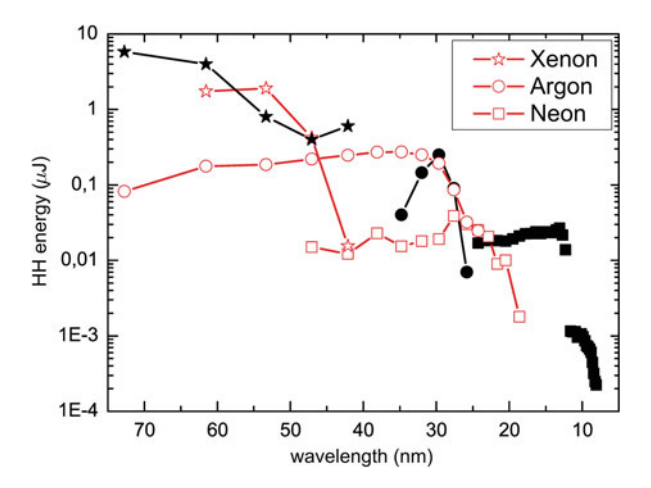


Fig. 4.2 Experimental scaling of the number of photons with the focal length. From [33]

Fig. 4.3 Optimized harmonic spectra. In *black*, data from [33], in *red*, data from [15, 32] and unpublished data. See Table 4.1 for explanations



decreases the effective intensity (in Fig. 4.1b, the chosen medium length was 5 cm). Figure 4.1b shows a f^4 trends for low pressure, where f is the focal length, and f^6 at P=5 Torr. This complex behavior was attributed to the fact that the peak laser intensity was below saturation intensity, which implies that the harmonic in some cases shifts to the cutoff region. Figure 4.2 shows a linear evolution of the photon number with the focal spot.

The loose focusing geometry is well adapted to the high power laser commercially available today, and have allowed several research groups to demonstrate microjoule level harmonic beams [13, 32, 33]. Figure 4.3 summarizes some of the optimized spectra from the literature as well as some unpublished data points obtained on the coherent diffractive imaging beamline at CEA-Saclay (see [13–15]) for different gases (see Table 4.1 for experimental parameters). Conversion efficiency in the 10^{-4} range are now reached for low harmonic orders in xenon. Plateau harmonic in argon

Gas	Lab	E_{laser} (mJ)	f(m)	L_{med} (cm)	Symbol in Fig. 4.3
Xenon	RIKEN, Japan	14	5	14	Black filled stars
Xenon	CEA, France	25	5	0.03	Red hollow stars
Argon	RIKEN, Japan	50	5	10	Black filled circles
Argon	CEA, France	15	5.5	8	Red hollow circles
Neon	RIKEN, Japan	50	10	5	Black filled squares
Neon	RIKEN, Japan	130	10	4	Black filled squares
Neon	CEA, France	28	5.5	5.5	Red hollow squares

Table 4.1 Experimental parameters for Fig. 4.3

(λ between 60 and 30 nm) can be generated with an efficiency better than 10^{-5} . One or more additional orders of magnitude are lost when using neon to generate radiation around 20 nm or below, leading to conversion efficiencies close to 10^{-6} (Fig. 4.4).

4.3.2 Quasi Phase Matching

For high harmonic orders (typically when λ gets below 20 nm) L_{abs} becomes very large (>mm) and L_{coh} , decreasing as a power function of q, will be smaller than L_{abs} . Fulfilling (4.4) becomes impossible, and perfect phase matching cannot be achieved. New schemes have been proposed in order to optimize the macroscopic coherent construction of the harmonic field. The main idea is to cancel the HHG process in the medium region where the polarization and the harmonic field are out

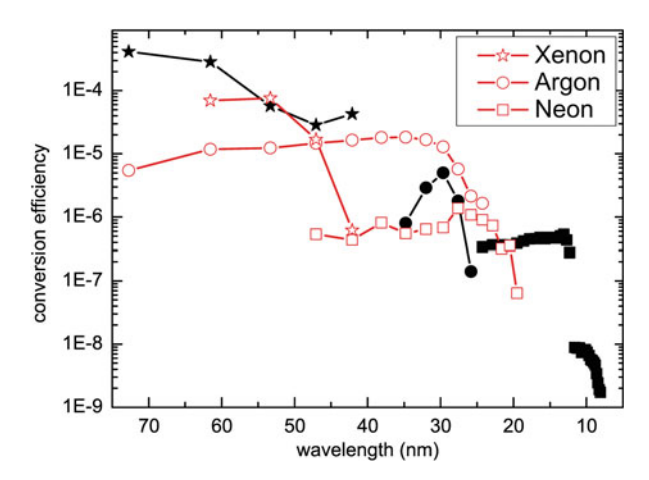


Fig. 4.4 Harmonic generation efficiency. In *black*, data from [33], in *red*, data from [15, 32] and unpublished data. See Table 4.1 for explanations

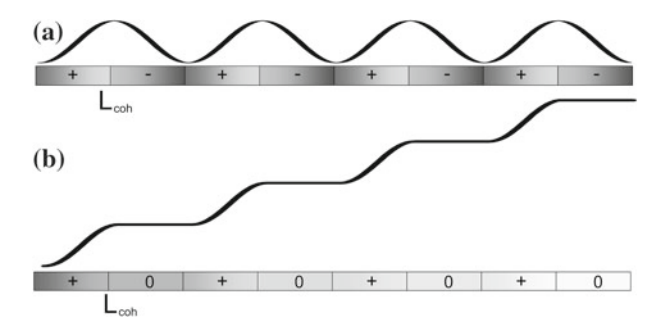


Fig. 4.5 Principle of quasi phase matching. a Phase matching is not achieved: the harmonic field amplitude oscillates with a period of $2L_{coh}$. b The quasi phase matching geometry cancels out HHG when the fields are dephased, the harmonic field can build up efficiently over the medium

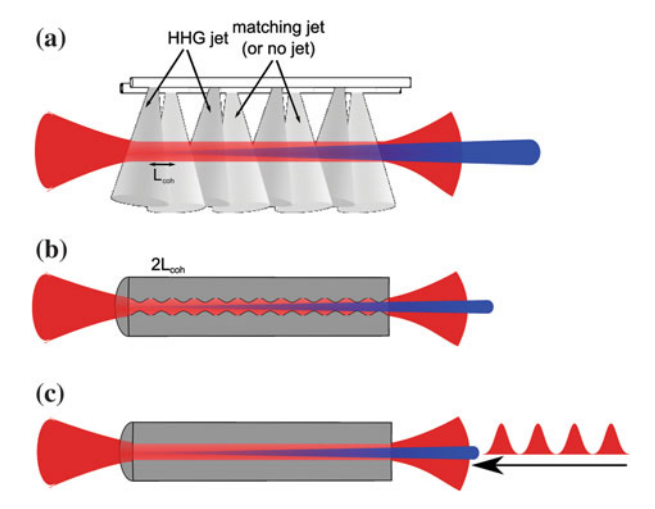


Fig. 4.6 Different quasi phase matching geometry. a Array of gas jets. b Modulated fiber. c Train of counter propagating pulses

of phase, similarly to quasi phase matching (QPM) schemes in the visible domain. In this scheme, HHG reaches the absorption limit when the *effective* medium length over which the field builds up (in principle, an odd multiple of $L_{coh}/2$) is larger than L_{abs} (Fig. 4.5).

A first solution is to physically modulate the medium by changing its density periodically (Fig. 4.6a). The effect of a set of successive gas jets has been studied both theoretically [35, 36] and experimentally [37–39]. This geometry not only periodically suppresses HHG, but it also suppresses absorption between the jets. Willner et al. designed a multijet array made of a succession of six argon jets separated by hydrogen jets, leading to a total argon length of $700\,\mu\text{m}$, that they compare with

a 700 μ m long jet. They observed an enhancement of H27 signal by a factor 36, corresponding to quasi phase matching, for a total HHG efficiency of 3×10^{-6} (1.2 $\times10^{-5}$ for H19) [39]. The jet geometry prevents any damage, while the entrance and exit holes of a cell or a capillary get destroyed by the laser. Consequently, no deterioration of the system appears over time, even when coupling high laser energies. However, the period of the modulation is difficult to fine tune, especially in Willner et al. configuration.

HHG in capillaries and fibers presents the advantages of a laser guiding geometry, preventing laser defocusing, which ensures a constant intensity over the whole medium length. Moreover, phase matching can be reached by adjusting the gas pressure inside the capillary. However, this fails when ionization becomes too important, preventing generation of high orders. Consequently, adapted quasi phase matching schemes have been proposed. It is possible to manufacture modulated fibers, with a core diameter that is modulated with L_{coh} (or a multiple of L_{coh} (Fig. 4.6b)). The modulation allows compensating for the phase mismatch induced by the plasma contribution, hence increasing the signal [40, 41].

Mode beating in a fiber has also been used to modulate the laser intensity on axis and achieve QPM [42]. While in principle only the coupling of two modes creates a regular periodic modulation allowing perfect QPM, it is experimentally difficult to achieve. Due to imperfect matching of the laser with the fiber, fiber imperfection and ionization, the coupling of a laser inside a fiber will more often lead to multi mode beating. However, the less regular resulting intensity modulation can also lead to an enhancement of the signal, somehow reduced compare with perfect QPM. Zepf and coworkers thus observed an enhancement by three orders of magnitude of water window harmonics (\approx 4 nm) generated in argon. However, coupling the laser beam into the first and 20th modes only, as in the numerical simulation showed in [42], or reproducing on a daily basis the same multi mode coupling, is not easily achieved.

A more versatile way towards quasi phase matching is to use a weak counterpropagation pulse (Fig. 4.6c) [43]. The modulation of the main electromagnetic field by the counter-propagating field suppresses HHG in the overlap regions. Robinson et al. proposed a technique using birefringent crystals or acousto-optic dispersive filter to generate trains of up to 100 pulses with arbitrary pulse separation [44], which opens the way towards a full control of QPM. Using a train of three weak pulses, Zhang and collaborators measured an enhancement by a factor 300 of H45 emission in an argon filed capillary, bringing otherwise cutoff harmonics to the same level of orders in the plateau [45].

Finally, other wavelengths can be used to modulate the medium: for instance, chirped orthogonal THz radiation was numerically shown to increase the conversion efficiency by three orders of magnitude in the cutoff [46].

4.3.3 Artificial Tailoring of the Laser Pulses

QPM schemes require a good control over the medium properties. Imperfect modulations lead to a reduced signal growth. Other possibilities, relying on passive or active shaping of the generating laser, in either spectral or spatial domains, have been proposed to optimize phase matching and HHG. Passive control relies on a given fixed modification of the beam, for instance creating diffractionless beams, while active control relies on learning genetic algorithms that modify given properties (phase front, chirp, ...) to maximize a fitness function (which can be related to a total number of emitted photons, the contrast between some harmonic orders, ...).

Diffractionless beams keep their transverse amplitude and spatial phase almost constant during their propagation. Consequently, they are good alternative to the loose focusing geometry mentioned in Sect. 4.3.1. They can be produced by focusing a ring shaped laser pulse [47] or using axicons [47–49] for instance. In the first case, using a Bessel-Gauss beam leads to an increase of the third harmonic conversion efficiency from a gas cell. The effect of axicons to HHG were studied numerically in [48]. They found that the brightness of H21 generated in argon could be increased by at least two orders of magnitude compare to the Gaussian case thanks to the improved spatial properties of the harmonic emission.

While beam shaping can be used to improve phase matching, another solution is to enlarge the focal spot, hence increasing the generation volume and the number of emitters. This is one of the effect of loose focusing, as the beam waist is proportional to the focal length. However, coupling high laser energy without exceeding the saturation intensity requires very long focal lengths [33]. Alternative solutions have been proposed to spatially tailor the beam focus with a reasonable size focal length. Using a phase mask before the lens, Boutu and collaborators created a flat top profile at focus, enlarging the beam profile compared to what is given by propagation of the Gaussian beam [50]. However, no gain was observed when comparing with the optimized Gaussian beam generation, because of laser energy limitations.

An efficient way to optimize HHG is the use of learning genetic algorithms. Using a fitness function that can be defined by the number of XUV photons, the shape of the spectrum or the XUV spatial profile, the algorithm modifies a set of parameters (usually some characteristic of the laser beam) to optimize the output [51]. The algorithm can modify the laser spectral phase by the use of a acousto-optic programmable filter (a "Dazzler" for instance) in order to spectrally shift the harmonic lines [52]. Control over the laser spectral phase has also been achieved through the use of a deformable mirror set in a place inside the laser chain were the spectral components are spatially separated [53]. Boyko et al. showed that depending on the laser total energy, the genetic algorithm modifies the laser pulse so that the saturation intensity is reached in the medium: when the energy is low, the optimization results in a Fourier limited pulse to maximize the intensity. When the energy is too high, the shaped laser pulses present a long leading edge with a gentle slope in order to obtain a longer duration for HHG [54].

Most of the studies use deformable mirrors to control the beam spatial profile, looking at the XUV flux (either integrated or for a single harmonic order) for optimization [55–57]. Eyring et al. used a pulse shaper to optimize the infrared laser focal spot [58], assuming that the HHG optimum would be reached with the best focus.

Characterization of the spatial wavefront, which is sometimes used as the criterion for laser optimization, is not limited to visible and near infrared lasers, as Hartman sensors have been designed for XUV wavelengths [59]. Aberrations of the XUV beam need to be minimized in order to optimize the beam focal spot. As to now, no iterative procedure was performed with this criterion, but several authors reported on the measurement of the XUV spatial phase as a "manual" optimization tool [15, 60, 61]. Due to the high non linearity of the HHG mechanism, it is however difficult to establish a clear link between the infrared laser and the XUV beam.

4.4 High Repetition Rate Sources

Today intense lasers allow for the generation of high flux XUV photon radiation. Sub-microjoule level pulses enable the study of non linear effects, pulse duration measurement by autocorrelation and single shot coherent diffractive imaging. However, the low repetition rate of those lasers (usually a few Hz to a few 10 s of Hz) is a severe limitation to their application to a larger set of problems. Coincidence measurements, for which the number of event per laser shot has to be one or less, are then prohibited. Moreover, some experiments in solid state physics where space charge effects need to be avoided relies more on repetition rate than in intense single bursts of photons. Lock-in detection schemes use a fast modulation of the pump laser to give access to very small variations of signals.

Kilohertz amplified laser systems are now reaching 10 mJ of energy and more. Up to now, no optimization work has been reported from such systems, but few mJ kHz systems have already led to interesting results. Dao et al. reported 5×10^{10} photons per shot for harmonics from argon (wavelength between 20 and 32 nm) and up to 10^{10} photons/harmonic cm² s for He harmonics (between 10 and 16 nm) from a 5 mJ, 1 kHz system [62]. Using a 7 mJ, 1 kHz system, Lambert et al. measured 10^{10} photons per shot at $\lambda = 44$ nm, corresponding to an energy of 50 nJ [24]. With a lower energy system, Jakubczak and coworkers reached 0.652 μ J/s for argon harmonics (90 nJ/s for a single harmonic at 30 nm) [63]. Multi-10 kHz are currently less energetic, however using very short focal length lenses, intensities in the HHG range are reachable. Integrated photon flux have been demonstrated above 10^9 photons/s in argon and xenon [64, 65]. Finally, repetition rate of several MHz can be obtained using intra cavity HHG schemes at an energy level of several hundreds of nanowatts [66, 67].

Other technologies are explored to generate high power high repetition rate lasers, as a promising alternative to Titanium-Sapphire based lasers. Based on doped fiber amplification stages, they lase in the near infrared domain. By adapting the chirp pulse amplification technique, millijoule level systems have been developed [71, 72]. Moreover, the pulse duration can be shortened using spectral broadening in

Table 4.2	Experimental results with amplified fiber laser systems

Reference	[68]	[68]	[69]	[69]	[70]
Technology	FCPA	NC-FCPA	NC-FCPA	FCPA	FCPA
Pulse energy (μJ)	80	580	100	28	100
Rep. rate (kHz)	1000	50	100	1000	100
Duration (fs)	500	45	270		500
Average power (W)	80	29	10	28	10
Intensity at focus (10 ¹⁴ W/cm ²)	0.42	7.6	0.71	0.2	0.6
Shortest wavelength (nm)	49 (Xe)	≤17 (Ar)	33 (Ar)	68.7 (Xe)	38.1 (Ar, Kr)
Strongest order (nm)	54	49 (Kr)	41.2 (Ar)	79.2 (Xe)	54–93.6 (Xe)
Photons per second		7.9×10^{11}			4.5×10^{12} (full spectrum)
Efficiency		1.2×10^{-7}			5×10^{-7}

noble gas filled hollow fibers in order to reach gigawatt peak power. Using short focal length lenses, intensities above $10^{13}\,\mathrm{W/cm^2}$ are easily reached, hence making HHG possible. Table 4.2 shows the most recent published results using such sources. The photon flux per second already reaches the same level as usual loose focusing geometries at long wavelengths, and similar flux in the water window range are soon expected.

4.5 Conclusion

High flux high order harmonic sources are nowadays producing intense coherent ultrashort XUV photons beams. Perfect phase matching conditions can be reached for moderately low harmonic orders, using loose focusing and long generating media. For shorter wavelengths, clever quasi phase matching schemes allow optimizing the overall macroscopic construction of the harmonic field. While the photon flux at the source can be important, special care has to be taken to propagate the XUV radiation towards the experiment. The first step is to remove the infrared field that copropagates with the harmonics. When the laser fluence is low, simple metallic filters can be used, either free standing or supported by a mesh to encerase the thermal conductivity. However, when high energy lasers are used, other schemes are required, as it is not always possible to put the filters far enough from the focus. A first solution is to generate harmonics with an annular beam, created by inserting a small beam blocker at the center of the infrared beam before the focusing lens. After the generation medium, an iris is used to block the fundamental radiation, while the harmonic beam, less divergent, is transmitted. However, this technique is not very

adapted to high flux sources, as most of the infrared energy is lost. Beamsplitters have been developed that consist in plates set at Brewster's angle for the fundamental frequency. Due to the grazing incidence, the harmonic reflectivity is of the order of several tens of percents, while the infrared attenuation rate is around 10^{-4} – 10^{-5} [73]. Kojima and collaborators performed an extensive study of several materials suitable for this technique [74]. SiC is an interesting candidate, that is already used in some HHG XUV beamlines [73]. A similar technique uses fused silica plates with an anti–reflective coating for the infrared radiation. At grazing incidence, the reflectivity for the harmonics is above 50 % [13]. Grazing incidence metallic optics can then be used to focus the XUV radiations at the experiment interaction point when broadband radiation is needed. Thanks to continuous development, multilayer coated mirrors offer now high reflectivity when a specific spectral range is needed. Overall, a loss of one to two orders of magnitude in photon numbers is to be expected.

Using intense low repetition rate lasers, time resolved single shot studies of ultrafast phenomena and nonlinear optics are now possible. On the other hand, very high repetition rate systems are becoming competitive and generate similar number of photons per seconds, and applications in solid state physics (i.e. XPEEM imaging) and coincidence experiments should be attempted very soon.

While the photon flux is still several orders of magnitude below what produce free electron lasers (FEL), high efficiency HHG sources clearly have an important role to play, thanks to their very good spatial (coherence, wavefront ...) and temporal (femtosecond to attosecond duration, zero temporal jitter with the laser pulse) properties. Finally, the "room scale" size and cost of such XUV radiation sources is also negligible in comparison to big facilities like FEL.

References

- J. Seres, E. Seres, A.J. Verhoef, G. Tempea, C. Streli, P. Wobrauschek, V. Yakovlev, A. Scrinzi, C. Spielmann, F. Krausz, Nature 433, 596 (2005)
- T. Popmintchev, M.C. Chen, D. Popmintchev, P. Arpin, S. Brown, S. Aliauskas, G. Andriukaitis, T. Baliunas, O.D. Mcke, A. Pugzlys, A. Baltuka, B. Shim, S.E. Schrauth, A. Gaeta, C. Hernndez-Garca, L. Plaja, A. Becker, A. Jaron-Becker, M.M. Murnane, H.C. Kapteyn, Science 336, 1287 (2012)
- Z. Chang, A. Rundquist, H. Wang, M.M. Murnane, H.C. Kapteyn, Phys. Rev. Lett. 79(16), 2967 (1997)
- M.C. Chen, P. Arpin, T. Popmintchev, M. Gerrity, B. Zhang, M. Seaberg, D. Popmintchev, M.M. Murnane, H.C. Kapteyn, Phys. Rev. Lett. 105, 173901 (2010)
- T. Ditmire, E.T. Gumbrell, R.A. Smith, J.W.G. Tisch, D.D. Meyerhofer, M.H.R. Hutchinson, Phys. Rev. Lett. 77, 4756 (1996)
- 6. L. Le Déroff, P. Salières, B. Carré, D. Joyeux, D. Phalippou, Phys. Rev. A 61, 043802 (2000)
- 7. L. Le Déroff, P. Salières, B. Carré, Opt. Lett. 23, 1544 (1998)
- 8. P. Salières, A. L'Huillier, M. Lewenstein, Phys. Rev. Lett. 74, 3776 (1995)
- M. Bellini, C. Lynga, A. Tozzi, M.B. Gaarde, T.W. Hansch, A. L'Huillier, C.G. Wahlstrom, Phys. Rev. Lett. 81(2), 297 (1998)
- 10. T. Sekikawa, A. Kosuge, T. Kanai, S. Watanabe, Nature **432**, 605 (2004)
- 11. Y. Nabekawa, H. Hasegawa, E.J. Takahashi, K. Midorikawa, Phys. Rev. Lett. 94, 043001 (2005)

 P. Tzallas, E. Skantzakis, L.A.A. Nikolopoulos, G.D. Tsakiris, D. Charalambidis, Nat. Phys. 7, 781 (2011)

- A. Ravasio, D. Gauthier, F.R.N.C. Maia, M. Billon, J.P. Caumes, D. Garzella, M. Géléoc, O. Gobert, J.F. Hergott, A.M. Pena, H. Perez, B. Carré, E. Bourhis, J. Gierak, A. Madouri, D. Mailly, B. Schiedt, M. Fajardo, J. Gautier, P. Zeitoun, P.H. Bucksbaum, J. Hajdu, H. Merdji, Phys. Rev. Lett. 103, 028104 (2009)
- D. Gauthier, M. Guizar-Sicairos, X. Ge, W. Boutu, B. Carré, J.R. Fienup, H. Merdji, Phys. Rev. Lett. 105, 093901 (2010)
- X. Ge, W. Boutu, D. Gauthier, F. Wang, A. Borta, B. Barbrel, M. Ducousso, A.I. Gonzalez, B. Carré, D. Guillaumet, M. Perdrix, O. Gobert, J. Gautier, G. Lambert, F.R.N.C. Maia, J. Hajdu, P. Zeitoun, H. Merdji, Opt. Express 21, 11441 (2013)
- B. Dromey, M. Zepf, A. Gopal, K. Lancaster, M. Wei, K. Krushelnick, M. Tatarakis, N. Vakakis, S. Mouistaizis, R. Kodama, M. Tampo, C. Stoeckl, R. Clarke, H. Habara, D. Neely, S. Karsch, P. Norreys, Nat. Phys. 2, 456 (2006)
- 17. C. Thaury, H. George, F. Quere, R. Loch, J.P. Geindre, P. Monot, P. Martin, Nat. Phys. 4, 631 (2008)
- 18. P.B. Corkum, Phys. Rev. Lett. **71**, 1994 (1993)
- 19. P. Balcou, P. Salières, A. L'Huillier, M. Lewenstein, Phys. Rev. A 55(4), 3204 (1997)
- P. Salières, B. Carré, L.L. Déroff, F. Grasbon, G.G. Paulus, H. Walther, R. Kopold, W. Becker, D.B. Miloevic, A. Sanpera, M. Lewenstein, Science 292, 902 (2001)
- H. Merdji, M. Kovacev, W. Boutu, P. Salières, F. Vernay, B. Carré, Phys. Rev. A 74, 043804 (2006)
- T.T. Liu, T. Kanai, T. Sekikawa, S. Watanabe, Phys. Rev. A: At. Mol. Opt. Phys. 73, 063823 (2006)
- I.J. Kim, G.H. Lee, S.B. Park, Y.S. Lee, T.K. Kim, C.H. Nam, T. Mocek, K. Jakubczak, Appl. Phys. Lett. 92, 021125 (2008)
- G. Lambert, J. Gautier, C.P. Hauri, P. Zeitoun, C. Valentin, T. Marchenko, F. Tissandier, J.P. Goddet, M. Ribiere, G. Rey, M. Fajardo, S. Sebban, New J. Phys. 11, 083033 (2009)
- S. Watanabe, K. Kondo, Y. Nabekawa, A. Sagisaka, Y. Kobayashi, Phys. Rev. Lett. 73, 2692 (1994)
- F. Brizuela, C.M. Heyl, P. Rudawski, D. Kroon, L. Rading, J.M. Dahlstrom, J. Mauritsson, P. Johnsson, C.L. Arnold, A. L'Huillier, Sci. Rep. 3 (2013). doi:10.1038/srep01410
- 27. A. Heinrich, W. Kornelis, M.P. Anscombe, C.P. Hauri, P. Schlup, J. Biegert, U. Keller, J. Phys. B: At. Mol. Opt. Phys. 39, S275 (2006)
- E.J. Takahashi, T. Kanai, K.L. Ishikawa, Y. Nabekawa, K. Midorikawa, Phys. Rev. Lett. 99, 053904 (2007)
- I.P. Christov, J. Zhou, J. Peatross, A. Rundquist, M.M. Murnane, H.C. Kapteyn, Phys. Rev. Lett. 77, 1743 (1996)
- 30. K.J. Schafer, K.C. Kulander, Phys. Rev. Lett. **78**, 638 (1997)
- 31. E. Constant, D. Garzella, P. Breger, E. Mével, C. Dorrer, C.L. Blanc, F. Salin, P. Agostini, Phys. Rev. Lett. 82, 1668 (1999)
- 32. J.F. Hergott, M. Kovacev, H. Merdji, C. Hubert, Y. Mairesse, E. Jean, P. Breger, P. Agostini, B. Carré, P. Salièes, Phys. Rev. A 66, 021801 (2002)
- 33. E. Takahashi, Y. Nabekawa, H. Mashiko, H. Hasegawa, A. Suda, K. Midorikawa, IEEE J. Sel. Top. Quantum Electron. 10, 1315 (2004)
- 34. W. Boutu, T. Auguste, J.P. Caumes, H. Merdji, B. Carré, Phys. Rev. A 84, 053819 (2011)
- 35. T. Auguste, B. Carré, P. Salières, Phys. Rev. A: At. Mol. Opt. Phys. 76, 011802 (2007)
- X. Wang, M. Chini, Q. Zhang, K. Zhao, Y. Wu, D.A. Telnov, S.I. Chu, Z. Chang, Phys. Rev. A 86, 021802 (2012)
- 37. J. Seres, V.S. Yakovlev, E. Seres, C. Streli, P. Wobrauschek, C. Spielmann, F. Krausz, Nat. Phys. 3, 878 (2007)
- 38. A. Pirri, C. Corsi, M. Bellini, Phys. Rev. A: At. Mol. Opt. Phys. 78, 011801 (2008)
- A. Willner, F. Tavella, M. Yeung, T. Dzelzainis, C. Kamperidis, M. Bakarezos, D. Adams, M. Schulz, R. Riedel, M.C. Hoffmann, W. Hu, J. Rossbach, M. Drescher, N.A. Papadogiannis, M. Tatarakis, B. Dromey, M. Zepf, Phys. Rev. Lett. 107, 175002 (2011)

- 40. E.A. Gibson, A. Paul, N. Wagner, R. Tobey, D. Gaudiosi, S. Backus, I.P. Christov, A. Aquila, E.M. Gullikson, D.T. Attwood, M.M. Murnane, H.C. Kapteyn, Science **302**, 95 (2003)
- 41. A. Paul, R. Bartels, R. Tobey, H. Green, S. Weiman, I. Christov, M. Murnane, H. Kapteyn, S. Backus, Nature 421, 51 (2003)
- M. Zepf, B. Dromey, M. Landreman, P. Foster, S.M. Hooker, Phys. Rev. Lett. 99, 143901 (2007)
- 43. J. Peatross, S. Voronov, I. Prokopovich, Opt. Express 1, 114 (1997)
- T. Robinson, K. O'Keeffe, M. Zepf, B. Dromey, S.M. Hooker, J. Opt. Soc. Am. B 27, 763 (2010)
- 45. X. Zhang, A. Lytle, T. Popmintchev, X. Zhou, H. Kapteyn, M. Murnane, O. Cohen, Nat. Phys. 3, 270 (2007)
- 46. K. Kovacs, E. Balogh, J. Hebling, V. Toşa, K. Varjú, Phys. Rev. Lett. 108, 193903 (2012)
- C. Altucci, R. Bruzzese, C. de Lisio, A. Porzio, S. Solimeno, V. Tosa, Opt. Lasers Eng. 37, 565 (2002)
- 48. T. Auguste, O. Gobert, B. Carré, Phys. Rev. A: At. Mol. Opt. Phys. 78, 033411 (2008)
- A. Averchi, D. Faccio, R. Berlasso, M. Kolesik, J.V. Moloney, A. Couairon, P.D. Trapani, Phys. Rev. A: At. Mol. Opt. Phys. 77, 021802 (2008)
- W. Boutu, T. Auguste, O. Boyko, I. Sola, P. Balcou, L. Binazon, O. Gobert, H. Merdji, C. Valentin, E. Constant, E. Mével, B. Carré, Phys. Rev. A 84, 063406 (2011)
- 51. C. Winterfeldt, C. Spielmann, G. Gerber, Rev. Mod. Phys. 80, 117 (2008)
- 52. D.H. Reitze, S. Kazamias, F. Weihe, G. Mullot, D. Douillet, F. Aug, O. Albert, V. Ramanathan, J.P. Chambaret, D. Hulin, P. Balcou, Opt. Lett. 29, 86 (2004)
- R. Bartels, S. Backus, E. Zeek, L. Misoguti, G. Vdovin, I.P. Christov, M.M. Murnane, H.C. Kapteyn, Nature 406, 164 (2000)
- O. Boyko, C. Valentin, B. Mercier, C. Coquelet, V. Pascal, E. Papalazarou, G. Rey, P. Balcou, Phys. Rev. A: At. Mol. Opt. Phys. 76, 063811 (2007)
- D. Yoshitomi, J. Nees, N. Miyamoto, T. Sekikawa, T. Kanai, G. Mourou, S. Watanabe, Appl. Phys. B 78, 275 (2004)
- P. Villoresi, S. Bonora, M. Pascolini, L. Poletto, G. Tondello, C. Vozzi, M. Nisoli, G. Sansone, S. Stagira, S.D. Silvestri, Opt. Lett. 29, 207 (2004)
- T. Pfeifer, R. Kemmer, R. Siptzenpfeil, D. Walter, C. Winterfeldt, G. Gerber, C. Speilmann, Opt. Lett. 30, 1497 (2005)
- 58. S. Eyring, C. Kern, M. Zürch, C. Spielmann, Opt. Express 20, 5601 (2012)
- I. Mercer, E. Mevel, R. Zerne, A. L'Huillier, P. Antoine, C.G. Wahlström, Phys. Rev. Lett. 77, 1731 (1996)
- J. Gautier, P. Zeitoun, C. Hauri, A.S. Morlens, G. Rey, C. Valentin, E. Papalarazou, J.P. Goddet, S. Sebban, F. Burgy, P. Mercère, M. Idir, G. Dovillaire, X. Levecq, S. Bucourt, M. Fajardo, H. Merdji, J.P. Caumes, Eur. Phys. J. D 48, 459 (2008)
- J. Lohbreier, S. Eyring, R. Spitzenpfeil, C. Kern, M. Weger, C. Spielmann, New J. Phys. 11, 023016 (2009)
- 62. L.V. Dao, S. Teichmann, J. Davis, P. Hannaford, J. Appl. Phys. 104, 023105 (2008)
- K. Jakubczak, T. Mocek, B. Rus, J. Polan, J. Hrebicek, M. Sawicka, P. Sikocinski, J. Sobota, T. Fort, L. Pina, Opto-Electron. Rev. 19, 169 (2011)
- M.C. Chen, M.R. Gerrity, S. Backus, T. Popmintchev, X. Zhou, P. Arpin, X. Zhang, H.C. Kapteyn, M.M. Murnane, Opt. Express 17, 17376 (2009)
- 65. C.M. Heyl, J. Gdde, A. L'Huillier, U. Hfer, J. Phys. B: At. Mol. Opt. Phys. 45, 074020 (2012)
- C. Gohle, T. Udem, M. Herrmann, J. Raushenberger, R. Holzwarth, H. Schuessler, F. Krausz, T. Hansch, Nature 436, 234 (2005)
- 67. D.C. Yost, T.R. Schibli, J. Ye, Opt. Lett. 33, 1099 (2008)
- 68. S. Hädrich, M. Krebs, J. Rothhardt, H. Carstens, S. Demmler, J. Limpert, A. Tünnermann, Opt. Express 19, 19374 (2011)
- J. Boullet, Y. Zaouter, J. Limpert, S. Petit, Y. Mairesse, B. Fabre, J. Higuet, E. Mével, E. Constant, E. Cormier, Opt. Lett. 34, 1489 (2009)
- 70. A. Cabasse, G. Machinet, A. Dubrouil, E. Cormier, E. Constant, Opt. Lett. 37(22), 4618 (2012)

71. F. Röser, T. Eidam, J. Rothhardt, O. Schmidt, D.N. Schimpf, J. Limpert, A. Tünnermann, Opt. Lett. 32, 3495 (2007)

- S. Hädrich, J. Rothhardt, M. Krebs, F. Tavella, A. Willner, J. Limpert, A. Tünnermann, Opt. Express 18, 20242 (2010)
- 73. E.J. Takahashi, H. Hasegawa, Y. Nabekawa, K. Midorikawa, Opt. Lett. 29, 507 (2004)
- Y. Kojima, A.A. Eilanlou, Y. Furukawa, Y. Nabekawa, E.J. Takahashi, F. Kannari, K. Midorikawa, Jpn. J. Appl. Phys. 51, 062601 (2012)

Chapter 5 Seeding Free Electron Lasers with High Order Harmonics Generated in Gas

Marie-Emmanuelle Couprie and Luca Giannessi

Abstract Short wavelength Free Electron Lasers (FEL) may operate in the Self Amplified Spontaneous Emission (SASE) configuration, where the spontaneous radiation originated by the electron shot noise is gradually amplified. This generally leads to an output pulse consisting of uncorrelated temporal spikes with a limited longitudinal coherence length. When a FEL amplifier is seeded by a coherent light source, the coherence properties of the seed are transferred to the initial electron-beam modulation, allowing for an improved control of the longitudinal properties of the emitted radiation. The spiky structure is suppressed both in the temporal domain and spectral domain and the bunching process becomes more efficient. Associated intensity and jitter fluctuations are reduced, as well as the arrival-time jitter. In addition the use of an external seed reduces the saturation length and therefore the associated costs of the device. High order harmonics generated in gas permit to seed a FEL amplifier in the vacuum ultra-violet, enabling the direct generation of seeded-Free Electron Laser radiation directly at short wavelengths. We analyze here the basic requirements for the seed source in terms of seed level versus the electron shot noise, and the problems of coupling of the seed source to the FEL. We also review the most recent achievements with HHG seeding, in particular on SCSS Test Accelerator, SPARC and SFLASH.

M.-E. Couprie (⊠)

Synchrotron SOLEIL, L'Orme des Merisiers, Saint-Aubin, BP48, 91 192 Gif-sur-Yvette Cedex, France e-mail: couprie@synchrotron-soleil.fr

L. Giannessi

ENEA C. R. Frascati, Via Enrico Fermi, 45 00044 Frascati, Rome, Italy e-mail: luca.giannessi@enea.it

L. Giannessi

Elettra-Sincrotrone Trieste, S.S.14-km 163.5 in AREA Science Park, 34149 Basovizza, Italy

© Springer-Verlag Berlin Heidelberg 2015
F. Canova and L. Poletto (eds.), *Optical Technologies for Extreme-Ultraviolet and Soft X-ray Coherent Sources*, Springer Series in Optical Sciences 197, DOI 10.1007/978-3-662-47443-3_5

5.1 Introduction

Accelerator-based light sources [1] produce short wavelength, widely tuneable radiation, either in storage rings (second or third generation) with partial transverse coherence, or in linear accelerators (linac) combined to FEL amplifiers. The latter, considered as fourth generation light sources, provide short pulses, improved coherence and higher brilliance. The radiation mechanism is the synchrotron radiation emission by accelerated relativistic charged particles, when submitted to a magnetic field in bending magnets or in insertion devices, undulators or wigglers [2], made of an alternated succession of magnets, which allow the number of curvatures to be increased and the radiation to be reinforced. The polarization properties of the emitted light depend on the electron orbit in the specific undulator configuration, which can be linear or helical. Electrons subject to the periodic sinusoidal magnetic field (period λ_u and peak field B_u) along the transverse direction undergo smooth sinusoidal oscillations in the transverse plane and emit synchrotron radiation at each bend of the trajectory. Interference takes place at the wavelengths λ_n such that $n\lambda_n = \lambda_u(1-\beta_s)$, with n an integer, and with β_s the longitudinal reduced velocity of the electrons. In the linear polarized undulator case, we have

$$\beta_s = \left(1 - \frac{1}{2\gamma^2} \left(1 + \frac{K_u^2}{2}\right)\right) \tag{5.1}$$

with $\gamma = E/m_0c^2$ and $K_u = e_0B_u\lambda_u/(2\pi m_0c)$, E being the electron beam energy, m_0 the electron rest mass, e_0 the electron charge and c the speed of light in vacuum. The fundamental resonant wavelength is obtained for n = 1, i.e., for $\lambda_1 = \lambda_u(1-\beta_s)$. The resonant wavelength and its harmonics may be then expressed as:

$$\lambda_n = \frac{\lambda_u}{2\gamma^2 n} \left(1 + \frac{K_u^2}{2} \right) \tag{5.2}$$

The wavelength λ_n of the emitted radiation can be controlled through a modification of the beam energy or through the undulator magnetic field (by changing the gap for permanent magnet insertion devices or the power supply current for electromagnetic insertion devices). Indicating with N_u the number of undulator magnetic periods, in the time domain an observer receives a train of N_u optical periods, which can be considered as quasi-continuous emission of radiation with respect to the bending magnet radiation. The radiation spectrum, i.e., the square modulus of the Fourier transform of the field associated to this train of pulses, is then composed by a series of square "sinc" functions, centered on odd harmonics. The "homogeneous" (referring to the case of a single electron) relative linewidth of the harmonics is given by $\Delta \lambda/\lambda_n = 1/(nN_u)$. The emission is narrow in the frequency domain. An "inhomogeneous" broadening of the undulator line may result from the electron beam energy spread, size and divergence [3]. Synchrotron radiation is tunable from infra-red to X-rays, has low divergence, small source size, and may posses different

polarization properties. The duration of radiation pulses is determined by the length of the electron bunches from which the former are generated. The repetition rate of the source depends on the type of accelerator used to produce the electron bunches. It may be in the MHz range in storage rings, MHz-kHz range in superconducting linacs and 10-100 Hz range in normal conducting linacs. Third generation light sources, based on storage rings designed to minimize the electron beam transverse emittances (the product of beam size by beam divergence), and to host a high number of insertion devices for the generation of radiation, provide a high average brilliance and a partial transverse coherence. Typical duration of the generated light pulses is in the range of a few ps, unless specific optics [4] or slicing scheme [5, 6] are implemented. These schemes are generally associated to a reduction of the total photon flux available. On the other side, in FELs [7] longitudinal coherence is achieved by phasing the emitting electrons undergoing the emission process: a light wave at the resonant wavelength λ , which may be the spontaneous synchrotron emission progressing with the electron beam along the undulator or stored in an optical cavity, or an external seed from a laser or another coherent source, interacts with the electron bunch in the undulator, inducing an energy modulation of the electrons; this energy modulation is gradually transformed into a density modulation by the dispersion properties of the undulator itself, and the coherent emission from the modulated beam at λ_0 and λ/n (fundamental and harmonics) [8] leads to the amplification of the light wave. The wave is amplified to the expense of the electron kinetic energy. Like for synchrotron radiation, the tunability is achieved through the magnetic field of the undulator or through electron beam energy. Operation at short wavelengths requires high beam energies to reach the desired resonant wavelength (hundreds of MeV to several GeV for VUV/soft-X and hard X-rays). The superposition of the optical wave with the electron bunch is essential for an efficient energy exchange. The lack of suitable mirrors for the realization of an optical cavity to store the radiation has driven the design of short wavelength FELs towards very long undulators, to extend the interaction region, and towards increased electron beam density (small emittances and high current) to enhance the coupling between the beam and the wave in a single pass through the undulator. In single pass FELs, transverse coherence depends on the size of the emitting source in phase space, which for a diffracton-limited source should be smaller than the corresponding radiation phase-space area. This poses constraints on the desired electron beam emittance, which should be of the order of the emitted wavelength or smaller.

5.2 Seeding and Harmonic Generation, a Particular FEL Configuration

5.2.1 Oscillator

The first FEL operation in 1977 at MARK-III (Stanford, USA) in the infra-red [9], as well as the second FEL (first at visible wavelengths) in 1983 at ACO (Orsay, France) [10] were based on an oscillator configuration [11, 12]. In the oscillator

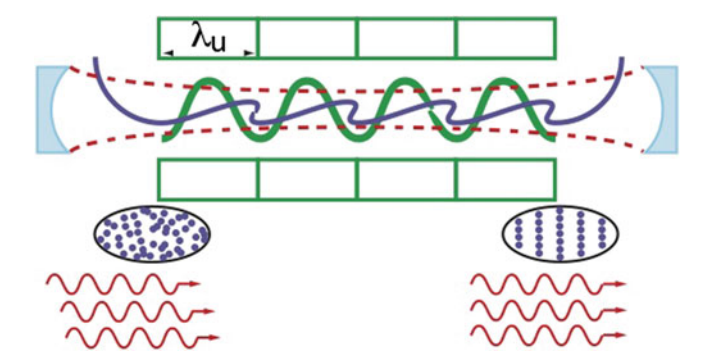


Fig. 5.1 Sketch of the oscillator configuration: the undulator, (*green*), induces a trajectory oscillating in the *horizontal* plane of the electron bunch (*blue*, without and with bunching), with unphased emission at the undulator entrance, and phased emission after bunching is established

configuration, as shown in Fig. 5.1, synchrotron radiation is stored in an optical cavity designed to ensure multiple interactions with the periodic electron beam current provided by a radio frequency accelerator. This periodic interaction amplifies the stored radiation synchronous with the electron current periodicity, leading to a train of laser pulses, with a mechanism analogous to the temporal gain modulation used to shorten the pulse duration in active mode-locked lasers. In the frequency domain the radiation spectrum is determined by the FEL gain bandwidth and by the optical cavity bandpass. FEL oscillators cover a spectral range from the THz to the VUV, where mirrors are available. First FEL applications started in the infrared and in the UV [13–16] in 1993. Various FEL oscillators were built down to the ultraviolet [17–22] and down to VUV at ELETTRA (Trieste, Italy) [16, 23, 24]. Extensions to shorter wavelengths [25–27] have been proposed in the VUV-Soft X-ray range and recently in the hard X-ray range of the spectrum [28] where the X-ray pulses are stored in a Bragg cavity. This scheme, which could provide high repetition rate, fully transversely and longitudinally coherent X-rays with very low spectral bandwidth, is envisaged to be implemented on the JAEA ERL [29].

5.2.2 High Gain and Self Amplified Spontaneous Emission

The lack of mirrors suited for the realization of an optical cavity in the VUV or X-rays has pushed the design of the first short-wavelength FEL sources towards the Self Amplified Spontaneous Emission (SASE) configuration, where the spontaneous synchrotron radiation emitted by the beam is then amplified by the FEL process in a single pass along the undulator. The conversion from electron kinetic energy to energy of the optical wave has the typical behavior of an instability, with an exponental growth regime followed by a saturation process [30–34]. The gain of the instability in a cold beam (i.e., zero emittances and no incoherent energy spread) is

described by the universal scaling parameter ρ_{fel} , that is recalled here in the case of a planar undulator,

$$\rho_{fel} = \frac{1}{4\pi\gamma} \left[\frac{2\pi^2}{\Sigma_b} \left(f_b \left(\xi \right) \lambda_u K_u \right)^2 \frac{I_{peak}}{I_A} \right]^{\frac{1}{3}}$$
 (5.3)

where Σ_b is the electron beam cross section, I_{peak} is the e-beam peak current and $I_A = e_0 c/r_0 \sim 17\,\mathrm{kA}$ is the Alfven current (being e_0 the electron charge and r_0 the electron classical radius). The function $f_b(\xi) = J_0(\xi) - J_1(\xi)$, where $\xi = K_u^2/(4+2K_u^2)$ is a factor arising from the average over the longitudinal fast motion typical of the electron orbit in linear undulators. The e-folding (gain) length L_G , for the power associated to the electromagnetic wave as resulting from the 1-dimensional theory in the cold beam limit is given by the general expression,

$$L_G = \frac{\lambda_u}{4\pi\sqrt{3}\rho_{fel}} \tag{5.4}$$

After a distance $L_{sat} \sim 20L_G$ the FEL output signal saturates at a power $P_{sat} \sim \rho_{fel} P_{beam}$ where $P_{beam} = I_{peak} \gamma m_0 c^2 / e_0$ is the peak power carried by the electron beam. The natural line width of the output radiation from the SASE process in the classical regime is of the order of the parameter ρ_{fel} . The frequency spectrum of the emitted radiation corresponds to the white noise associated to the initial electron random distribution, filtered by the FEL gain bandwidth and the emission usually presents poor longitudinal coherence properties, with a structure constituted by a series of longitudinal spikes uncorrelated in phase [35–38]. Ultra short electron bunches may lead to the generation of a single isolated radiation spike, as proposed [39–41] and later demonstrated [42]. Thanks to recent accelerator advances (high peak current, small energy spread, low emittance), long undulator, linac based, single pass SASE FEL are blooming worldwide. They now provide tuneable coherent subps pulses in the UV/X-ray region, with GW peak powers and a substantial increment in peak and average brilliance with good transverse coherence resulting from the low electron beam emittance and from the amplification process [43]. The first evidence of high gain starting from noise was obtained at the Laboratoire d'Utilisation du Rayonnement Electromagnétique at Orsay [44], at Brookhaven National Laboratory [45] and at University of California, Los Angeles [46]. Saturation was achieved in the visible at LEUTL (Argonne, USA) [47] and some years later in the VUV-Soft X-ray at FLASH (Germany, 30–4.5 nm) [48], at the SCSS Test Accelerator (Japan, 40-60 nm) [49] and in 2010 at FERMI (Italy, 20-100 nm), where for the first time a user facility implemented the amplification of a seed [50] (see next section). In the hard X-ray range, the first tuneable fs X-ray FEL operated in 2009 at the Linear Coherent Light Source at 0.15 nm (LCLS, Stanford, USA, 2 mJ, 14 GeV) [51, 52]. Lasing was obtained at the FERMI FEL facility in Italy in 2010, at the wavelength of 52 nm. Later on, in June 2011, at SACLA (Japan) [53], the wavelength of 0.12 nm was obtained with an electron energy of 8 GeV. This trend will continue in the next years with the realization of the European XFEL [54], the Korean XFEL [55], the

SwissFEL [56] and the Shanghai FEL [57]. These sources represent the brightest X-ray beams ever produced on earth and exploited by scientists in a wide variety of experiments. Fifty years after the laser discovery [58], the emergence of several mJ X-ray lasers for users in the Angstrom range constitutes a major breakthrough [59], opening a new era for scientific applications.

5.2.3 Seeding and Harmonic Generation

Instead of initiating the FEL process from the stochastic synchrotron emission, one can seed a FEL amplifier by an external coherent source. The coherence properties of the seed are transferred to the electron modulation, leading to coherent emission at the undulator resonance and at its harmonics. The FEL may therefore operate as an amplifier of the initial seed, capable of increasing the peak power of a light source to approximately the same P_{sat} value characteristic of SASE saturation. The presence of the seed suppresses the spikes in the output pulse, shortens the undulator length necessary to reach the saturation power and reduces the intrinsic shot-to shot fluctuations associated to the SASE process [60].

In a seeded FEL, as shown in Fig. 5.2a, b, a sufficiently intense input field generates an efficient bunching even in a short undulator, leading to coherent emission of undulator radiation and of its higher order harmonics. Coherent harmonic generation was first observed at ACO (Orsay, France) [61] in the UV and VUV [62, 63], then at SuperACO FEL (Orsay, France) [64] in the VUV, at MAX-Lab [65], and more recently at ELETTRA [66, 67], DUKE [68] storage rings and at Maxlab linac [69]. Later on, at UVSOR (Okazaki, Japan), further dynamics investigations were carried on the appearance of synchrotron sidebands [70, 71] and on the laser injection intensity dependance [72]. Issues regarding operation in helical configuration were also the subject of further investigations [69, 71, 73].

The higher order harmonic components of the density modulation induced by the FEL process may be exploited in a "harmonic converter" configuration [74], to multiply the frequency, and extend the original spectral range of operation, of the FEL. In [75] the modulated beam at the exit of a FEL oscillator, injected in a single pass FEL amplifier, was proposed as a method to initiate the FEL amplification from a modulation stronger than that associated to the natural electron beam shot noise. The High Gain Harmonic Generation scheme (HGHG) [60, 76], shown in Fig. 5.2 consists of a short undulator seeded by a strong optical wave. The injected laser induces the energy modulation of the electron bunch in a first undulator, which is followed by a small chicane converting the energy modulation into a density modulation. The radiation is then generated in a second undulator tuned at the fundamental of the first or at one of its higher order harmonics (cascade scheme). The two undulator resonances can be also tuned to have one of the higher order harmonics in common, as in the situation shown in Fig. 5.2d [77].

Wavelength tuning may be obtained by simultaneously changing the seed wavelength and the undulator gap [78] or by applying a chirp (frequency drift) on the

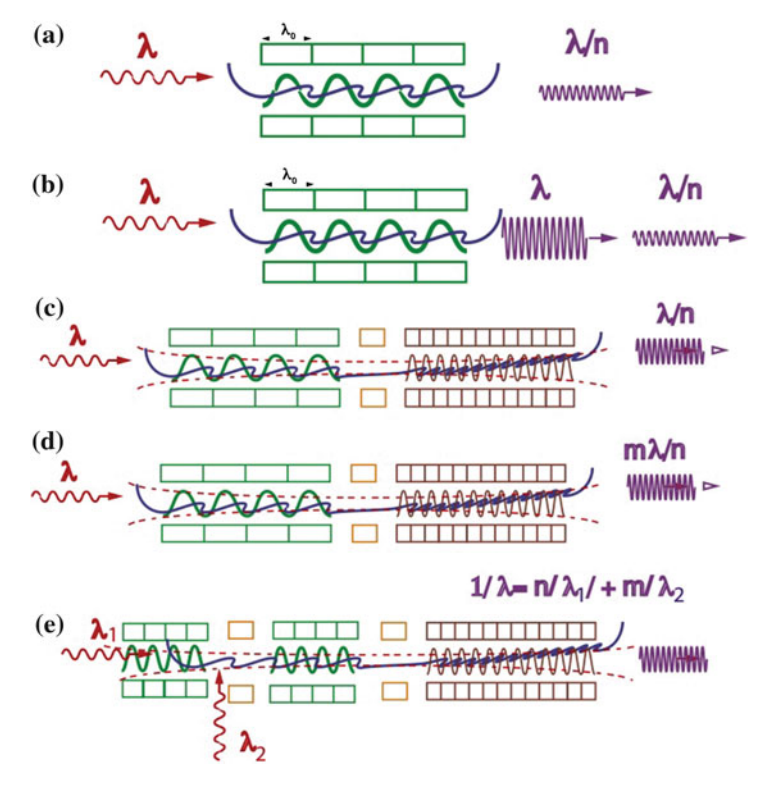


Fig. 5.2 Seeding configuration with a coherent source tuned on the resonant wavelength of the undulator. **a** Coherent Harmonic Generation in the low gain regime: the laser induced efficiently energy exchange and consequent density modulation leads to coherent harmonic emission, **b** High gain seeding case with significant seed amplification thanks to the FEL process, **c** High Gain Harmonic Generation: the first undulator being tuned on the seed wavelength, the second one on a harmonic of the seed, **d** Harmonic cascade where undulator fundamental frequencies have one of the higher order harmonic as a common frequency **e** Echo Enable Harmonic Generation (EEHG)

modulated electron bunch [79]. Coherent Nonlinear Harmonics of the fundamental wavelength are also generated [80]. FEL pulse temporal and spectral distributions result from the seed itself, but may be deeply altered by the FEL saturation process. The radiation field indeed slips over the electron current because of the different propagation velocity along the undulator. The path difference at the end of the undulator is indicated as "slippage length". Depending on the duration of the seed pulse with respect to the slippage length, different regimes can occur. When slippage length is much shorter than the pulse length, the intensity at the peak of the pulse entering earlier in saturation suddenly drops leading to a pulse splitting regime. The local heating of the electrons induced by saturation leads to the separation of the pulse in two different branches. This regime is of particular interest of pump-probe two-color experiments [81] and may be combined with a frequency chirp of the seed to obtain frequency-separated pulses [82, 83]. When the pulse length is comparable to the

slippage length, the FEL dynamics enters a strongly nonlinear superradiant regime, exhibiting pulse duration narrowing and further intensity increase [35, 84–86], as observed experimentally at BNL (USA) [87]. In superradiant regime, emission of harmonics is enhanced: simultaneous emission of harmonics up to the 11th order have been observed at SPARC [88].

At the FERMI FEL facility, the only existing VUV/soft X-ray seeded FEL user facility, the HGHG cascade scheme is implemented in FEL-1, to generate fully coherent radiation pulses in the VUV spectral range [50]. The seed laser is based on an optical parametric amplifier continuously tuneable in the range 230–260 nm, delivering pulses of few tens of microjoules. Radiation resulting from conversion up to the 13th harmonic of the seed is routinely delivered to user experiments. Test experiments have shown that in specific conditions, the generation of very high harmonics, up to order 29 is possible [89]. Nevertheless it is the energy spread induced during the beam modulation process, the main limiting factor for achieving efficient energy conversion at very high frequency conversion factors.

The Echo Enabled Harmonic Generation (EEHG) [90] scheme (Fig. 5.2e) is a concept, without equivalent in classical optics, where two successive laser-electron interactions are performed, using two undulators, in order to imprint a "sheet-like structure" in phase space and to provide higher order harmonics with a lower induced energy spread. The EEHG has been experimentally demonstrated at the Next Linear Collider Test Accelerator at SLAC [91] and at the Shanghai FEL Test Facility [92]. From a conceptual point of view it constitutes a breakthrough in up-frequency conversion in terms of compactness and pulse properties (e.g., duration and wavelengths). Schemes derived from EEHG such as the Triple Mode Chicane open perspectives for very short wavelength (nm) and short duration at moderate cost [93]. The other alternatives to reach shorter wavelengths consist in starting from a shorter seed wavelength, or in repeating the HGHG conversion process, seeding a second FEL modulator-amplifier device with the radiation produced in a first FEL converter. The latter scheme is based on the fresh bunch injection technique concept [94, 95], recently demonstrated at the SDUV-FEL [96] and at FERMI [97]. At FERMI the FEL-2 source has reached conversion factors corresponding to the 65th harmonic of the seed, delivering radiation to experimental stations in the soft-X-ray region of the spectrum. An alternative to the complexity of multiple conversion stages, is that of starting directly with a short wavelength coherent seed, such as High order Harmonics generated in Gas (HHG) [98, 99]. After the first ideas [100, 101], HHG seeding has been demonstrated at the SCSS Test Accelerator at 160 nm [102] and later on at 60 nm [103] and at 30 nm at s-FLASH [104]. Meanwhile the first demonstration of frequency multiplication from an HHG-seeded FEL was achieved at SPARC [105], by upconversion of the third harmonic of the Ti:Sa drive laser, generated in a gas cell. The hard X-ray region of the spectrum is presently out of reach for an externally seeded FEL. Self-seeding [106] suits better the hard X-ray domain: a monochromator installed after the first undulator spectrally cleans the radiation before the last amplification in the final undulator. Recently, self-seeding with the spectral cleaning of the SASE radiation in a crystal monochromator [107] produced with the first promising results [108, 109].

5.3 HHG Seeding and Harmonic Generation Process

Developments in femtosecond laser technology are making the direct seeding of a FEL amplifier in the VUV a viable solution. Harmonic generation in gas is one of the most promising methods to generate radiation at short wavelengths in the VUV–EUV region of the spectrum, to be used as an input seed. The high order harmonics result from the strong non-linear polarisation induced on rare-gas atoms, such as Ar, Xe, Ne and He, by the focused intense electromagnetic field of a pump laser. The most important characteristics of the process are described by the three-step semi-classical model [110, 111] illustrated in Fig. 5.3.

As the strength of the external electromagnetic field is comparable to that of the internal static field V_c of the atom in the interaction region close to laser focus, atoms ionize by tunnelling of the outer electrons. The ejected free electrons, far from the core, are then accelerated in the external laser field and gain a kinetic energy E_C . Those which are driven back close to the core can either be scattered or recombine to the ground state emitting a burst of XUV photons every half-optical cycle. Correspondingly in the spectral domain, the harmonic spectrum includes the odd harmonics of the fundamental laser frequency. The characteristic distribution of intensities is almost constant for harmonic order in the "plateau" region, where, depending on the generating gas, the conversion efficiency varies in the range 10^{-4} – 10^{-7} . For higher orders, in the "cut-off" region, the conversion efficiency decreases rapidly.

The upper spectral limit is given by the so-called "cut-off law", $E_{cut-off} = V_p + 3.2U_p$, with V_p the gas ionization energy, U_p the ponderomotive energy [112].

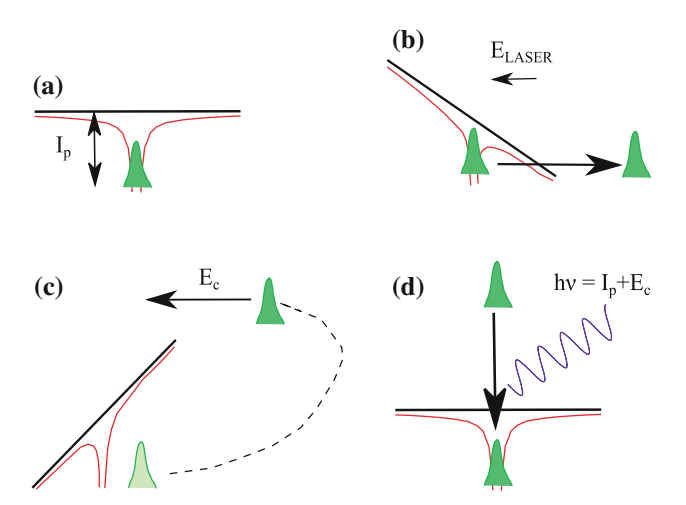


Fig. 5.3 Three-step semi-classical model: **a** initial state of the gas atom at zero field, I_p : ionization potential, **b** electron tunnelling **c** electron acceleration and gain of kinetic energy E_C , **d** radiative recombination and emission of XUV burst

According to the three-step model and the cut-off law, the lighter is the gas (i.e., the higher is the ionization energy, and the laser intensity which can be applied without ionizing the atom) the higher is the cut-off energy. High order harmonics are linearly polarized sources between 100 and 3 nm (12–400 eV), of high temporal and spatial coherence, emitting very short pulses (less than 100 fs), with a relatively high repetition rate (up to few kHz). The radiation spectrum is completely tuneable in the VUV–XUV region. The harmonic radiation is emitted on the axis of the laser propagation with a small divergence (1–10 mrad). Fraction of a microjoule of energy can be obtained at wavelengths down to 25–30 nm.

5.3.1 Shot Noise and Comparison with Available Seed Power

The critical question about the requirements in terms of intensity, bandwidth and phase stability at short wavelengths to efficiently seed a FEL amplifier is here addressed. The input seed, in order to be effective, must be intense enough to overcome the beam shot noise, which is the source for the SASE FEL process. We may estimate the relation between the electron shot noise at the FEL resonant frequency and the intensity of the associated field.

In the small-signal regime the FEL dynamics is well represented by an integral equation which can be cast to include the presence of a source term associated to the electron beam shot noise [113]:

$$\frac{d}{d\tau}a(\tau) = -2\pi g_0 b_1 e^{-i\nu_0 \tau} + i\pi g_0 \int_0^{\tau} d\xi \xi e^{-i\nu_0 \xi} a(\tau - \xi)$$
 (5.5)

Here $\tau=z/N\lambda_u$ is the position along the N periods undulator. In deriving 5.5 it is assumed a single resonant mode for the field, at frequency ω , defined, with respect to the resonant frequency $\omega_0=2\gamma^2\omega_u/(1+K_u^2/2)$, with $\omega_u=2\pi c/\lambda_u$, by the detuning parameter $\nu_0=2\pi N(\omega_0-\omega)/\omega_0$. Without loss of generality we consider the case of a linear undulator, where the gain coefficient g_0 is defined as $g_0=2\pi(N/\gamma)^3(\lambda_u K_u f_b(\xi))^2 I_{peak}/\Sigma_b I_A$, where I_{peak} is the beam currrent, I_A is the Alfvén current, $f_b(\xi)$ is the Bessel factor gain correction, as previously defined and Σ_b is the electron beam cross section. The small gain coefficient g_0 is related to the FEL parameter ρ_{fel} by the relation $4\pi N \rho_{fel}=(\pi g_0)^{1/3}$. The field $a(\tau)$ in Colson's dimensionless units [8] is related to the radiation intensity by the relation $I_L=I_s|a|^2/8\pi^2$, with $I_s=P_{beam}/2Ng_0\Sigma_b$, and where P_{beam} is the electron beam power, i.e. $P_{beam}=I_{peak}m_0c^2\gamma/e_0$.

The source term in 5.5 is proportional to the bunching coefficient b_1 , where for any integer n, b_n is

$$b_n = \frac{1}{\lambda} \int_0^{\lambda} \rho_e(\zeta) e^{-i2\pi n \zeta/\lambda} d\zeta$$
 (5.6)

i.e. the Fourier coefficient of the longitudinal electron beam density distribution $\rho_e(\zeta)$ at the resonant wavelength λ .

Equation 5.5 describes the initial evolution of the FEL instability, which may be initiated by a seed $a(0) \neq 0$, or by a modulated beam, $b_1 \neq 0$. At the same order in the field, 5.5 would contain an additional term proportional to b_2 which may be important in a seeded FEL where a pre-bunched beam is injected into a radiator with a pre-existing laser field 2. This term may be neglected here where we limit the application of the integral 5.5 to the startup process.

Let's consider the case $b_1 \neq 0$, a(0) = 0 and ignore the second term on the r.h.s. of 5.5. The evolution of the field is given by

$$a(\tau) = -2\pi g_0 b_1 \frac{\left(1 - e^{-i\nu_0 \tau}\right)}{\nu_0} \tag{5.7}$$

representing the coherent spontaneous emission power growth, which is quadratic with the position along the undulator. The transition to the exponential gain regime occurs when the second term on the r.h.s. of 5.5 becomes larger than the first one, i.e.

$$\left| -2\pi g_0 b_1 e^{-i\nu_0 \tau} \right| < \left| i\pi g_0 \int_0^{\tau} d\xi \xi e^{-i\nu_0 \xi} a\left(\tau - \xi\right) \right| \tag{5.8}$$

We may find the threshold value of τ by assuming that during the phase of quadratic growth the gain is negligible, substituting the solution 5.7 in 5.8 and solving for τ . The threshold, assuming perfect detuning ($\nu_0 = 0$) is

$$\tau_{th} \simeq \frac{1}{(\pi g_0)^{1/3}} \tag{5.9}$$

And the field at the threshold is

$$a(\tau_{th}) = -2 \left(\pi g_0\right)^{2/3} b_1 \tag{5.10}$$

This expression depends on the electron beam modulation at the undulator entrance. We may now consider an ideal case where this modulation is exactly zero and where the process is initiated by an input seed of dimensionless amplitude a_0 . We consider therefore 5.5, in the case $b_1 = 0$ and $a(0) = a_0$. The solution [31–33] reads:

$$a(\tau) = \frac{a_0}{3} \left\{ e^{-i(\pi g_0)^{1/3}\tau} + e^{-\frac{i}{2}(\pi g_0)\left(1 + i\sqrt{3}\right)\tau} + e^{-\frac{i}{2}(\pi g_0)\left(1 - i\sqrt{3}\right)\tau} \right\}$$
(5.11)

On the r.h.s. of 5.11, the first and the third complex exponentials have null or negative real arguments, while the second one has a positive real argument leading to exponential growth, with a (power) dimensionless folding length $\widetilde{L}_g = \sqrt{3} (\pi g_0)^{1/3}$,

equivalent to $L_g = \lambda_u/4\pi\sqrt{3}\rho_{fel}$ in the coordinate z along the undulator. The equivalent input intensity associated to a given beam pre-bunching, may be derived by imposing that the magnitude of the field associated to the exponentially growing root, equals $|a(\tau_{th})|$, i.e.:

$$\left|a_{0_{eq}}\right| = 6\left(\pi g_0\right)^{2/3} e^{-\frac{\sqrt{3}}{2}} \left|b_1\right|$$
 (5.12)

In terms of seed intensity, by squaring the previous expression and converting to dimensioned quantities, we get

$$I_{0_{eq}} = 9e^{-\sqrt{3}} \frac{P_{beam}}{\Sigma_b} \rho_{fel} |b_1|^2 \simeq 1.6 \frac{P_{beam}}{\Sigma_b} \rho_{fel} |b_1|^2$$
 (5.13)

In order to estimate the minimum necessary seed intensity for a FEL amplifier we need to calculate the bunching coefficient b_1 for a randomly distributed electron beam. We define the normalised longitudinal distribution of a discrete number n_e of electrons at the random longitudinal positions ζ_i , as

$$\rho_e(\zeta) = \frac{1}{n_e} \sum_{i=1}^{n_e} \delta(\zeta - \zeta_i)$$
 (5.14)

The corresponding bunching coefficient, according to the definition in 5.6 is given by the sum of n_e complex phasors with random phases, which scales as

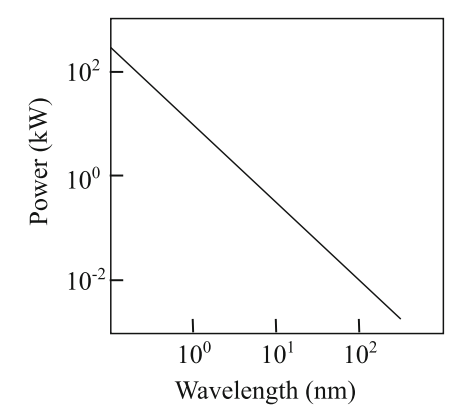
$$b_1 = \frac{1}{n_e} \sum_{i=1}^{n_e} e^{-i2\pi n\zeta_i/\lambda} = \mathcal{O}\left(\frac{1}{\sqrt{n_e}}\right)$$
 (5.15)

The Fourier coefficient considered in 5.6 is calculated over one period of the resonant field λ_0 , but the microscopic electron distribution is not a periodic function of the longitudinal coordinate and the average has to be calculated over a length larger than λ_0 , to account for interference of the fields emitted by electrons separated by more than a wavelength. A random, infinitely extended, point-like electron distribution such as 5.14, has a white-noise spectral distribution, while a FEL amplifier has a relative amplification-bandwidth of the order of $\sim 2\rho_{fel}$ [35] and only the noise in this spectral range will be amplified. We need then to calculate the fluctuations in a frequency range $\Delta\omega\sim 2\omega\rho_{fel}$ and the portion of beam that we have to consider for the average, has to be of the order of the cooperation length, $l_c\sim \lambda_0/4\pi\rho_{fel}$. The number of electrons in one cooperation length is

$$n_{ec} = I_{peak} l_c / e_0 c = I_{peak} \lambda_0 / \left(4\pi e_0 c \rho_{fel}\right)$$
 (5.16)

We may therefore estimate the shot noise intensity of interest by combining 5.13, 5.15 and 5.16

Fig. 5.4 Calculated shot noise associated power as a function of the operating wavelength. Parameters: $\rho_{fel} \sim 10^{-3}$, $\lambda_u = 3$ cm and $K_u = 2$



$$I_{sn} \sim 18e^{-\sqrt{3}}\omega \frac{\rho_{fel}^2}{\Sigma_L} \gamma m_0 c^2 \sim 3 \omega \rho_{fel}^2 \gamma m_0 c^2$$
 (5.17)

This function is proportional to the square of the ρ_{fel} parameter, grows linearly with the frequency and with the electron beam energy. Assuming typical values for the main parameters ($\rho_{fel} \sim 10^{-3}$, $\lambda_u = 3 \, \mathrm{cm}$ and K = 2) we have plotted in Fig. 5.4 the power corresponding to the intensity 5.17 over a transverse mode area equivalent to the electron beam transverse size.

The shot noise power scales as $\propto \lambda_0^{-3/2}$. While it is simple to achieve the necessary intensity threshold in the visible range, it becomes more and more difficult in the VUV and in the soft X-rays. In addition, it is reasonable to request a contrast ratio of $10-10^2$ between the seed and the background noise. Especially at short wavelengths the seed pulse length is shorter than the electron bunch, and an additional factor has to be considered in order to preserve the desired contrast in the spectral domain. The seed has to be transported and matched to the electron beam size over the undulator. These aspects are critical in the case of HHG sources [114]. The losses transporting and matching the beam to the electrons were estimated at 50% under the best conditions. While harmonics generated in gas have a width of the order of 10^{-2} , the typical gain bandwidth of a FEL is 10^{-3} , therefore an additional order of magnitude is lost because of the matching in the spectral domain. The seed intensity should overcome the shot noise level by a factor ranging between 2×10^3 and (more realistically) 10^4 .

In Fig. 5.5 experimental data obtained with HHG sources at different laboratories, as reported earlier in this book, in Fig. 4.3 are shown. The dashed line represents the FEL shot-noise equivalent-energy derived from 5.17 and multiplied by the factor 10⁴.

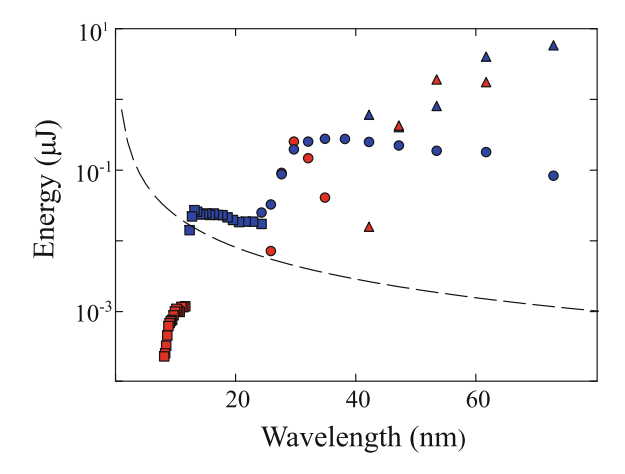


Fig. 5.5 Pulse energy as a function of the wavelength for different HHG sources and gas type. *Triangles* refer to Xenon: 14 mJ drive laser energy (*blue*), 25 mJ laser energy (*red*). *Squares* refer to Neon: 50 mJ (*blue*), 130 mJ (*red*). *Circles* refer to Argon: 15 mJ (*blue*), 50 mJ (*red*). Data taken from [115–117]. The dashed line represents the FEL shot noise equivalent energy scaled to a pulse length of 50 fs, derived from 5.17, multiplied by the factor 10^4

5.3.2 HHG Seeded FEL Dynamics

While specific FEL configuration devoted to preserving the HHG attosecond pulse structure have been proposed [118], in HHG-seeding the longitudinal profile and spectral bandwidth of the HHG seed are modified significantly by the FEL interaction well before saturation [119, 120]. Start-to-end simulations of the electron beam dynamics in a single-pass FEL have been widely used to understand the dynamics of the coupled system of electrons and fields undergoing the FEL process. In order to analyse the amplification process of the large-bandwidth seed in the FEL amplifier, start-to-end simulations including the process of harmonic generation in the gas jet were done [119]. The high-order harmonic spectra have been simulated using a 3D non-adiabatic model that includes both the single-atom response and the effect of the propagation of the XUV field inside the gas jet, in the framework of the Strong Field Approximation (SFA) [121]; in this model the atom is ionized via tunnelling by the IR field, and the freed electron is then accelerated by the electric field of the driving pulse. For a particular emission instant, the electron can be driven back to the parent ion and can recombine with the ground state, emitting the energy in excess as a photon in the extreme ultraviolet region or soft X-ray region [112]. Propagation effects are extremely relevant for a correct simulation of the time structure of the harmonic radiation. Indeed usually the single atom response is characterized by a complex time-structure (usually few attosecond pulses for each half optical cycle), whereas the macroscopic time structure of the XUV radiation is characterized by a single attosecond-pulse for each optical half-cycle. The origin of this difference is related to the phase matching mechanism operating during the propagation of the XUV field

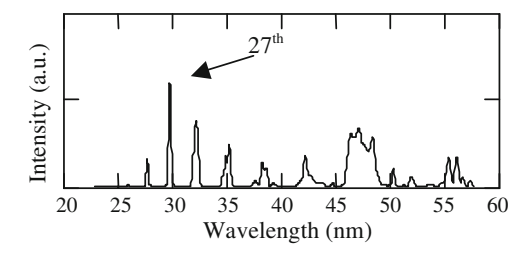


Fig. 5.6 Short wavelength spectrum of the simulated HHG seed field (Simulations by Sansone et al. in [119]). Gaussian beam with a 50 μ m beam waist focused 3 mm before a Neon gas-jet with a thickness of 1 mm. The pulse duration is 30 fs (FWHM) with a peak intensity in the focus of 10^{14} W/cm²

inside the gas jet. In the process of high-order harmonic-generation, the electron can follow two different paths to recombine with the parent ion. These two paths are usually referred to as the "short" and the "long" path, as they are characterized by different times spent by the electron in the continuum of energy states. For the short path, this time is usually less than half the optical period, while for the long path, this time is typically of the order of the laser period [112, 122]. The coherent superposition of the contributions of these two paths induces the generation of two attosecond pulses for each optical half-cycle of the driving laser field. The coherent interference of the dipole emission of the different atoms inside the gas jet leads to different phase-matching conditions for the two paths. The relative contribution of the two paths to the harmonic spectra can be enhanced or reduced by changing the relative position of the gas jet with respect to the laser focus. The phase-matching condition in the HHG process is indeed determined by the geometric phase of the driving pulse and by the phase accumulated by the electron wave-packet during its motion. In particular conditions (gas jet positioned few millimeters after the laser focus [123]), it is possible to efficiently select the contribution of the short path, leading to the selection of only one XUV pulse for each half-cycle of the driving IR field [124]. In another condition (gas jet before, or close to, the laser focus), the contribution of the long paths increases and the time structure of the generated XUV radiation is more complex. An example of the high-frequency portion of the spectrum (20–60 nm) of the on-axis radiation is shown in Fig. 5.6.

As mentioned above, the spectrum contains the odd harmonics of the Ti:Sa resonant wavelength (800 nm). In [119] the FEL dynamics was studied using the code GENESIS 1.3 [125] which relies on the slowly varying envelope approximation (SVEA). The code is therefore not suited to describe the evolution of the wide bandwidth optical field extending from the IR to the UV. For this reason the bandwidth of the input signal is reduced by numerically filtering the seed centered at the resonant wavelength corresponding to the 27th harmonic of the Ti:Sa (Fig. 5.6), with different bandwidths as shown in Fig. 5.7.

Considering a FEL configuration with the parameters listed in Table 5.1, the FEL parameter is $\rho_{fel}\sim 10^{-3}$ and an estimate of the seed intensity necessary

Fig. 5.7 Seed bandwidth reduction with various simulated filters. Al filter data from Center for X-ray optics Lawrence Berkeley National Laboratory's Materials Sciences Division (http://henke.lbl.gov/optical_constants/)

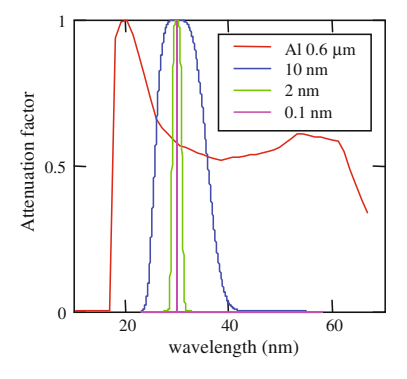


Table 5.1 Parameters of the FEL simulation

Parameter	Value	Units	
Beam energy	1	GeV	
Peak current	1	kA	
Energy spread	0.06	%	
Betatron function	6	m	
Undulator period	4.2	cm	
K_u	2.97		
Periods	58 × 8		

to override the e-beam shot noise, as calculated in the previous section, is about $I_{sn} \approx 0.3 \text{ MW/cm}^2$.

The seed spot size and divergence have been matched to the e-beam optical functions by propagation through a drift + lens + drift optical system, and the field evolution in the FEL amplifier has been simulated with GENESIS 1.3. The radiation power as a function of the longitudinal coordinate in the electron beam frame (horizontal) and position along the undulator at the coordinate z (vertical) is shown in Fig. 5.8. The power is normalized at each z. The plots have been obtained by applying different numerical filters, as shown in Fig. 5.7, to the input seed. The input seed energies, 2.5 nJ at 10 nm, 1 nJ at 2 nm and 0.5 nJ at 0.1 nm have been chosen in order for the energy in a bandwidth $2\rho_{fel}$, to be roughly the same (0.5 nJ) in the three cases.

The fine structure present in the case where the seed is filtered with 10 nm bandwidth, is wiped out by the small bandwidth of the FEL. The different filtering affects the pulse shape only before saturation, which occurs at about 15 m in all cases. Thereafter the pulse enters the superradiant regime where the pulse length is related to the peak power and becomes the same in all cases. The input seed intensity is 15MW/cm^2 at 10 nm, 8.5 MW/cm^2 at 2 nm, and 4 MW/cm^2 at 0.1 nm, always much larger than I_0 . In Fig. 5.9, the simulation corresponding to 0.1 nm has been repeated with input

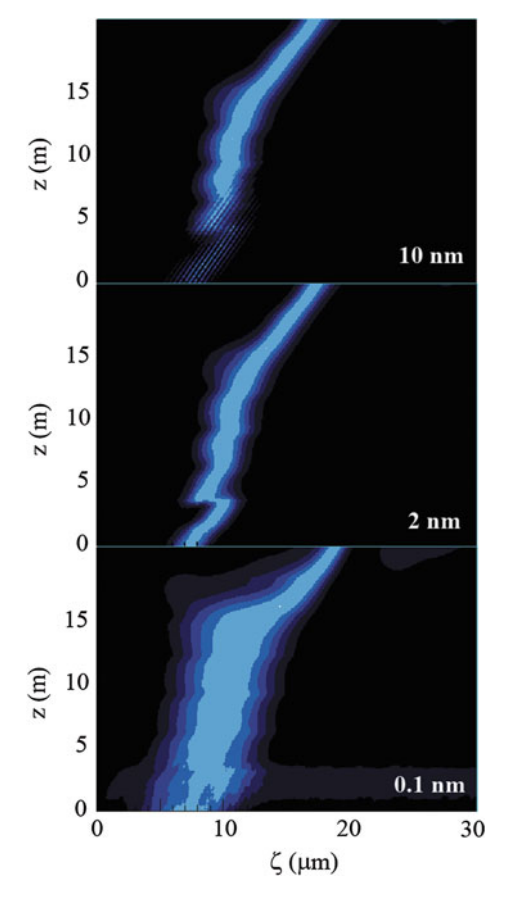


Fig. 5.8 Normalized longitudinal profile of the radiation power as a function of the longitudinal coordinate in the electron beam frame (ζ) as it evolves along the undulator (coordinate z). The input seed has been filtered with different band pass filters (*low right corner*), as shown in Fig. 5.7

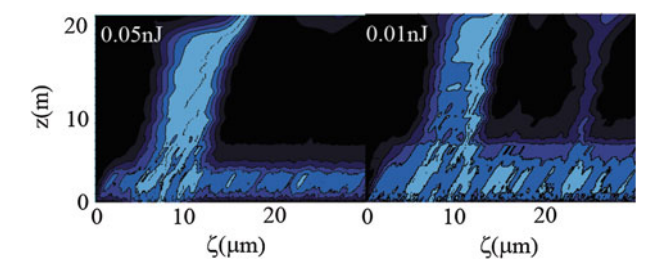


Fig. 5.9 Same as in Fig. 5.8 (with 0.1 nm BW) approximately at the threshold IO (*left*), and *below* threshold (*right*)

energies 0.05 and 0.01 nJ, corresponding to intensities close to the threshold I_{sn} . In these cases SASE spikes are clearly visible at the beginning. In the 0.01 nJ seed energy case, a structure in the pulse with loss of longitudinal coherence is present and SASE spikes compete with the seeded signal until saturation.

5.4 Coupling the Seed Source to the FEL

5.4.1 HHG Chamber Design for FEL Seeding

The implementation of HHG seeding in FELs usually involves the use of several chambers to separate the region hosting the gas interaction region, from the high vacuum required by the accelerator [126]. First, the HHG seeding chamber with its associated laser, in general located inside the accelerator tunnel is equipped with a gas cell or jet. The choice of the gas is determined by the required HHG wavelength (Xe in the case of the SCSS Test Accelerator, for example). A second chamber handles the transverse focus of the seed in the first undulator (Fig. 5.10). Finally an injection chamber, contains a set of steering mirrors located in a magnetic chicane or dogleg of the accelerator. The laser generating the harmonic can be located either outside the accelerator tunnel (as in the SCSS Test Accelerator) or inside it (as in the SPARC case). The first approach imposes remote control of several elements. Intensity losses on the HHG transport should be minimized to keep the seed level sufficiently above the shot noise. The infra-red laser that generates HHG is eliminated by the narrow spectral bandwidth of the HHG transport mirrors, by plates at Brewster angle, or simply by the gain bandwidth of the FEL itself. At 60 nm the optimized design [103] implied a SiC harmonic-separator mirror, set at the Brewster angle (69°), for the Ti:Sa

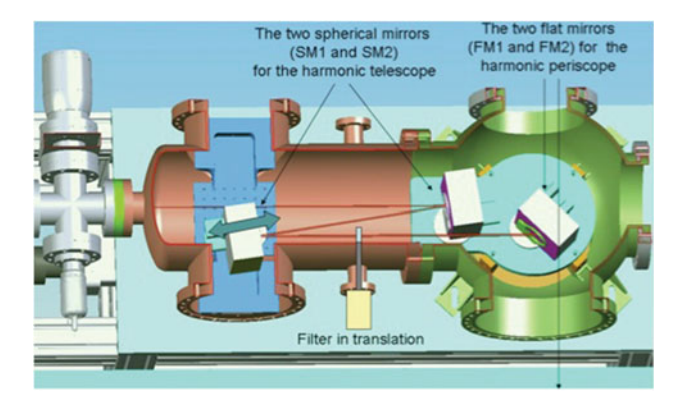


Fig. 5.10 CATIA software 3D drawing view of the mirror chamber used first at SCSS Test Accelerator HHG seeding for spectral selection and transverse beam shaping, comporting two spherical mirrors and a first periscope mirror

pump laser. By introducing a pair of Pt-coated, nearly-normal-incidence mirrors, both the collimation and the focusing of the HHG radiation were achieved. The sFLASH seed laser system produces 800 nm, 30 mJ adjustable pulse length (down to 30 fs). It is connected to the accelerator tunnel by a 7 m long tube. The first undulator is located 5 m after the point of injection into the tunnel.

Offline metrology of high-order harmonics for free-electron laser seeding has been carried out in detail [127]. Online diagnostics characterizing the HHG in terms of spectrum, energy, beam position and shape, consists typically of spectrometer [128], photodiodes and microchannel plates.

5.4.2 Spectral Tuning, Tuneability, Polarisation Matching, Optical Transport and Synchronization

Spectral tuning between the HHG seed and the undulator resonance should of course be properly performed. The undulator gap is adjusted for the radiation to be resonant with the HHG seed. To tune a seeded FEL, one may change either the laser wavelength that generates the HHG, or use few cycle HHG leading to broad band HHG radiation [129, 130], coupled with an undulator gap change. The electric field of the seed should properly match to that of the undulator radiation. For the usual case of a linear undulator, the polarisation of the seed should be aligned accordingly, and this imposes some constraints on the angles of the HHG optical transport. When a helical undulator is used, circularly polarized HHG could also be employed [131, 132], otherwise circulary polarized FEL radiation may be more easily generated by injecting the pre-modulated beam into a circularly-polarized undulator.

For the HHG transport, a typical value of M2 of 3.5 can be considered at 60 nm. Mirror choices result from the targeted HHG wavelength, as for example CaF₂ for 160 nm, SiC for 60 nm. Filter such as Al, Sn insure an additional spectral selection.

The sub-picosecond synchronization between the electron beam and the seed pulse is achieved by locking the oscillator of the laser generating the harmonics to the highly stable clock of the accelerator. The timing can be first adjusted with a few ps resolution using a fast photodiode or a streak camera (such as Hamamatsu Photonics FESCA-200-C6138), detecting the 800 nm laser light and the OTR emission from the electron beam. An optical delay line on the IR laser path allows for a fine adjustment of the synchronization. Depending on the electron bunch length, synchronization can be critical, and significantly affect the performances of the seeded FEL. At SCSS Test Accelerator seeding, a feedback on the timing has been implemented with an electro-optical crystal, enabling a significant improvement of the synchronization stability [133].

5.5 Achievements with HHG Seeding

HHG seeding as been carried out at several facilities. The first demonstration was obtained at SCSS Test Accelerator at 160 nm [102] and at 60 nm [103] with an upgraded HHG apparatus, at SPARC [105] with the demonstration of a cascaded configuration and at 30 nm, at S-FLASH [104, 134].

5.5.1 Direct Seeding Mode

In the first demonstration of HHG seeding index HHG seeding [102], the 160-nm HHG seed was strongly amplified in the first 4.5 m of the undulator at the SCSS test accelerator facility, resulting in three orders of magnitude higher intensity of the output pulse than in unseeded conditions. The saturation length was reduced by a factor of 2 and the fundamental wavelength was accompanied by the Non Linear Harmonics (NLH) at 54 and 32 nm. Figure 5.11 compares the single-shot spectra of the seed, the SASE and the seeded FEL with one (a) or two (b) undulator segments at 160 nm. A clear amplification occurs with seeding and even at low seed energy (0.53 nJ per pulse). With one undulator segment, the HHG seeded FEL is 500 times more intense than the seed and 2600 times more than the non-saturated SASE. Its pulse energy is 0.34J. The amplification factor agrees with GENESIS [125] or PERSEO [135] simulations. The HHG broadband seed (FWHM relative spectral width: 0.54 % for 0.53 nJ, 0.75 % for 4.3 nJ) properly suits the FEL spectral gain (0.88%). With the HHG seed, the spectra do not exhibit the random spikes characteristic of SASE emission and reflect instead the seed Gaussian-like shape, with a spectral narrowing (from 0.54 to 0.46 % (0.53 nJ seed) and 0.75–0.44 % (4.3 nJ seed)) as expected from theory. The seeded emission is red-shifted with respect to the SASE one, probably because of a change of the FEL resonance condition due to an energy loss of the electrons and/or to a possible chirp in the beam energy. The red-shift is larger with two undulator segments.

The influence of the seed level [136] for this first demonstration experiment is illustrated in Fig. 5.12. Amplification is observed when the seed energy is larger than 1.4 pJ, but the spiky SASE structure in the spectrum is suppressed only when the seed energy is about one order of magnitude larger (8.8 pJ). To this energy corresponds a seed peak power, which is about one order of magnitude larger than the shot noise. The power evolution from GENESIS and PERSEO simulations (gain length of 0.43 m) well agrees with the experimental data (gain length of 0.65 m).

Figure 5.13 shows that light up to the seventh harmonic of the FEL resonance can be measured while in presence of the seed. The seventh harmonic could not be detected when the FEL amplifier was operated with no seed, in SASE mode. A significant increase of the non linear harmonics signal, as compared to the unseeded case, was also observed at the third and fifth harmonics, which were amplified by factors 312 and 47 for the third (0.3 nJ at 53.55 nm) and for the fifth (12 pJ at 32.1 nm)

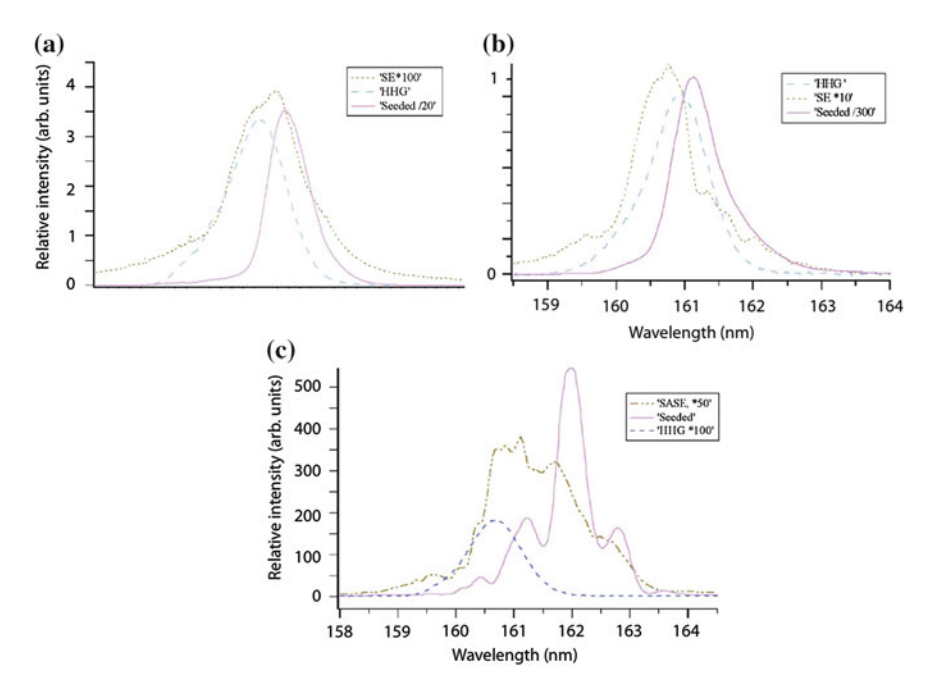


Fig. 5.11 First HHG seeding at SCSS Test Accelerator. HHG seeding at the fundamental wavelength 160 nm: a Seed: $4.3\,\mathrm{nJ}$, one undulator b Seed: $0.53\,\mathrm{nJ}$, one undulator, c Seed: $4.3\,\mathrm{nJ}$, two undulators. Experimental conditions: Ti:Sapphire laser (800 nm, 20 mJ, 100 fs FWHM, 10 Hz) loosely-focused geometry (7 m lens) on a 9 mm-long xenon gas cell, generating 3rd–21st odd harmonics. The 5th harmonic occurs at 160 nm, with 1 μ J per pulse, 50 fs (FWHM) duration. SCSS test accelerator (150 MeV, $0.35\,\mathrm{nC}$, 1 ps FWHM, 10 Hz) consists of a 500 kV pulsed DC electron gun (CeB₆ thermionic cathode), S-band ($2.856\,\mathrm{MHz}$) and C-band ($5.712\,\mathrm{MHz}$) acceleration sections. Two $4.5\,\mathrm{m}$ long in-vacuum undulator sections at 3 mm gap: period 15 mm, tuned at 160 nm, separated by $1.5\,\mathrm{m}$ drift space. Detection after a Au coated SiO₂ flat mirror (85 angle of incidence) into a Shimatsu Corp dispersive spectrometer vertical and horizontal slits followed by a concave laminar grating (Au coating, concave laminar grating of $N=2,400\,\mathrm{lines/mm}$) equipped with a high sensitivity back-illuminated CCD camera (Princeton Instruments PI*SX 400)

respectively. Spectral narrowing was also observed at the harmonics (from 2.66 to 0.84% for the third harmonic and 2.54–1.1% for the fifth harmonic) [137].

The next significant step was achieved by seeding the FEL amplifier at higher order harmonics, i.e. the thirteenth harmonic generated in a Xe gas cell at 60 nm [103]. A new set-up of the HHG chamber was been installed at the SCSS Test Accelerator operating at 250 MeV, with improved diagnostics of the HHG radiation before injection. The energy-per-pulse injected was 2 nJ, corresponding to 40 kW (50 fs pulse duration). The seeded FEL exhibited a sharp increase in the spectral intensity for several shots, with a typical hit rate of 0.3 %, resulting from the timing jitter between the seeding laser pulse and the electron bunch. The pulse energy of the seeded FEL (1.3 μ J), is twice as large as in SASE mode (0.7 μ J) and 650 times larger than the HHG seed (2 nJ). The spectrum of the seeded radiation is blue-shifted

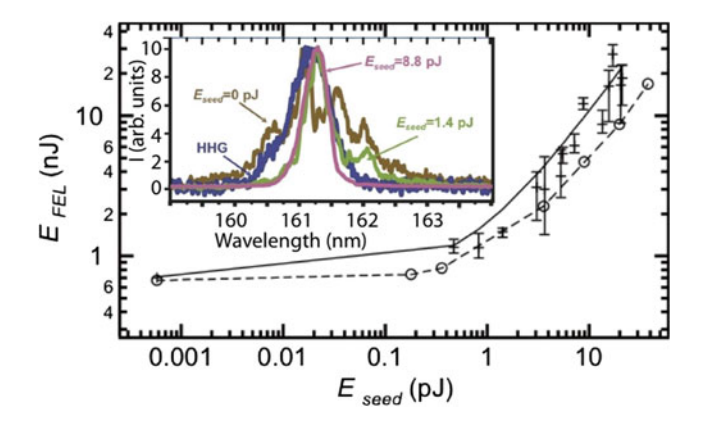


Fig. 5.12 SCSS Test Accelerator FEL power versus 160 nm HHG seed level intensity and associated spectra (*inset*): *Bars* peak-to-valley range of experimental values obtained for five consecutive shots. *Full line* Analytical calculation, 0.65 m gain length. *Dashed line* GENESIS simulation with a relative energy spread of 0.04 %, a peak current of 123 A, a normalised emittance of 0.83 π mm mrad

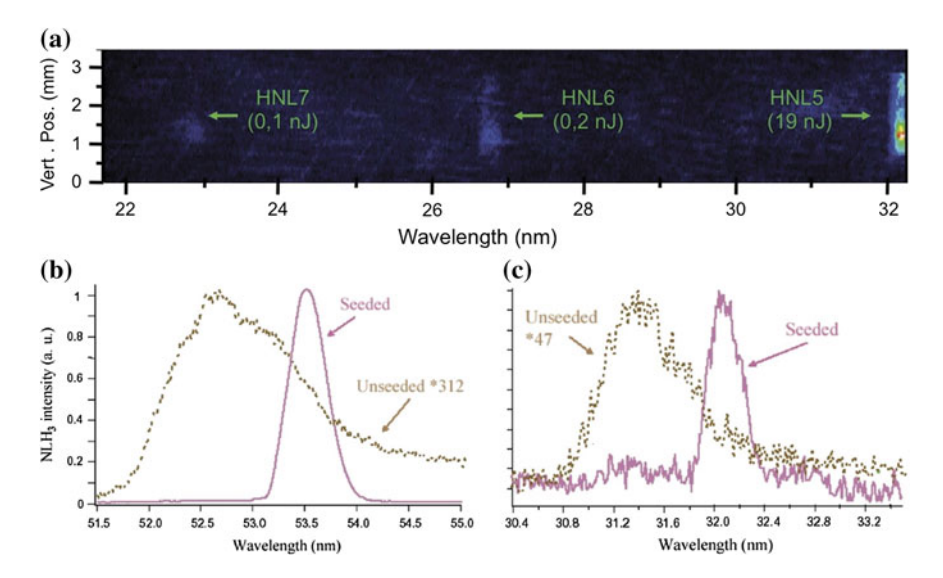


Fig. 5.13 Non Linear harmonics of SCSS Test Accelerator FEL seed with HHG at 60 nm **a** fifth to seventh harmonic image of the spectrometer. Comparison of SASE and seeded FEL harmonics of third order (**b**) and fifth one (**c**)

compared to that of the HHG seed by about 0.3 nm. Thanks to the temporal feedback provided by an electro-optical measurement [133], the hit rate was improved by two orders of magnitude, reaching 24 %. This HHG seeded FEL was also made available for user operation. Further improvements and extensions are expected in the next future with the move of SCSS Test Accelerator to the SACLA site, the upgrade

of the accelerator enabling the FEL to operate down to 3 nm at a beam energy of 1.4 GeV. The plan is to perform HHG seeding, and then possibly to combine it with HGHG.

Direct seeding at even shorter wavelengths was attempted at FLASH [104]. The seed wavelength was 38 nm, the 21st harmonic of the 800 nm Ti:Sa laser, generated by injecting up to 50 mJ of infrared light in a gas filled capillary. The VUV light, with a pulse energy of about 2 nJ, was either sent to the accelerator or to in-tunnel diagnostic system. A proof of the interaction and amplification of the seed, coupled to the electron bunch, was clearly obtained. This is the shortest wavelength where harmonics generated in gas have been amplified in a single-pass FEL [134].

5.5.2 Cascaded FEL Configuration

The cascaded scheme was proposed with the goal of increasing the frequency upconversion of seeded FELs. An efficient electron-beam modulation, when typical energy per pulse is as in Fig. 5.5, can be reached only after some amplification in the FEL modulator. This experiment was done for the first time at SPARC [105], where the dependence of the FEL performances on the length of the modulator was studied. The SPARC FEL amplifier [38, 138] is driven by a high brightness accelerator providing energies between 80 and 180 MeV and an undulator composed by six variable gap, modules. The flexibility offered by the variable gap configuration of the SPARC undulator (see Fig. 5.14) and the natural synchronization of the electron beam with the laser driving the photo-injector, made the SPARC layout particularly suited for a number of experiments, where the FEL amplifier was seeded by an external laser source [88, 139].

The main component of the seed generation system is a regenerative amplifier (LEGEND HFE, Coherent Inc.), seeded by the same oscillator driving the

Fig. 5.14 View of the sequence of undulators of the SPARC amplifier



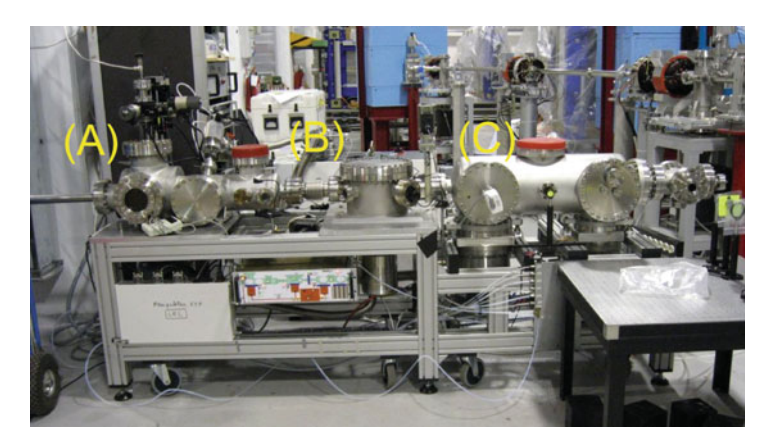


Fig. 5.15 Harmonic generation chamber realized at CEA

photocathode amplifier. This solution ensured sufficient synchronization between the seed laser and the electron bunch. The laser delivered up to 2.5 mJ at 800 nm with a pulse duration of about 120 fs. The laser was focused by a 2 m focal length lens to an in-vacuum cell, where a valve synchronized to the 10 Hz timing system of SPARC, injected argon gas at 15 bar. The gas interaction chamber was designed and built at CEA [140] for the specific purpose of this experiment. The generation chamber and the injection system are shown in Fig. 5.15:

The laser enters from the left side in chamber (A), where the gas cell is located. The cell is directly connected to the accelerator transfer line through chambers (B) and (C), therefore a differential vacuum pumping system is required. This is the main motivation of chamber (B) where irises and additional pumping enabled to reduce the background pressure from 10^{-4} mbar in (A) to 10^{-8} mbar in (C). Chamber (C) on the right hosts two spherical mirrors used to match the seed beam to the electron beam size in the center of the undulator. The UV pulse was injected into the SPARC undulator by means of a periscope; a magnetic chicane deflected the e-beam from its straight path. High-order odd harmonics of the Ti:Sa laser may be generated at the wavelengths 266, 160, 114 nm and lower, but the available electron beam energy was only compatible with 266 and 160 nm. The latter wavelength was used for a "direct seeding" FEL amplifier experiment, reproducing the situation previously studied at the SCSS Test Accelerator. At the longer seed wavelength, the gap tuning of the undulators permitted to set the resonance both at 266 nm and at its second harmonic. The six undulators could be independently tuned at the seed wavelength, operating as modulators, or at its second harmonic, 133 nm, as radiators of a frequency-doubling cascade. The total number of six radiators was unchanged in order to keep the same geometry for the radiation collection at the end of the undulator line, where the diagnostic, consisting of an in-vacuum spectrometer [128], was installed. The seed energy per pulse was limited to about 50 nJ and was amplified by the FEL process

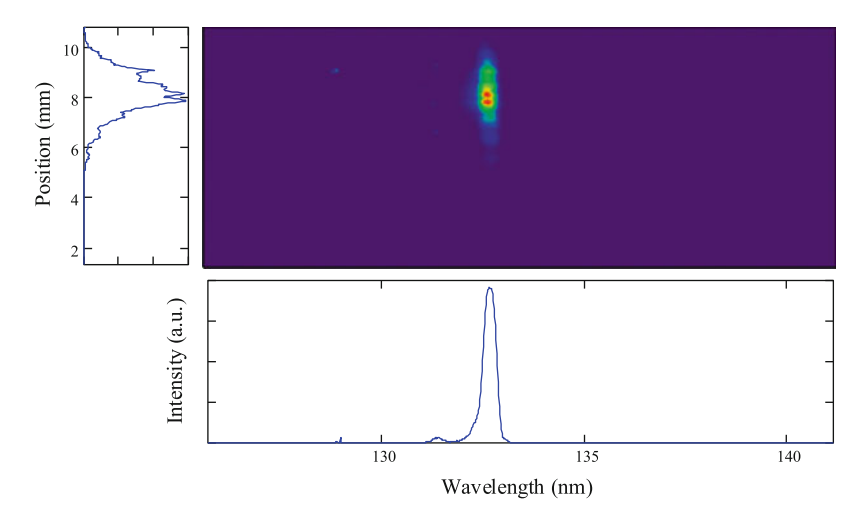


Fig. 5.16 Spectrum of the signal from the FEL amplifier at SPARC

in the first part of the undulator. The experiment was done with an electron beam energy of 176 MeV and with a modest peak current of about 50–70 A.

The higher output energy of 1 mJ at 133 nm was obtained with four undulators as modulators and two undulators as radiators at 133 nm, corresponding to magnetic length of about 8.4 m for the modulator and 4.2 m for the radiator. The estimated gain length in the modulator was about 1.1 m, sufficient to increase the input seed to a level close to FEL saturation. A typical spectrum, obtained in single-shot mode in this configuration, is shown in Fig. 5.16.

This experiment demonstrated the feasibility of a cascaded FEL configuration seeded by harmonics generated in gas, where the modulator operated in high gain conditions. Up to $\sim 4 \times 10^{12}$ photons at 133 nm were produced in "single" line spectra with a spectral width lower than 0.2%; the typical SASE spikes were suppressed.

5.6 Conclusion

A FEL amplifier seeded by HHG enables the possibility of reaching VUV wavelengths in a direct seeding configuration. With sufficient seed energy, a single stage cascade initiated at VUV wavelength would also permit reaching the carbon-K edge and the water-window spectral region with singly peaked spectral and temporal distribution and with the pulse synchronization properties typical of the solid-state laser source generating the seed. Such a FEL would be competitive with FELs based on the double stage cascade and fresh bunch injection technique, such as FERMI FEL-2 [97], by reducing the fluctuations generated by the FEL in a multiple-stage cascade and by allowing for a greater electron bunch compression and higher peak current.

The latter is one of the limiting factors when the stages of a multiple stage FEL have to operate all with the same electron bunch. This configuration, with a proper handling of the jitter and of the intensity fluctuations, would be of great interest for pump-probe experiments in the soft X-rays, e.g. to extrapolate at shorter wavelengths the seeding technique used at FERMI, where the FEL-1 single stage has been driven by two independent pulses to study the time-evolution of the diffraction pattern produced by a titanium-grating, in a typical pump-probe experiment [141]. HHG seeding can also be considered on laser-wakefield-acceleration based FELs [142], where so far only undulator spontaneous emission has been observed [143, 144]. Besides strong quadrupoles located very close to the electron source [145] to handle the large divergence of these beams, electron beam manipulation by chicane decompression [146] or by the use of transverse gradient undulator [147] suggest that significant amplification with the present LWFA performance has become possible. This will be tested in the LUNEX5 project [148]. Multiple-wavelength seeding, such as in the Triple Modulator Chicane [93], are also promising techniques. The main present limitation of HHG as a seed for FEL amplifiers lies in the level of the seed intensity relative to the FEL shot noise. Improvement of the efficiency of the HHG [149] are of great interest, and further advances in seeding FELs by HHG will clearly benefit from the progresses of the HHG sources themselves.

Acknowledgments The authors wish to thank Giuseppe Dattoli for the numerous useful discussions on the FEL theory, to acknowledge the contribution of Giuseppe Sansone, Salvatore Stagira and Mauro Nisoli for providing their results on the simulations of the HHG seed in combination with the FEL amplification. They wish to thank Bertrand Carr, Luca Cultrera, Massimo Ferrario, Daniele Filippetto, David Garzella, Toru Hara, Tetsuya Ishikawa, Hideo Kitamura, Marie Labat, Guillaume Lambert, Marcello Quattromini, Pascal Salières, Tsumoru Shintake, Tagashi Togashi, Carlo Vicario, Makina Yabashi and more in general all the colleagues from the SPARC and SCSS Test Accelerator teams, for their support in the experiments of HHG seeding at SCSS Test Accelerator and of high gain harmonic generation seeded by harmonics in gas at SPARC. They finally thank Carlo Callegari for his careful reading of the manuscript and for his constructive comments.

References

- 1. M.E. Couprie, J.M. Filhol, C.R. Phys. 9(5-6), 487 (2008). doi:10.1016/j.crhy.2008.04.001
- F. Ciocci, G. Dattoli, A. Torre, A. Renieri, Insertion Devices for Synchrotron Radiation and Free Electron Laser (Series on Synchrotron Radiation Techniques and Applications) (World Scientific Pub Co Inc, 2000). http://www.amazon.com/Insertion-Synchrotron-Radiation-Techniques-Applications/dp/9810238320Dtechkie-203D9810238320
- 3. G. Dattoli, A. Renieri, Il Nuovo Cimento B 59(1), 1 (1980). doi:10.1007/BF02739044
- 4. D.A.D. Deacon, J.M.J. Madey, Phys. Rev. Lett. 44, 449 (1980). doi:10.1103/PhysRevLett.44.
- A.A. Zholents, M.S. Zolotorev, Phys. Rev. Lett. 76, 912 (1996). doi:10.1103/PhysRevLett. 76.912
- 6. R.W. Schoenlein, Science 287(5461), 2237 (2000). doi:10.1126/science.287.5461.2237
- 7. J.M.J. Madey, J. Appl. Phys. **42**(5), 1906 (1971). doi:10.1063/1.1660466
- 8. W. Colson, IEEE J. Quant. Electron. 17(8), 1417 (1981). doi:10.1109/JQE.1981.1071273

- D.A.G. Deacon, L.R. Elias, J.M.J. Madey, G.J. Ramian, H.A. Schwettman, T.I. Smith, Phys. Rev. Lett. 38, 892 (1977). doi:10.1103/PhysRevLett.38.892
- M. Billardon, P. Elleaume, J.M. Ortega, C. Bazin, M. Bergher, M. Velghe, Y. Petroff, D.A.G. Deacon, K.E. Robinson, J.M.J. Madey, Phys. Rev. Lett. 51, 1652 (1983). doi:10.1103/PhysRevLett.51.1652
- R.R. Freeman, B.M. Kincaid, Production of Coherent XUV and Soft X-rays Using a Transverse Optical Klystron (American Institute of Physics, College Park, 1984), pp. 278–292. doi:10. 1063/1.34677
- R. Coisson, F.D. Martini, Free-Electron Generators of Coherent Radiation (Addison-Wesley, New York, 1982), Physics of Quantum Electronics, vol. IX, chap. Free-electron relativistic scatterer for UV-generation
- M.E. Couprie, F. Merola, P. Tauc, D. Garzella, A. Delboulbe, T. Hara, M. Billardon, Rev. Sci. Instrum. 65(5), 1485 (1994). doi:10.1063/1.1144880
- G.S. Edwards, R.H. Austin, F.E. Carroll, M.L. Copeland, M.E. Couprie, W.E. Gabella, R.F. Haglund, B.A. Hooper, M.S. Hutson, E.D. Jansen et al., Rev. Sci. Inst. 74(7), 3207 (2003). doi:10.1063/1.1584078
- M. Marsi, M.E. Couprie, L. Nahon, D. Garzella, T. Hara, R. Bakker, M. Billardon, A. Delboulbé, D. Indlekofer, A. Taleb-Ibrahimi, Appl. Physi. Lett. 70(7), 895 (1997). doi:10.1063/1.118307
- M. Trovò, J.A. Clarke, M.E. Couprie, G. Dattoli, D. Garzella, A. Gatto, L. Giannessi, S. Günster, N. Kaiser, M. Marsi, M.W. Poole, D. Ristau, R.P. Walker, Nucl. Instrum. Methods Phys. Res., Sect. A: Accelerators, Spectrometers, Detectors, and Associated Equip. 483(1–2), 157 (2002)
- N.A. Vinokurov, I.B. Drobyazko, G.N. Kulipanov, V.N. Litvinenko, I.V. Pinayev, Rev. Sci. Instrum. 60(7), 1435 (1989). doi:10.1063/1.1141084
- M. Billardon, D. Garzella, M.E. Couprie, Phys. Rev. Lett. 69, 2368 (1992). doi:10.1103/ PhysRevLett.69.2368
- H. Hama, M. Hosaka, Nucl. Instrum. Methods Phys. Res., Sect. A: Accelerators, Spectrometers, Detectors, and Associated Equip. 429(1–3), 172 (1999). doi:10.1016/S0168-9002(99)00099-6
- K. Yamada, N. Sei, H. Ohgaki, T. Mikado, S. Sugiyama, T. Yamazaki, Nucl. Instrum. Methods Phys. Res., Sect. A: Accelerators, Spectrometers, Detectors, and Associated Equip. 445(1–3), 173 (2000). doi:10.1016/S0168-9002(00)00058-9
- V. Litvinenko, B. Burnham, J. Madey, Y. Wu, Nucl. Instrum. Methods Phys. Res., Sect. A: Accelerators, Spectrometers, Detectors, and Associated Equip. 358(1–3), 334 (1995). doi:10. 1016/0168-9002(94)01290-3
- D. Nolle, D. Garzella, A. Geisler, L. Gianessi, M. Hirsch, H. Quick, M. Ridder, T. Schmidt, K. Wille, Nucl. Instrum. Methods Phys. Res., Sect. A: Accelerators, Spectrometers, Detectors, and Associated Equip. 445(1–3), 128 (2000). doi:10.1016/S0168-9002(00)00044-9
- R.P. Walker, J.A. Clarke, M.E. Couprie, G. Dattoli, M. Eriksson, D. Garzella, L. Giannessi, M. Marsi, L. Nahon, D. Nölle, D. Nutarelli, M.W. Poole, H. Quick, E. Renault, R. Roux, M. Trovò, S. Werin, K. Wille, Nucl. Inst. Meth. Phys. Res. A 475, 20 (2001). doi:10.1016/ S0168-9002(01)01529-7
- M. Marsi, M. Trovò, R.P. Walker, L. Giannessi, G. Dattoli, A. Gatto, N. Kaiser, S. Günster, D. Ristau, M.E. Couprie, D. Garzella, J.A. Clarke, M.W. Poole, Appl. Phys. Lett. 80(16), 2851 (2002). doi:10.1063/1.1471934
- F. Ciocci, G. Dattoli, A. De Angelis, B. Faatz, F. Garosi, L. Giannessi, P. Ottaviani, A. Torre, IEEE J. Quant. Electron. 31(7), 1242 (1995). doi:10.1109/3.391087
- 26. G. Dattoli, J. Appl. Phys. 95(6), 3211 (2004). doi:10.1063/1.1645649.
- 27. D. Alesini, M. Alessandroni, M.P. Anania, S. Andreas, M. Angelone, A. Arcovito, F. Arnesano, M. Artioli, L. Avaldi, D. Babusci, A. Bacci, A. Balerna, S. Bartalucci, R. Bedogni, M. Bellaveglia, F. Bencivenga, M. Benfatto, S. Biedron, V. Bocci, M. Bolognesi, P. Bolognesi, R. Boni, R. Bonifacio, M. Boscolo, F. Boscherini, F. Bossi, F. Broggi, B. Buonomo, V. Calo', D. Catone, M. Capogni, M. Capone, M. Castellano, A. Castoldi, L. Catani, G. Cavoto, N.

Cherubini, G. Chirico, M. Cestelli-Guidi, E. Chiadroni, V. Chiarella, A. Cianchi, M. Cianci, R. Cimino, F. Ciocci, A. Clozza, M. Collini, G. Colo', A. Compagno, G. Contini, M. Coreno, R. Cucini, C. Curceanu, S. Dabagov, E. Dainese, I. Davoli, G. Dattoli, L.D. Caro, P.D. Felice, S.D. Longa, G.D. Monache, M.D. Spirito, A.D. Cicco, C.D. Donato, D.D. Gioacchino, D.D. Giovenale, E.D. Palma, G.D. Pirro, A. Dodaro, A. Doria, U. Dosselli, A. Drago, R. Escribano, A. Esposito, R. Faccini, A. Ferrari, M. Ferrario, A. Filabozzi, D. Filippetto, F. Fiori, O. Frasciello, L. Fulgentini, G.P. Gallerano, A. Gallo, M. Gambaccini, C. Gatti, G. Gatti, P. Gauzzi, A. Ghigo, G. Ghiringhelli, L. Giannessi, G. Giardina, C. Giannini, F. Giorgianni, E. Giovenale, L. Gizzi, C. Guaraldo, C. Guazzoni, R. Gunnella, K. Hatada, S. Ivashyn, F. Jegerlehner, P.O. Keeffe, W. Kluge, A. Kupsc, M. Iannone, L. Labate, P.L. Sandri, V. Lombardi, P. Londrillo, S. Loreti, M. Losacco, S. Lupi, A. Macchi, S. Magazu', G. Mandaglio, A. Marcelli, G. Margutti, C. Mariani, P. Mariani, G. Marzo, C. Masciovecchio, P. Masjuan, M. Mattioli, G. Mazzitelli, N.P. Merenkov, P. Michelato, F. Migliardo, M. Migliorati, C. Milardi, E. Milotti, S. Milton, V. Minicozzi, S. Mobilio, S. Morante, D. Moricciani, A. Mostacci, V. Muccifora, F. Murtas, P. Musumeci, F. Nguyen, A. Orecchini, G. Organtini, P.L. Ottaviani, E. Pace, M. Paci, C. Pagani, S. Pagnutti, V. Palmieri, L. Palumbo, G.C. Panaccione, C.F. Papadopoulos, M. Papi, M. Passera, L. Pasquini, M. Pedio, A. Perrone, A. Petralia, C. Petrillo, V. Petrillo, M. Pillon, P. Pierini, A. Pietropaolo, A.D. Polosa, R. Pompili, J. Portoles, T. Prosperi, C. Quaresima, L. Quintieri, J.V. Rau, M. Reconditi, A. Ricci, R. Ricci, G. Ricciardi, E. Ripiccini, S. Romeo, C. Ronsivalle, N. Rosato, J.B. Rosenzweig, G. Rossi, A.A. Rossi, A.R. Rossi, F. Rossi, D. Russo, A. Sabatucci, E. Sabia, F. Sacchetti, S. Salducco, F. Sannibale, G. Sarri, T. Scopigno, L. Serafini, D. Sertore, O. Shekhovtsova, I. Spassovsky, T. Spadaro, B. Spataro, F. Spinozzi, A. Stecchi, F. Stellato, V. Surrenti, A. Tenore, A. Torre, L. Trentadue, S. Turchini, C. Vaccarezza, A. Vacchi, P. Valente, G. Venanzoni, S. Vescovi, F. Villa, G. Zanotti, N. Zema, M. Zobov, ArXiv (2013). arXiv:1307.7967

- K.J. Kim, Y. Shvyd'ko, S. Reiche, Phys. Rev. Lett. 100, 244802 (2008). doi:10.1103/ PhysRevLett.100.244802
- R. Hajima, N. Nishimori, N. Sei, M. Shimada, N. Nakamura, in *Proceedings of FEL2012*, Nara, Japan (2012), pp. 433–436. http://www.jacow.org
- 30. A.M. Kondratenko, E.L. Saldin, Part. Accelerators 10, 207 (1980)
- 31. H. Haus, IEEE J. Quant. Electron. 17(8), 1427 (1981). doi:10.1109/JQE.1981.1071289
- G. Dattoli, A. Marino, A. Renieri, F. Romanelli, IEEE J. Quant. Electron. 17(8), 1371 (1981). doi:10.1109/JQE.1981.1071268
- R. Bonifacio, C. Pellegrini, L. Narducci, Opt. Commun. 50(6), 373 (1984). doi:10.1016/0030-4018(84)90105-6
- 34. K.J. Kim, Phys. Rev. Lett. 57, 1871 (1986). doi:10.1103/PhysRevLett.57.1871
- 35. R. Bonifacio, L. De Salvo, P. Pierini, N. Piovella, C. Pellegrini, Phys. Rev. Lett. 73, 70 (1994). doi:10.1103/PhysRevLett.73.70
- E. Saldin, E. Schneidmiller, M. Yurkov, Opt. Commun. 148(4–6), 383 (1998). doi:10.1016/ S0030-4018(97)00670-6
- Y. Ding, A. Brachmann, F.J. Decker, D. Dowell, P. Emma, J. Frisch, S. Gilevich, G. Hays, P. Hering, Z. Huang, R. Iverson, H. Loos, A. Miahnahri, H.D. Nuhn, D. Ratner, J. Turner, J. Welch, W. White, J. Wu, Phys. Rev. Lett. 102, 254801 (2009). doi:10.1103/PhysRevLett.102. 254801
- 38. L. Giannessi, D. Alesini, P. Antici, A. Bacci, M. Bellaveglia, R. Boni, M. Boscolo, F. Briquez, M. Castellano, L. Catani, E. Chiadroni, A. Cianchi, F. Ciocci, A. Clozza, M.E. Couprie, L. Cultrera, G. Dattoli, M. Del Franco, A. Dipace, G. Di Pirro, A. Doria, A. Drago, W.M. Fawley, M. Ferrario, L. Ficcadenti, D. Filippetto, F. Frassetto, H.P. Freund, V. Fusco, G. Gallerano, A. Gallo, G. Gatti, A. Ghigo, E. Giovenale, A. Marinelli, M. Labat, B. Marchetti, G. Marcus, C. Marrelli, M. Mattioli, M. Migliorati, M. Moreno, A. Mostacci, G. Orlandi, E. Pace, L. Palumbo, A. Petralia, M. Petrarca, V. Petrillo, L. Poletto, M. Quattromini, J.V. Rau, S. Reiche, C. Ronsivalle, J. Rosenzweig, A.R. Rossi, V. Rossi Albertini, E. Sabia, L. Serafini, M. Serluca, I. Spassovsky, B. Spataro, V. Surrenti, C. Vaccarezza, M. Vescovi, C. Vicario, Phys. Rev. ST Accel. Beams 14, 060712 (2011). doi:10.1103/PhysRevSTAB.14.060712

- E.L. Saldin, E.A. Schneidmiller, M.V. Yurkov, Phys. Rev. ST Accel. Beams 9, 050702 (2006). doi:10.1103/PhysRevSTAB.9.050702
- J. Rosenzweig, D. Alesini, G. Andonian, M. Boscolo, M. Dunning, L. Faillace, M. Ferrario, A. Fukusawa, L. Giannessi, E. Hemsing et al., Nucl. Inst. Meth. Phys. Res. Sect. A: Accelerators. Spectrometers, Detectors and Associated Equip. 593(1–2), 39 (2008). doi:10.1016/j.nima. 2008.04.083
- 41. S. Reiche, P. Musumeci, C. Pellegrini, J. Rosenzweig, Nucl. Inst. Meth. Phys. Res. Sect. A: Accelerators. Spectrometers, Detectors and Associated Equip. **593**(1–2), 45 (2008). doi:10. 1016/j.nima.2008.04.061
- L. Giannessi, A. Bacci, M. Bellaveglia, F. Briquez, M. Castellano, E. Chiadroni, A. Cianchi, F. Ciocci, M.E. Couprie, L. Cultrera, G. Dattoli, D. Filippetto, M. Del Franco, G. Di Pirro, M. Ferrario, L. Ficcadenti, F. Frassetto, A. Gallo, G. Gatti, M. Labat, G. Marcus, M. Moreno, A. Mostacci, E. Pace, A. Petralia, V. Petrillo, L. Poletto, M. Quattromini, J.V. Rau, C. Ronsivalle, J. Rosenzweig, A.R. Rossi, V. Rossi, Albertini, E. Sabia, M. Serluca, S. Spampinati, I. Spassovsky, B. Spataro, V. Surrenti, C. Vaccarezza, C. Vicario. Phys. Rev. Lett. 106, 144801 (2011). doi:10.1103/PhysRevLett.106.144801
- R. Bachelard, P. Mercère, M. Idir, M.E. Couprie, M. Labat, O. Chubar, G. Lambert, P. Zeitoun, H. Kimura, H. Ohashi, A. Higashiya, M. Yabashi, M. Nagasono, T. Hara, T. Ishikawa, Phys. Rev. Lett. 106, 234801 (2011). doi:10.1103/PhysRevLett.106.234801
- 44. R. Prazeres, J.M. Ortega, F. Glotin, D.A. Jaroszynski, O. Marcouillé, Phys. Rev. Lett. 78, 2124 (1997). doi:10.1103/PhysRevLett.78.2124
- M. Babzien, I. Ben-Zvi, P. Catravas, J.M. Fang, T.C. Marshall, X.J. Wang, J.S. Wurtele, V. Yakimenko, L.H. Yu, Nucl. Inst. Meth. Phys. Res. A 407, 267 (1998). doi:10.1016/S0168-9002(98)00033-3
- M. Hogan, C. Pellegrini, J. Rosenzweig, G. Travish, A. Varfolomeev, S. Anderson, K. Bishofberger, P. Frigola, A. Murokh, N. Osmanov et al., Phys. Rev. Lett. 80(2), 289 (1998). doi:10.1103/PhysRevLett.80.289.
- 47. S.V. Milton, E. Gluskin, N.D. Arnold, C. Benson, W. Berg, S.G. Biedron, M. Borland, Y.C. Chae, R.J. Dejus, P.K.D. Hartog, B. Deriy, M. Erdmann, Y.I. Eidelman, M.W. Hahne, Z. Huang, K.J. Kim, J.W. Lewellen, Y. Li, A.H. Lumpkin, O. Makarov, E.R. Moog, A. Nassiri, V. Sajaev, R. Soliday, B.J. Tieman, E.M. Trakhtenberg, G. Travish, I.B. Vasserman, N.A. Vinokurov, X.J. Wang, G. Wiemerslage, B.X. Yang, Science 292(5524), 2037 (2001). doi:10.1126/science.1059955
- 48. W. Ackermann, G. Asova, V. Ayvazyan, A. Azima, N. Baboi, J. Bähr, V. Balandin, B. Beutner, A. Brandt, A. Bolzmann, R. Brinkmann, O.I. Brovko, M. Castellano, P. Castro, L. Catani, E. Chiadroni, S. Choroba, A. Cianchi, J.T. Costello, D. Cubaynes, J. Dardis, W. Decking, H. Delsim-Hashemi, A. Delserieys, G. di Pirro, M. Dohlus, S. Düsterer, A. Eckhardt, H.T. Edwards, B. Faatz, J. Feldhaus, K. Flöttmann, J. Frisch, L. Fröhlich, T. Garvey, U. Gensch, C. Gerth, M. Görler, N. Golubeva, H.J. Grabosch, M. Grecki, O. Grimm, K. Hacker, U. Hahn, J.H. Han, K. Honkayaara, T. Hott, M. Hüning, Y. Iyanisenko, E. Jaeschke, W. Jalmuzna, T. Jezynski, R. Kammering, V. Katalev, K. Kavanagh, E.T. Kennedy, S. Khodyachykh, K. Klose, V. Kocharyan, M. Körfer, M. Kollewe, W. Koprek, S. Korepanov, D. Kostin, M. Krassilnikov, G. Kube, M. Kuhlmann, C.L.S. Lewis, L. Lilje, T. Limberg, D. Lipka, F. Löhl, H. Luna, M. Luong, M. Martins, M. Meyer, P. Michelato, V. Miltchev, W.D. Möller, L. Monaco, W.F.O. Müller, O. Napieralski, O. Napoly, P. Nicolosi, D. Nölle, T. Nuñez, A. Oppelt, C. Pagani, R. Paparella, N. Pchalek, J. Pedregosa-Gutierrez, B. Petersen, B. Petrosyan, G. Petrosyan, L. Petrosyan, J. Pflüger, E. Plönjes, L. Poletto, K. Pozniak, E. Prat, D. Proch, P. Pucyk, P. Radcliffe, H. Redlin, K. Rehlich, M. Richter, M. Roehrs, J. Roensch, R. Romaniuk, M. Ross, J. Rossbach, V. Rybnikov, M. Sachwitz, E.L. Saldin, W. Sandner, H. Schlarb, B. Schmidt, M. Schmitz, P. Schmüser, J.R. Schneider, E.A. Schneidmiller, S. Schnepp, S. Schreiber, M. Seidel, D. Sertore, A.V. Shabunov, C. Simon, S. Simrock, E. Sombrowski, A.A. Sorokin, P. Spanknebel, R. Spesyvtsev, L. Staykov, B. Steffen, F. Stephan, F. Stulle, H. Thom, K. Tiedtke, M. Tischer, S. Toleikis, R. Treusch, D. Trines, I. Tsakov, E. Vogel, T. Weiland, H. Weise, M.

- Wellhöfer, M. Wendt, I. Will, A. Winter, K. Wittenburg, W. Wurth, P. Yeates, M.V. Yurkov, I. Zagorodnov, K. Zapfe, Nat. Photonics 1, 336 (2007). doi:10.1038/nphoton.2007.76
- 49. T. Shintake, H. Tanaka, T. Hara, T. Tanaka, K. Togawa, M. Yabashi, Y. Otake, Y. Asano, T. Bizen, T. Fukui et al., Nat. Photonics 2(9), 555 (2008). doi:10.1038/nphoton.2008.134
- E. Allaria, R. Appio, L. Badano, W. Barletta, S. Bassanese, S. Biedron, A. Borga, E. Busetto,
 D. Castronovo, P. Cinquegrana et al., Nat. Phot. 6, 699 (2012). doi:10.1038/nphoton.2012.
 233
- 51. P. Emma, R. Akre, J. Arthur, R. Bionta, C. Bostedt, J. Bozek, A. Brachmann, P. Bucksbaum, R. Coffee, F.J. Decker, Y. Ding, D. Dowell, S. Edstrom, A. Fisher, J. Frisch, S. Gilevich, J. Hastings, G. Hays, P. Hering, Z. Huang, R. Iverson, H. Loos, M. Messerschmidt, A. Miahnahri, S. Moeller, H.D. Nuhn, G. Pile, D. Ratner, J. Rzepiela, D. Schultz, T. Smith, P. Stefan, H. Tompkins, J. Turner, J. Welch, W. White, J. Wu, G. Yocky, J. Galayda, Nat. Photonics 4, 641 (2010). doi:10.1038/nphoton.2010.176
- Z. Huang, A. Brachmann, F.J. Decker, Y. Ding, D. Dowell, P. Emma, J. Frisch, S. Gilevich, G. Hays, P. Hering, R. Iverson, H. Loos, A. Miahnahri, H.D. Nuhn, D. Ratner, G. Stupakov, J. Turner, J. Welch, W. White, J. Wu, D. Xiang, Phys. Rev. ST Accel. Beams 13, 020703 (2010). doi:10.1103/PhysRevSTAB.13.020703
- 53. T. Ishikawa, H. Aoyagi, T. Asaka, Y. Asano, N. Azumi, T. Bizen, H. Ego, K. Fukami, T. Fukui, Y. Furukawa, S. Goto, H. Hanaki, T. Hara, T. Hasegawa, T. Hatsui, A. Higashiya, T. Hirono, N. Hosoda, M. Ishii, T. Inagaki, Y. Inubushi, T. Itoga, Y. Joti, M. Kago, T. Kameshima, H. Kimura, Y. Kirihara, A. Kiyomichi, T. Kobayashi, C. Kondo, T. Kudo, H. Maesaka, X.M. Maréchal, T. Masuda, S. Matsubara, T. Matsumoto, T. Matsushita, S. Matsui, M. Nagasono, N. Nariyama, H. Ohashi, T. Ohata, T. Ohshima, S. Ono, Y. Otake, C. Saji, T. Sakurai, T. Sato, K. Sawada, T. Seike, K. Shirasawa, T. Sugimoto, S. Suzuki, S. Takahashi, H. Takebe, K. Takeshita, K. Tamasaku, H. Tanaka, R. Tanaka, T. Tanaka, T. Togashi, K. Togawa, A. Tokuhisa, H. Tomizawa, K. Tono, S. Wu, M. Yabashi, M. Yamaga, A. Yamashita, K. Yanagida, C. Zhang, T. Shintake, H. Kitamura, N. Kumagai, Nat. Photonics 6, 540 (2012). doi:10.1038/nphoton. 2012.141
- 54. M. Altarelli, et al., The european X-ray laser project xfel. Technical design report, XFEL (2006). http://www.xfel.eu
- 55. J.H. Han, H.S. Kang, I.S. Ko, in *Proceedings of IPAC2012*, New Orleans, Louisiana, USA (2012), pp. 1735–1737. http://www.jacow.org
- 56. S.o.b.o.t.F.T. Reiche, in *Proceedings of IPAC2012*, New Orleans, Louisiana, USA (2011), pp. 223–226. http://www.jacow.org
- 57. Z. Zhao, D.o.b.o.t.F.T. Wang, in *Proceedings of FEL2010*, Malm?, Sweden, (2010), pp. 15–19. http://www.jacow.org
- 58. C.H. Townes, A century of nature twenty-one discoveries that changed science and the world (University of Chicago Press, 2003), Chap. 8. The first laser. www.press.uchicago.edu/ucp/books/book/chicago/C/bo3639243.html
- 59. B. McNeil, Nat. Photonics **3**(7), 375 (2009). doi:10.1038/nphoton.2009.110
- L.H. Yu, M. Babzien, I. Ben-Zvi, L.F. DiMauro, A. Doyuran, W.S. Graves, E.D. Johnson, S. Krinsky, R. Malone, I. Pogorelsky, J. Skaritka, G. Rakowsky, L. Solomon, X.J. Wang, M. Woodle, V. Yakimenko, S.G. Biedron, J.N. Galayda, E. Gluskin, J. Jagger, V. Sajaev, I. Vasserman, Science 289(5481), 932 (2000). doi:10.1126/science.289.5481.932
- B. Girard, Y. Lapierre, J.M. Ortega, C. Bazin, M. Billardon, P. Elleaume, M. Bergher, M. Velghe, Y. Petroff, Phys. Rev. Lett. 53, 2405 (1984). doi:10.1103/PhysRevLett.53.2405
- R. Prazeres, J. Ortega, C. Bazin, M. Bergher, M. Billardon, M. Couprie, M. Velghe, Y. Petroff, Nucl. Inst. Meth. Phys. Res. Sect. A: Accelerators. Spectrometers, Detectors and Associated Equip. 272(1–2), 68 (1988). doi:10.1016/0168-9002(88)90197-0
- R. Prazeres, J.M. Ortega, C. Bazin, M. Bergher, M. Billardon, M.E. Couprie, H. Fang, M. Velghe, Y. Petroff, Europhys. Lett. (EPL) 4(7), 817 (1987). doi:10.1209/0295-5075/4/7/010
- 64. R. Prazeres, P. Guyot-Sionnest, J. Ortega, D. Jaroszynski, M. Billardon, M. Couprie, M. Velghe, Y. Petroff, Nucl. Inst. Meth. Phys. Res. Sect. A: Accelerators. Spectrometers, Detectors and Associated Equip. 304(1–3), 72 (1991). doi:10.1016/0168-9002(91)90823-9

- S. Werin, M. Eriksson, J. Larsson, A. Persson, S. Svanberg, Nucl. Inst. Meth. Phys. Res. A 290, 589 (1990). doi:10.1016/0168-9002(90)90579-U
- G. De Ninno, E. Allaria, M. Coreno, F. Curbis, M.B. Danailov, E. Karantzoulis, A. Locatelli,
 T.O. Menteş, M.A. Nino, C. Spezzani, M. Trovò, Phys. Rev. Lett. 101, 053902 (2008). doi:10.
 1103/PhysRevLett.101.053902
- G. De Ninno, E. Allaria, M. Coreno, S. Chowdhury, F. Curbis, M.B. Danailov, B. Diviacco, M. Ferianis, E. Karantzoulis, E.C. Longhi, I.V. Pinayev, C. Spezzani, M. Trovò, V.N. Litvinenko, Phys. Rev. Lett. 100, 104801 (2008). doi:10.1103/PhysRevLett.100.104801
- V.N. Litvinenko, Nucl. Inst. Meth. Phys. Res. Sect. A: Accelerators. Spectrometers, Detectors and Associated Equip. 507(1–2), 265 (2003). doi:10.1016/S0168-9002(03)00927-6
- N. Čutić, F. Lindau, S. Thorin, S. Werin, J. Bahrdt, W. Eberhardt, K. Holldack, C. Erny,
 A. L'Huillier, E. Mansten, Phys. Rev. ST Accel. Beams 14, 030706 (2011). doi:10.1103/ PhysRevSTAB.14.030706
- M. Labat, M. Hosaka, A. Mochihashi, M. Shimada, M. Katoh, G. Lambert, T. Hara, Y. Takashima, M.E. Couprie, Eur. Phys. J. D 44(1), 187 (2007). doi:10.1140/epjd/e2007-00177-6
- M. Labat, M. Hosaka, M. Shimada, N. Yamamoto, M. Katoh, M.E. Couprie, Phys. Rev. Lett. 102, 014801 (2009). doi:10.1103/PhysRevLett.102.014801
- T. Tanikawa, M. Adachi, H. Zen, M. Hosaka, N. Yamamoto, Y. Taira, M. Katoh, Appl. Phys. Expr. 3(12), 122702 (2010). doi:10.1143/APEX.3.122702
- C. Spezzani, E. Allaria, M. Coreno, B. Diviacco, E. Ferrari, G. Geloni, E. Karantzoulis, B. Mahieu, M. Vento, G. De Ninno, Phys. Rev. Lett. 107, 084801 (2011). doi:10.1103/ PhysRevLett.107.084801
- 74. I. Boscolo, V. Stagno, Nuovo Cimento B 58(2), 267 (1980). doi:10.1007/BF02874012
- R. Barbini, F. Ciocci, G. Dattoli, A. Dipace, L. Giannessi, G. Maino, C. Mari, C. Marina, C. Ronsivalle, E. Sabia, A. Torre, in *Proceedings of the Prospects for a 1 A Free Electron Laser*, ed. by J. C. Gallardo (Sag Harbor, New York, April 22–27 1990) (BNL 52273)
- E. Allaria, G. De Ninno, Phys. Rev. Lett. 99, 014801 (2007). doi:10.1103/PhysRevLett.99. 014801
- L. Giannessi, P. Musumeci, New J. Phys. 8(11), 294 (2006). doi:10.1088/1367-2630/8/11/ 294
- E. Allaria, A. Battistoni, F. Bencivenga, R. Borghes, C. Callegari, F. Capotondi, D. Castronovo,
 P. Cinquegrana, D. Cocco, M. Coreno, et al., New J. Phys. 14, 113009 (2012). doi:10.1088/ 1367-2630/14/11/113009. In press
- L.H. Yu, L. DiMauro, A. Doyuran, W.S. Graves, E.D. Johnson, R. Heese, S. Krinsky, H. Loos, J.B. Murphy, G. Rakowsky, J. Rose, T. Shaftan, B. Sheehy, J. Skaritka, X.J. Wang, Z. Wu, Phys. Rev. Lett. 91(7), 074801 (2003). doi:10.1103/PhysRevLett.91.074801
- G. Dattoli, P.L. Ottaviani, S. Pagnutti, J. Appl. Phys. 97(11), 113102 (2005). doi:10.1063/1. 1886890
- 81. M. Labat, N. Joly, S. Bielawski, C. Szwaj, C. Bruni, M.E. Couprie, Phys. Rev. Lett. **103**, 264801 (2009). doi:10.1103/PhysRevLett.103.264801
- 82. G. De Ninno, B. Mahieu, E. Allaria, L. Giannessi, S. Spampinati, Phys. Rev. Lett. 110, 064801 (2013). doi:10.1103/PhysRevLett.110.064801
- B. Mahieu, E. Allaria, D. Castronovo, M.B. Danailov, A. Demidovich, G. De Ninno, S. Di Mitri, W.M. Fawley, E. Ferrari, L. Fröhlich, D. Gauthier, L. Giannessi, N. Mahne, G. Penco, L. Raimondi, S. Spampinati, C. Spezzani, C. Svetina, M. Trovò, M. Zangrando, Opt. Express 21, 22728 (2013). doi:10.1364/OE.21.022728
- R. Bonifacio, L. De Salvo Souza, P. Pierini, N. Piovella. Nucl. Instrum. Meth. Phys. Res., Sect. A 296(1–3), 358 (1990). doi:10.1016/0168-9002(90)91234-3
- R. Bonifacio, N. Piovella, B.W.J. McNeil, Phys. Rev. A 44, R3441 (1991). doi:10.1103/ PhysRevA.44.R3441
- L. Giannessi, P. Musumeci, S. Spampinati, J. Appl. Phys. 98(4), 043110 (2005). doi:10.1063/ 1.2010624

- T. Watanabe, X.J. Wang, J.B. Murphy, J. Rose, Y. Shen, T. Tsang, L. Giannessi, P. Musumeci,
 S. Reiche, Phys. Rev. Lett. 98, 034802 (2007), doi:10.1103/PhysRevLett.98.034802
- L. Giannessi, M. Artioli, M. Bellaveglia, F. Briquez, E. Chiadroni, A. Cianchi, M.E. Couprie,
 G. Dattoli, E. Di Palma, G. Di Pirro, M. Ferrario, D. Filippetto, F. Frassetto, G. Gatti, M. Labat, G. Marcus, A. Mostacci, A. Petralia, V. Petrillo, L. Poletto, M. Quattromini, J.V. Rau,
 J. Rosenzweig, E. Sabia, M. Serluca, I. Spassovsky, V. Surrenti, Phys. Rev. Lett. 108, 164801
 (2012). doi:10.1103/PhysRevLett.108.164801
- 89. L. Giannessi, et al., in *Proceedings of the 2012 FEL Conference*, (Nara, Japan 2012), p. MOOB6. http://www.jacow.org
- 90. G. Stupakov, Phys. Rev. Lett. 102, 074801 (2009). doi:10.1103/PhysRevLett.102.074801
- D. Xiang, E. Colby, M. Dunning, S. Gilevich, C. Hast, K. Jobe, D. McCormick, J. Nelson, T.O. Raubenheimer, K. Soong, et al., Phys. Rev. Lett. 105(11) (2010). doi:DOIurl10.1103/PhysRevLett.105.114801
- 92. Z.T. Zhao, D. Wang, J.H. Chen, Z.H. Chen, H.X. Deng, J.G. Ding, C. Feng, Q. Gu, M.M. Huang, T.H. Lan et al., Nat. Photonics 6(6), 360 (2012). doi:10.1038/nphoton.2012.105
- 93. D. Xiang, G. Stupakov, New J. Phys. **13**(9), 093028 (2011). doi:10.1088/1367-2630/13/9/093028
- I. Ben-Zvi, K.M. Yang, L.H. Yu, Nucl. Inst. Meth. Phys. Res. A 318, 726 (1992). doi:10. 1016/0168-9002(92)91147-2
- 95. L.H. Yu, I. Ben-Zvi, Nucl. Inst. Meth. Phys. Res. A **393**, 96 (1997). doi:10.1016/S0168-9002(97)00435-X
- 96. B. Liu, W.B. Li, J.H. Chen, Z.H. Chen, H.X. Deng, J.G. Ding, Y. Fan, G.P. Fang, C. Feng, L. Feng, Q. Gu, M. Gu, C. Guo, D.Z. Huang, M.M. Huang, W.H. Huang, Q.K. Jia, T.H. Lan, Y.B. Leng, D.G. Li, W.M. Li, X. Li, G.Q. Lin, L. Shang, L. Shen, C.X. Tang, G.L. Wang, L. Wang, R. Wang, X.T. Wang, Z.S. Wang, Z.S. Wang, H.F. Yao, K.R. Ye, L.X. Yin, L.Y. Yu, J.Q. Zhang, M. Zhang, M. Zhang, T. Zhang, W.Y. Zhang, S.P. Zhong, Q.G. Zhou, D. Wang, Z.T. Zhao, Phys. Rev. ST Accel. Beams 16, 020704 (2013). doi:10.1103/PhysRevSTAB.16.020704
- 97. E. Allaria, D. Castronovo, P. Cinquegrana, P. Craievich, M. Dal Forno, M.B. Danailov, G. D'Auria, A. Demidovich, G. De Ninno, S. Di Mitri, et al., Nat. Photonics **7**(11), 913 (2013). doi:10.1038/nphoton.2013.277
- 98. M. Ferray, A. L'Huillier, X.F. Li, L.A. Lompre, G. Mainfray, C. Manus, J. Phys. B: At. Mol. Opt. Phys. **21**(3), L31 (1988). doi:10.1088/0953-4075/21/3/001
- A. McPherson, G. Gibson, H. Jara, U. Johann, T.S. Luk, I.A. McIntyre, K. Boyer, C.K. Rhodes,
 J. Opt. Soc. Am. B 4(4), 595 (1987). doi:10.1364/JOSAB.4.000595
- M.E. Couprie, M. Belakhovsky, B. Gilquin, D. Garzella, M. Jablonka, F. Méot, P. Monot, A. Mosnier, L. Nahon, A. Rousse, Nucl. Inst. Meth. Phys. Res. A 528, 557 (2004). doi:10.1016/j.nima.2004.04.101
- D. Garzella, T. Hara, B. Carré, P. Salières, T. Shintake, H. Kitamura, M.E. Couprie, Nucl. Inst. Meth. Phys. Res. A 528, 502 (2004). doi:10.1016/j.nima.2004.04.089
- G. Lambert, T. Hara, D. Garzella, T. Tanikawa, M. Labat, B. Carre, H. Kitamura, T. Shintake, M. Bougeard, S. Inoue et al., Nat. Phys. 4(4), 296 (2008). doi:10.1038/nphys889
- 103. T. Togashi, E.J. Takahashi, K. Midorikawa, M. Aoyama, K. Yamakawa, T. Sato, A. Iwasaki, S. Owada, T. Okino, K. Yamanouchi, F. Kannari, A. Yagishita, H. Nakano, M.E. Couprie, K. Fukami, T. Hatsui, T. Hara, T. Kameshima, H. Kitamura, N. Kumagai, S. Matsubara, M. Nagasono, H. Ohashi, T. Ohshima, Y. Otake, T. Shintake, K. Tamasaku, H. Tanaka, T. Tanaka, K. Togawa, H. Tomizawa, T. Watanabe, M. Yabashi, T. Ishikawa, Opt. Express 19, 317 (2011). doi:10.1364/OE.19.000317
- 104. C. Lechner, et al., in *Proceeding of FEL 2012*, (Nara, Japan, 2012)
- 105. M. Labat, M. Bellaveglia, M. Bougeard, B. Carré, F. Ciocci, E. Chiadroni, A. Cianchi, M.E. Couprie, L. Cultrera, M. Del Franco, G. Di Pirro, A. Drago, M. Ferrario, D. Filippetto, F. Frassetto, A. Gallo, D. Garzella, G. Gatti, L. Giannessi, G. Lambert, A. Mostacci, A. Petralia, V. Petrillo, L. Poletto, M. Quattromini, J.V. Rau, C. Ronsivalle, E. Sabia, M. Serluca, I. Spassovsky, V. Surrenti, C. Vaccarezza, C. Vicario, Phys. Rev. Lett. 107, 224801 (2011). doi:10.1103/PhysRevLett.107.224801

- J. Feldhaus, E. Saldin, J. Schneider, E. Schneidmiller, M. Yurkov, Opt. Commun. 140(4–6), 341 (1997). doi:10.1016/S0030-4018(97)00163-6
- G. Geloni, V. Kocharyan, E. Saldin, J. Mod. Opt. 58(16), 1391 (2011). doi:10.1080/09500340.
 2011.586473
- J. Amann, W. Berg, V. Blank, F.J. Decker, Y. Ding, P. Emma, Y. Feng, J. Frisch, D. Fritz, J. Hastings et al., Nat. Photonics 6(10), 693 (2012). doi:10.1038/nphoton.2012.180
- 109. M. Yabashi, T. Tanaka, Nat. Photonics 6(10), 648 (2012). doi:10.1038/nphoton.2012.237
- 110. P.B. Corkum, Phys. Rev. Lett. **71**, 1994 (1993). doi:10.1103/PhysRevLett.71.1994
- 111. K.C. Kulander, K.J. Schafer, J.L. Krause, *Dynamics of Short-Pulse Excitation, Ionization and Harmonic Conversion* (Springer, Berlin, 1993). doi:10.1007/978-1-4615-7963-2_10
- M. Lewenstein, P. Balcou, M.Y. Ivanov, A. L'Huillier, P.B. Corkum, Phys. Rev. A 49, 2117 (1994). doi:10.1103/PhysRevA.49.2117
- G. Dattoli, L. Giannessi, A. Torre, J. Opt. Soc. Am. B 10(11), 2136 (1993). doi:10.1364/ JOSAB.10.002136
- S. Biedron, M. Ferrario, L. Giannessi, S. Werin, Synchrotron Radiat. News 22(4), 5 (2009). doi:10.1080/08940880903113885
- E. Takahashi, Y. Nabekawa, H. Mashiko, H. Hasegawa, A. Suda, K. Midorikawa, IEEE J. Sel. Top. Quant. Electron. 10(6), 1315 (2004). doi:10.1109/JSTQE.2004.838077
- J.F. Hergott, M. Kovacev, H. Merdji, C. Hubert, Y. Mairesse, E. Jean, P. Breger, P. Agostini,
 B. Carré, P. Salières, Phys. Rev. A 66, 021801 (2002). doi:10.1103/PhysRevA.66.021801
- 117. X. Ge, W. Boutu, D. Gauthier, F. Wang, A. Borta, B. Barbrel, M. Ducousso, A.I. Gonzalez, B. Carré, D. Guillaumet, M. Perdrix, O. Gobert, J. Gautier, G. Lambert, F.R.N.C. Maia, J. Hajdu, P. Zeitoun, H. Merdji, Opt. Express 21, 11441 (2013). doi:10.1364/OE.21.011441
- 118. B.W.J. McNeil, N.R. Thompson, D.J. Dunning, B. Sheehy, J. Phy. B: At. Mol. Opt. Phys. **44**(6), 065404 (2011). doi:10.1088/0953-4075/44/6/065404
- L. Giannessi, M. Quattromini, C. Frascati, P. Musumeci, G. Sansone, S. Stagira, M. Nisoli, S. De Silvestri, in 28th International Free Electron Laser Conference, FEL 2006, pp. 248–251 (2006)
- J. Wu, P.R. Bolton, J.B. Murphy, X. Zhong, Appl. Phys. Lett. 90(2), 021109 (2007). doi:10. 1063/1.2431455
- E. Priori, G. Cerullo, M. Nisoli, S. Stagira, S. De Silvestri, P. Villoresi, L. Poletto, P. Ceccherini, C. Altucci, R. Bruzzese, C. de Lisio, Phys. Rev. A 61, 063801 (2000). doi:10.1103/PhysRevA. 61.063801
- G. Sansone, C. Vozzi, S. Stagira, M. Nisoli, Phys. Rev. A 70, 013411 (2004). doi:10.1103/ PhysRevA.70.013411
- P. Balcou, P. Sali'eres, A. L'Huillier, M. Lewenstein, Phys. Rev. A 55, 3204 (1997). doi:10. 1103/PhysRevA.55.3204
- P. Salieres, B. Carr?, M. Le D?roff, F. Grasbon, G.G. Paulus, H. Walther, R. Kopold, W. Becker, D.B. Milosevic, A. Sanpera, M. Lewenstein, Science 292(5518), 902 (2001). doi:10.1126/science.108836
- 125. S. Reiche, Nucl. Inst. Meth. Phys. Res. Sect. A: Accelerators. Spectrometers, Detectors and Associated Equip. **429**(1–3), 243 (1999). doi:10.1016/S0168-9002(99)00114-X
- G. Lambert, M. Bougeard, W. Boutu, P. Breger, B. Carré, M.E. Couprie, D. Garzella, H. Merdji, M. P, P. Salières, T. Hara, H. Kitamura, T. Shintake, (2005), pp. 224–227
- C. Erny, E. Mansten, M. Gisselbrecht, J. Schwenke, R. Rakowski, X. He, M.B. Gaarde, S. Werin, A. L'Huillier, New J. Phys. 13(7), 073035 (2011). doi:10.1088/1367-2630/13/7/ 073035
- L. Poletto, F. Frassetto, M. Artioli, M.d. Franco, M. Labat, A. Petralia, M. Quattromini,
 L. Giannessi. J. Phys: Conf. Ser. 425(12), 122011 (2013). doi:10.1088/1742-6596/425/12/122011
- E. Goulielmakis, M. Schultze, M. Hofstetter, V.S. Yakovlev, J. Gagnon, M. Uiberacker, A.L. Aquila, E.M. Gullikson, D.T. Attwood, R. Kienberger et al., Science 320(5883), 1614 (2008). doi:10.1126/science.1157846

- B.E. Schmidt, A.D. Shiner, M. Giguère, P. Lassonde, C.A. Trallero-Herrero, J.C. Kieffer, P.B. Corkum, D.M. Villeneuve, F. Légaré, J. Phys. B At. Mol. Phys. 45(7), 074008 (2012). doi:10. 1088/0953-4075/45/7/074008
- X. Zhou, R. Lock, N. Wagner, W. Li, H.C. Kapteyn, M.M. Murnane, Phys. Rev. Lett. 102, 073902 (2009). doi:10.1103/PhysRevLett.102.073902
- 132. Y. Mairesse, J. Higuet, N. Dudovich, D. Shafir, B. Fabre, E. Mével, E. Constant, S. Patchkovskii, Z. Walters, M.Y. Ivanov, O. Smirnova, Phys. Rev. Lett. 104, 213601 (2010). doi:10.1103/PhysRevLett.104.213601
- 133. H. Tomizawa, in *Proceedings of Beam Instrumentation Workshop (BIW12*), (Jefferson Lab, USA, 2012)
- 134. S. Ackermann, A. Azima, S. Bajt, J. Bödewadt, F. Curbis, H. Dachraoui, H. Delsim-Hashemi, M. Drescher, S. Düsterer, B. Faatz, M. Felber, J. Feldhaus, E. Hass, U. Hipp, K. Honkavaara, R. Ischebeck, S. Khan, T. Laarmann, C. Lechner, T. Maltezopoulos, V. Miltchev, M. Mittenzwey, M. Rehders, J. Rönsch-Schulenburg, J. Rossbach, H. Schlarb, S. Schreiber, L. Schroedter, M. Schulz, S. Schulz, R. Tarkeshian, M. Tischer, V. Wacker, M. Wieland, Phys. Rev. Lett. 111, 114801 (2013). doi:10.1103/PhysRevLett.111.114801
- 135. L. Giannessi, *Proceedings of FEL 2006 Conference Germany*, pp. 91-94 (2006). http://www.jacow.org
- G. Lambert, T. Hara, M. Labat, T. Tanikawa, Y. Tanaka, M. Yabashi, D. Garzella, B. Carré,
 M.E. Couprie, Europhys. Lett. 88, 54002 (2009). doi:10.1209/0295-5075/88/54002
- T. Tanikawa, G. Lambert, T. Hara, M. Labat, Y. Tanaka, M. Yabashi, O. Chubar, M.E. Couprie, EPL (Europhys. Lett.) 94(3), 34001 (2011). doi:10.1209/0295-5075/94/34001
- 138. M. Ferrario, D. Alesini, A. Bacci, M. Bellaveglia, R. Boni, M. Boscolo, M. Castellano, L. Catani, E. Chiadroni, S. Cialdi, A. Cianchi, A. Clozza, L. Cultrera, G. Di Pirro, A. Drago, A. Esposito, L. Ficcadenti, D. Filippetto, V. Fusco, A. Gallo, G. Gatti, A. Ghigo, L. Giannessi, C. Ligi, M. Mattioli, M. Migliorati, A. Mostacci, P. Musumeci, E. Pace, L. Palumbo, L. Pellegrino, M. Petrarca, M. Quattromini, R. Ricci, C. Ronsivalle, J. Rosenzweig, A.R. Rossi, C. Sanelli, L. Serafini, M. Serio, F. Sgamma, B. Spataro, F. Tazzioli, S. Tomassini, C. Vaccarezza, M. Vescovi, C. Vicario, Phys. Rev. Lett. 99, 234801 (2007). doi:10.1103/PhysRevLett.99.234801
- 139. L. Giannessi, M. Bellaveglia, E. Chiadroni, A. Cianchi, M.E. Couprie, M. Del Franco, G. Di Pirro, M. Ferrario, G. Gatti, M. Labat, G. Marcus, A. Mostacci, A. Petralia, V. Petrillo, M. Quattromini, J.V. Rau, S. Spampinati, V. Surrenti, Phys. Rev. Lett. 110, 044801 (2013). doi:10.1103/PhysRevLett.110.044801
- M. Labat, M. Hosaka, M. Shimada, M. Katoh, M.E. Couprie, Phys. Rev. Lett. 101, 164803 (2008). doi:10.1103/PhysRevLett.101.164803
- 141. E. Allaria, F. Bencivenga, R. Borghes, F. Capotondi, D. Castronovo, P. Charalambous, P. Cinquegrana, M.B. Danailov, G. de Ninno, A. Demidovich, S. di Mitri, B. Diviacco, D. Fausti, W.M. Fawley, E. Ferrari, L. Froehlich, D. Gauthier, A. Gessini, L. Giannessi, R. Ivanov, M. Kiskinova, G. Kurdi, B. Mahieu, N. Mahne, I. Nikolov, C. Masciovecchio, E. Pedersoli, G. Penco, L. Raimondi, C. Serpico, P. Sigalotti, S. Spampinati, C. Spezzani, C. Svetina, M. Trovò, M. Zangrando, Nat. Commun. 4, 2476 (2013). doi:10.1038/ncomms3476
- 142. K. Nakajima, Nat. Phys. 4(2), 92 (2008). doi:10.1038/nphys846
- 143. H.P. Schlenvoigt, K. Haupt, A. Debus, F. Budde, O. Jäckel, S. Pfotenhauer, H. Schwoerer, E. Rohwer, J.G. Gallacher, E. Brunetti, R.P. Shanks, S.M. Wiggins, D.A. Jaroszynski, Nat. Phys. 4, 130 (2008). doi:10.1038/nphys811
- 144. M. Fuchs, R. Weingartner, A. Popp, Z. Major, S. Becker, J. Osterhoff, I. Cortrie, B. Zeitler, R. Hörlein, G.D. Tsakiris, U. Schramm, T.P. Rowlands-Rees, S.M. Hooker, D. Habs, F. Krausz, S. Karsch, F. Grüner, Nat. Phys. 5, 826 (2009). doi:10.1038/nphys1404
- 145. M.P. Anania, D. Clark, S.B. van der Geer, M.J. de Loos, R. Isaac, A.J.W. Reitsma, G.H. Welsh, S.M. Wiggins, D.A. Jaroszynski, Transport of ultra-short electron bunches in a free-electron laser driven by a laser-plasma wakefield accelerator (SPIE—International Society for Optical Engineering, 2009), pp. 735, 916–735, 916–10. doi:10.1117/12.820455

- A.R. Maier, A. Meseck, S. Reiche, C.B. Schroeder, T. Seggebrock, F. Grüner, Phys. Rev. X 2(3), 031019 (2012). doi:10.1103/PhysRevX.2.031019
- Z. Huang, Y. Ding, C.B. Schroeder, Phys. Rev. Lett. 109, 204801 (2012). doi:10.1103/ PhysRevLett.109.204801
- M.E. Couprie, C. Benabderrahmane, P. Betinelli, F. Bouvet, A. Buteau, L. Cassinari, J. Daillant, J.C. Denard, P. Eymard, B. Gagey et al., J. Phys: Conf. Ser. 425(7), 072001 (2013). doi:10.1088/1742-6596/425/7/072001
- F. Brizuela, C.M. Heyl, P. Rudawski, D. Kroon, L. Rading, J.M. Dahlström, J. Mauritsson, P. Johnsson, C.L. Arnold, A. L'Huillier, Sci. Rep. 3, 1410 (2013). doi:10.1038/srep01410

Chapter 6 Temporal Characterization of Ultrashort Extreme-Ultraviolet and Soft X-ray Pulses

Michele Devetta, Matteo Negro, Salvatore Stagira and Caterina Vozzi

Abstract The impressive technological advances in the generation of ultrashort XUV and soft X-ray light pulses have triggered the quest for novel techniques, able to characterize these pulses in the temporal domain. In this chapter we will present and discuss the most important methods for temporal pulse characterization, with particular emphasis on attosecond pulses generated by high-order harmonics and on femtosecond soft X-ray pulses emitted by free electron lasers.

6.1 Measurement of Attosecond Pulses

The development of novel experimental techniques for the temporal characterization of sub-femtosecond XUV pulses generated by high-order harmonics, represented a breakthrough in attosecond science. Two general methods have been proposed and demonstrated so far. The first one is a cross-correlation method, very similar to the standard streak camera approach widely used for the measurement of much longer pulses. The second technique exploits non linear effects induced by the attosecond pulses. In the following we will review several aspects of these two approaches.

M. Devetta · M. Negro · S. Stagira (⋈) · C. Vozzi Istituto di Fotonica e Nanotecnologie - IFN - CNR & Physics Department, Politecnico di Milano, 20133 Milan, Italy e-mail: salvatore.stagira@polimi.it

M. Negro

e-mail: matteo.negro@polimi.it

M. Devetta

e-mail: michele.devetta@ifn.cnr.it

C. Vozzi

e-mail: caterina.vozzi@ifn.cnr.it

© Springer-Verlag Berlin Heidelberg 2015 F. Canova and L. Poletto (eds.), *Optical Technologies for Extreme-Ultraviolet and Soft X-ray Coherent Sources*, Springer Series in Optical Sciences 197, DOI 10.1007/978-3-662-47443-3_6 116 M. Devetta et al.

6.1.1 The Attosecond Streak Camera

In order to obtain the full temporal characterization of attosecond bursts it is possible to follow a cross-correlation approach: the so-called "streak camera" method. Indeed, all the application of isolated attosecond pulses proposed and demonstrated so far are based on this approach. In this kind of measurements the attosecond pulse ionizes a target gas by single photon absorption, generating an electron wave-packet. If the process happens away from any atomic resonance, the electron wave packet is a perfect replica of the attosecond light pulse. A non-stationary filter is required to access the temporal properties of the attosecond pulse [1]. This can be realized if the ionization process triggered by the attosecond burst happens in the presence of a streaking IR pulse, which acts as an ultrafast phase modulator on the electron wave packet. A simple sketch of this kind of measurement is depicted in Fig. 6.1a. It is possible to demonstrate that the sequence of photo-ionization spectra as a function of the delay τ between the attosecond and the IR pulses contains enough information for the complete reconstruction of the temporal amplitude and phase of both the attosecond pulse and the streaking IR pulse at the same time. This technique is known as Frequency-Resolved Optical Gating for Complete Reconstruction of Attosecond Bursts (FROG-CRAB) [2]. For the description of the photo-ionization process by the attosecond pulse, the photo-electron spectrum is given by $|a_v|^2$, where a_v is the transition amplitude between the atomic ground state and a state in the continuum with momentum v. This amplitude can be described in the framework of first order perturbation theory as (in atomic units):

$$a_{\mathbf{v}} = -i \int_{-\infty}^{\infty} dt \ \mathbf{d}_{\mathbf{v}} \ \mathbf{E}_{X}(t) \ e^{i(W+I_{P})t}$$
 (6.1)

In this expression, $\mathbf{E}_X(t)$ is the electric field of the attosecond pulse, $\mathbf{d}_{\mathbf{v}}$ is the dipole matrix element between the ground state and the continuum, W is the final kinetic energy of the electron and I_P is the ionization potential of the atom. Equation (6.1) highlights the close relation between the photo-electron wave-packet and the electric field of the attosecond pulse in absence of atomic resonances [3]. As already mentioned, for the temporal reconstruction of the attosecond electron wave-packet it is necessary to acquire the photo-electron spectra in presence of an external lowfrequency field. The latter acts as a phase gate in the measurement. It is possible to derive the expression of the transition amplitude $a_{\rm v}$ in these conditions, by solving the Schroedinger equation for an atom in a classical electromagnetic field under certain approximations, namely (a) Single Active Electron approximation (SAE)—the atom is considered hydrogen-like and multiple ionization is neglected; (b) Strong Field Approximation (SFA)—the electron in the continuum is influenced only by the external electric field, the influence of the parent ion Coulomb potential is neglected; (c) only ground state and continuum states are considered—no influence of the atomic bound states is considered. With these approximations, the expression for $a_{\rm v}$ reads [2, 4]:

$$a_{\mathbf{v}}(\tau) = -i \int_{-\infty}^{\infty} dt e^{i\phi(t)} \mathbf{d}_{\mathbf{p}(t)} \mathbf{E}_{X}(t - \tau) e^{i(W + I_{P})t}$$
(6.2)

where τ is the delay between the attosecond and the IR pulse, $\mathbf{p}(t) = \mathbf{v} + \mathbf{A}(t)$ is the instantaneous kinetic momentum, $\mathbf{A}(t)$ is the vector potential of the IR pulse, $\mathbf{d}_{\mathbf{p}(t)}$ is the dipole matrix element between the ground state and the continuum state with momentum $\mathbf{p}(t)$ and $\phi(t)$ is the phase modulation due to the external IR pulse. The latter is imposed to the electron wave-packet during the ionization process and can be written as follows:

$$\phi(t) = \int_{-t}^{\infty} dt' \left[\mathbf{v} \cdot \mathbf{A}(t') + \mathbf{A}^2(t')/2 \right]. \tag{6.3}$$

For deriving the expression of the phase modulation, one can assume a linearly polarized IR pulse, whose electric field has the form $\mathbf{E}_{IR} = \mathbf{E}_0(t) \cos(\omega_{IR}t)$ and whose temporal duration is long enough to assume the *Slowly Varying Envelope approximation (SVEA)*. With these assumptions, the phase modulation $\phi(t)$ reads as the sum of three contributions [2]:

$$\phi_1(t) = \int_{-t}^{\infty} dt' \ U_p(t') \tag{6.4}$$

$$\phi_2(t) = \frac{\sqrt{8WU_p}}{\omega_{IR}} \cos\theta \cos(\omega_{IR}t)$$
 (6.5)

$$\phi_3(t) = -\frac{U_p}{2\omega_{IR}} \sin(2\omega_{IR}t). \tag{6.6}$$

Here $U_P=E_0^2(t)/(4\omega_{I\!R}^2)$ is the ponderomotive energy and θ is the angle between the electron velocity v and the polarization direction of the IR field. From the equations above, it appears that the phase modulation has two oscillating components: $\phi_2(t)$ and $\phi_3(t)$ at frequency ω_{IR} and $2\omega_{IR}$ respectively. Considering that often $W \gg U_P$, the phase term $\phi_2(t)$ is the leading one for all the observation angles θ , but $\theta \approx \pi/2$. The maximum energy shift of the measured photo-electron spectrum due to IR field, is given by the maximum value of $|\partial \phi/\partial t|$ [3]. Thus the expression (6.5) allows to identify the requirements on the phase modulation for the characterization of the electron wave-packet, leading to the correct reconstruction of the attosecond pulse: the phase modulation should be fast enough and the bandwidth of the phase modulation should be a large fraction of the bandwidth of the attosecond pulse to be characterized. In Fig. 6.1b it is shown an example of CRAB trace: a sequence of photo-ionization spectra calculated as a function of the delay τ between the attosecond pulse and the IR streaking pulse. The photo-electron spectra have been calculated for photo-ionization by a 300-as chirped XUV pulse (transform limited pulse duration: 100 as) in the presence of a 5-fs 750-nm streaking pulse. In this calculation, the photoelectron spectra are detected around $\theta \approx 0^{\circ}$. The trace

M. Devetta et al.

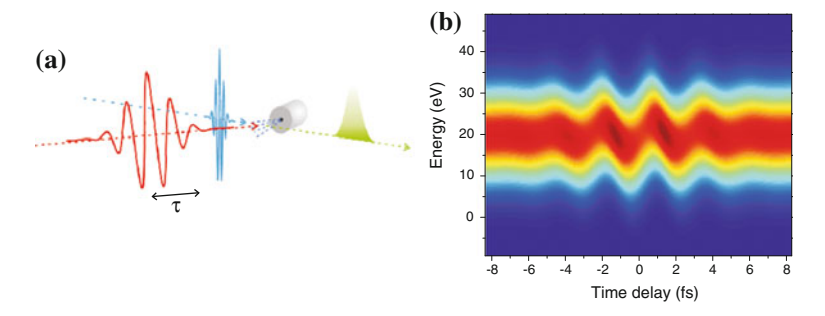


Fig. 6.1 a Simple scheme of the attosecond streaking experiment. **b** CRAB trace calculated for photo-ionization by a chirped attosecond pulse (transform-limited pulse duration: 100 as, actual pulse duration: 300 as)

oscillations correspond to the oscillation of the vector potential $\mathbf{A}(t)$ of the streaking IR pulse.

In *Frequency Resolved Optical Gating (FROG)*, a standard cross-correlation method for the complete characterization of ultrashort pulses in the femtosecond domain, a gate pulse is used to temporally "sample" the electric field of the pulse to be characterized through a nonlinear optical interaction [5]. The FROG trace is given by

$$S(\omega, t) = \left| \int_{-\infty}^{\infty} dt \ G(t) \ E(t - \tau) \ e^{i\omega t} \right|^2$$
 (6.7)

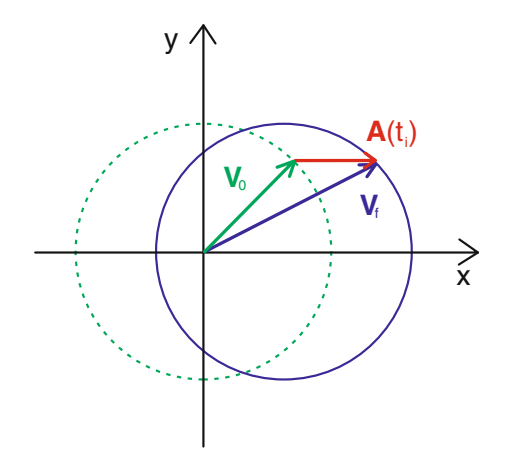
and it corresponds to the sequence of temporal slices acquired as a function of the delay τ between the electric field E(t) and the gate pulse G(t) during the sampling process.

The similarity between FROG-CRAB and FROG appears now clearly by comparing (6.2) and (6.7): the sequence of photoelectron spectra $|a_{\mathbf{v}}|^2$ is exactly like a FROG spectrogram in which the gate is the phase gate $G(t) = e^{i\phi(t)}$. From the CRAB trace it is then possible to retrieve the amplitude and phase of the attosecond XUV pulse by applying an iterative algorithm, like the *Principal Component Generalized Projection Algorithm (PCGPA)* [6].

6.1.2 Semiclassical Model for Attosecond Streaking

A physical picture of streaking-like attosecond measurements and attosecond pulse characterization can be gained with a simple semiclassical model for atomic photoionization. Since the central frequency of the attosecond pulse ω_{XUV} is very different from the one of the streaking IR pulse ω_{IR} , photo-ionization can be depicted as a two-step process [7]. During the photo-ionization process driven by the attosecond pulse, an electron is freed by the parent ion and it is promoted in a continuum state

Fig. 6.2 Sketch of the semiclassical interpretation for attosecond streaking: dashed curve is the photo-electron velocity distribution without the streaking IR field; solid curve shows how the velocity distribution is affected by the streaking IR field



at the time t_i with an initial velocity \mathbf{v}_0 and a corresponding initial kinetic energy $W_0 = v_0^2/2 = \omega_{XUV} - I_P$. In the standard conditions $U_p \gg \omega_{IR}$ and $\omega_{XUV} \gg I_p$, the motion of the electron in the external streaking field $\mathbf{E}_{IR}(t) = \mathbf{E}_0(t) \cos{(\omega_{IR}t + \psi)}$ can be calculated by classical mechanics and the velocity of the electron as a function of time turns out to be

$$\mathbf{v}(t) = -\mathbf{A}(t) + [\mathbf{v}_0 + \mathbf{A}(t_i)]. \tag{6.8}$$

The first contribution to the electron velocity corresponds to the fast quiver motion of the electron in the streaking field and it vanishes when the IR pulse is gone-by. Thus the final drift velocity of the electron reads $\mathbf{v}_f = \mathbf{v}_0 + \mathbf{A}(t_i)$ and it is proportional to the vector potential of the streaking field at the time of ionization. To visualize the influence of the streaking field on the electron velocity Fig. 6.2 shows the electron velocity distribution in the xy plane perpendicular to the propagation direction of the XUV and IR pulses: the dashed curve corresponds to the velocity distribution without the streaking field, which is a circle centered on 0 with radius $|\mathbf{v}_0|$. The effect of the streaking field results in the shift of the electron velocity distribution by $\mathbf{A}(t_i)$: considering a linearly polarized streaking field this shift occurs in a direction parallel to the IR electric field and the distribution moves back and forth as a function of the ionization time t_i , as sketched in Fig. 6.2, solid curve. In these conditions the electron drift kinetic energy is given by:

$$W = W_0 + 2U_p \cos(2\theta) \sin^2 \phi_i \pm \alpha (8W_0 U_p)^{1/2} \cos \theta \sin \phi_i,$$
 (6.9)

where U_P is the ponderomotive energy at t_i , $\phi_i = \omega_{IR}t_i + \psi$ and $\alpha = \{1 - (2U_p/W_0)\sin^2\theta\sin^2\phi_i\}^{1/2}$. Equation (6.9) shows the role of the observation angle θ on the measured electron velocity: the strongest modulation can be observed for $\theta = 0^\circ$, with the drift kinetic energy W oscillating around W_0 as a function of the ionization time through the phase ϕ_i . It is worth noting that this semiclassical model properly describes the process only if the attosecond electron wave-packet is shorter than one half-optical-cycle of the IR field. Otherwise, electrons emit-

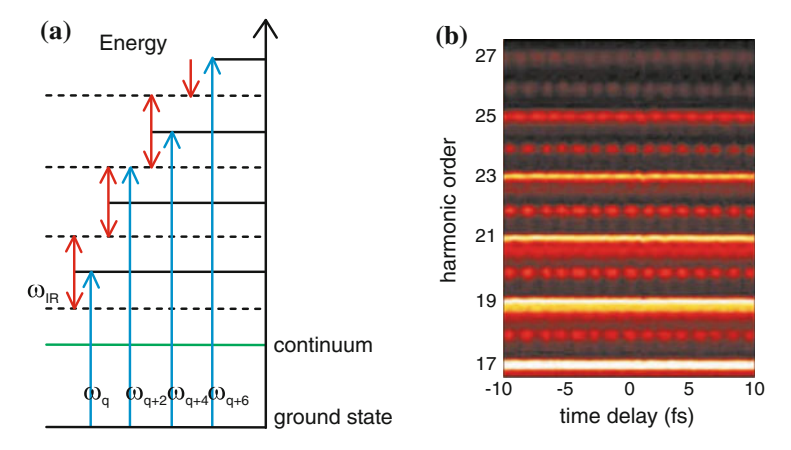


Fig. 6.3 a Scheme of the RABBIT measurement. **b** Example of a sequence of photoelectron spectra acquired in a RABBIT experiment. Figure adapted from [10]

ted at different times are mapped onto the same energy and quantum interference effects have to be taken into account. In this semiclassical picture, it is very clear how the depicted mechanism shows a close connection with the well-established streak-camera approach for the measurement of visible pulses in the picosecond time domain. Here the temporal information is encoded in the energy distribution of the photo-electron wave-packet, while in a standard streak camera measurement the pulse temporal profile is mapped into the spatial distribution of electrons.

6.1.3 RABBIT: Measurement of Attosecond Pulse Trains

It is worth noting that the approach described so far can be applied also for the characterization of attosecond pulse trains. In this case, the FROG-CRAB technique represents a generalization of the *Reconstruction of Attosecond Beating By Interference of Two-photons transitions (RABBIT)* method [8, 9]. The RABBIT technique relies on the measurement of photoelectron energy distribution generated in the ionization process of a noble gas driven by the superposition of as pulse train and the fundamental streaking IR field. In such an experiment, sidebands appear in between photoelectron peaks corresponding to adjacent harmonics. The intensity of these sideband peaks is modulated as a function of the delay between the XUV and IR pulse. From the amplitude of this modulation the phase relation between adjacent harmonics can be retrieved. A sketch of this measurement technique is depicted in Fig. 6.3 with a sample of a RABBIT trace. With respect to the FROG-CRAB, the RABBIT does not allow to reconstruct the full temporal profile of the attosecond pulse train because it does not exploit the full information of the photoelectron spectra.

By means of RABBIT technique, the first observation of an attosecond pulse train was achieved in 2001 by Paul et al. [8]. In that experiment, the harmonic spectrum containing harmonics up to the 19th were focused on an argon gas jet together with a fraction of the fundamental 800-nm beam. The analysis of the sidebands in the photoelectron spectra allowed to retrieve the phase between the harmonics. By measuring the relative harmonic intensity it was possible to characterize the average intensity profile of the attosecond pulse train corresponding to a sequence of 250-as pulses spaced by half of the optical cycle of the fundamental driving field. Subsequently, a train of 170-as pulses has been generated by amplitude and phase control of harmonics generated in argon and has been characterized by means of RABBIT approach by Lopez-Martens et al. in 2005 [11]. More recently the same technique was exploited by Gustafsson et al. for the characterization of a train of as pulses as short as 130 as generated in neon [12]. In this case the intrinsic chirp of the attosecond pulse related to the quasi-linear variation of the harmonic emission time as a function of the harmonic frequency [13] was compensated by the negative group-delay dispersion associated to propagation through a Zr filter following the approach proposed by Kim et al. [14].

6.1.4 Isolated Attosecond Pulse Characterization: Experimental Results

The streak camera approach was applied for the first time in 2001 by Hentschel et al. [15], who reported the measurement of an isolated attosecond pulse generated by spectral selection in the cutoff region of the harmonic emission generated in neon by a 7-fs driving pulse. In this experiment the central portion of the fundamental IR beam was blocked by a Zr filter and the transmitted XUV beam was focused together with the remaining annular part of the IR beam onto a krypton target by a concentric piezo-controlled double mirror which acted as a delay stage. The spectral selection of the cutoff region was performed exploiting the inner part of the concentric double mirror, consisting of a Mo/Si multilayer [16]. The out-coming XUV pulse spanned a bandwidth of \approx 5 eV around 90 eV. From the measurement of the delay-dependent photoelectron spectral width, a pulse duration of 650 ± 150 as has been measured. The same experimental approach has allowed in 2004 to measure isolated attosecond pulses as short as 250 as [17]. In 2006 Sansone et al. provided the first demonstration of the FROG-CRAB technique for the complete characterization of an isolated attosecond pulse [18]. In this experiment, the attosecond pulse generation was achieved by means of the polarization gating technique applied to few-cycle IR pulses with stable carrier-envelope phase. A sketch of the experimental setup is shown in Fig. 6.4a: the driving beam for HHG was separated from the streaking beam by a drilled mirror, the inner part was transmitted by birefringent plates in order to obtain the proper polarization state for gating the harmonic emission. Harmonics were generated in an argon cell and were transmitted through an Al filter for

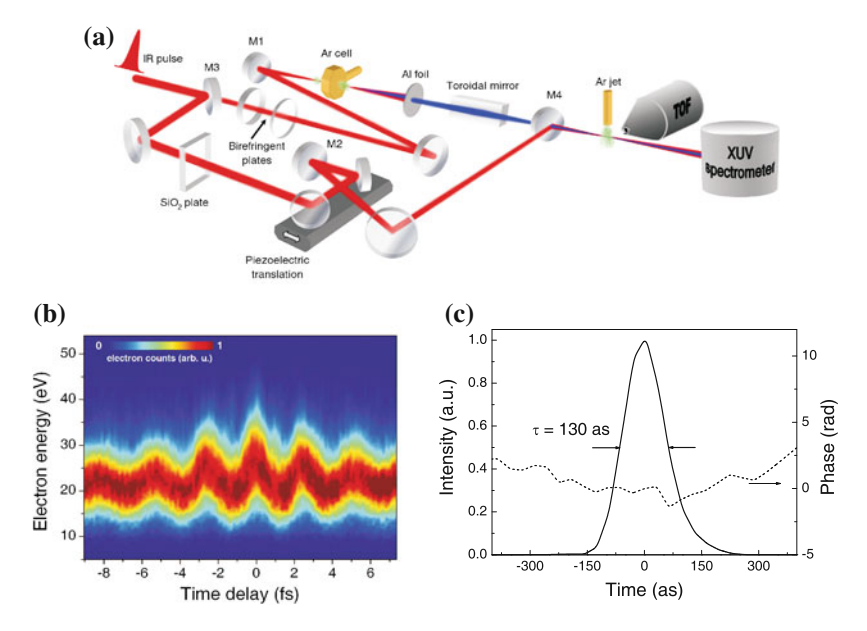


Fig. 6.4 a Experimental setup for the generation and measurement of attosecond pulses, here the isolated attosecond pulse is generated by polarization gating technique. *M1*, *M2* spherical mirrors, *M3*, *M4* drilled mirrors, *TOF* time of flight electron spectrometer. **b** Experimental FROG-CRAB trace; the attosecond pulse and the streaking field come from a 5-fs 800-nm phase-stabilized pulses with modulated polarization state. **c** Reconstruction by PCGPA algorithm of temporal intensity profile and phase of the attosecond pulse from the trace shown in (**b**). Figure adapted from [18]

removing the fundamental IR beam and for dispersion compensation of the intrinsic harmonic chirp. The XUV beam was collinearly recombined with the annular streaking beam in a second drilled mirror. The two beams were focused on a second argon jet for the photo-ionization measurement and the delay was controlled by a piezoelectric translation stage with 1 nm resolution. Photoelectrons were acquired with an acceptance angle of $\pm 2^{\circ}$ around $\theta = 0^{\circ}$, with θ being the angle between the electron momentum and the driving filed polarization direction. The measurement is shown in Fig. 6.4b: as described in Sect. 6.1.2 the vector potential of the streaking pulse produces the periodic oscillation observable in the CRAB trace. The temporal characterization of the attosecond pulse was extracted using the PCGPA: a pulse duration of 130 as corresponding to 1.2 optical cycle of the carrier frequency was measured as shown in Fig. 6.4c. In 2008 the FROG-CRAB technique was exploited for the measurement of isolated attosecond pulses obtained by spectral selection of the HHG cutoff region. In this case the XUV spectrum was generated by sub 1.5-cycle 800-nm laser pulses and it allowed the production of 80 ± 5 as isolated pulses [19].

6.1.5 XUV Non-linear Optics

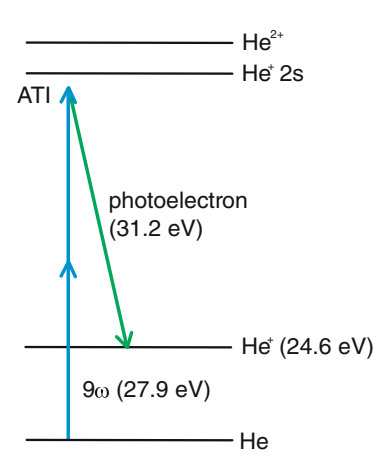
An approach widely followed for the characterization of femtosecond visible or near-infrared pulses is based on nonlinear effects: for instance intensity or interferometric autocorrelation is measured by using second-harmonic generation in nonlinear crystals. Both the most widespread techniques for the complete reconstruction of the laser pulses, FROG [5] and spectral interferometry for direct electric-field reconstruction (SPIDER) [20], are based on nonlinear effects in suitable crystals. However the extension of these methods to attosecond metrology presents some difficulties. The low photon yield of the currently available attosecond sources and the low nonlinear cross-section in the XUV have prevented the application of nonlinear optics in this spectral region so far. Nonlinear processes induced by XUV attosecond pulses unavoidably lead to ionization in the multi-photon regime due to the high photon energy. This is because the XUV field intensity usually does not exceed 10¹⁴ W/cm², which corresponds to a Keldish parameter calculated for argon of $\gamma \simeq 31$ [21]. The photoelectron yield $Y^{(2)}$ for a second-order process, considering an interaction volume V with an atomic density n_a is given by: $\hat{Y}^{(2)} = \sigma^{(2)} F^2 \tau n_a V$. Here $\sigma^{(2)}$ represents the two-photon cross-section, which is of the order of 10^{-49} to 10^{-52} cm⁴ s for excess energies ranging from zero to the ionization energy [22], F is the photon flux and τ is the pulse duration. Indeed from this expression it is clear how the XUV field intensity should exceed 10⁸ W/cm² in order to have a measurable two-photon ionization yield. This explains why the observation of two-photon processes driven by attosecond pulses in the XUV spectral range is a quite critical experimental issue [23].

Nevertheless a number of nonlinear processes have been exploited so far to measure the duration of ultrashort XUV pulses: (i) two-photon above threshold ionization (ATI); (ii) two-photon absorption in atoms; (iii) two-photon double ionization; (iv) Coulomb explosion of diatomic molecules via two-photon double ionization. In 2004 the temporal characterization of the ninth harmonic of 400-nm sub-10-fs driving pulses was obtained by Sekikawa et al. by means of the autocorrelation technique, based on two-photon above-threshold ionization of helium [24, 25].

As shown in the level diagram of Fig. 6.5, the photon energy of the ninth harmonic (27.9 eV) is higher than the first He ionization threshold, while two-photon absorption is below the double ionization threshold. In the process of two-photon ATI a second photon is absorbed in addition to the one required for ionization of the helium atom. In the experiment of Sekikawa et al. two delayed replica of the driving pulse at 400 nm were focused with no spatial overlap into an argon gas jet for high-order harmonic generation. The generated ninth harmonic, spectral filtered by an aluminum foil in order to eliminate the fundamental and low-order harmonics, was focused into an helium gas jet by an Sc/Si multilayer spherical mirror (2 nJ harmonic pulse energy on target). The resulting photoelectrons were collected and resolved in energy by a magnetic bottle photoelectron spectrometer. The number of photoelectrons with energy corresponding to the two-photon ATI peak (at 31.2 eV), measured as a function of the time delay between the two ninth-harmonic pulses, yielded an autocorrelation

124 M. Devetta et al.

Fig. 6.5 Sketch of two-photon above-threshold ionization process in helium

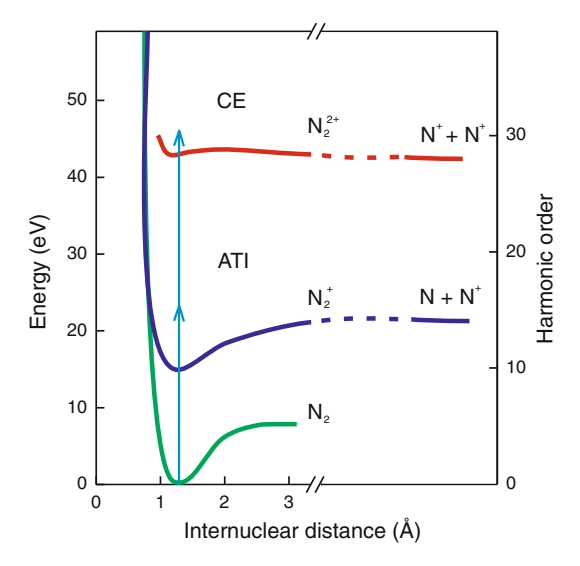


trace, which showed a minimum pulse duration of 950 ± 90 as. In a recent experiment the ninth harmonic pulses at $27.9\,\mathrm{eV}$ have been fully characterized in the temporal domain, i.e. in amplitude and phase, by using FROG based on two-photon ATI in He [26]. The measured shortest pulse duration was 860 as with a flat phase.

Two-photon absorption (TPA) ionization of helium induced by high-order harmonics of a Ti:sapphire laser was firstly observed by Kobayashi et al. in 1998 [27]. Upon acquiring the He⁺ vield induced by two-photon absorption they were able to obtain the autocorrelation trace of the ninth harmonic, which showed a pulse duration of 27 fs. In 2003 the exploitation of the same nonlinear process allowed the first demonstration of an autocorrelation measurement of a train of attosecond pulses, reported by Tzallas et al. [28]. In this experiment, the harmonics from seventh to fifteenth were generated in a xenon jet and transmitted through an indium filter and then injected into a volume autocorrelator. The XUV beam was divided in two parts by means of a split spherical mirror, which focused the two beams in a helium gas jet and allowed to tune the delay τ between the two pulse replica. The He⁺ yield induced by TPA was measured as a function of τ by a time-of-flight mass spectrometer, and provided the second-order autocorrelation signal. A clear attosecond structure is present in the measured ion yield signal which shows a period double with respect to the driving laser field. From this signal it was possible to estimate the average duration of the attosecond pulses in the train, resulting in 780 ± 80 as.

In 2005, two-photon double ionization (TPDI) of He induced by femtosecond harmonic pulses was exploited to detect the autocorrelation trace of the 27th harmonic (42-eV photon energy) of Ti:sapphire laser pulses [29]. Here, a beam separator of silicon-carbide divided into two parts was used for obtaining the two harmonic pulse replicas; one of the two halves of the separator was mounted on a translation unit in order to introduce a controllable delay between the two pulse replicas. In this experiment, the yield of doubly charged helium ions as a function of the delay provided the autocorrelation trace: the shortest measured pulse duration was 8 fs,

Fig. 6.6 Sketch of potential energy curves for N_2 , N_2^+ and N_2^{2+}



with a 24-nJ pulse energy (corresponding to an intensity in the focal point of $1.7 \times 10^{13} \text{ W/cm}^2$). So far TPDI has not been reported in the attosecond regime.

As a last approach, Coulomb explosion of diatomic molecules following twophoton double ionization was recently suggested as a method for measuring the interferometric autocorrelation of an attosecond pulse train [23, 30], due to the larger nonlinear cross section of this process with respect to noble-gas atoms. The experimental apparatus is analogous to the one describe above for TPDI of helium [29]; however, in this case the authors have used N₂ molecules as a target instead of He atoms, and two-photon absorption was triggered by harmonics from the 9th to the 19th. The estimated intensity of the 11th harmonic at the focal point was 3×10^{14} W/cm². A sketch of the energy levels of N₂ molecule and ions relevant for the measurement is shown in Fig. 6.6. The measured time-of-flight mass spectrum exhibits a two-peak structure corresponding to N⁺ ions produced by Coulomb explosion of N_2^{2+} ions induced by two-photon double ionization. This two peaks can be assigned to ions sharing the same kinetic energy release of 5 eV, that are emitted in the forward and backward directions. By integrating the ion yield as a function of the temporal delay between the two XUV pulse replicas, one obtains the interferometric autocorrelation trace of the train of attosecond pulses, which indeed shows bunches with a periodicity twice that of the driving laser field. The estimated duration of the pulse envelope is 320 as full width at half maximum, corresponding to \sim 1.3 optical cycles of the carrier frequency of the 11th harmonic.

126 M. Devetta et al.

6.2 Temporal Characterization of Pulses Generated by FELs

A major problem faced in the characterization of light pulses emitted by Free Electron Lasers, in particular when operated in SASE configuration, comes from the intrinsic jitter in the arrival time of the emitted pulses as well as from fluctuations in their temporal behavior and spectral content. Several approaches have been proposed for the determination of FEL pulse structure and duration; we can group them in two main sets, namely autocorrelation and cross-correlation techniques. In the following we will discuss these two different approaches in detail.

6.2.1 Autocorrelation of XUV FEL Pulses

A standard approach for the determination of the structure and duration of ultrashort laser pulses, that can be applied also to FEL pulses, is based on nonlinear intensity autocorrelation; in this technique the pulse that one wants to analyze is split into two identical replicas which are then focused in a nonlinear medium, whose response is detected as a function of the delay between the two replicas. The average duration of the intensity envelope of the FEL pulse can be afterwards deduced from the delay-dependent autocorrelation trace. The autocorrelation might carry additional information about the temporal coherence of the pulse, which is particularly important for FELs operating in SASE configuration; it is worth noting that information about temporal coherence [32] and spatiotemporal coherence [33, 34] in FEL pulses is also extracted from linear autocorrelation measurements.

Differently from the infrared and visible domains, where transmission beam splitters are available, in the XUV spectral region the two pulse replicas are very often produced by geometrical or wave-front splitting of the measured pulse; for applications to FEL pulses, this splitting has been accomplished by exploiting a grazing incidence Mach–Zehnder geometry [35] or using a splitting multilayer mirror [31]. In the XUV spectral domain, the nonlinear effect exploited for intensity autocorrelation is non-linear non-sequential single or multiple ionization of atoms or molecules; in general, the ionization yield is proportional to I^n , where I is the intensity of the XUV pulse in the target medium and n is the number of absorbed photons.

Several implementation of autocorrelation measurements have been exploited for the characterization of FEL pulses, for instance by two-photon single ionization of helium at a photon energy of 20.45 eV [31], by two-photon double ionization of helium at photon energies of 51.8 eV [36] and 47.0 eV [35], by triple ionization of argon [37] at a photon energy of 28 eV and by four-photon multiple ionization of nitrogen at a photon energy of 38 eV [38]. A common feature in all those measurements is the appearance of a sharp central peak in the temporal trace of the ionization yield (see for instance Fig. 6.7), that is attributed to the pulse longitudinal coherence time.

It is worth noting that the estimation of the average FEL pulse duration requires to perform a numerical modeling taking into account the statistical fluctuations in

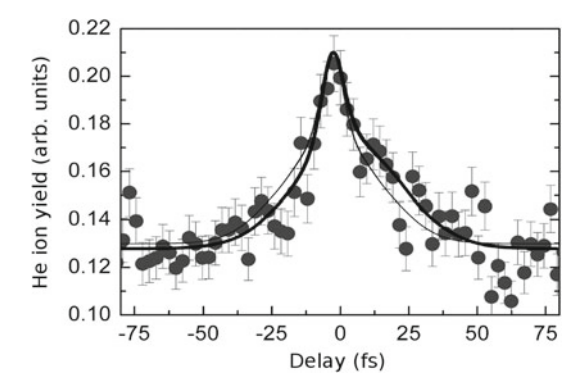


Fig. 6.7 Autocorrelation trace of FEL pulses measured at the Spring-8 Compact SASE Source. *Symbols* experimental He⁺ ion yield plotted as a function of the pump-probe delay using 20.45 eV photons; *thin solid line* theoretical model assuming identical pulse replica taking into account the experimental peak intensity. *Thick solid line* theoretical model including pulse-front tilt. Figure adapted from [31]

the pulse spectrum as well as several additional effects like the pulse front tilt, the focusing geometry inside the autocorrelator and the asymmetry in the energy content of the two arms [31]. The importance of these effects is illustrated in Fig. 6.7, which shows the autocorrelation trace measured at the Spring-8 Compact SASE Source facility emitting XUV pulses with a 20.45 eV photon energy [31], exploiting the two-photon single ionization in helium. The experimental trace (shown as symbols) appears asymmetric; a fit based on the Partial Coherence Method (PCM, [39]) assuming identical pulse replicas (thin solid line) is unable to reproduce the experimental outcome. The inclusion of a modest pulse front tilt allows a better agreement between experiment and numerical modeling; in particular, from the modeling, Moshammer and coworkers estimated an average pulse duration of 28.3 fs FWHM, a longitudinal coherence time of 8.5 fs and a pulse front tilt of about 0.02° [31].

6.2.2 Cross-Correlation Measurements Involving XUV FEL Pulses

Experiments performed at FEL facilities often require the synchronization of the FEL pulse with pulses produced by an independent laser source. In such cases, the temporal resolution achievable in the experiment can be determined by cross-correlation measurements involving the two pulses. Differently from autocorrelation, that is a self-referencing technique not affected by fluctuations in the arrival time of the FEL pulse, cross-correlation measurements severely depend on the relative jitter between the FEL and the auxiliary laser source. Such jitter can amount, in FELs operating in SASE configuration, to hundreds of femtoseconds [40].

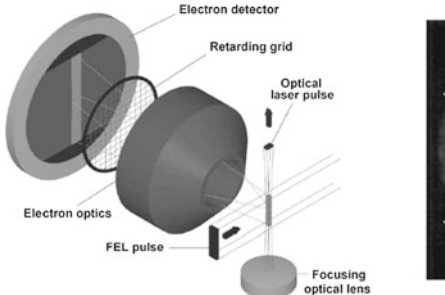
Several techniques have been exploited for determining at the same time the relative jitter and the temporal structure of the FEL pulse; most of them are based

on the detection of photoelectrons generated in a gaseous target by the FEL pulse in presence of an assisting IR light pulse. Two different regimes of interaction can be considered according to the duration of the FEL pulse with respect to the optical cycle of the assisting field: when the FEL pulse duration is much longer than half the optical cycle of the IR pulse, the interaction leads to the so called Laser-Assisted Photoelectric Effect (LAPE) [41] that consists in the absorption or emission of one or more IR photons from electrons ionized by the XUV FEL pulse. These absorption and emission events give rise to sidebands at respectively higher and lower electron kinetic energies with respect to the center of the primary photoelectron spectrum produced by the FEL pulse. The larger is the temporal overlap between the two pulses, the higher is the number as well as the intensity of these sidebands.

On the other hand when the FEL pulse has a duration shorter than half the optical cycle of the assisting pulse, the interaction leads to the so called ponderomotive electron streaking [42]: the assisting field (also called streaking field) leads to a variation of the final electron kinetic energy, which depends on the value of the IR vector potential at the time of ionization. Electrons ionized by the FEL pulse at different times will experience different streaking fields and will carry different kinetic energies; hence there will be a mapping of the temporal domain onto the energy domain that can be suitably exploited for a reconstruction of both the streaking pulse and the FEL pulse.

6.2.2.1 Cross-Correlations Exploiting LAPE

The first attempts of cross-correlations were based on the analysis of sidebands produced in the photoelectron spectra by the interaction of the FEL pulse with a near infrared (IR) femtosecond pulse inside a gaseous target [10, 40]. Cross-correlation based on LAPE can be performed by scanning the delay between the pulses and recording the overall photoelectron spectra [40] or by choosing a proper electron energy region where a sideband appears and acquiring single-shot signals with a



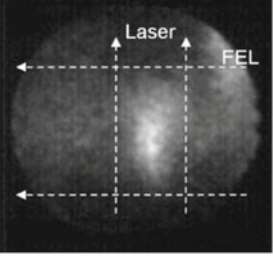


Fig. 6.8 Photoelectrons generated in a gas jet by LAPE produce, by an electron lens system with a high-pass energy filter (shown on the *left*), a two-dimensional image of the FEL-IR pulse cross-correlation (shown on the *right*), thereby mapping time onto a space coordinate. In this way, information about pulse duration and relative timing between the pulses can be obtained without a delay scan. Figure adapted from [10]

position sensitive electron energy spectrometer [10]. The former approach allows to monitor all sideband orders, hence it is more sensitive to the relative delay between FEL and IR pulses; however it is intrinsically a multi-shot measurement, thus it can provide only a statistical information about the pulse durations and/or the delay jitter.

On the other hand, the second approach allows in principle a single-shot acquisition. Figure 6.8 shows the setup of a proof-of-principle experiment performed by Cunovic and coworkers at the free-electron laser in Hamburg (FLASH) [10]: the FEL and the IR beams cross at a right angle inside a Kr gas jet; a suitable electron imaging system translates the position-dependent sideband signal into a cross-correlation in the temporal domain. The authors found a temporal width of the detected signal of about 1.9 ps. This outcome is the convolution among the experimental time window, the jitter between the two pulses and their pulse widths. Taking into account the much shorter durations of the pulses (estimated as 30 fs for the FEL pulse and 150 fs for the IR pulse), it was inferred that the measured temporal width was almost completely ascribed to the FEL jitter.

6.2.2.2 Cross-Correlations Based on Photoelectron Streaking

Photoelectron streaking is nowadays a fundamental tool for measuring attosecond XUV pulses [42]. Attosecond technology exploits near-IR streaking fields (typically at 800 nm), since the streaking optical cycle is in such a case much longer than the duration of the measured XUV pulse. Photoelectron streaking can be in principle applied also to the characterization of XUV FEL pulses; however the duration of

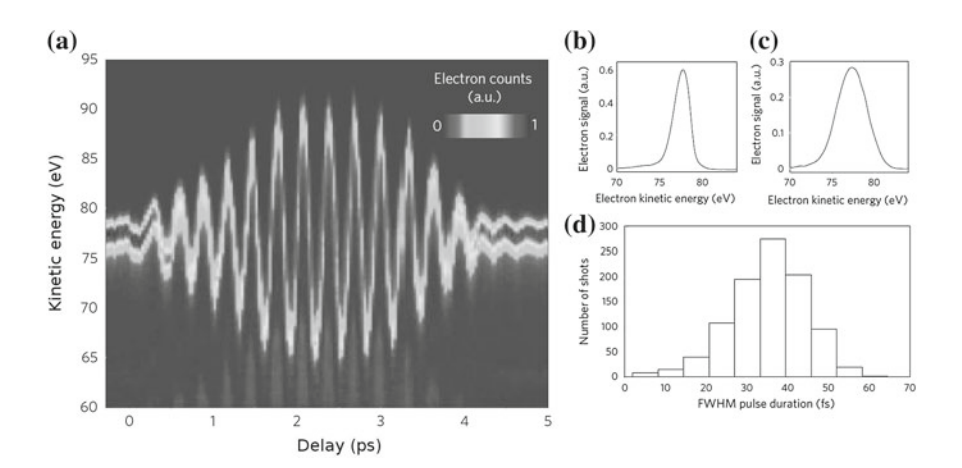


Fig. 6.9 a Streaked photoelectron energy spectra generated in krypton by 13.5-nm FEL pulses in presence of 92-μm THz pulses as a function of the delay. **b**, **c** Photoelectron spectra measured **b** perpendicularly and **c** within the polarization plane of the THz streaking field. **d** Distribution of FEL pulse durations (FWHM) retrieved over 1000 FEL shots assuming gaussian temporal pulse shape. Figures adapted from [43]

these pulses is in the order of tens of femtoseconds, thus requiring streaking fields with an optical cycle two orders of magnitude longer than that of near-IR fields. In a pioneering experiment performed at the FLASH facility, Frühling and coworkers have shown that terahertz (THz) pulses with central wavelength around 100 µm can be exploited for the characterization of FEL pulses by a streaking technique [43]. Figure 6.9 (panel a) shows a sequence of photoelectron energy spectra obtained in a krypton gas jet by the interaction of 13.5-nm FEL pulses with 92-µm THz pulses as a function of temporal delay. It is worth noting that the THz pulses were generated in a dedicated undulator line exploiting the same electron bunch used for XUV pulse emission, hence the two pulses were synchronized [43]. As clearly visible from the figure, the streaking effect is noticeable in spite of the low peak intensity (about $3 \times 10^8 \text{ W/cm}^2$) of the THz field, since the ponderomotive potential of the streaking field is proportional to the square of the streaking wavelength [43]. The streaking effect can be also seen by comparing the photoelectron spectra acquired in the direction perpendicular (panel b) and parallel (panel c) to the polarization direction of the THz field; the former corresponds to the soft X-ray spectrum shifted by the krypton ionization potential, whereas the latter shows the spectral broadening induced by the streaking field in correspondence of the zero crossing of the THz vector potential [43].

A suitable elaboration of the measured streaked spectra allowed to retrieve the statistical distribution of FEL pulse durations over 1000 shots (see panel d in Fig. 6.9), which was found to be 35 ± 7 fs FWHM.

Although the approach exploited in [43] can be successfully used for the FEL pulse characterization, it does not provide any information about the jitter in the arrival time of the pulse, since the streaking field is intrinsically synchronized to it. Tavella et al. showed that the jitter in the arrival time of the FEL pulse with respect to a reference Ti:Sapphire laser pulse can be monitored by single shot measurements of the parasitic THz emission from the electron bunch; the THz emission was characterized in time domain by a single-shot version of electro-optic sampling (EOS) based on the reference laser [45]. In a subsequent experiment performed at FLASH,

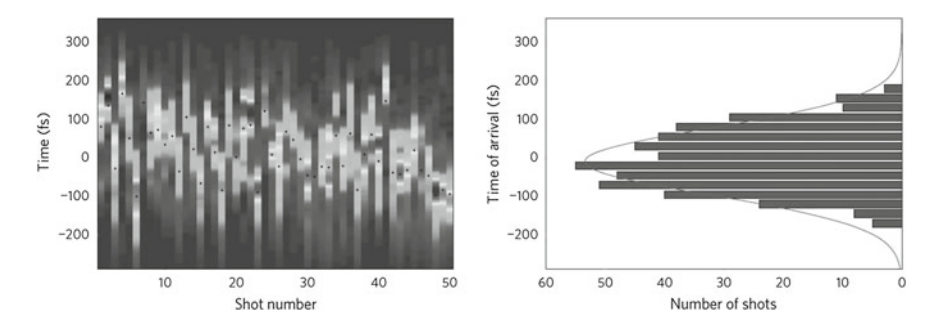


Fig. 6.10 Left panel 50 consecutive single-shot FEL pulse measurements. Right panel Distribution of arrival times determined over about 450 shots; the distribution has a width of about 87 fs r.m.s. Figures adapted from [44]

Grguraš et al. showed that THz streaking can be used for both measuring the temporal profile and the arrival time of the FEL pulses on a single-shot basis [44]. They generated the THz pulses by optical rectification of 3-mJ, 50-fs pulses produced by a Ti:Sapphire laser; this approach provides very stable THz emission, which was independently characterized by electro-optical sampling exploiting a small portion of the same Ti:Sapphire beam [44]. Single-shot photoelectron spectra were detected in a helium gas jet upon the interaction with 10- μ J, 258-eV FEL pulses; the single-cycle streaking field (2-ps temporal duration, energy of about 4 μ J) was centered around 0.6 THz. Left panel in Fig. 6.10 shows a set of 50 consecutive single-shot FEL pulse measurements retrieved after the THz streaking field was taken into account; a distribution of FEL pulse arrival times, determined over 450 shots, is shown in the right panel of the same figure. The authors found that the distribution of arrival times measured from the retrieved FEL pulse measurements has a width of about 87 fs r.m.s.

6.2.2.3 Optical Cross-Correlations

Cross-correlation measurements based on electron detection require a dedicated electron spectrometer in high vacuum conditions and are limited by space charge effects; optical cross-correlation methods would not be limited by these requirements. In this framework, a different approach for the characterization of XUV-IR cross-correlation has been demonstrated by Gahl and coworkers at FLASH [46]; a 39.5 ± 0.5 eV pulse generated by the FEL impinged on a clean and undoped GaAs(100) surface. The optical reflectivity of the sample was probed by a delayed 800-nm laser pulse (or by its second harmonic) with a temporal duration FWHM of about 120-150 fs. The excitation of the sample induced by the FEL pulse leads to a dramatic change in the reflectivity, in particular to a drop that recovers in few picoseconds.

This behavior is illustrated in Fig. 6.11, which shows the distribution of transient reflectivity changes induced in the GaAs sample as a function of the nominal delay between the FEL and the IR pulses, acquired on a very large number of shots. Gahl and coworkers found that very different statistical distributions of the signal are found at different nominal delays and, in particular, detection of the reflectivity changes around the nominal zero delay allows to efficiently monitor the temporal jitter between the two pulses.

The approach demonstrated in [46] was soon improved to the single-shot regime by Maltezopoulos et al. by exploiting the same working principle, but with unfocused pump and probe beam impinging on the GaAs surface [47]. The FLASH (at $28\,\mathrm{nm}$) and the probe (at $400\,\mathrm{nm}$) beams, forming a right angle, were overlapped on the target; the probe light reflected from the semiconductor surface was in this case imaged onto a bidimensional detector. It is worth noting that different positions along the target surface correspond to different delays between the two pulses. Since the FEL pulse reduces the reflectivity of GaAs, the onset of the reflectivity change imprinted on the probe beam can be used to directly map the delay between the FEL and the probe pulse [47]. Using this approach, the authors found a delay jitter of about $\pm 250\,\mathrm{fs}$

M. Devetta et al.

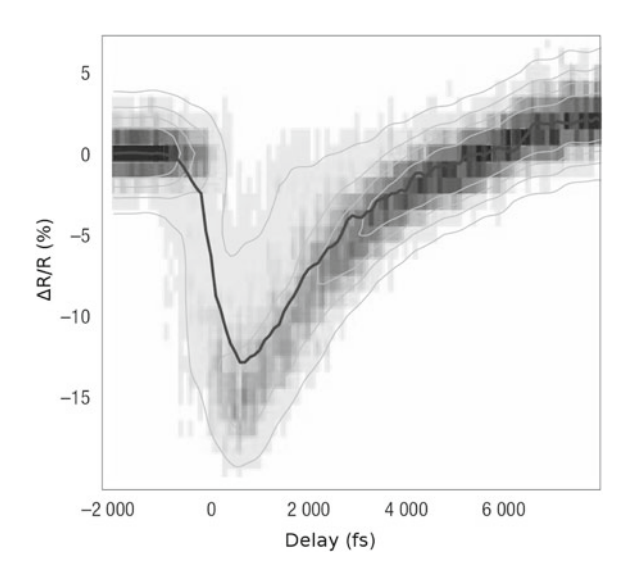
r.m.s. between the FEL and the 400-nm laser pulse. The single-shot implementation of the optical cross-correlation technique has been also successfully exploited at higher photon energies at the Linac Coherent Light Source (LCLS) [48, 49].

A different approach for the optical cross-correlation of FEL and IR pulses has been proposed by Bionta et al. and implemented again at LCLS [50]: the 1-keV FEL pulse was collinearly combined with a visible probe pulse having a continuum spectrum spanning the 500–900 nm spectral region. The visible pulse was chirped by propagation inside glass blocks up to a temporal duration of about 3 ps. The two pulses were then sent through a 500-nm thick membrane of Si₃N₄. The FEL pulses created free carriers via photo-ionization of core electrons, which altered the optical properties of the membrane. The chirped continuum pulse probed the transient changes in optical transmission. These changes were imprinted in the transmitted probe spectrum and measured by a spectrometer. It is worth noting that the chirped nature of the pulse allows a temporal to spectral mapping, which has been exploited for reconstructing the arrival time of the FEL pulse with respect to the probe one. The authors found a natural jitter in the arrival time of the FEL pulse of about 180 fs r.m.s. [50].

6.3 Conclusions

In this chapter we have reviewed several methods for the temporal characterization of XUV and X-ray pulses on the femtosecond and attosecond time scales. In particular in the first section we have considered isolated attosecond pulses and attosecond pulse trains generated by high order harmonic emission. In the second section we focused on the measurement of femtosecond soft X-ray pulses produced by free

Fig. 6.11 Distribution of transient reflectivity changes induced in GaAs by 39.5-eV pulses generated at FLASH and probed by 800-nm laser pulses; the *thick solid line* shows the average reflectivity change. Figure adapted from [46]



electron lasers. Indeed, both these pulse sources represent nowadays cutting edge tools for time-resolved experiments in atomic and molecular physics, which require a reliable temporal characterization of the exploited source.

Acknowledgments We acknowledge financial support from the European Research Council under the European Community's Seventh Framework Programme (FP7/2007-2013)/ERC grant agreement n.307964-UDYNI and Contract no. 228334 JRA-INREX (Laserlab Europe III) and from the Italian Ministry of Research and Education (ELI project—ESFRI Roadmap).

References

- 1. I.A. Walmsley, V. Wong, J. Opt. Soc. Am. B 13, 2453 (1996)
- 2. Y. Mairesse, F. Quéré, Phys. Rev. A **71**, 011401 (2005)
- 3. F. Quere, Y. Mairesse, J. Itatani, J. Mod. Opt. **52**, 339 (2005)
- M. Lewenstein, P. Balcou, M.Y. Ivanov, A. L'Huillier, P.B. Corkum, Phys. Rev. A 49(3), 2117 (1994)
- 5. R. Trebino, Frequency-Resolved Optical Gating: The Measurement of Ultrashort Laser Pulses (Kluwer Academic Publishers, Boston, 2000)
- 6. D. Kane, IEEE, J. Sel. Top. Quantum Electron. 35, 421 (1999)
- J. Itatani, F. Quere, G.L. Yudin, M.Y. Ivanov, F. Krausz, P.B. Corkum, Phys. Rev. Lett. 88, 173903 (2002)
- 8. P. Paul, E. Toma, P. Breger, G. Mullot, F. Augé, P. Balcou, H. Muller, P. Agostini, Science 292, 1689 (2001)
- 9. H.G. Muller, Appl. Phys. B **74**, S17 (2002)
- S. Cunovic, N. Muller, R. Kalms, M. Krikunova, M. Wieland, M. Drescher, T. Maltezopoulos, U. Fruhling, H. Redlin, E. Plonjes-Palm, J. Feldhaus, Appl. Phys. Lett. 90, 121112 (2007)
- R. López-Martens, K. Varjú, P. Johnsson, J. Mauritsson, Y. Mairesse, P. Salières, M.B. Gaarde, K.J. Schafer, A. Persson, S. Svanberg, C.G. Wahlström, A. L'Huillier, Phys. Rev. Lett. 94, 033001 (2005)
- E. Gustafsson, T. Ruchon, M. Swoboda, T. Remetter, E. Pourtal, R. López-Martens, P. Balcou, A. L'Huillier, Opt. Lett. 32, 1353 (2007)
- Y. Mairesse, A. de Bohan, L.J. Frasinski, H. Merdji, L.C. Dinu, P. Monchicourt, P. Breger, M. Kovačev, R. Taieb, B. Carré, H.G. Muller, P. Agostini, P. Salières, Science 302, 1540 (2003)
- 14. K.T. Kim, C.M. Kim, M.G. Baik, G. Umesh, C.H. Nam, Phys. Rev. A 69, 051805(R) (2004)
- M. Hentschel, R. Kienberger, C. Spielmann, G. Reider, N. Milosevic, T. Brabec, P. Corkum, U. Heinzmann, M. Drescher, F. Krausz, Nature 414, 509 (2001)
- M. Drescher, M. Hentschel, R. Kienberger, G. Tempea, C. Spielmann, G.A. Reider, P.B. Corkum, F. Krausz, Science 291, 1923 (2001)
- R. Kienberger, E. Goulielmakis, M. Uiberacker, A. Baltuška, V. Yakovlev, F. Bammer, A. Scrinzi, T. Westerwalbesloh, U. Kleineberg, U. Heinzmann, M. Drescher, F. Krausz, Nature 427, 817 (2004)
- G. Sansone, E. Benedetti, F. Calegari, C. Vozzi, L. Avaldi, R. Flammini, L. Poletto, P. Villoresi,
 C. Altucci, R. Velotta, S. Stagira, S. De Silvestri, M. Nisoli, Science 314, 443 (2006)
- E. Goulielmakis, M. Schultze, M. Hofstetter, V.S. Yakovlev, J. Gagnon, M. Uiberacker, A.L. Aquila, E.M. Gullikson, D.T. Attwood, R. Kienberger, F. Krausz, U. Kleineberg, Science 320, 1614 (2008)
- 20. C. Iaconis, I.A. Walmsley, Opt. Lett. 23, 792 (1998)
- 21. L. Keldysh, Sov. Phys. JETP **20**, 1307 (1965)
- 22. L.A.A. Nikolopoulos, P. Lambropoulos, J. Phys. B: At. Mol. Opt. Phys. 34, 545 (2001)
- 23. K. Midorikawa, Y. Nabekawa, A. Suda, Prog. Quantum Electron. 32, 43 (2008)

M. Devetta et al.

- 24. T. Sekikawa, A. Kosuge, T. Kanai, S. Watanabe, Nature **432**, 605 (2004)
- N. Miyamoto, M. Kamei, D. Yoshitomi, T. Kanai, T. Sekikawa, T. Nakajima, S. Watanabe, Phys. Rev. Lett. 93, 083903 (2004)
- A. Kosuge, T. Sekikawa, X. Zhou, T. Kanai, S. Adachi, S. Watanabe, Phys. Rev. Lett. 97, 263901 (2006)
- 27. Y. Kobayashi, T. Sekikawa, Y. Nabekawa, S. Watanabe, Opt. Lett. 23, 64 (1998)
- 28. P. Tzallas, D. Charalambidis, N. Papadogiannis, K. Witte, G. Tsakiris, Nature 426, 267 (2003)
- 29. Y. Nabekawa, H. Hasegawa, E.J. Takahashi, K. Midorikawa, Phys. Rev. Lett. 94, 043001 (2005)
- Y. Nabekawa, T. Shimizu, T. Okino, K. Furusawa, H. Hasegawa, K. Yamanouchi, K. Midorikawa, Phys. Rev. Lett. 97, 153904 (2006)
- R. Moshammer, T. Pfeifer, A. Rudenko, Y.H. Jiang, L. Foucar, M. Kurka, K.U. Kühnel, C.D. Schröter, J. Ullrich, O. Herrwerth, M.F. Kling, X.J. Liu, K. Motomura, H. Fukuzawa, A. Yamada, K. Ueda, K.L. Ishikawa, K. Nagaya, H. Iwayama, A. Sugishima, Y. Mizoguchi, S. Yase, M. Yao, N. Saito, A. Belkacem, M. Nagasono, A. Higashiya, M. Yabashi, T. Ishikawa, H. Ohashi, H. Kimura, T. Togashi, Opt. Express 19, 21698 (2011)
- 32. W.F. Schlotter, F. Sorgenfrei, T. Beeck, M. Beye, S. Gieschen, H. Meyer, M. Nagasono, A. Föhlisch, W. Wurth, Opt. Lett. **35**, 372 (2010)
- R. Mitzner, B. Siemer, M. Neeb, T. Noll, F. Siewert, S. Roling, M. Rutkowski, A.A. Sorokin, M. Richter, P. Juranic, K. Tiedtke, J. Feldhaus, W. Eberhardt, H. Zacharias, Opt. Express 16, 19909 (2008)
- A. Singer, F. Sorgenfrei, A.P. Mancuso, N. Gerasimova, O.M. Yefanov, J. Gulden, T. Gorniak,
 T. Senkbeil, A. Sakdinawat, Y. Liu, D. Attwood, S. Dziarzhytski, D.D. Mai, R. Treusch, E. Weckert, T. Salditt, A. Rosenhahn, W. Wurth, I.A. Vartanyants, Opt. Express 20, 17480 (2012)
- 35. F. Sorgenfrei, W.F. Schlotter, T. Beeck, M. Nagasono, S. Gieschen, H. Meyer, A. Fohlisch, M. Beye, W. Wurth, Rev. Sci. Instrum. **81**, 043107 (2010)
- R. Mitzner, A.A. Sorokin, B. Siemer, S. Roling, M. Rutkowski, H. Zacharias, M. Neeb, T. Noll, F. Siewert, W. Eberhardt, M. Richter, P. Juranic, K. Tiedtke, J. Feldhaus, Phys. Rev. A 80, 025402 (2009)
- A. Senftleben, T. Pfeifer, Y.H. Jiang, A. Rudenko, O. Herrwerth, L. Foucar, M. Kurka, K.U. Kühnel, M. Kübel, M.F. Kling, A. Yamada, K. Motomura, K. Ueda, S. Düsterer, R. Treusch, C.D. Schröter, R. Moshammer, J. Ullrich, J. Phys.: Conf. Ser. 388, 032011 (2012)
- 38. Y.H. Jiang, T. Pfeifer, A. Rudenko, O. Herrwerth, L. Foucar, M. Kurka, K.U. Kühnel, M. Lezius, M.F. Kling, X. Liu, K. Ueda, S. Düsterer, R. Treusch, C.D. Schröter, R. Moshammer, J. Ullrich, Phys. Rev. A 82, 041403 (2010)
- 39. T. Pfeifer, Y. Jiang, S. Düsterer, R. Moshammer, J. Ullrich, Opt. Lett. 35, 3441 (2010)
- P. Radcliffe, S. Dusterer, A. Azima, H. Redlin, J. Feldhaus, J. Dardis, K. Kavanagh, H. Luna, J.P. Gutierrez, P. Yeates, E.T. Kennedy, J.T. Costello, A. Delserieys, C.L.S. Lewis, R. Taieb, A. Maquet, D. Cubaynes, M. Meyer, Appl. Phys. Lett. 90, 131108 (2007)
- 41. T.E. Glover, R.W. Schoenlein, A.H. Chin, C.V. Shank, Phys. Rev. Lett. 76, 2468 (1996)
- 42. F. Krausz, M. Ivanov, Rev. Mod. Phys. 81(1), 163 (2009)
- 43. U. Fruhling, M. Wieland, M. Gensch, T. Gebert, B. Schutte, M. Krikunova, R. Kalms, F. Budzyn, O. Grimm, J. Rossbach, E. Plonjes, M. Drescher, Nat. Photon. 3, 523 (2009)
- 44. I. Grguras, A.R. Maier, C. Behrens, T. Mazza, T.J. Kelly, P. Radcliffe, S. Dusterer, A.K. Kazansky, N.M. Kabachnik, T. Tschentscher, J.T. Costello, M. Meyer, M.C. Hoffmann, H. Schlarb, A.L. Cavalieri, Nat. Photon. 6, 851 (2012)
- 45. F. Tavella, N. Stojanovic, G. Geloni, M. Gensch, Nat. Photon. 5, 162 (2011)
- C. Gahl, A. Azima, M. Beye, M. Deppe, K. Dobrich, U. Hasslinger, F. Hennies, A. Melnikov, M. Nagasono, A. Pietzsch, M. Wolf, W. Wurth, A. Fohlisch, Nat. Photon. 2, 165 (2008)
- 47. T. Maltezopoulos, S. Cunovic, M. Wieland, M. Beye, A. Azima, H. Redlin, M. Krikunova, R. Kalms, U. Frühling, F. Budzyn, W. Wurth, A. Föhlisch, M. Drescher, New J. Phys. **10**(3), 033026 (2008)
- S. Schorb, T. Gorkhover, J.P. Cryan, J.M. Glownia, M.R. Bionta, R.N. Coffee, B. Erk, R. Boll, C. Schmidt, D. Rolles, A. Rudenko, A. Rouzee, M. Swiggers, S. Carron, J.C. Castagna, J.D. Bozek, M. Messerschmidt, W.F. Schlotter, C. Bostedt, Appl. Phys. Lett. 100(12), 121107 (2012)

- M. Beye, O. Krupin, G. Hays, A.H. Reid, D. Rupp, S. de Jong, S. Lee, W.S. Lee, Y.D. Chuang,
 R. Coffee, J.P. Cryan, J.M. Glownia, A. Fohlisch, M.R. Holmes, A.R. Fry, W.E. White, C.
 Bostedt, A.O. Scherz, H.A. Durr, W.F. Schlotter, Appl. Phys. Lett. 100(12), 121108 (2012)
- M.R. Bionta, H.T. Lemke, J.P. Cryan, J.M. Glownia, C. Bostedt, M. Cammarata, J.C. Castagna, Y. Ding, D.M. Fritz, A.R. Fry, J. Krzywinski, M. Messerschmidt, S. Schorb, M.L. Swiggers, R.N. Coffee, Opt. Express 19(22), 21855 (2011)

Chapter 7 Optical Metrology—On the Inspection of Ultra-Precise FEL-Optics

Frank Siewert

Abstract Dedicated instrumentation is required to inspect the quality of optical elements like mirrors or gratings used in grazing incidence condition at FEL-beamlines. Comparing the quality of optical elements available with the advent of 3rd generation storage rings two decades ago to the state of the art of today an improvement by one order of magnitude in terms of figure error has been achieved. These achievements were mainly possible by improvements on deterministic surface finishing as well as by new developments on the field of metrology. This chapter will give an overview and description of the state of the art ex-situ metrology applied to measure synchrotron optical components.

7.1 Introduction

Mirrors and gratings of outmost precision used in grazing incidence are essential to collimate or focus synchrotron light or to provide monochromatic light of high spectral purity in synchrotron radiation (SR) beamlines. Optical elements for application at Free Electron Lasers (FEL) represent in some cases like for the European-XFEL [1] the most challenging pieces of X-ray optical elements of today. The precise characterization of such optics is fundamental to ensure the wave-front and coherence preserving transport of photons from its source in the undulator section of the FEL to the experimental station. Problems related to Bremsstrahlung and heat-load will cause significant deformation of shape, mainly on the first mirrors. This leads the beamline design to place the first mirrors in a large distance to the undulators also to avoid the optics to be damaged. Beamlines at VUV-FEL's like at the FLASH [2] or FERMI [3] usually have a length of 100 to 150 m. In case of the European-XFEL the beamline e.g. to serve the SPB-experiment will have a length of about 932 m [4].

F. Siewert (⊠)

Helmholtz Zentrum Berlin—Elektronenspeicherring BESSY-II, Institut für Nanometer Optik und Technologie, Albert-Einstein-Str. 15, 12489 Berlin, Germany

e-mail: frank.siewert@helmholtz-berlin.de

Optical elements at such beamlines are in use under extreme shallow incidence angles of a few mrad only (e.g. $4\pm0.04\,\mathrm{mrad}$ as designed for the focusing mirrors of the SPB-experiment at European-XFEL). This leads to large aperture sizes in meridional direction. Thus such mirrors will have a length up to $1000\,\mathrm{mm}$ and are characterized by a residual slope error of $50\,\mathrm{nrad}$ rms corresponding to a $2\,\mathrm{nm}$ pv residual figure error [5]. It is noted here that in case of some elliptical cylinder shaped focusing mirrors of $1000\,\mathrm{mm}$ length a residual slope error of $20\,\mathrm{nrad}$ rms is under discussion [4]. Finally these delicate optical elements have to be clamped in a shape preserving way. This chapter will mainly discuss the most critical part in ex-situ metrology for SR-optics the characterization of the long spatial figure error part the so called "slope error".

7.2 Slope Error and Micro-Roughness

Dedicated expertise and instrumentation have been established in the synchrotron community to measure the critical characteristics of high performance optical elements. Better knowledge describing the shape of an optical element enables optimizing the optics by applying deterministic surface finishing techniques like ion beam figuring (IBF) [6], computer aided polishing (CAP) [7] and elastic emission machining (EEM) [8]. Metrology data allows a better modeling, optimization and, in the final analysis, improved performance of X-ray optical systems. The quality of reflective optical elements can be described by their deviation from ideal shape at different spatial frequencies. Usually one distinguishes between the figure error, the low spatial error part ranging from aperture length to 1 mm frequencies, and the midand high spatial error part from 1 mm to 1 \mu m and from 1 \mu m to some 10 nm spatial frequencies respectively [9, 10]. In case of extreme sized beamlines up to a length of one kilometer with extreme shallow angle of incidence these ranges of shape error are shifting. It is assumed that the low spatial error part (slope error) of a 1000 mm long focusing mirror at the SPB-experiment at the European-XFEL will range from aperture length to about 10 mm. Corresponding to this the mid- and high spatial error part will follow this tendency and shift to 10 mm to 2 µm for the mid-spatial- and 2 μm to 20 nm for the high-spatial error part [4]. While the figure error will affect the imaging properties [11] of the system the higher spatial frequency errors will cause light to be deflected or scattered away from the spectral image [12, 13]. Figure 7.1 shows a 2-theta scan taken on a super-polished silicon substrate at 124eV for 5° angle of incidence [14]. The spectral reflection peak as well as the small and white angle scatter contribution is clearly identified.

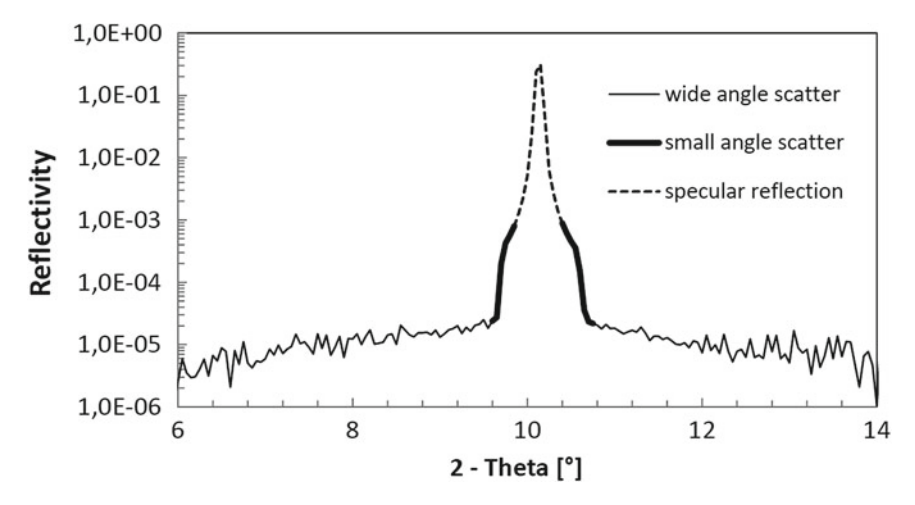


Fig. 7.1 2-Theta scan on a super-polished sample of single crystal silicon. The measurement was performed at the Optics-beamline at the BESSY-II synchrotron in Berlin [15]. The sample shows a micro-roughness of $S_q=0.06\,\mathrm{nm}$ rms as measured by used of a WLI magnification $20\times$ and $S_q=0.28\,\mathrm{nm}$ rms as measured by use of an AFM. Courtesy of S. Kuenstner and F. Schäfers (HZB)

The quantitative description of the surface errors of a reflecting optical element can be statistically interpreted in terms of the power spectral density function, PSD, and summarized as the slope error and the surface roughness. Based on Kirchhoff's theory of diffraction, Church and Takacs [16, 17] have developed a model to describe this (see also [18, 19]). The natural "system coherence length", W, is given by

$$W = \sqrt{2} \frac{\lambda}{\Theta \cos \theta_i} \tag{7.1}$$

with Θ as the angular radius of the system image (customer given), θ_i is the angle of incidence relative to the mirror plane and λ is the operating wavelength. W is approximately the length of the used aperture of the mirror of overall length L.

One can assume that the influence of the mirror errors on the image quality can be described by the on-axis Strehl factor for the grazing incidence case: 7.3 [17]. The on-axis Strehl factor

$$\frac{I(0)}{I_0(0)} \tag{7.2}$$

is given as the ratio of the on-axis intensity in the presence of real surface errors to its value for zero errors. For the grazing incidence case can be written for the Strehl ratio [17]:

$$\frac{I(0)}{I_0(0)} \approx 1 - \frac{8}{\Theta^2} \delta^2 - \left(\frac{4\pi}{\lambda} \cos \theta_i\right)^2 \sigma^2 \tag{7.3}$$

140 F. Siewert

where δ and σ are the bandwidth limited values of the rms values of the slope error (δ) and the roughness (σ) given by

$$\delta^2 = (2\pi)^2 \int_{1/L}^{1/W} df_x S_1(f_x) f_x^2$$
 [2]

and

$$\sigma^{2} = \int_{1/W}^{1/\lambda} df_{x} S_{1}(f_{x}).$$
 [2]

 $S_1(f_x)$ is the profile spectrum of the surface under test (SUT).

It is noted here that a Strehl ratio of 0.8 or larger is generally accepted within the X-ray-community as the indication for a high quality performing optical system in FEL-beamline application [20] and is corresponding to a rms wave front distortion of $\langle \lambda/14 \rangle$ known as the Maréchal criterion.

The surface roughness can be measured using an interferometric microscope (often referred to as with light interferometer (WLI)) for the mid spatial figure error or atomic force microscope (AFM) to measure the high-spatial figure error. The atomic force microscope (often referred to as scanning force microscope) is also used to inspect the grating profile, the ratio of lines and spaces as well as the groove roughness of diffractive optical elements like gratings of reflective zone plates. These instruments are commercial available and have been described in the literature widely [21, 22].

To inspect the slope error, a different measuring technique is used: interferometry or various types of surface profilers. The use of an interferometer, to inspect optical components, requires a reference of complementary shape and excellent quality. Due to the fact that many of the necessary optical components are of aspherical shape and are designed individually for each SR-beamline, such reference objects would cause an extraordinary expense for the metrology. In addition, the quality of the references used limits the accuracy of the result of the metrology. Because of the flat (grazing) angles used in SR-beamlines, synchrotron mirrors may have a length of up to 1 m and more and have a large ratio of length to width. Thus, basic conditions have lead to the idea of inspecting the shape of optical elements in the long dimension by slope measurement. A few slope measuring instruments have been developed during the last 25 years, foremost among them, the Long Trace Profiler (LTP) [23–25], the Nanometer Optical Component Measuring Machine (NOM) [26-33] and the Extended Shear Angle Difference Method (ESAD) [34, 35]. These methods are based on the principle of direct measurement of slope deviation and curvature and, in contrast to other methods, yield results without the need for a reference. The measurement result is directly traced back to SI1 base units angle and length. The measurement is a noncontact scan by using a laser source to create a measurement beam. Depending on the angular acceptance of the instrument, it is possible to measure the geometry of any

¹SI—is the International System of Units

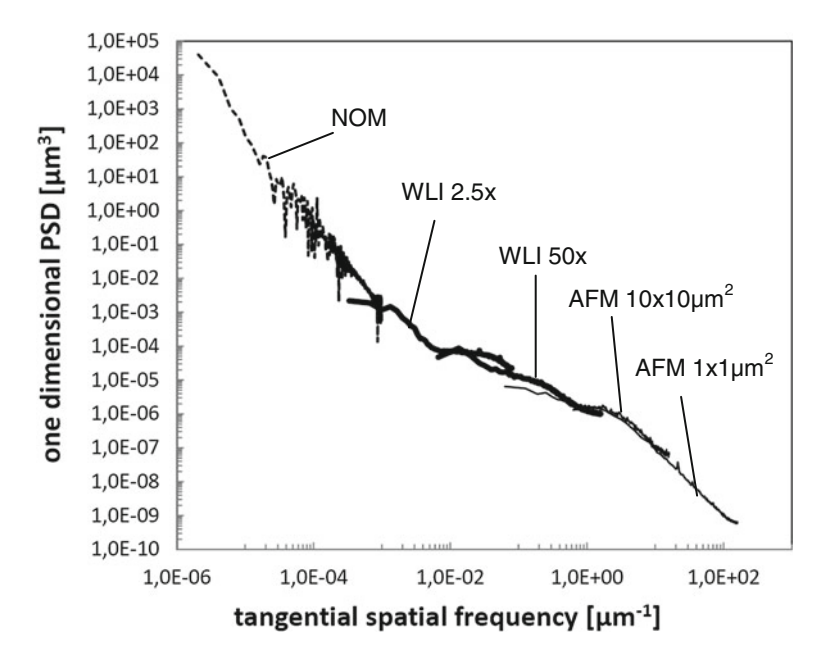


Fig. 7.2 Different measuring instruments cover different ranges of spatial frequency. Tangential 1D PSD spectra obtained with the BESSY-II-NOM, the Micromap WLI $(2.5\times,50\times)$ and the Atomic Force Microscope (AFM) on $10\times10\,\mu\text{m}^2$ and $1\times1\,\mu\text{m}^2$

reflective surface. Figure 7.2 shows the range of spatial frequencies to be inspected by using different metrological instruments. In the case shown, a beam distribution flat mirror for FLASH made of a polished silicon single crystal and coated with amorphous Carbon (a-C) was investigated using different measuring techniques over a spatial frequency range from $\sim 10^{-6}$ to $10^2 \, \mu m^{-1}$.

7.2.1 The Principle of Slope Measurement

To measure the shape of an optical element a test beam from a laser source is reflected from the surface under test (SUT). The relative position after reflection from the SUT is determined by the local shape and is detected on a sensor. The reflection of a test beam from a mirror along the axis of the instrument will depend on the angle, θ , of the mirror's normal with respect to the propagation direction of the laser beam [36, 37]. Figure 7.3 shows the measurement principle of a scanning penta prism set up as realized for the BESSY-NOM system. The 45° double reflection of the measurement beam prevent the pitch-error of the carriage to contribute as 1st error to the error budget of the measurement. To avoid beam distortion caused by inhomogeneity of glass the bulk penta prism is substituted by a 45° double mirror set up. These

142 F. Siewert

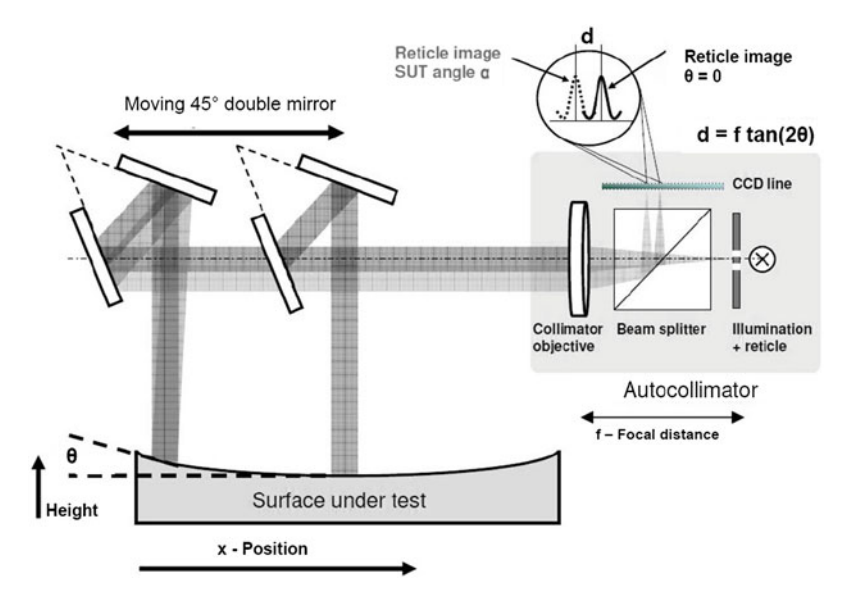


Fig. 7.3 Principle set-up of a scanning mirror based penta prism like slope measuring profiler with an autocollimator detector

mirrors are super-polished with a micro-roughness of 0.1 nm rms (as measured with a WLI) and have a flatness of $\lambda/100$ in the mounted state. The slope δ is

$$\delta(x) = \tan \theta = dy/dx \tag{7.6}$$

Figure 7.4 shows the slope profile and the corresponding profile of height for an ellipsoidal focusing mirror installed at beamline BL3 at FLASH [38] measured by use of a NOM. What is detected in the sensor is the change from one position x on the SUT to the next position $x + \Delta x$. From these data the height profile can be obtained by spatial integration of the slope function $\delta(x)$ over the abscissa x, see also Fig. 7.5. The height $h(x_k)$ function is given by

$$h(x_k) = h(x_0) + \sum_{m=1}^k \frac{dx}{2} \left[\delta(x_m) + \delta(x_{m-1}) \right]$$
 (7.7)

Applying improved integration algorithms such as spline interpolation became an option to handle more noisy data as well [39]. At least the point of interest is the relative slope along the line of inspection. Thus the residual figure/slope error is obtained by subtracting the desired shape profile for the theoretically perfect geometry from the raw slope data. In the shown case the residual figure error is gained by subtraction of an ideal elliptical profile, see Fig. 7.5. Figure 7.5 shows to the upstream and downstream mirror edges a typical "roll on roll off" indicating the aperture of

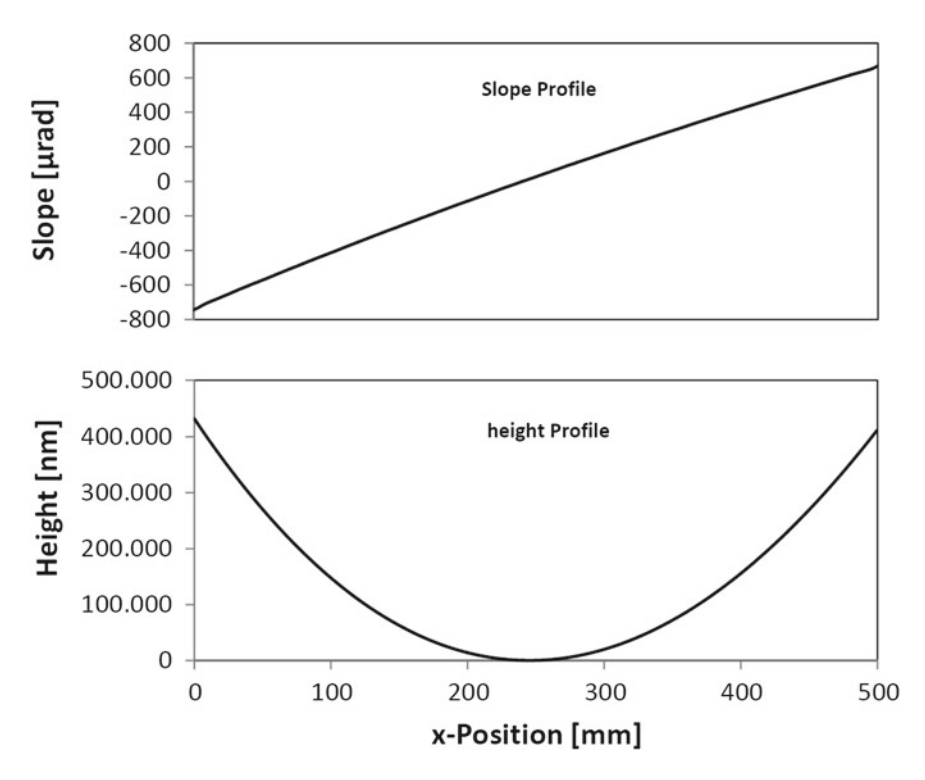


Fig. 7.4 Result of a direct slope measurement (NOM-scan): slope profile of an ellipsoidal focusing mirror along meridional axis (*top*) and the corresponding profile of height (*below*), obtained by integration of the slope data

the mirror finished by deterministic surface finishing. In this case computer aided polishing (CAP) was used. With this technology a residual slope error of $1.5\,\mu rad$ rms was achieved which is sufficient for use in the VUV-range.

Optical systems up to a length of $1600\,\mathrm{mm}$ in length can be aligned for inspection at the BESSY-NOM. The maximum possible scan length of the instrument is $1200\,\mathrm{mm}$. An additional y-table at the NOM allows moving the sample under test in y-direction and thus optics can be inspected by a complete surface slope mapping. The surface slope mapping [25] enables to provide surface topography data to calculate the required data matrix for deterministic surface finishing as well as to identify surface deformation caused by e.g. miss-clamping of the optics. Figure 7.6 shows the residual shape of an elliptical cylinder shaped re-focusing mirror before and after shape optimization by use of IBF [6]. Recently commissioned NOM-systems allow to measure optics up to a scan-length of $1500\,\mathrm{mm}$ [28, 30]. The spatial period range covered by NOM is from $1.7\,\mathrm{mm}$ to the aperture length [40]. Virtually any curved, reflective optical shape can be measured as long as the slope change is within a $\pm 5\,\mathrm{mrad}$ acceptance angle and the local curvature is larger than $5\,\mathrm{m}$ for highly reflective samples under test. Stitching techniques can be applied in case a long optical surface of significant curvature needs to be measured [41].

F. Siewert

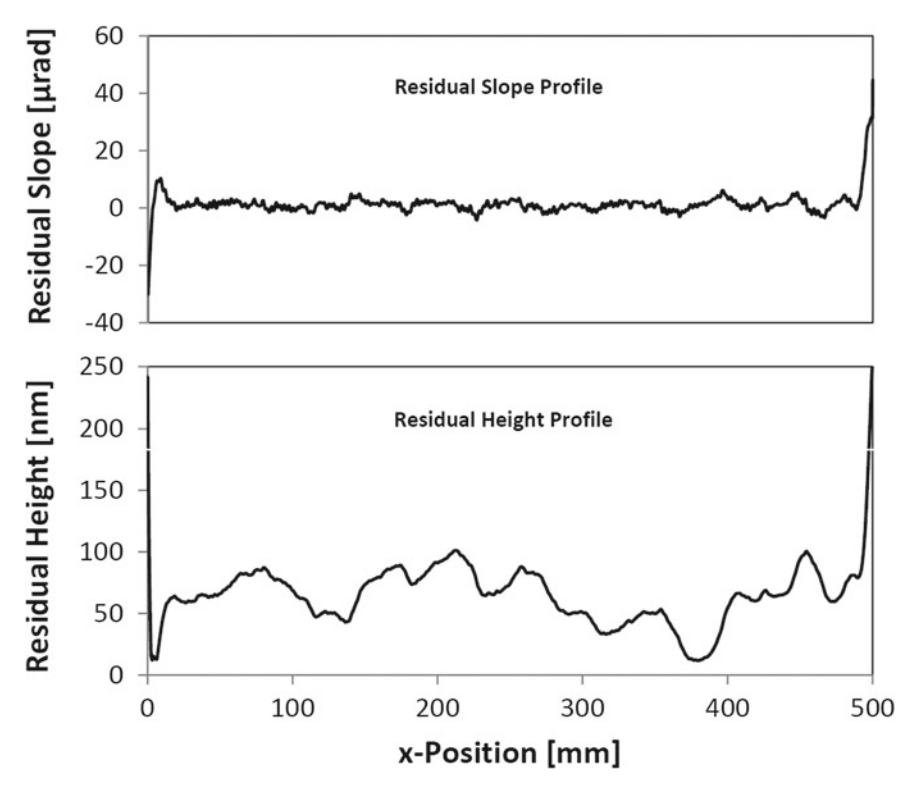


Fig. 7.5 Profile of residual slope of an ellipsoidal focusing mirror along meridional axis gained by subtraction of a ellipse profile (*top*) and the corresponding profile of height (*below*), obtained by integration of the slope data

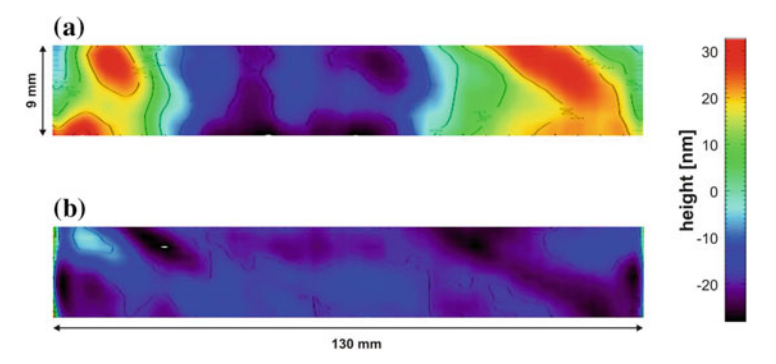


Fig. 7.6 Map of residual height after subtraction of the ideal ellipse parameter, **a** initial state before IBF-treatment 61 nm pv residual figure error, **b** final state 22 nm pv residual figure error

7.2.2 On the Calibration of Slope Measuring Profiler

It was shown recently that a careful characterization and calibration of the sensor in use is essential to achieve the required measurement performance [42, 43].

To characterize and calibrate slope measuring sensors dedicated equipment like the angle comparator [43] at the Physikalisch Technische Bundesanstalt (PTB) is used. A few years ago the so called universal test mirror (UTM) [44] was proposed. A vertical angle comparator (VAC) was developed at the BESSY-II Optics Laboratory for the characterization and calibration of angle measuring sensors, see Fig. 7.7 [42]. The VAC allows to characterize slope measuring profiler with an accuracy of ≤ 50 nrad rms along a measurement length of 1000 mm. It consists of a 1.3 m long Ushaped aluminum bar. The axis of the instrument is formed by a structure of a crossing flexure joint. A linear stepper motor actuator and two linear encoders (Heidenhain Certo CP 60 K) enable a controlled tilting of the VAC. The linear encoder provides a measuring uncertainty of ± 50 nm over a range of 60 mm. The measuring resolution of the Certo is ±5 nm, this corresponds to an tilting resolution of about 10 nrad about. A range of just ± 5 mm is needed to perform the calibration over the entire view field of the NOM-sensor. A test mirror is placed at the desired x-position under the penta-prism to perform a calibration measurement. By placing the test mirror at various positions this procedure is repeated along the scan length of the instrument. The calibration curve is gained by converting the change of height while tilting of the VAC to the corresponding angle value and subtracting the angle values of the autocollimator α_{AKF} , recorded simultaneously, see (7.8). With L_c the distance between the two Certos and dh_i the change of height measured by the Certos.

$$\alpha_{cal} = \arctan\left(\frac{dh_{Certo1} - dh_{Certo2}}{L_c}\right) - \alpha_{AKF}$$
 (7.8)

7.2.3 Super Polished Mirrors for FEL Application

In the past ultra-precise optical components were limited to a length of 100 mm e.g. as finished with the EEM-technology. Deterministic surface finishing technology, EEM as well as IBF, has been improved recently to optimize the shape of mirroror grating-substrates up to a length of 1000 mm and even longer. The first mirrors of such a length are expected to be manufactured within the next few years to be installed at the European XFEL within the years 2016/17. These finishing tools enable to optimize the long spatial error part of optics to an rms sub-nm-accuracy state as required for focusing mirrors at the Linac Coherent Light Source (LCLS) and in the near future for European-XFEL. Figure 7.8 gives an example of such a mirror as installed to focus photons in vertical direction in a KB-mirror set-up [45] at the Coherent X-ray Imaging (CXI) instrument at the LCLS [20]. The elliptical cylinder

F. Siewert

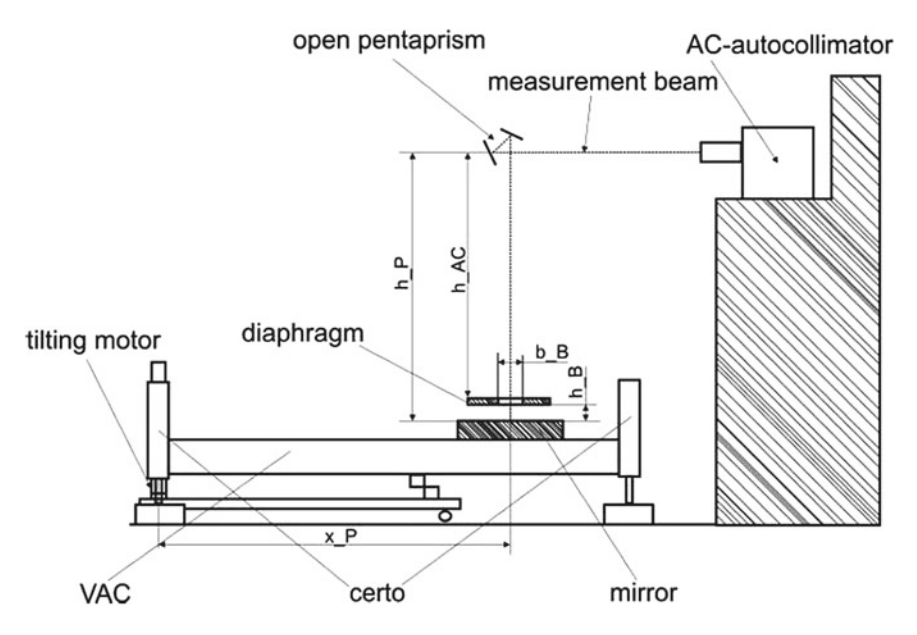


Fig. 7.7 Principle set-up of a vertical angle comparator for the calibration of slope measuring profiler

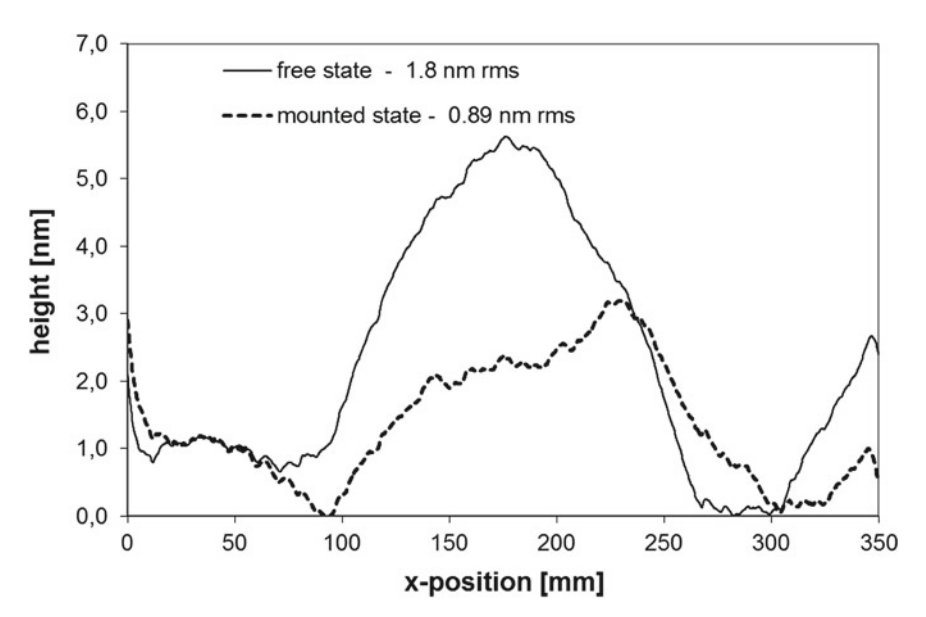


Fig. 7.8 Profile of residual height of a vertical focussing mirror at the CXI-Experiment at LCLS in the "free" and "mounted" state—in face up-condition

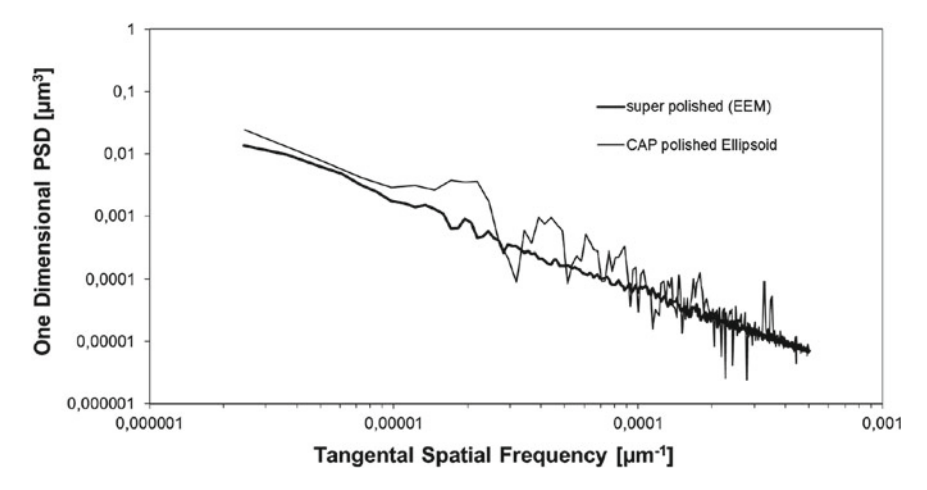


Fig. 7.9 Different finishing technology cause different characteristic residual. Comparison of two different focusing mirrors, an elliptical cylinder finished by Elastic Emission Machining (EEM) and a rotational ellipsoidal mirror (see also Fig. 7.5) made by Computer Aided Polishing (CAP)

shaped mirror of single crystal silicon and coated with B_4C is of 400 mm in length with an optimized aperture section of $350\,\mathrm{mm}\times20\,\mathrm{mm}$. The mirror was finished by use of the EEM-technology. A dedicated prefiguring was given to the mirror to compensate the impact of the gravitational sag on the mirror figure. Figure 7.9 shows a comparison of this mirror and the in Figs. 7.4 and 7.5 discussed ellipsoidal mirror in terms of PSD. It demonstrate that different finishing technology cause characteristic and individual residual to be identified in the spatial frequency spectra of the mirror profile (in meridional direction). Note the ellipsoidal mirror for FLASH is of significant stronger curvature compared to the LCLS-focusing mirror. Thus the ellipsoidal mirror can't be finished by use of EEM-technology. While EEM allows to apply a micro-polishing jet, the CAP-technology is characterized by used of a few-millimeter sized mechanical polishing tool which allows to realize an aspherical shape in meridional and sagittal direction.

Acknowledgments The author gratefully acknowledges A. Aquila and L. Samoylova (both with European XFEL) as well as F. Schäfers and A. Sokolov (HZB) for very helpful discussions and likes to thank Kai Tiedtke (DESY) and Sebastien Boutet (LCLS) for the opportunity to measure optical components for FEL application. This work was in part founded by the European Metrology Research Program EURAMET-JRP SIB58 Angles, Angle Metrology.

148 F. Siewert

References

 M. Altarelli, The European X-ray free-electron laser facility in Hamburg. Nucl. Instrum. Method B 269, 2845–2849 (2011)

- 2. K. Tiedtke et al., The soft x-ray free-electron laser FLASH at DESY: beamlines, diagnostics and end-stations. New J. Phys. 11, 023029 (2009)
- E. Allaria, C. Callegari, D. Cocco, W.M. Fawley, M. Kiskinova, C. Masciovecchio, F. Parmigiani, The FERMI@Elettra free-electron-laser source for coherent x-ray physics: photon properties, beam transport system and applications. New J. Phys. 12, 075002 (2010)
- A.P. Mancuso et al. Technical Design Report: Scientific Instrument SPB, XFEL.EU/TR-2013-004 (2013)
- H. Sinn et al. Technical Design Report: X-Ray Optics and Beam Transport, XFEL.EU TR-2012-006 (2012)
- H. Thiess, H. Lasser, F. Siewert, Fabrication of X-ray mirrors for synchrotron applications. Nucl. Instrum. Method A 616, 157–161 (2010)
- A. Seifert, in New Products for Synchrotron Application Based on Novel Surface Processing Developments. in AIP Conference Proceedings, vol. 879 (2006)
- 8. K. Yamauchi, H. Mimura, K. Inagaki, Y. Mori, Figuring with subnanometer-level accuracy by numerically controlled elastic emission machining. Rev. Sci. Instrum. **73**(11), 4028 (2002)
- 9. J.S. Taylor, G.E. Sommargren, D.W. Sweeney, R.M. Hudyama, The Fabrication and Testing of Optics for EUV Projection Lithography, UCRL-JC-128290 Rev 1 (1998)
- 10. F. Siewert, in *Modern Developments in X-Ray and Neutron Optics, Springer Series in Optical Sciences.* Slope Error and Surface Roughness (2008)
- 11. L. Samoylova, H. Sinn, F. Siewert, H. Mimura, K. Yamauchi, T. Tschentscher, Requirements on hard X-ray grazing incidence optics for European XFEL: analysis and simulation wavefront transformations. in *Proceedings of SPIE*, vol. 7360, 1–9 (2009)
- 12. J.E. Harvey, Modeling the image quality of enhanced reflectance x-ray multilayers as a surface power spectral density filter function, Appl. Opt. **34**(19) (1995)
- J.E. Harvey, Scattering effects in X-ray imaging systems. in *Proceedings of SPIE*, vol. 60, 2515–2532 (1995)
- F. Schäfers, R. Chimino, in Soft X-ray Reflectivity: From Quasi-Perfect Mirrors to Accelerator Walls. *Conference Proceedings C1206051*, (2013), pp. 105–115. arXiv:1308.1295 [physics.acc-ph]
- F. Schäfers, H-Ch. Mertins, F. Schmolla, I. Packe, N.N. Salashchenko, E.A. Shamov, Cr/Sc-Multilayers for the soft x-ray range. Appl. Opt. 37, 719–728 (1998)
- E.L. Church, P.Z. Takacs, Specification of glancing- and normal-incidence X-ray mirrors. Opt. Eng. 34(2), 353–360 (1995)
- 17. E.L. Church, P.Z. Takacs, Specification of surface figure and finish of X-ray mirrors in terms of system performance. Appl. Optics **32**(19), 3344–3531 (1993)
- 18. V.V. Yashchuk, M.R. Howells, W.R. McKinney, P.Z. Takacs, E. Church, in 21st Century Metrology for Synchrotron Radiation Optics—Understanding how to Specify and Characterize Optics. in *Proceedings of the 3rd International Whorkshop on Metrology for X-ray Optics*, Daegu (2006)
- V.V. Yashchuk, S.C. Irick, E.M. Gullikson, R.H. Malcolm, A.A. MacDowell, Wayne R.M., F. Salmassi, T. Warwick, Cross-check of different techniques for two-dimensional power spectral density measurements of x-ray optics, ed. by L. Assoufid, P. Z. Takacs, J.S. Taylor. Advances in Metrology for X-Ray and EUV Optics. in *Proceedings of SPIE*, vol. 5921, 18 (2005)
- F. Siewert, J. Buchheim, S. Boutet, G.J. Williams, P.A. Montanez, J. Krzywinski, R. Signorato, Ultra-precise characterization of LCLS hard X-ray focusing mirrors by high resolution slope measuring deflectometry, Opt. Expr. 4526, 20(4) (2012)
- 21. J.C. Wyant, White light interferometry. in *Proceedings of SPIE*, vol. 4737, 98–107 (2002)
- 22. G. Binnig, C.F. Quate, Ch. Gerber, Atomic Force Microscope. Phys. Rev. Lett. 56(9) (1986)
- Peter Takacs, Shinan Qian, Jeffrey Colbert, Design of a long trace surface profiler. in *Proceedings of SPIE*, vol. 749, 59–64 (1987)

- 24. P.Z. Takacs, S.-N. Qian, Surface Profiling Interferometer, United States Patent 4884697, 1989
- F. Siewert, T. Noll, T. Schlegel, T. Zeschke, H. Lammert, in The Nanometer Optical Component Measuring Machine: A new Sub-nm Topography Measuring Device for X-Ray Optics at BESSY. in AIP Conference Proceedings, vol. 705 (Mellvile, New York, 2004), pp. 847–850
- H. Lammert, T. Noll, T. Schlegel, F. Siewert, T. Zeschke, Optisches Messverfahren zur Ermittlung von Idealformabweichungen technisch polierter Oberflächen und Präzisionsmessmaschine zur Durchführung des Verfahrens. Patentschrift DE10303659 B4 2005.07.28
- F. Siewert, J. Buchheim, T. Zeschke, G. Brenner, S. Kapitzki, K. Tiedtke, Sub-nm accuracy metrology for ultra-precise reflective X-ray optics. Nucl. Instrum. Method A 635, 52–57 (2011)
- S.G. Alcock, K.J.S. Sawhney, S. Scott, U. Pedersen, R. Walton, F. Siewert, T. Zeschke, T. Noll, H. Lammert, The diamond-NOM: a non-contact profiler capable of characterizing optical figure error with sub-nm repeatability. Nucl. Instrum. Method A 616, 224–228 (2010)
- V.V. Yashchuk, S. Barber, E.E. Domning, J.L. Kirschman, G.Y. Morrison, B.V. Smith, F. Siewert, T. Zeschke, R. Geckler, A. Just, Sub-microradian surface slope metrology with the ALS Developmental Long Trace Profiler. Nucl. Instrum. Method A 616, 212–223 (2010)
- J. Nicolas, J.C. Martinez, Characterization of the error budget of the ALBA-NOM, Nucl. Instrum. Method A 710 (2013)
- 31. L. Assoufid et al. Development of a high performance gantry system for a new generation of optical slope measuring profilers, Nucl. Instrum. Method A 710 (2013)
- M. Idir, K. Kaznatcheev, S. Qian, R. Conley, Current status of the NSLS-II Optical Metrology Laboratory, Nucl. Instrum. Method A 710 (2013)
- V.V. Yashchuk, P.Z. Takacs, W.R. McKinney, L. Assoufid, F. Siewert, T. Zeschke, Development of a new generation of optical slope measuring profiler. Nucl. Instrum. Method A 616, 212–223 (2010)
- 34. I. Weingärtner, M. Schulz, C. Elster, Novel scanning technique for ultra-precise measurement of topography. in *Proceedings of SPIE*, 3782, 306–317 (1999)
- 35. C. Elster, I. Weingärtner, Solution for the shearing problem. Appl. Opt. 38, 5024–5031 (1999)
- S.C. Irick, Determining surface profile from sequential interference patterns from a long trace profiler, Rev. Sci. Instrum. 63 (1) (1992)
- 37. R. Signorato, M. Sanchez del Rio, Structured slope errors on real x-ray mirrors: ray tracing versus experiment. in *Proceedings of SPIE*, vol. 3152, 136–147 (1997)
- M. Bowler, F. Siewert, B. Faatz, K. Tiedtke, in Investigating the Effect of Mirror Imperfections in Photon Transport Systems for FELs, WEPC16, in *Proceedings of FEL* 2009, Liverpool, UK
- G. Ehret, M. Schulz, M. Stavridis, C. Elster, in A New Flatness Reference Measurement System Based on Deflectometry and Difference Defelctometry, ed. by W. Osten, M. Kujawinska Fringe 2009: 6th International Workshop on Advanced Optical Metrology (Springer, Berlin, 2009), pp. 318–323
- F. Siewert, J. Buchheim, T. Höft, T. Zeschke, A. Schindler, T. Arnold, Investigations on the spatial resolution of autocollimator-based slope measuring profilers. Nucl. Instrum. Methods A 710, 42–47 (2013)
- F. Polack, M. Thomasset, S. Brochet, A. Rommeveaux, An LTP stiching procedure with compensation of instrument errors: comparison of SOLEIL and ESRF results on strongly curved mirrors. Nucl. Instrum Methods A 616 207–211, (2010)
- F. Siewert, J. Buchheim, T. Zeschke, Calibration and characterization of 2nd generation slope measuring profiler. Nucl. Instrum. Method A 616, 119–127 (2010)
- Ralf D. Geckeler, Andreas Just, Michael Krause, Valeriy Yashchuk, Autocollimators for deflectometry: current status and future progress. Nucl. Instrum. Method A 616, 140–146 (2010)
- V. Yashchuk, W. McKinney, T. Warwick, T. Noll, F. Siewert, T. Zeschke, R. Geckeler, Proposal for a universal test mirror for characterization of slope measuring instruments. in *Proceedings* of SPIE, 5856–121, 2007
- 45. P. Kirkpatrick, A.V. Baez, Formation of optical images by X-rays. J. Opt. Soc. Am. **38**(9), 766–773 (1949)

Chapter 8 Multilayer Mirrors for Coherent Extreme-Ultraviolet and Soft X-ray Sources

Charles Bourassin-Bouchet, Sébastien de Rossi and Franck Delmotte

Abstract After a brief description of the theoretical principles of multilayer mirrors, we present the state of the art of experimental results obtained in the XUV range. We then focus on the specificities of multilayer mirrors for pico- and femtosecond sources, in terms of reflectivity, selectivity and stability. Finally, we report the recent advances in the development of multilayer mirrors for attosecond sources, from the design of the mirror to the characterization of such a component.

Since the first paper on this subject in 1972 [1], research on multilayer mirrors for XUV radiation has been boosted by the rapid development of coherent XUV sources and their applications. In 1985, T. Barbee wrote: "The high reflectivities of these molybdenum-silicon structures will make possible application of traditional optics approaches in the EUV and support new developments including free electron lasers". His prediction has been remarkably validated in the following decades. Nowadays, multilayer mirrors represent key components for the development of applications for coherent XUV sources. In a first part, we present the basic principles of XUV multilayer mirrors, their design and a brief review of experimental reflectivity reported up to now in the XUV domain. The second part deals with the specific properties of mirrors for pico and femtosecond sources. Finally, in the last part, we discuss the possibility of designing and characterizing multilayer mirrors to reflect and/or compress attosecond pulses.

C. Bourassin-Bouchet (\boxtimes) · S. de Rossi · F. Delmotte Laboratoire Charles Fabry, Institut d'Optique, CNRS, Univ Paris-Sud,

S. de Rossi

e-mail: sebastien.derossi@institutoptique.fr

F. Delmotte

e-mail: franck.delmotte@institutoptique.fr

² Avenue Augustin Fresnel, 91127 Palaiseau Cedex, France e-mail: charles.bourassin-bouchet@synchrotron-soleil.fr

8.1 Multilayer Mirrors for the XUV Spectral Range

Optical properties of materials in the XUV range are a major issue for the development of normal incidence mirrors. Actually, in this spectral domain, absorption occurs in all materials and refraction phenomena at interfaces are weak. For example, at a wavelength of 7 nm, the normal incidence reflectivity of a bulk mirror, i.e. a vacuum/material interface, is about 10^{-4} or less. The only way to increase the normal incidence reflectivity is to benefit from constructive interferences in a multilayer stack. In the previous example, the coefficient of reflection in amplitude is about 10^{-2} . Consequently, by adding in phase reflections at 100 successive interfaces, one can reach a reflectivity near 1 if neglecting absorption. This is the principle of multidielectric mirrors used in the visible range, which consist of a periodic stack of two transparent materials, one exhibiting a high index and the other one with a low index, and with a quarter wavelength optical thickness. In the XUV domain, the material absorption reduces the penetration depth of incident light into the stack, which limits the total reflectivity. At 7 nm wavelength, the absorption length is about 70 nm, that is 10 λ . Consequently, the incident light will "see" only the first 40 interfaces of the multilayer stack.

8.1.1 Multilayer Mirrors: Theory and Design

Consider a plane electromagnetic wave, with a wavelength λ_0 , propagating through an ideal interface between two media with complex indices \tilde{n}_i and \tilde{n}_j , see Fig. 8.1a. E (resp. E') is the electric field associated to the incident (resp. reflected) wave. The amplitude reflection coefficient $r_{i,i}$ at the j/i interface, also known as the Fresnel coefficient, is defined as the ratio of the reflected amplitude over the incident one. It can be calculated using the continuity relationships of the electric and magnetic fields at the interface. In the case of normal incidence, we obtain the equation given in Fig. 8.1a. The reflection coefficient r of a thin film deposited on a substrate can be calculated from the reflection coefficients at vacuum/layer and layer/substrate interfaces by taking into account the wave propagation through the layer, see formula in Fig. 8.1b. This propagation induces a complex phase delay, i.e. a real phase delay and an attenuation, called φ_1 . Through an iterative process, one can determine the reflection coefficient of a stack of thin films by adding the layers one by one onto the substrate. We consider here a stack of N thin layers and we designate by i and j two successive layers, see Fig. 8.1c. With the equation given in Fig. 8.1c, one can calculate the reflection coefficient r_i on top of layer j, assuming that layer j is the top layer of the stack, as a function of the reflection coefficient r_i at the previous step. Note that all the contributions arising from multiple reflections are included in this calculation. The reflection coefficient of the whole stack is then given by r_N . Knowing the latter quantity, one can deduce the reflected intensity $R(\lambda_0)$, that corresponds to $|r_N|^2$, and the phase shift $\varphi(\lambda_0)$ of the coating which equals arg (r_N) .

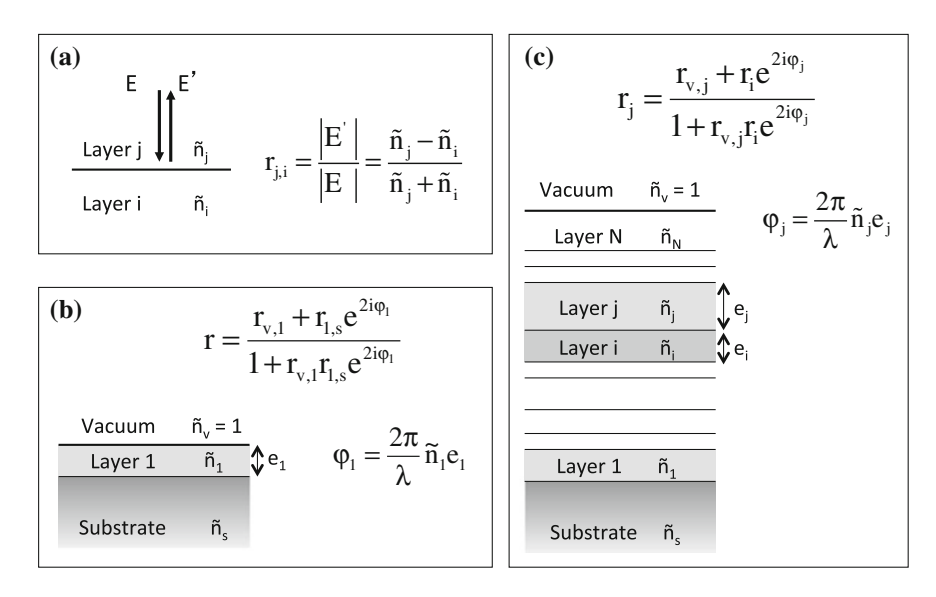
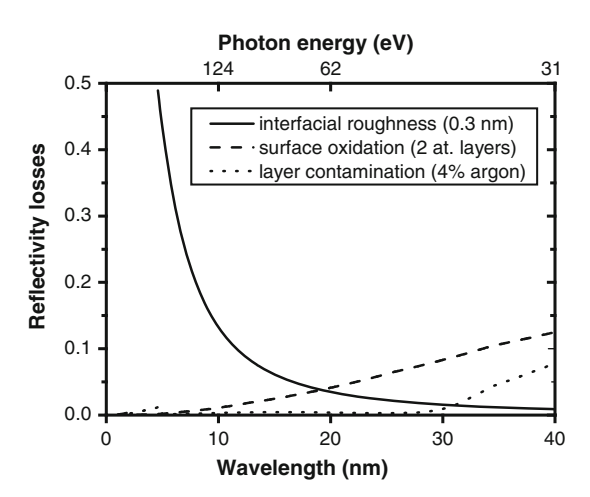


Fig. 8.1 a Reflection of an electric field on a perfect interface between two layers. $\bf b$ Reflection coefficient in the case of a layer deposited on a substrate. $\bf c$ Reflection coefficient in the case of a multilayer

For simplicity, we consider in the previous examples the case of normal incidence. However, similar equations can be derived in the case of oblique incidence, see for example [2]. This iterative approach is implemented for example in the IMD simulation code [3]. Note that other calculation methods exist, as the matrix formalism. A review on multilayer calculation formalisms is given in [4].

Even if the optimal multilayer structure that gives the absolute maximum reflectivity is a non-periodical stack, see for example Yamamoto's layer-by-layer design method [5], periodic multilayers are the most widely used in practice. Indeed periodic multilayers provide almost the same reflectivity and are much simpler to fabricate and to characterize. According to Bragg's law for a normal incidence mirror, its period thickness is approximately equal to half the first order peak wavelength. In order to get the highest theoretical reflectivity with a periodic multilayer mirror, one has to choose the optimal material pair. Yamamoto proposed an efficient method based on the graphical representation in the complex plane of material Fresnel coefficients [5]. Systematic computation of all material combinations can also be used to find the best pair. However, in order to estimate the real performances of multilayers, one has to take into account some imperfections such as interfacial and surface roughness, surface oxidation, layer contamination, etc. We compare in Fig. 8.2 the losses induced on the reflectivity of a multilayer by such imperfections. The effect of roughness can be calculated by using the Nevot-Croce formalism [6]. As expected, the losses induced by interfacial roughness become predominant when the wavelength decreases, see Fig. 8.2. On the other hand, the effect of surface oxidation becomes predominant

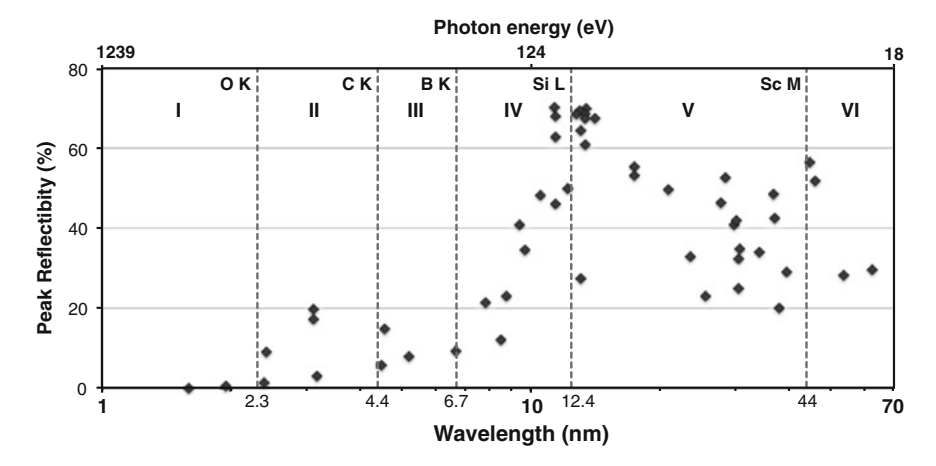
Fig. 8.2 Reflectivity losses due to oxydation, roughness or contamination



when wavelength increases. Finally, a typical layer contamination of a few percent induces negligible losses on the reflectivity, except for wavelengths above 30 nm.

8.1.2 Deposition and Characterization of Multilayers

In practice, for a given wavelength, the choice of materials in the multilayer has to be optimized, taking into account the material optical properties but also the ability to deposit these materials in smooth and thin layer stacks. Thus, it is necessary to control the deposition of high quality thin films with smooth interfaces for a large number of materials. For this reason, multilayer mirrors are generally deposited by using physical vapor deposition techniques such as magnetron sputtering, ion beam sputtering, e-beam evaporation or pulsed laser deposition. Magnetron sputtering is usually preferred because it gathers several advantages: simplicity, versatility, reproducibility, deposition of dense materials and smooth interfaces, possibility to coat curved surfaces. In practice, a uniformity better than 1 % is achievable on 200 mm diameter optics. The characterization of layer thicknesses can be accurately achieved by using grazing incidence X-ray reflectometry on laboratory apparatus [7, 8]. Some EUV reflectometers based on plasma sources have also been developed [9, 10]. However, the precise measurement of the coating performances in the XUV range requires synchrotron radiation sources, e.g. beamline 6.3.2 at ALS, beamline 7.2 at PTB, the BEAR beamline at ELETTRA or the Metrology beamline of SOLEIL. Structural and physico-chemical analysis are also required in order to get knowledge on the material quality (density, purity, stoichiometry), on interfacial phenomena between materials (interdiffusion, compound formation), or on the top layer surface evolution (contamination, oxidation). The most commonly used techniques are nuclear microanalysis (RBS, NRA), surface spectroscopy (XPS, XES, SIMS), and nanoscale microscopy (AFM, TEM).



 $\textbf{Fig. 8.3} \quad \text{Some experimental peak reflectivities reported in literature, along with the main absorption edges in the XUV range}$

8.1.3 State-of-the-Art of Normal Incidence Multilayer Mirrors

In the XUV domain, multilayer mirrors are the only way to obtain efficient near normal incidence reflectivity. Note that multilayer coatings are also widely used in grazing incidence configuration in the X-ray spectral domain (photon energy > 1 keV) in order to improve optical performances of spectrometry or imaging instruments [11–13]. However, we will focus only on near normal incidence mirrors in this subchapter. Nowadays, experimental near normal incidence reflectivity greater than 10 % have been reported in almost all of the XUV spectral ranges but specificities exist for each spectral region. More precisely, one can distinguish six regions delimited by the absorption edges of "spacer" materials, see Fig. 8.3.

In region I, below the oxygen K absorption edge ($\lambda < 2.3\,\mathrm{nm}$), the impact of interfacial roughness on the reflectivity becomes drastic and the layer thicknesses approach the atomic limit. Nevertheless, Windt et al. have reported Bragg's peak reflectivity up to 1% at 2.2 nm and 0.1% at 1.6 nm with W/B₄C periodic multilayers [14].

The spectral region II between O and C K edges $(2.3\,\mathrm{nm} < \lambda < 4.4\,\mathrm{nm})$, the so-called water window region, is of particular interest for X-ray microscopy of biological samples. The development of Cr/Sc multilayers in the late nineties made it possible to surpass the 10 % reflectivity limit in the vicinity of the Sc L edge $(3.1\,\mathrm{nm}$ wavelength) [15–17].

Several multilayer structures have been studied for spectral region III between C and B K absorption edges (4.4 nm < λ < 6.7 nm), including W/C, Ni/C, Co/C, Cr/C. Reflectivity close to 15 % has been obtained with Co/C multilayers near the C edge (at λ = 4.58 nm) [18]. However, these stacks become less efficient when the

wavelength increases and no reflectivity data higher than 10% has been published to date in the range from 5 to $6.5\,\mathrm{nm}$.

Region IV extends from the B K edge to the Si L edge (6.7 nm $< \lambda < 12.4$ nm). Boron carbide, more stable than pure boron, is generally used as a spacer in the short wavelength part of this region. Close to the B edge, the best reflectivity has been obtained with La/B₄C multilayers [19]. Recently, reflectivity in near normal incidence greater than 50 % has been reported by Chkhalo et al. [20]. Mo/B₄C multilayers with reflectivity up to 25 % at 6.7 nm are also commonly used. As in the case of region III, the reflectivity in region IV rapidly drops when the wavelength decreases. For example, the reflectivity of Mo/B₄C multilayers at 7.3 nm is only 6 % [21]. Mo/Y and Mo/Sr stacks with reflectivity ranging from 20 to 40 % have been developed for the 8–11 nm spectral region [22, 23]. For wavelengths greater than 11 nm, Mo/Be multilayers, firstly studied for the EUV lithography, can exhibit a reflectivity as high as 70 % [24].

Region V between the Si L edge and the Sc M edge $(12.4\,\mathrm{nm} < \lambda < 44\,\mathrm{nm})$ has been dominated for a long time by the Mo/Si multilayers introduced in 1985 by Barbee et al. [25]. This is still the case for the short wavelength part of this region, typically below 17 nm. In this range, Mo/Si experimental reflectivity varies from 70% at 13.5 nm (the EUV lithography wavelength) to about 40% at 17 nm. Beyond 17 nm, recent studies have allowed one to exceed the performances of Mo/Si, using for example B₄C/Mo/Si three-material multilayers [26], Al-based multilayers [27–29] or Mg-based multilayers [30, 31]. With the development of Sc/Si multilayers by Uspenskii et al. [32, 33], the wavelength region above 44 nm (Sc M edge), constituting the region VI, has become accessible to multilayer mirrors. More recently, reflectivity close to 30% has been measured at 62.5 nm with Si/Gd multilayers [27].

8.1.4 Specificities of Multilayer Mirrors for Coherent X-ray Sources

Coherent X-ray sources, such as synchrotron radiation (SR), high-harmonic generation (HHG), free electron lasers (FEL) or X-ray lasers (XRL), can emit XUV flashes ranging from the picosecond to the attosecond timescale. In order to efficiently reflect such ultrashort pulses off a multilayer mirror, the latter must have a bandpass broader than the pulse spectrum and a well-controlled phase. This being said, there is a natural distinction between the design of a multilayer stack for pico/femtosecond pulses, and for attosecond pulses. In the first case, the pulse spectrum never exceeds a few tenths of electron-volts, which always fits in the Bragg's peak of a periodic multilayer stack. Moreover, the phase of such a mirror being always linear throughout the reflectivity peak, the pulse can be efficiently reflected off a simple periodic stack. In the case of attosecond pulses, the XUV spectrum can be a hundred-eV large. Therefore a special effort has to be made during the optimization to obtain multilayer structures exhibiting a broadband reflectivity and a controlled phase.

	FEL	SR	XRL	HHG	
High reflectivity	*	**	**	*	
High selectivity	_	_	_	**	
High stability	**	*	*	_	

Table 8.1 Main requirements (** = Most important parameter, * = second most important parameter, - = less important parameter) for multilayer mirrors as a function of the kind of source

Table 8.2 High efficiency multilayer mirrors, i.e. mirrors with experimental near normal incidence reflectivity above 50% (incidence angle of 17° for Chkhalo et al. and <10° for the rest of them)

Year	Materials	Wavelength (nm)	References
1985	Mo/Si	13	Barbee et al. [25]
1995	Mo/Be	11	Skulina et al. [34]
2004	Sc/Si	46	Yulin et al. [35]
2009	Mg/Sc/SiC	28	Aquila et al. [36]
2010	Al/Mo/SiC	17	Meltchakov et al. [28]
2013	La/B ₄ C/C	6.8	Chkhalo et al. [20]

8.2 Multilayer Mirrors for Picosecond and Femtosecond Sources

Concerning multilayer mirrors for pico/femtosecond sources, the main requirements are a high reflectivity, a high (or controlled) selectivity and/or a high stability. The predominant factor depends on the source type as illustrated in Table 8.1. In this part, we will present the recent progresses that have been made to improve these three parameters.

8.2.1 High Reflectivity Mirrors

Table 8.2 presents a synthetic view of multilayer mirrors that provide near normal incidence reflectivity greater than 50 % and that we refer to as "high efficiency" multilayer mirrors. T. Barbee was the first one, in 1985, to produce high efficiency mirrors with the well-known Moly-silicon multilayers around 13 nm. Ten years after, Mo/Be multilayers were developed as a potential solution for EUV lithography coatings at 11 nm. Then Sc/Si extended the spectral domain of high efficiency mirrors to higher wavelengths. Since then, three new high efficiency multilayer mirrors have been reported. It is worth noticing that these last three mirrors consist of a combination of three materials.

Larruquert has demonstrated theoretically the interest of using more than two materials in aperiodic multilayer structures [37]. Following his work, we have been

able to increase the reflectivity in the 20-40 nm wavelength range by adding a third material in a periodic structure. We have also studied theoretically and experimentally the increase of reflectance generated by adding a third material in a periodic multilayer structure [26]. Simulations show that multilayers made of B₄C, Mo and Si materials present higher reflectivity than two components multilayers (B₄C/Si and Mo/Si) if they are deposited in the optimal order, that is B₄C over Mo over Si. B₄C/Mo/Si structures present a theoretical reflectivity of 42 % at 32 nm and experimental reflectivity up to 37 %. This represents a significant increase compared to B₄C/Si or Mo/Si multilayers which have an experimental reflectivity about 25 % at 32 nm. Other researchers have also taken advantage of this "three material effect". Thereby, Yulin et al. have shown an improvement in the reflectivity of Sc/Si multilayers at a wavelength of 45 nm when adding a Cr layer at the Si-on-Sc interface [35]. Moreover, Aguila et al. have demonstrated an increase of reflectivity from 46 to 52 % around 28 nm by adding Sc material in Mg/SiC multilayers [36]. These Mg/Sc/SiC multilayers thus provide the highest reflectivity ever reached at this wavelength. Due to the presence of an absorption edge at 70 eV (17 nm), Aluminum is of particular interest as a spacer material for high reflectivity EUV multilayers. In the past few years, several Al-based two- and three-components multilayers have been studied [28, 29, 38, 39]. The actual issue in such multilayers is the large roughness of Al layers associated with their polycrystalline structure. In fact, two-components multilayers Al/SiC and Al/B4C still present non-negligible interfacial roughness (about 1 nm RMS), which induces a significant loss of reflectivity compared to the theoretical ideal case. However, by optimizing the deposition process and by adding a refractory material (Mo or W) in the periodic stack, we have been able to smooth the interfaces down to \sim 0.5 nm. Moreover, these multilayers benefit from the three material effect that enhances the theoretical reflectivity in the 17–40 nm range, as shown in Fig. 8.4. Thus, in the case of Al-based multilayers, the addition of a third material improves both the theoretical reflectivity and the experimental interface quality. Experimental reflectivity up to 56% has been obtained recently near the Al L edge with Al/Mo/SiC multilayers, which is the reflectivity record for such a wavelength.

8.2.2 High Selectivity Mirrors

Narrowband Mirrors

Several authors have addressed the problem of spectral selectivity of multilayer mirrors. As early as 1990, Boher et al. proposed to use multilayers made of two low-Z materials in order to reduce the mirror bandwidth. They obtained interesting preliminary results with Si/SiO₂ and Si/Si₃N₄ multilayers. Since then, a lot of low-Z multilayers have been studied by different authors: Si/B₄C [40], C/Si [41], MoSi/Si [42], B/Si [43], Si/C and Si/SiC [44]. Another potential solution to reduce the bandwidth of the multilayer is to work at a high Bragg's peak order. Usually, multilayer mirrors work at the first Bragg's order in order to optimize the reflectivity. Choosing a higher order Bragg's peak is an efficient way to obtain narrowband mirrors in the

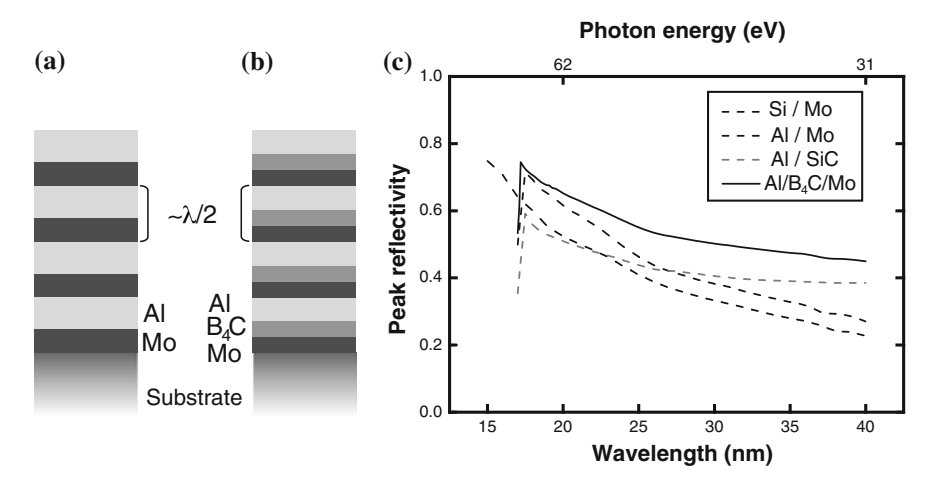


Fig. 8.4 Periodic multilayer with a two and b three-materials. c Theoretical peak reflectivity with respect to the wavelength: Mo/Si, Al/Mo, Al/SiC and Al/B₄C/Mo

case of high efficiency multilayers such as Mo/Si ones. As a matter of fact, when increasing the Bragg's order, the bandwidth decreases faster than the reflectivity. Thus, one can obtain a very narrowband mirror with a non-negligible reflectivity value. For example, when working at the fifth order instead of the first one, the theoretical bandwidth of a Mo/Si mirror is reduced by a factor of 5 (from 0.6 to 0.12 nm) while the theoretical reflectivity is only reduced by a factor of 2 (from 75 % down to 39 %). Experimental results with Mo/Si mirrors up to the tenth order have been reported by Feigl et al. [45].

Mirrors with Antireflection Layers

Concerning selectivity, another important issue concerns the rejection of unwanted spectral regions, and especially in the Vacuum Ultra-Violet (VUV) domain (60 nm < $\lambda < 200 \,\mathrm{nm}$) where some coherent sources such as HHG or FEL deliver intense radiations. In order to use the XUV emission, one has to efficiently filter out these VUV components. In fact, most of the materials used in XUV multilayer mirrors present a significant surface reflectivity. As shown in Fig. 8.5a, the normal incidence reflectivity for typical materials ranges from 10 to 60% in the VUV range. The solution generally implemented is to use metallic filters in transmission in order to suppress the VUV emission. Such components consist of ~100 nm thick freestanding materials and are mechanically fragile. Moreover their optical transmission is significant only close to absorption edges. In practice, few materials are available in such filter form, and their use is limited to some specific wavelength regions. Another possible solution is to filter out the VUV light with the multilayer mirror itself. Indeed the penetration depth in the VUV being typically around 10 nm, only the top layers of the stack will contribute to the spectral response of the mirror in this region. Thus, by a proper choice of top layers material and thickness, one can minimize the VUV reflectivity while preserving the high XUV reflectivity. To do so, the top layer has to

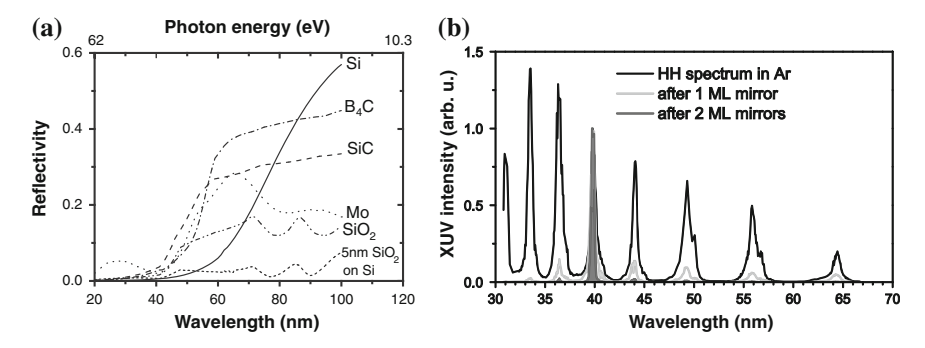


Fig. 8.5 a Theoretical normal incidence reflectivity of several materials in the VUV range. **b** HHG wavelength spectra measured without mirror (*black full line*), measured with one mirror (*light grey line*) and deduced for two mirrors (*grey shaded area*). The three harmonic 21 peak signals are equalized to illustrate rejection of other harmonics. Figure **b** is taken from [46]

act as an anti-reflection (AR) layer for the VUV light. If one adds a $5\,\mathrm{nm}$ thick SiO_2 layer on top of bulk silicon, one obtains a very low reflectivity (less than a few percents) on the all VUV range, see Fig. $8.5\,\mathrm{a}$. In this case, interferences between waves reflected off vacuum/SiO₂ and SiO₂/Si interfaces provide an efficient AR effect.

Several authors have reported such an AR effect by performing "top-layer engineering". In 2007, Bajt optimized mirrors for the FLASH FEL in order to reflect the second order harmonic of FLASH at 16 nm, and to reject its fundamental emission at 32 nm. The optimized top layer was a thick Si layer (>40 nm). They obtained reflectivity values greater than 40% at 16 nm and lower than 1% at 32 nm over a large angular range (incidence in the range 30–60°) [47]. Corso et al. used a similar approach to produce FERMI FEL multilayer mirrors. They optimized Pd/B₄C multilayers with specific top layers in order to reflect the third harmonic at 6.67 nm and to reject the fundamental emission [48].

For the purpose of EUV lithography development, Van Harpen et al. proposed to use a Si_3N_4 top layer on Mo/Si multilayers that acts as an AR layer for VUV light (up to 200 nm). They demonstrated a reduction of the VUV reflectance by a factor of five while maintaining a reflectance greater than 60% at 13.5 nm [49]. In order to improve the spectral purity of multilayer mirrors used for the selection of one harmonic in an HHG spectrum, we have optimized SiO_2 AR coating both on B_4 C/Si multilayers (for the selection of harmonics 21-25) and Sc/Si multilayers (for selection of harmonics 17-19). As depicted in Fig. 8.5b, such SiO_2 AR layers present a good rejection of low order harmonics in the VUV and provide an efficient solution to select one harmonic with an enhanced spectral purity. These optimized multilayer mirrors have been used for the study of dissociative ionization of molecules induced by HHG femtosecond XUV pulses [46, 50].

Mirrors with a Controlled Spectral Response These few examples demonstrate that top layer engineering is a good way to reject a specific wavelength or a spectral region. However, when the top layer thickness increases too much, the XUV peak

reflectivity drops, which constitutes the main limit of this approach. In order to overcome this difficulty, one can replace the top layer by a second periodic multilayer. If the two multilayers are properly matched, the increase of the top multilayer total thickness will not degrade the XUV peak reflectivity. Such bi-periodic multilayers open the way to obtain high rejection rate for several wavelengths close to the XUV peak reflectivity. Moreover, we have shown that the first and second Bragg's peak position can be tuned by adding a buffer layer between both periodic multilayers [51]. Figure 8.6 shows an example of dual-band multilayer mirror designed for the coronal imaging of the sun. The mirror reflects both 17.4 and 33.5 nm emission lines with a good rejection of the 30.4 nm emission line. As shown in the figure, one can tune the position of the other rejections by optimizing the top multilayer and the buffer layer thicknesses. Such multilayer structures, initially developed for the Solar Orbiter ESA mission, are of particular interest for applications on HHG or FEL sources.

Going from a periodic to a bi-periodic structure is a way to increase the degrees of freedom in the optimization of the spectral response. This approach can be pushed further by considering non-periodic structures. Up to now, most of the studies related to non-periodic multilayers aims at optimizing reflectivity in a given spectral range rather than at a specific wavelength. As soon as 1996, Loevezijn et al. studied the effect of thickness disorder in periodic multilayers and proposed a systematic optimization method to design non periodic multilayers with optimized integrated reflectivity on a specific spectral range [52]. Michette et al. proposed a similar method but applied to a more general case: they took into account interfacial roughness, layer thickness errors and non-sharp boundaries [53]. Note that such a depth-graded or aperiodic mirror can be very useful for applications that require broad angular acceptance. For example, depth-graded Mo/Si multilayer mirrors reflecting between 50 and 60% in the 0–16°

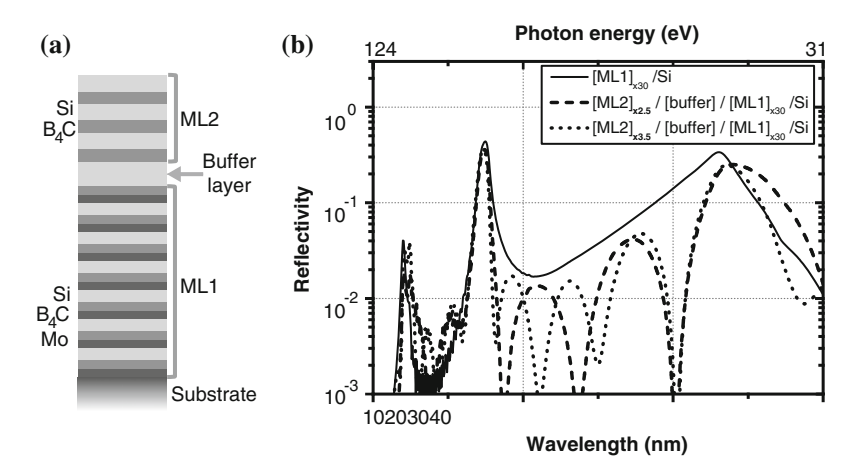


Fig. 8.6 a Design of a dual band coating consisting of a superposition of two periodic multilayers (ML1 and ML2) spaced by a buffer layer. **b** Theoretical reflectivity of two mirrors optimized to reflect both the 17.4 and 33.5 nm emission lines and to reject the 30.4 nm emission line. The reflectivity of the first periodic multilayer (ML1) is also depicted for comparison [51]

angular bandpass have been reported for the production of EUV lithography optics [54]. Corso et al. have also used such an aperiodic approach to optimize AR layers on a periodic stack [48].

8.2.3 High Stability Mirrors

Multilayer mirrors are widely used on EUV and X-ray FEL to transport or focus the beam. Considering the pulse duration and brilliance of these sources, the temporal, thermal and irradiation stability of multilayer mirrors turns out to be a major issue [47, 48].

Concerning multilayer thermal stability, temperature damage threshold is usually related to different physico-chemical phenomena, depending on the materials. In some systems, such as Mo/Si or Sc/Si, the increase of temperature produces a decrease in the period thickness. It has been demonstrated that this phenomenon, known as "period contraction", is related to the growth of interdiffusion layers at interfaces [55–57]. Figure 8.7 shows that the threshold for this phenomenon is typically of 100 °C for Sc/Si and 250 °C for Mo/Si multilayers. Other systems do not exhibit any period contraction. For example, Mo/B4C periods are almost stable up to 600 °C but the growth of interlayers with temperature induces changes in mechanical stress, from compressive to tensile, and a small decrease of reflectivity [21].

In some cases, these damage thresholds are too low and an improvement of the thermal stability is required. One solution is to add thin layers of a few tenths of nanometers of a third material at both interfaces. It has been shown that carbon layers or carbon or nitride compounds such as SiC, SiN and B₄C improve the thermal stability of Mo/Si without significant reduction of peak reflectivity [57–59]. Figure 8.7 illustrates the effect of such barrier layers on the temperature damage threshold in the case of Mo/Si and Sc/Si multilayers. Barrier layers proved to be efficient even for material pairs with low thermal stability such as Sc/Si. Several authors have reported experimental results with ScN, SiN, W, Cr or CrB₂ barrier layers in order to improve Sc/Si thermal stability. An interesting study of reactive diffusion in Sc/Si together with a comparison between different barrier materials can be found in [60].

A significant effort has been made in the past 10 years on the optimization of Mo/Si multilayers for EUV lithography, including barrier layers and capping layers in order to improve thermal and temporal stability. All these progresses benefit coherent EUV sources and their applications in different scientific fields. Louis et al. have recently published a detailed review on these technological developments [61]. A thorough report on ultrathin films that could be used as capping layers to protect and extend the lifetime of multilayer optics is given in [62].

The stability of multilayer mirrors exposed to intense XUV radiation has become a real concern with the development of FEL sources. Nevertheless, some studies have been reported with other coherent sources such as X-ray lasers. For example, Grisham et al. have investigated the damage threshold and damage mechanism of Sc/Si multilayer mirrors exposed to focused nanosecond pulses at 46.9 nm with a compact capillary-discharge laser. They have reported damage thresholds of about

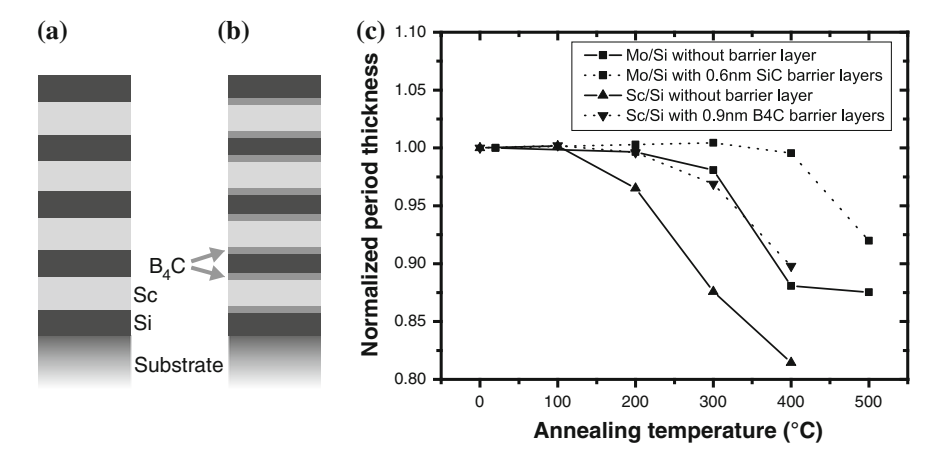


Fig. 8.7 Diagram of a Sc/Si multilayer mirror without (a) and with (b) B_4C barrier layers. c Evolution of the multilayer period thickness as a function of the annealing temperature for Mo/Si, Mo/SiC/Si/SiC, Sc/Si and Sc/ B_4C /Si/ B_4C (one hour annealing under argon atmosphere)

80 mJ/cm² [63]. Concerning stability to FEL radiation, several experiments have been implemented on the FLASH source. Hau-Riege et al. have studied the stability to radiation on B₄C and SiC thin films to be used for X-ray FEL optics. They reported a strong wavelength dependence for both thin films between 13 and 32 nm, with a damage threshold in the range 320–350 mJ/cm² at 13 nm, and 10 times lower at 32 nm [64]. Louis et al. have determined the threshold for irreversible damage of Mo/Si multilayers exposed to FLASH FEL 13.5 nm radiation to be 45 mJ/cm² [65]. Similar studies have been reported also in the single shot regime [66]. The damage mechanisms of multilayer optics exposed to FEL radiation have been investigated, in particular for Mo/Si [66] and MoN/SiN multilayers [67].

8.3 Multilayer Mirrors for Attosecond Sources

As opposed to pico/femtosecond XUV sources, the development of mirrors for attosecond pulses requires a "phase engineering" of the multilayer structures. This imposes to use new approaches for the design and the characterization of such mirrors.

8.3.1 Specificities of the Attosecond Regime

Attosecond pulses have been obtained exclusively with HHG sources so far. One of their specificities lies in their spectral phase. Apart from the highest energies of the

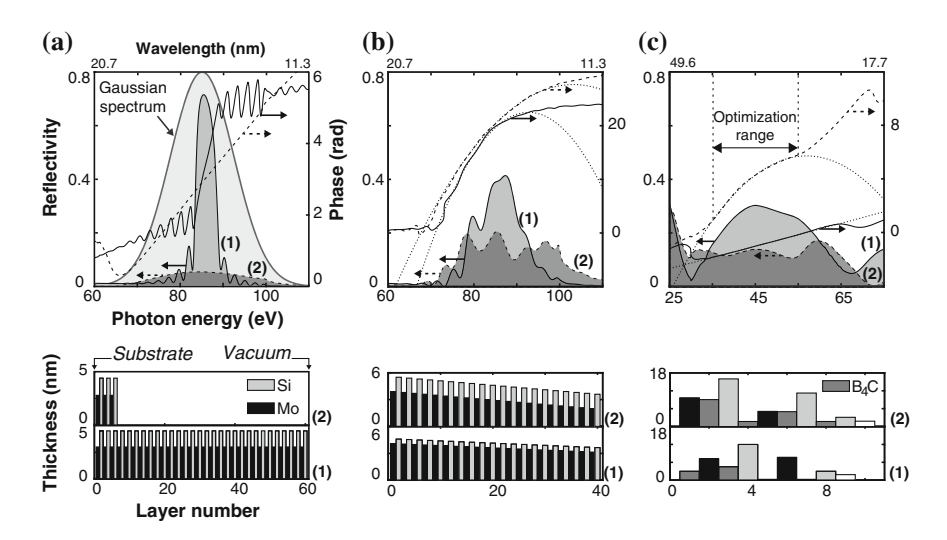


Fig. 8.8 Spectral responses, and the corresponding structures, of multilayer mirrors for attosecond pulses in the case of, $\bf a$ a periodic Mo/Si stack, $\bf b$ a gradient Mo/Si structure, and $\bf c$ an aperiodic Mo/B₄C/Si stack. In $\bf a$ is also depicted a gaussian 18 eV FWHM spectrum corresponding to a 100 as pulse in the time domain in the absence of group delay dispersion. In $\bf b$ and $\bf c$, the dotted lines represent the parabolic fits of the spectral phase of the mirrors

spectrum, called the cut-off region, the spectral content of these pulses always exhibits a Group Delay Dispersion (GDD), also known as the attochirp, see Chap. 3, that tends to increase their duration. Equation (8.1) gives the evolution with the amount of GDD of the FWHM duration τ of a gaussian pulse, τ_0 being the duration in the chirp-free case:

$$\tau = \tau_0 \sqrt{1 + \frac{16 \ln 2^2 G D D^2}{\tau_0^2}} \tag{8.1}$$

As an example, a gaussian spectrum with a FWHM of 18 eV, see Fig. 8.8a, corresponds to a Fourier-transform limited pulse duration τ_0 of 100 as FWHM. However, a typical GDD of 20,000 as 2 /rad changes this duration into 556 as FWHM. Consequently, the compensation of this attochirp could potentially lead to much shorter pulses.

To do so, one needs to filter the attosecond radiation with a dispersive component exhibiting the opposite GDD along with a low absorption in the considered spectral range. The easiest way to proceed is to make use of the natural dispersion of materials such as metallic filters [68] or gas cells [69]. This solution is straightforward to implement but is not tunable, the dispersion being imposed by the chosen material. The second possibility relies on the angular dispersion of a diffraction grating [70]. Such a grating compressor allows a more flexible control of the chirp rate which can be set by the geometry of the system. However, such systems always require one or two

pairs of angularly dispersive components, making their alignment rather complex. The last solution consists in using a structured medium, such as a reflective multilayer mirror. In that case, the dispersion of the component is set by the interferences in the structure. Consequently, a single mirror offers potentially arbitrary shaping capabilities [71–73].

8.3.2 Design of Attosecond Mirrors

The effective shaping/transport of an attosecond pulse with a multilayer mirror depends on the quality of its structure.

Structure of the Multilayer Stack

As a logical starting point, one can first consider a periodic multilayer structure with N periods and working near normal incidence. The spectral bandwidth of such an optical resonator is approximately λ_{Bragg}/N , λ_{Bragg} being the wavelength at the Bragg's peak. Consider mirror (1) in Fig. 8.8a, that is a Mo/Si stack composed of N=30 periods. One obtains a reflectivity peak around 85 eV which is much narrower than the broadband spectrum to reflect. The direct solution is to decrease the number of periods of the stack, which increases the mirror bandwidth at the price however of a decrease of the Bragg's peak reflectivity, see mirror (2) in Fig. 8.8a. Moreover, the phase being linear throughout the Bragg's peak in both cases, the pulse will accumulate a time delay during its penetration into the structure, but its temporal shape will remain unchanged. Consequently, despite a low reflectivity, low-period multilayer stacks are well suited to the transport of attosecond pulses. This simple solution can be exploited in the cut-off region of a HHG spectrum where the GDD is zero [74].

In order to get a broadband mirror with a tailored spectral phase, one needs to consider more sophisticated multilayer structures. Following the strategy developed for chirped mirrors for femtosecond infrared pulses [75, 76], it is possible to design a stack where the period varies with depth. One thus creates a structure where the Bragg's phase matching is fulfilled at a given depth for a given wavelength. If the period increases linearly with depth, larger wavelengths will be reflected deeper in the stack while short wavelengths will be reflected off the surface. One therefore obtains a mirror with a negative GDD, that is a parabolic convex spectral phase as shown in Fig. 8.8b, enabling the attochirp compensation. This approach is valid only in spectral regions where the used materials are not too absorbent, that is in the 70–100 eV range for Mo/Si structures.

At higher energy, silicon becomes too absorbent and a substitute, such as Lanthanum, must be used [77]. Below 70 eV, molybdenum and silicon are still usable but gradient structures are no longer adapted. Indeed, their dispersive absorption needs to be taken into account and the design of a broadband phase-controlled multilayer structure becomes non trivial. This requires using optimization algorithms and leads to totally aperiodic structures. Moreover, a third material, usually boron carbide, is often added to increase reflectivity, see Sect. 8.2.1, and to get more degrees

of freedom. Two examples of such structures are depicted in Fig. 8.8c, showing a linear phase and a quadratic convex phase for an efficient transport or compression of attosecond pulses in the 35–55 eV range [78].

Optimization Procedure

Optimization algorithms are needed to design totally aperiodic structures. Indeed, consider a multilayer stack with N periods, not more than a few tens in practice because of absorption. Each of these periods can contain m materials, in general only two or three due to the limited space in the deposition machine. And consider that each layer can take n values of thickness, typically a few hundreds, the minimum thickness being imposed by the deposition technique. The number of combinations is thus $n^{m \times N}$, that makes $\sim 100^{3 \times 10}$ possible stacks in practice. Since it is not reasonable to test all these combinations to identify the most suitable one, the search for a solution in the minimum time requires highly efficient global algorithms, such as those belonging to the class of metaheuristics. Several approaches have been explored such as the use of simulated annealing algorithms [78], genetic algorithms [79], or home-made algorithms [80]. These algorithms always rely on an objective function to minimize in the least squares sense and which depends on the quantities one wants to optimize. In the case of attosecond mirrors, one can optimize the multilayer performances in the spectral domain [73, 80], such as its peak reflectivity, its bandwidth or the shape of its spectral phase, or in the time domain. The latter procedure consists in optimizing directly the features of the reflected attosecond pulse, such as its duration, the relative intensity of its secondary peaks compared to the main temporal burst, or its deviation from a gaussian pulse profile [72, 81].

8.3.3 Characterization of Attosecond Mirrors

Since attosecond mirrors are designed to control both the pulse amplitude and phase, their characterization requires the measurement of the mirror complex response, that is its reflectivity and phase. The characterization of the mirror reflectivity is well-established, and can be performed with a good precision on a synchrotron metrology beam line, the procedure being identical for a broadband reflectivity and for Bragg's peak one. Therefore, we only consider now the issue of the phase characterization of a multilayer mirror.

Characterization by Photocurrent Measurement

The first solution is known as the Total Electron Yield (TEY) technique. It builds upon the pioneering work made by Pepper [82] in the seventies on the photoelectric effect occurring in thin films illuminated by XUV light, as shown in Fig. 8.9a. During the reflection of light off the mirror, the incident and reflected electric fields overlap inside the stack without interacting unless a phenomenon that is sensitive to the square modulus of the field occurs locally. This is precisely what happens with the photoelectric effect, the latter creating photoelectrons everywhere in the multilayer structure. However, those are much more numerous in the top layer because of the depletion of the XUV photons as they penetrate in the stack. Moreover the mean

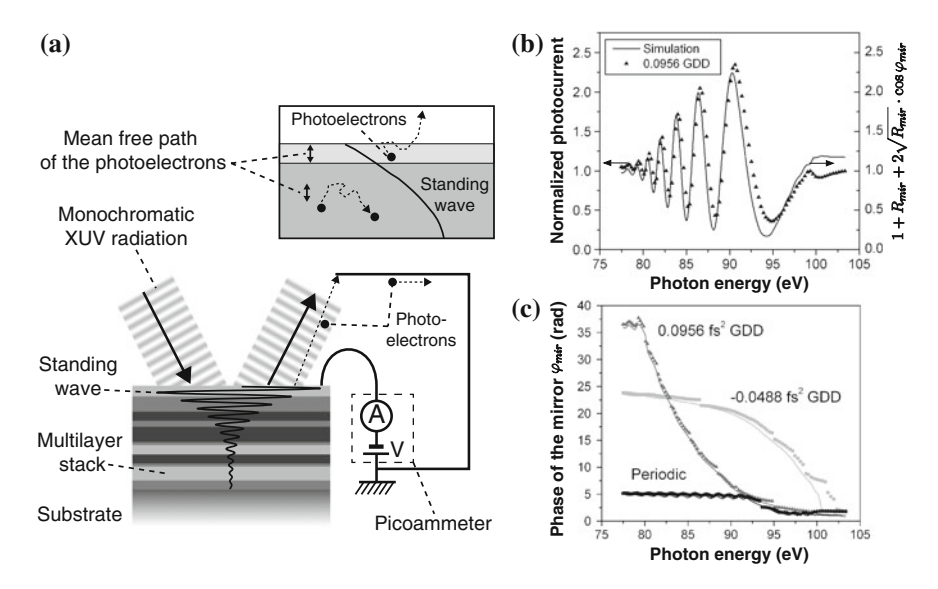


Fig. 8.9 a Principle of the measurement of the phase of a multilayer mirror via photocurrent measurements. **b** Theoretical and measured normalized photocurrents for a multilayer stack exhibiting a GDD of 95.6×10^3 as². **c** Phases simulated (*continuous lines*) and measured with the TEY technique (symbols) in the case of a positively (*grey curve*) and negatively (*light grey curve*) chirped mirrors, and in the case of a periodic Mo/Si stack (*black curve*). Figures **b** and **c** are taken from [83]

free path of photoelectrons is usually of a few tenths of nanometers in the structure, so that the photocurrent measured on top of the stack will be mainly composed of electrons coming from the top layer. One can then state that this photocurrent i_{mir} will be proportional to the light intensity at the surface of the mirror, that is set by the standing wave formed by the superimposition of the incident A_{in} and reflected A_{out} electric fields:

$$i_{mir}(\omega) = C(\omega) \cdot |A_{in}(\omega) + A_{out}(\omega)|^{2}$$

$$= C(\omega) \cdot |A_{in}|^{2} \cdot \left[1 + R_{mir} + 2\sqrt{R_{mir}} \cdot \cos(\varphi_{mir}) \right]$$
(8.2)

Therefore, by measuring such a photocurrent along with the mirror's reflectivity R_{mir} , one can access the phase shift φ_{mir} induced by the multilayer mirror on the incident light. In equation (8.2), $C(\omega)$ is a coefficient representing the ability of a given material to emit photoelectrons in given illumination conditions. In order to get rid of this unknown, the strategy consists in measuring the photocurrent $i_{ref}(\omega)$ of a reference sample having the same coefficient $C(\omega)$. To make sure this condition is fulfilled, the reference sample must be made of the same material as the one composing the top layer of the mirror. The reflectivity of this single layer reference sample is mostly very low, which allows one to approximate that $i_{ref}(\omega)$ equals $C(\omega) \cdot |A_{in}|^2$. Therefore, knowing the ratio i/i_{ref} , called the normalized photocur-

rent, and the reflectivity of the mirror to characterize gives rise to the phase shift $\varphi_{mir}(\omega)$:

$$\frac{i_{mir}(\omega)}{i_{ref}(\omega)} \approx 1 + R_{mir} + 2\sqrt{R_{mir}} \cdot \cos(\varphi_{mir})$$
 (8.3)

In practice, such a measurement can be performed on a synchrotron beam line. It requires putting an anode at the surface of the mirror to collect the photocurrent and linking it to picoammeter, see Fig. 8.9a. An example of photocurrent measurement and of phase reconstruction is reported in Fig. 8.9b, c.

This technique was introduced for the characterization of attosecond mirrors by Aquila et al. [83]. It is particularly suited for the phase characterization of multilayers in the 70–100 eV range, where it is rather straightforward to find low reflectivity reference mirrors. But it has also been demonstrated near absorption edges [84], and for very large spectral ranges [81].

Characterization by Direct Measurement of Attosecond Pulses

Another approach for characterizing the phase of multilayer mirrors consists in measuring the attosecond pulses reflected off the mirror. One thus directly observes the impact of the mirror on the pulse [72, 77, 85]. However, in order to fully characterize the multilayer, one has to measure the pulse with and without the mirror. The variation of the pulse spectral phase after reflection thus corresponds to the phase shift induced by the mirror. If such a differential measurement has already been used to characterize the dispersion of metallic filters [68], its implementation in the case of mirrors is more problematic. Indeed, the reflective optic deviates the beam, and the procedure thus requires a major move of the attosecond pulse detector. In order to maintain the same experimental geometry, it can be convenient to use a reference mirror with a well-known, and usually simple, phase response such as a silver coated mirror [78]. A first measurement with the reference mirror gives access to the incident light properties. The measurement is then repeated with the mirror to characterize to access the reflected pulse. This technique has been used to characterize the mirror (2) in Fig. 8.8c, the result of this measurement is depicted in Fig. 8.10a. Such measurements were also attempted for by Morlens et al. [86]. Finally, a comparison between the phases obtained with the TEY technique and via the direct characterization of attosecond pulses has also been reported, and tends to show that both techniques lead to similar results [87].

Examples of Attosecond Pulse Compression with Multilayer Mirrors

The shortest attosecond pulses produced to date lie in the 60–70 as range [69, 88, 89], and make use of the natural dispersion of argon cells or zirconium filters to compensate for the attochirp. However, recent achievements show that similar performances could be achieved with multilayers [78, 81, 85]. Figure 8.10 illustrates two examples of such a post-compression of attosecond pulses with multilayer mirrors.

In Fig. 8.10a is depicted the experimental characterization of the mirror (2) described in Fig. 8.8c. Its reflectivity was measured on a synchrotron and its group

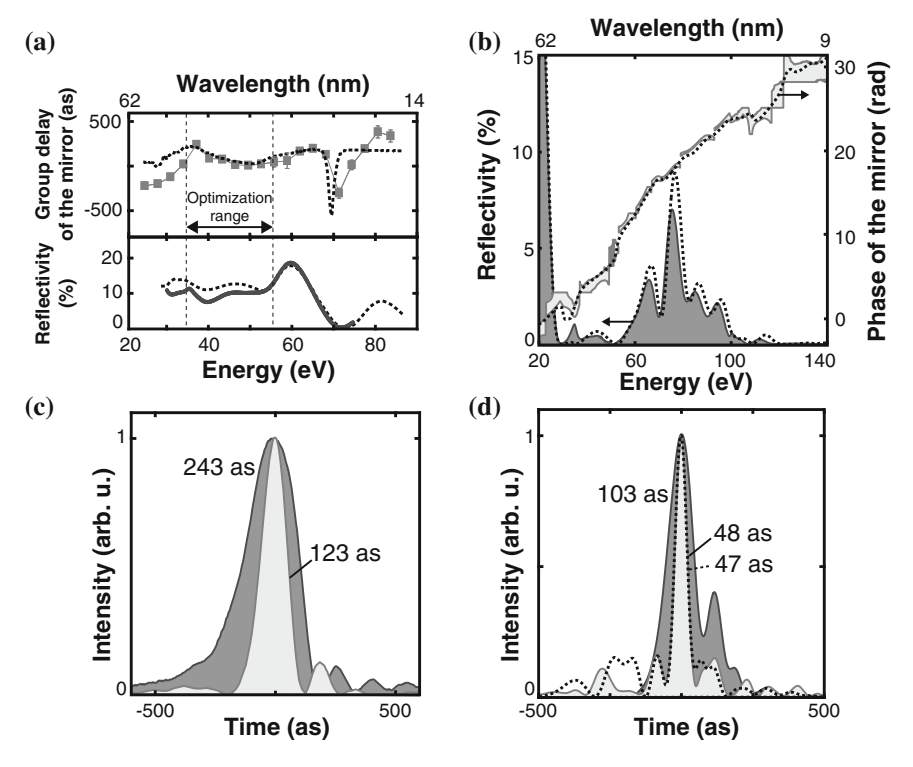


Fig. 8.10 a Measurement of the reflectivity (*thick grey curve*) and group delay (*grey squares*) of mirror (2) described in Fig. 8.8c and taken from [78]. The *black dotted lines* correspond to the simulated properties. **b** Measurements (*shaded lines*) and simulations (*dotted lines*) of the reflectivity and phase of a broadband multilayer mirror optimized in the time domain. Data taken from [81]. **c** Attosecond pulses measured after reflection off a reference silver mirror (*dark grey curve*), and off the mirror in (**a**) (*light grey curve*). **d** Simulated incident pulse (dark grey curve) used for the time-domain optimization of the mirror in (**b**), along with the reflected pulse profile retrieved from the simulations (*black dotted line*) and from the measurements in (**b**) (*light grey line*). The FWHM duration is indicated for each pulse

delay, that is the derivative of its spectral phase, on an attosecond beam line [78]. This aperiodic mirror has been optimized to exhibit a negative GDD on the 35–55 eV range. This is confirmed by the measurements, the mirror group delay being linearly decreasing in this range. The compression capability of this mirror is clearly visible in the time domain. Figure 8.10c shows the temporal profile of the radiation in the 35–55 eV range reflected off a zero phase reference mirror and off the multilayer mirror. In the second case, the pulse duration is decreased by a factor of two, down to 123 as.

As as second example, we depict in Fig. 8.10b the spectral features of a multilayer mirror optimized to compress below 50 as the 103 as pulse shown in Fig. 8.10c [81]. The spectral phase of the mirror has been measured with the TEY technique on

the 20–140 eV range. The agreement between the pulse profiles obtained from the simulations of the mirror and from its measured properties confirms the sub-50 as compression capability.

8.4 Conclusion

Research carried out on XUV multilayer mirrors in the past 40 years have provided firstly a better understanding of the physics of X-ray multilayer structures, and secondly a huge number of technological progresses in the development of new optical components for this spectral range. Nowadays, multilayer mirrors for XUV radiation have become essential for the development of coherent source applications. Even if they rely on a mature technology, it remains many scientific and technologic challenges to address in the future: the improvement of the mirror reflectivity in some specific wavelength regions, the development of new deposition processes in order to obtain ultra-smooth interfaces, a better understanding and control of multilayer stability and mechanical stress induced by multilayer coatings. Top layer engineering and more generally optimization of aperiodic structures are two very promising ways to obtain spectral responses suited to pico and femtosecond sources. Regarding attosecond sources, one challenge will be to develop multilayers adapted to higher energy ranges, up to the water window.

References

- 1. E. Spiller, Appl. Phys. Lett. **20**, 365 (1972)
- 2. D.T. Attwood (ed.), Soft X-rays and Extreme Ultraviolet Radiation: Principles and Applications (Cambridge University Press, Cambridge, 2000)
- 3. D.L. Windt, Comput. Phys. 12, 360 (1998)
- 4. B. Pardo, T. Megademini, J.M. André, Rev. Phys. Appl. 23, 1579 (1988)
- 5. M. Yamamoto, T. Namioka, Appl. Opt. 31, 1622 (1992)
- 6. L. Nevot, P. Croce, Rev. Phys. Appl. 15, 761 (1980)
- 7. L. Nevot, B. Pardo, J. Corno, Rev. Phys. Appl. 23, 1675 (1988)
- 8. F. Bridou, B.A. Pardo, J. Opt. 21, 183 (1990)
- 9. E.M. Gullikson, J.H. Underwood, P.C. Batson, V. Nikitin, J. X-ray Sci. Technol. 3, 283 (1992)
- 10. S. Döring, F. Hertlein, A. Bayer, K. Mann, Appl. Phys. A **107**, 795 (2012)
- 11. D.L. Windt, S. Donguy, C.J. Hailey, J. Koglin, V. Honkimaki et al., Appl. Opt. 42, 2415 (2003)
- H. Maury, F. Bridou, P. Troussel, E. Meltchakov, F. Delmotte, Nucl. Instr. Meth. Phys. Res. A 621, 242 (2010)
- 13. F. Bridou, F. Delmotte, P. Troussel, B. Villette, Nucl. Instr. Meth. Phys. Res. A 680, 69 (2012)
- 14. D.L. Windt, E.M. Gullikson, C.C. Walton, Opt. Lett. 27, 2212 (2002)
- K. Sakano, M. Yamamoto, Proc. SPIE 3767, EUV, X-Ray, and Neutron Optics and Sources, 238 (November 23, 1999)
- F. Eriksson, G.A. Johansson, H.M. Hertz, E.M. Gullikson, U. Kreissig et al., Opt. Lett. 28, 2494 (2003)
- 17. F. Schäfers, M. Mertin, D. Abramsohn, A. Gaupp, H.C. Mertins et al., Nucl. Instr. Meth. Phys. Res. A 467, 349 (2001)

- 18. I.A. Artyukov, Y. Bugayev, O.Y. Devizenko, R.M. Feschenko, Y.S. Kasyanov et al., Proc. SPIE 5919, Soft X-ray Lasers and Applications VI, 59190E (September 13, 2005)
- J.M. André, P. Jonnard, C. Michaelsen, J. Wiesmann, F. Bridou et al., X-ray Spectrom. 34, 203 (2005)
- N.I. Chkhalo, S. Künstner, V.N. Polkovnikov, N.N. Salashchenko, F. Schäfers et al., Appl. Phys. Lett. 102, 011602 (2013)
- 21. M. Barthelmess, S. Bajt, Appl. Opt. **50**, 1610 (2011)
- C. Montcalm, B.T. Sullivan, S. Duguay, M. Ranger, W. Steffens et al., Opt. Lett. 20, 1450 (1995)
- 23. B. Sae-Lao, C. Montcalm, Opt. Lett. 26, 468 (2001)
- 24. C. Montcalm, S. Bajt, P.B. Mirkarimi, E.A. Spiller, F.J. Weber et al., Proc. SPIE 3331, Emerging Lithographic Technologies II, 42 (June 5, 1998)
- 25. T.W. Barbee Jr, S. Mrowka, M.C. Hettrick, Appl. Opt. 24, 883 (1985)
- 26. J. Gautier, F. Delmotte, M. Roulliay, F. Bridou, M.F. Ravet et al., Appl. Opt. 44, 384 (2005)
- 27. D.L. Windt, J.A. Bellotti, B. Kjornrattanawanich, J.F. Seely, Appl. Opt. 48, 5502 (2009)
- E. Meltchakov, C. Hecquet, M. Roulliay, S. De Rossi, Y. Menesguen et al., Appl. Phys. A 98, 111 (2010)
- E. Meltchakov, A. Ziani, F. Auchère, X. Zhang, M. Roulliay et al., Proc. SPIE 8168, Advances in Optical Thin Films IV, 816819 (October 03, 2011)
- T. Ejima, A. Yamazaki, T. Banse, K. Saito, Y. Kondo, S. Ichimaru, H. Takenaka, T. Ejima, Y. Kondo, M. Watanabe, Jpn. J. Appl. Phys. 40, 376 (2001)
- 31. M. Fernández-Perea, R. Soufli, J.C. Robinson, R. De Marcos, J.A. Méndez et al., Opt. Express **20**, 24018 (2012)
- 32. Y.A. Uspenskii, S.V. Antonov, V.Y. Fedotov, A.V. Vinogradov, Proc. SPIE 3156, Soft X-ray Lasers and Applications II, 288 (November 1, 1997)
- Y.A. Uspenskii, V.E. Levashov, A.V. Vinogradov, A.I. Fedorenko, V.V. Kondratenko et al., Nucl. Instr. Meth. Phys. Res. A 448, 147 (2000)
- K.M. Skulina, C.S. Alford, R.M. Bionta, D.M. Makowiecki, E.M. Gullikson et al., Appl. Opt. 34, 3727 (1995)
- 35. S.A. Yulin, F. Schaefers, T. Feigl, N. Kaiser, Proc. SPIE 5193, Advances in Mirror Technology for X-Ray, EUV Lithography, Laser, and Other Applications, 155 (January 13, 2004)
- 36. A. Aquila, F. Salmassi, Y. Liu, E.M. Gullikson, Opt. Express 17, 22102 (2009)
- 37. J.I. Larruquert, J. Opt. Soc. Am. A 19, 385 (2002)
- 38. D.L. Windt, J.A. Bellotti, Appl. Opt. 48, 4932 (2009)
- 39. O. Zhong, W. Li, Z. Zhang, J. Zhu, O. Huang et al., Opt. Express 20, 10692 (2012)
- J.M. Slaughter, B.S. Medower, R.N. Watts, C. Tarrio, T.B. Lucatorto et al., Opt. Lett. 19, 1786 (1994)
- 41. M. Grigonis, E.J. Knystautas, Appl. Opt. 36, 2839 (1997)
- 42. H. Hara, S. Nagata, R. Kano, K. Kumagai, T. Sakao et al., Appl. Opt. 38, 6617 (1999)
- 43. M.F. Ravet, F. Bridou, A. Raynal, B. Pardo, J.P. Chauvineau et al., J. Appl. Phys. 89, 1145 (2001)
- 44. D.L. Windt, S. Donguy, J. Seely, B. Kjornrattanawanich, Appl. Opt. 43, 1835 (2004)
- 45. T. Feigl, S. Yulin, N. Benoit, N. Kaiser, Microelectron. Eng. 83, 703 (2006)
- P. Billaud, M. Géléoc, Y.J. Picard, K. Veyrinas, J.F. Hergott et al., J. Phys. B: At. Mol. Opt. Phys. 45, 194013 (2012)
- 47. S. Bajt, H.N. Chapman, E. Spiller, S. Hau-Riege, J. Alameda et al., Proc. SPIE 6586, Damage to VUV, EUV, and X-ray Optics, 65860J (May 18, 2007)
- A. Jody Corso, P. Zuppella, D.L. Windt, M. Zangrando, M.G. Pelizzo, Opt. Express 20, 8006 (2012)
- M.M.J.W. van Herpen, R.W.E. van de Kruijs, D.J.W. Klunder, E. Louis, A.E. Yakshin et al., Opt. Lett. 33, 560 (2008)
- P. Billaud, M. Géléoc, F. Delmotte, M. Roulliay, Y.J. Picard et al., UVX 2012–11e Colloque sur les Sources Cohérentes et Incohérentes UV, VUV et X; Applications et Développements Récents, 01018, EDP Sciences (2013)

- C. Hecquet, F. Delmotte, M.F. Ravet-Krill, S. de Rossi, A. Jérôme et al., Appl. Phys. A 95, 401 (2009)
- 52. P. van Loevezijn, R. Schlatmann, J. Verhoeven, B.A. van Tiggelen, E.M. Gullikson, Appl. Opt. **35**, 3614 (1996)
- 53. A.G. Michette, Z. Wang, Opt. Commun. 177, 47 (2000)
- A.E. Yakshin, I.V. Kozhevnikov, E. Zoethout, E. Louis, F. Bijkerk, Opt. Express 18, 6957 (2010)
- H. Maury, P. Jonnard, J.M. André, J. Gautier, M. Roulliay et al., Thin Solid Films 514, 278 (2006)
- 56. J. Gautier, F. Delmotte, M. Roulliay, M.F. Ravet, F. Bridou et al., Proc. SPIE 5963, Advances in Optical Thin Films II. 59630X (October 04, 2005)
- 57. S. Bajt, J.B. Alameda, T.W. Barbee Jr, W.M. Clift, J.A. Folta et al., Opt. Eng. 41, 1797 (2002)
- 58. H. Takenaka, H. Ito, T. Haga, T. Kawamura, J. Synchrotron Rad. 5, 708 (1998)
- 59. S. Braun, H. Mai, M. Moss, R. Scholz, A. Leson, Jpn. J. Appl. Phys. 41, 4074 (2002)
- Y.P. Pershyn, E.N. Zubarev, V.V. Kondratenko, V.A. Sevryukova, S.V. Kurbatova, Appl. Phys. A 103, 1021 (2011)
- 61. E. Louis, A.E. Yakshin, T. Tsarfati, F. Bijkerk, Prog. Surf. Sci. 86, 255 (2011)
- 62. S. Bajt, N.V. Edwards, T.E. Madey, Surf. Sci. Rep. 63, 73 (2008)
- 63. M. Grisham, G. Vaschenko, C.S. Menoni, J.J. Rocca, Y.P. Pershyn et al., Opt. Lett. 29, 620 (2004)
- S.P. Hau-Riege, R.A. London, R.M. Bionta, D. Ryutov, R. Soufli et al., Appl. Phys. Lett. 95, 111104 (2009)
- E. Louis, A.R. Khorsand, R. Sobierajski, E.D. van Hattum, M. Jurek et al., Proc. SPIE 7361, Damage to VUV, EUV, and X-ray Optics II, 73610I (May 18, 2009)
- A.R. Khorsand, R. Sobierajski, E. Louis, S. Bruijn, E.D. van Hattum et al., Opt. Express 18, 700 (2010)
- 67. R. Sobierajski, S. Bruijn, A.R. Khorsand, E. Louis, R.W.E. van de Kruijs et al., Opt. Express 19, 193 (2011)
- R. López-Martens, K. Varjú, P. Johnsson, J. Mauritsson, Y. Mairesse et al., Phys. Rev. Lett. 94, 033001 (2005)
- 69. D.H. Ko, K.T. Kim, J. Park, J.H. Lee, C.H. Nam, New J. Phys. 12, 063008 (2010)
- 70. L. Poletto, F. Frassetto, P. Villoresi, J. Opt. Soc. Am. B 25, B133 (2008)
- A. Wonisch, T. Westerwalbesloh, W. Hachmann, N. Kabachnik, U. Kleineberg et al., Thin Solid Films 464–465, 473 (2004)
- A. Wonisch, U. Neuhäusler, N.M. Kabachnik, T. Uphues, M. Uiberacker et al., Appl. Opt. 45, 4147 (2006)
- 73. A.S. Morlens, P. Balcou, P. Zeitoun, C. Valentin, V. Laude et al., Opt. Lett. 30, 1554 (2005)
- E. Goulielmakis, M. Schultze, M. Hofstetter, V.S. Yakovlev, J. Gagnon et al., Science 320, 1614 (2008)
- 75. R. Szipöcs, K. Ferencz, C. Spielmann, F. Krausz, Opt. Lett. **19**, 201 (1994)
- 76. G. Steinmeyer, D.H. Sutter, L. Gallmann, N. Matuschek, U. Keller, Science 286, 1507 (1999)
- 77. M. Hofstetter, A. Aquila, M. Schultze, A. Guggenmos, S. Yang et al., New J. Phys. 13, 063038 (2011)
- 78. C. Bourassin-Bouchet, Z. Diveki, S. de Rossi, E. English, E. Meltchakov et al., Opt. Express 19, 3809 (2011)
- 79. A.L. Aquila, F. Salmassi, F. Dollar, Y. Liu, E. Gullikson, Opt. Express 14, 10073 (2006)
- 80. M. Suman, F. Frassetto, P. Nicolosi, M.G. Pelizzo, Appl. Opt. 46, 8159 (2007)
- 81. C. Bourassin-Bouchet, S. de Rossi, J. Wang, E. Meltchakov, A. Giglia et al., New J. Phys. 14, 023040 (2012)
- 82. S.V. Pepper, J. Opt. Soc. Am. **60**, 805 (1970)
- 83. A. Aquila, F. Salmassi, E. Gullikson, Opt. Lett. 33, 455 (2008)
- 84. M. Suman, G. Monaco, M.G. Pelizzo, D.L. Windt, P. Nicolosi, Opt. Express 17, 7922 (2009)
- 85. M. Hofstetter, M. Schultze, M. Fieß, B. Dennhardt, A. Guggenmos et al., Opt. Express 19, 1767 (2011)

- A.S. Morlens, R. López-Martens, O. Boyko, P. Zeitoun, P. Balcou et al., Opt. Lett. 31, 1558 (2006)
- 87. R.A. Loch, A. Dubrouil, R. Sobierajski, D. Descamps, B. Fabre et al., Opt. Lett. 36, 3386 (2011)
- 88. K. Zhao, Q. Zhang, M. Chini, Y. Wu, X. Wang et al., Opt. Lett. 37, 3891 (2012)
- 89. M. Schultze, E.M. Bothschafter, A. Sommer, S. Holzner, W. Schweinberger et al., Nature **493**, 75 (2012)

Chapter 9 Gratings for Ultrashort Coherent Pulses in the Extreme Ultraviolet

Taro Sekikawa

Abstract We discuss the recent new applications of gratings for ultrashort light pulses in the extreme ultraviolet (XUV) and soft X-ray range. A special emphasis is placed on the applications to high harmonics that are generated by the nonlinear interaction between the ultrashort laser pulses and atoms or molecules. We present the development and characterization of optical systems that use gratings to select single harmonic with the preserved pulse duration.

9.1 Introduction

Gratings that disperse optical waves ranging from the far-infrared to soft X-ray have been widely used in various types of spectroscopy for wavelength selection [1]. In addition, with the development of laser technologies, gratings found extensive use in laser systems and optical devices for pulse manipulation, such as pulse stretch, pulse compression, and pulse shaping [2]. The working principles and operation of gratings are well established and, accordingly, the manufacturing technology has been well developed to satisfy sub-angstrom precision and to improve the efficiency of diffraction.

The development of synchrotron light sources stimulated the interest in the extreme ultraviolet (XUV) and soft X-ray spectroscopy. Synchrotron radiation has the continuous spectrum and various types of gratings are used to select and to focus the XUV and soft X-ray waves on the target; thus, gratings have become one of the key optical elements in these types of spectroscopy. A detailed description of gratings that are specialized for XUV and soft X-ray light waves is given in the book edited by Samson and Ederer [3].

T. Sekikawa (⊠)

Department of Applied Physics, Hokkaido University, Kita 13 Nishi 8, Kita-ku, Sapporo 060-8628, Japan e-mail: sekikawa@eng.hokudai.ac.jp

This article focuses on another application of gratings in the XUV and soft X-ray regimes, namely on their application to high harmonics of ultrashort laser pulses. The generation of high harmonics by intense ultrashort laser pulses was first reported in 1987 [4, 5]. The intensities of higher-order harmonics of ultrashort laser pulses were found to be much higher than those that are predicted by a perturbative approach, up to the cut-off energy that was determined by the peak intensity of the laser pulse. The mechanism of the nonperturbative intensity distribution is now well understood, and can be explained using the so-called three-step model [6]. High harmonics can cover the XUV and soft X-ray regions, and recently were even shown to extend to the hard X-ray region [7]. Because the process of high harmonic generation retains the coherence of the driving laser, the generated high harmonics also constitute coherent light. In particular, the high harmonics are characterized by a temporal coherence, and hence the corresponding temporal pulse durations are in the femtosecond and attosecond regimes [8–10]. This provides us with the unique opportunity to investigate the ultrafast phenomena in the XUV and soft X-ray regions, because the pulse durations of synchrotron radiation are on the order of picoseconds and thus are not short enough to be used in femtosecond spectroscopy. In addition, recent developments in laser technology make it possible to deliver harmonic photons that are comparable to those obtained from synchrotron light sources [11]. Therefore, high harmonics pulses are promising ultrashort XUV and soft X-ray light sources complementary to synchrotron light sources. Of course, state-of-the-art X-ray free electron lasers (XFEL) deliver XUV and soft X-ray pulses that are more intense than those obtained with high harmonics [12]. However, the compactness of a system for the generation of high harmonics and the high temporal resolution breaking into the attosecond regime should make high harmonics somewhat advantageous over the XFEL.

Gratings can also play an important role in the application of high harmonics to ultrafast spectroscopy. Since the driving laser pulses and all harmonics copropagate, it is necessary to separate a single harmonic from the others. The first application of high harmonics to the time-resolved photoelectron spectroscopy was demonstrated by using a grating to select a single harmonic order [13]. However, the diffraction on a grating introduces the pulse-front tilt and broadens the pulse duration. To compensate for the pulse-front tilt and to keep the pulse duration as close to its original value as possible, a time-delay compensated monochromator (TDCM) employing diffraction gratings was proposed and developed for the isolation of a single harmonic from the others [14, 15].

The advantages of a TDCM over a multilayer mirror, which is another method for selecting a single harmonic without the temporal stretch of the pulse duration, are as follows: (i) The wavelength can be tuned simply by rotating the gratings; (ii) The spectral purity is better, because the other harmonics are completely eliminated by a spatial slit; (iii) In general, a thin metal filter that is used to stop a strong fundamental light can be removed from the system, because the fundamental light is also spatially separated after diffraction. Consequently, following the removal of a filter, the throughput can be improved approximately by one order of magnitude, making the total throughput of a TDCM comparable to that obtained by using multilayer

mirrors. Thus, a TDCM will provide unique opportunities that allow gaining insight into phenomena inaccessible by the synchrotron light sources. In this article, we describe the recent progress on a TDCM, along with some background on gratings that is necessary to understand a TDCM.

9.2 Grating for the Extreme Ultraviolet and Soft X-ray

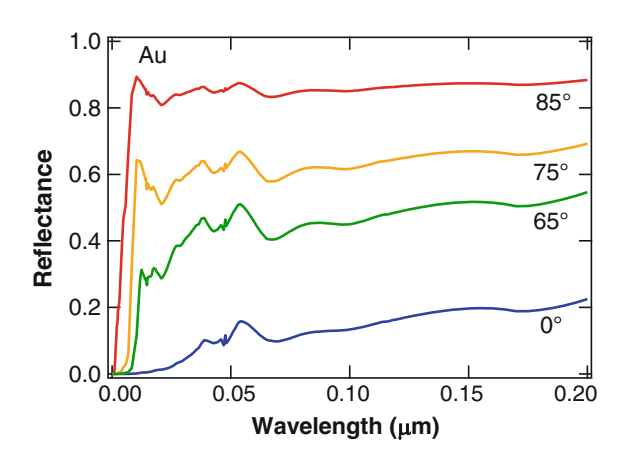
9.2.1 Absorption and Reflectance

XUV and soft X-ray lights have large absorption coefficients for almost all materials, including air. There are no windows and lenses for focusing, and very thin metal foils are used as band pass filters. Therefore, optical systems are basically constructed from reflective components. However, for a small incidence angle ϕ , the reflectance in the XUV and soft X-ray range is small, and it is especially true for the wavelengths that are shorter than 30 nm. Thus, to increase the reflectance, it is necessary to make the incidence angle ϕ larger than about 70°. For example, the reflectance R of the s-polarized light is expressed as:

$$R = \left| \frac{\cos \phi - \sqrt{n^2 - \sin^2 \phi}}{\cos \phi + \sqrt{n^2 - \sin^2 \phi}} \right|^2, \tag{9.1}$$

where n is a complex refractive index. Gold and platinum are often used as a coating on optical components. Figure 9.1 shows the reflectance of gold, calculated using 9.1, with reference to a handbook edited by Palik [16]. Although for all grazing-incidence angles the spectrum of reflectance is almost constant for wavelengths longer than 10 nm, the maximal reflectance is still less than 0.9, even

Fig. 9.1 Reflectance spectra of gold in the extreme ultraviolet and soft X-ray range, at incidence angles of 0°, 65°, 75°, and 85°



for the incidence angle of 85°. This indicates that multiple reflections lead to a large intensity loss. Therefore, an optical system has to be constructed with the minimal number of optical components. To increase the reflectance and to extend to the shorter wavelengths, s-polarization is preferred to p-polarization because of its higher reflectance

9.2.2 Grating

9.2.2.1 The Grating Equation

The diffraction gratings that are used for the XUV and soft X-ray are classified into two categories: plane and concave gratings. As was described in Sect. 9.2.1, the reflectance loss of optical coatings in the XUV and soft X-ray lights is almost one order of magnitude larger than that in the visible light. Thus, in order to reduce the number of the optical components, the concave gratings are often used for diffraction as well as for the focusing of light.

Figure 9.2 shows the relationship between the angles of incidence (α) and diffraction (β) on a grating, which can be expressed as:

$$d(\sin\alpha + \sin\beta) = m\lambda, \qquad m = 0, \pm 1, \pm 2, \dots \tag{9.2}$$

where d, λ , and m denote the groove spacing, the wavelength, and the integer diffraction order, respectively. When the light is reflected, $\beta_0 = -\alpha$, and thus, m = 0. For positive (m = 1) and negative (m = -1) orders, $\beta_1 > -\alpha$ and $\beta_{-1} < -\alpha$, respectively. The same relationships describe the diffraction on a concave grating.

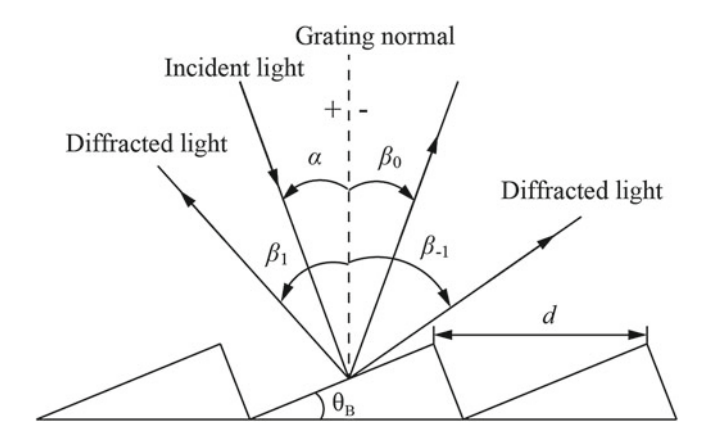


Fig. 9.2 Diffraction by a plane grating. The sign convention for the angles α and β is shown by the + and - signs on either side of the grating normal. θ_B is the blaze angle

A measure of the separation between the different wavelengths of the diffracted light is called the angular dispersion, and is expressed as:

$$\frac{d\beta}{d\lambda} = \frac{m}{d\cos\beta} \tag{9.3}$$

As the groove spacing decreases, the angular dispersion increases, i.e., the angular separation between the wavelengths increases for a given diffraction order m.

The efficiency of a grating to the first order diffraction increases with the addition of a simple smooth triangular groove profile (shown in Fig. 9.2), under the "blaze condition" of $2d \sin \theta_B = \lambda$, where θ_B is the blaze angle. The highest efficiency is obtained when the condition $\alpha - \beta = 0$ is also satisfied. This condition is known as the "Littrow blaze condition." The triangular groove profile is generated by the mechanical ruling or by the ion etching. A different profile, a sinusoidal groove, can be obtained using interferometric (holographic) techniques. Sinusoidal gratings have somewhat different efficiencies. Thus, the groove profile has to be checked before it is used.

9.2.2.2 Rowland Mount of a Concave Grating

When a concave grating that has a curvature R is illuminated from an off-axis point A (see Fig. 9.3), the diffracted beam has two foci: tangential (B) and sagittal (C) foci. Here, O is located at the center of the grating, and the spherical center of the grating is in the AOB plane. The grooves on the grating are ruled along the direction that is vertical to the AOB plane. Then, the tangential focus B, where a diffracted beam is focused in the tangential direction, is determined from the following equation:

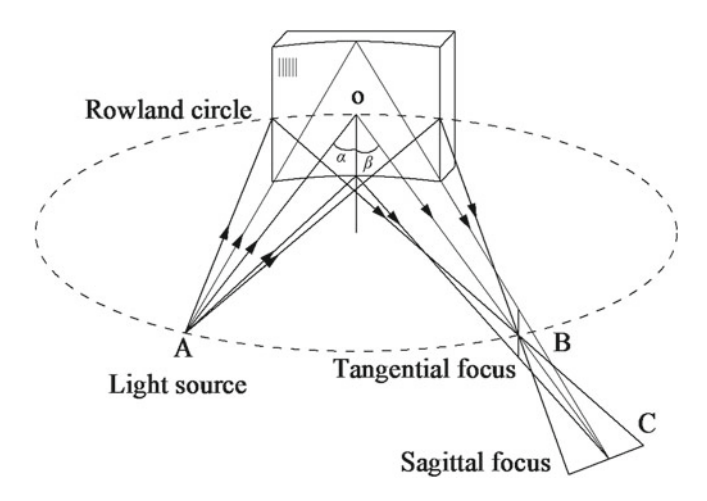


Fig. 9.3 Rowland mount of a concave grating

$$\frac{\cos^2 \alpha}{r} + \frac{\cos^2 \beta}{r'} = \frac{\cos \alpha + \cos \beta}{R},\tag{9.4}$$

where r = OA, r' = OB. One solution of 9.4 is:

$$r = R\cos\alpha, r' = R\cos\beta. \tag{9.5}$$

These relationships show that both the light source A and the tangential focus B are located on the same circle that has a diameter R; such a circle is called the Rowland circle. The spectrum of the light source is horizontally focused on the circumference of the Rowland circle. Thus, the spectrum of the light source can be measured by placing a detector on the Rowland circle. Different harmonic orders can also be separated by placing a slit. However, because of the large astigmatism of the diffracted beam, the refocusing of the separated beam on target does not appear to be promising.

9.2.2.3 Toroidal Grating

The sagittal focus of a concave grating is given by

$$\frac{1}{r} + \frac{1}{r'} = \frac{\cos \alpha + \cos \beta}{R}.\tag{9.6}$$

As shown in Fig. 9.3, in this case, the sagittal focus is different from the tangential focus. One solution for 9.6 is

$$r = R/\cos\alpha, r' = R/\cos\beta.$$
 (9.7)

In this solution, A and C are not located on the Rowland circle. However, when the curvature of the grating in the vertical direction has a different value $R' = R \cos^2 \alpha$, the light emitting point, the tangential and sagittal foci can be located on the same Rowland circle for the 0th order reflected light. The aberration of the diffracted light can be corrected by varying the density of the grooves and, then, the diffracted light can also be focused at a particular point on the Rowland circle. Toroidal gratings for monochromators and flat-field spectrographs are commercially available. Therefore, it is easier to handle the diffracted beam by a toroidal, rather than a concave, grating.

9.2.2.4 Conical Mount of a Plane Grating

As described in Sect. 9.2.1, the reflectance loss of the XUV and soft X-ray light by a metal coating is not negligible even at the grazing incidence. As a result, the total diffraction efficiency of a traditional diffraction grating is on the order of 0.1. Higher efficiency gratings are desired for the application to high harmonics as well as for the spectroscopy. Thus, the improvement in the efficiency has been extensively

investigated. The diffraction efficiency of a ruled grating was found to be enhanced by one order of magnitude and could approach the reflectivity of a plane mirror when the beam was incident on the blazed grating nearly parallel to the grooves [17–19]. This condition is called the conical mount or the off-plane mount. One reason for the lower diffraction efficiency in the traditional mount is the imperfect shape of the illuminated triangular profile of the grooves, which results in the absorption and scattering of the incident light. Conversely, in the conical mount, the total groove width is illuminated and the diffraction is insensitive to the triangular profile. Hence, the diffraction efficiency of the conical mount is higher than that of the traditional mount.

However, because the parallel beam should be illuminated on a plane grating, the construction of the optical system that separates the harmonic orders requires at least three optical elements: the plane grating, the collimating mirror, and the focusing mirror. This might make the construction of the optical system more complicated than the use of a concave or toroidal mirror.

Figure 9.4 shows the geometry of the conical diffraction. The direction of the incident beam is described by two parameters: the altitude γ , which is the angle between the incident beam and the direction of a groove on the grating, and the azimuth α , which is defined as zero if it lies in the plane that is perpendicular to the surface of the grating and parallel to the grooves. The diffracted beams are on the cone that has a half angle of γ . The 0th order and the diffracted light beams emerge at the azimuth angles of $-\alpha$ and β , respectively. These angles are related by the following equation:

$$d\sin\gamma(\sin\alpha + \sin\beta) = m\lambda. \quad m = 0, \pm 1, \pm 2, \dots \tag{9.8}$$

The diffraction efficiency is maximized when

$$\alpha + \beta = 2\theta_B,\tag{9.9}$$

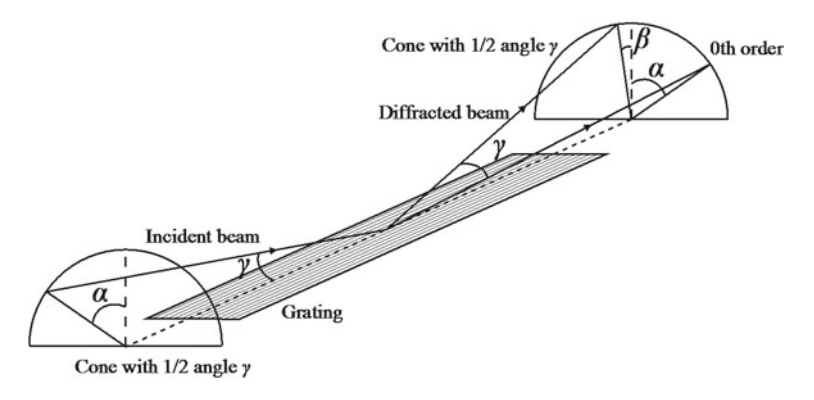


Fig. 9.4 The geometry of the conical mount

where θ_B is the blaze angle of the grating. Under this condition, the shadow that is generated by the triangular profile of the groove is minimized when $\alpha = \theta_B$. Consequently, the optimal performance will be achieved under the condition of

$$\alpha = \beta = \theta_{\rm B}.\tag{9.10}$$

9.3 Time-Preserving Monochromator Using a Single Grating

One of the first application of high harmonics to time-resolved spectroscopy was demonstrated in the pioneering work by Haight et al. [13]. They used a concave or a toroidal grating both to select a single order harmonic pulse and to focus high harmonic pulses on the target samples. As has already been described in the Introduction, the diffraction on a grating prolongs the pulse duration owing to the pulse-front tilt. In the case of the first order diffraction, the difference in the optical path lengths of two diffracted beams from the adjacent grooves on a grating is one wavelength λ . The total difference in the optical path length across the beam amounts to $N\lambda$, where N is the total number of the illuminated grooves. Thus, although the wave front of the beam is still preserved after the diffraction, the pulse front across the beam's cross-section is tilted, and the effective pulse duration is stretched by $N\lambda/c$ for the first order diffraction, where c is the velocity of light. For example, let us consider the pulse stretch when a 500 lines/mm grating is illuminated by 40-nm light over a surface of 10 mm. The number of illuminated groove lines is 5000, leading to a pulse stretch of 670 fs, which is significantly longer compared with the pulse durations of 20–100 fs delivered by a commercial standard laser system.

To reduce the pulse-front tilt, one approach is to use a grating that has a lower groove density. If the pulse front tilt is smaller than the original pulse duration, the pulse duration of the selected harmonic is still comparable to the original pulse duration. Based on this idea, a time-preserving monochromator that uses a single grating in the conical mount was recently proposed [20], and the pulse duration was characterized experimentally [21]. The condition for preserving the pulse duration $\Delta \tau$ after the diffraction from N grooves is given by

$$m\lambda L/(d\cos\alpha) \cong m\lambda L/d \le c\Delta\tau,$$
 (9.11)

where L is the beam diameter of the light source after collimation and the azimuth angle is assumed to be small. When the center wavelength, the groove density, and the beam diameter are 35 nm, 60 line/mm, and 1.8 mm, respectively, the pulse-front tilt becomes 13 fs. In [21], the measured pulse duration was 24 fs, somewhat longer than the pulse-front tilt. This confirms that a temporal response of a single-grating monochromator specially designed for ultrashort pulses is as short as few tens of femtoseconds. At the output of the monochromator, the photon flux was 1.6×10^{10} photons/s, with a pulse repetition rate of 1 kHz. Such photon flux is higher than those

obtained using the time-delay compensated monochromators, which are described in the next section.

9.4 Time-Delay Compensated Monochromator

9.4.1 Compensation of Time Delay Introduced by Diffraction

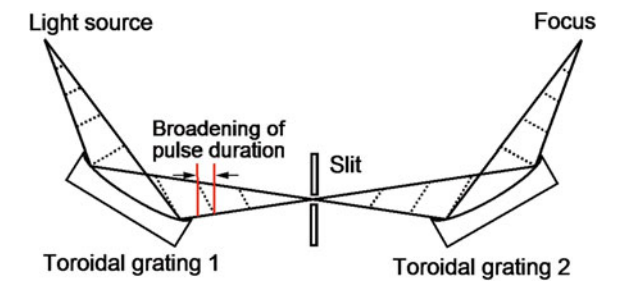
Although the time-preserving monochromator is useful in the separation of a single harmonic order, it is very sensitive to the cross section of the beam on a grating. For example, if the beam diameter becomes 5 mm, the front tilt of the pulse immediately becomes larger than 50 fs, and the time-preserving monochromator is no longer useful. Thus, it is still very important to consider the compensation of the pulse-front tilt.

The idea of using a TDCM for high harmonic pulses was first proposed by Villoresi [15]. Two schemes for normal and grazing incidence regimes were discussed. In this article, we will elaborate on the grazing incidence scheme, because, as described in Sect. 9.2.2.2, the Rowland mount for the normal incidence induces large astigmatism for the vertical direction, and because the beam profile at the exit of a TDCM should be largely distorted. Conversely, in the grazing incidence scheme, the astigmatism can be reduced by using the toroidal gratings.

Figure 9.5 shows the schematic presentation of the grazing incidence scheme of a TDCM. A pair of toroidal gratings is aligned symmetrically with respect to the slit. The basic idea of the time-delay compensation is as follows: The first toroidal grating separates the harmonic orders spatially and focuses the selected harmonic pulses on the slit. However, the pulse duration becomes longer because of the pulse-front tilt. The separated harmonic pulses propagate to the second grating. The second grating corrects the pulse-front tilt induced by the first grating, when the number of the irradiated grooves on the second grating is the same as that of the first grating.

Based on the fundamental idea of a TDCM, the construction of the system requires that two critical conditions will be satisfied: (i) The number of the irradiated grooves on the two gratings should be the same, in order to compensate for the pulse-front

Fig. 9.5 Schematic of a time-delay compensated monochromator (TDCM). The *dotted lines* indicate the pulse front inside the beam. The distance between the *red lines* corresponds to the broadening of the pulse duration after diffraction



tilt. (ii) Since the output diffraction angle α (λ) of the beam from a TDCM depends on the wavelength λ , the compensated bandwidth is limited by the following: Let us assume that both the incident angle to the first grating and the output angle from the second grating are α_0 for the center wavelength λ_0 . Then, the output angle α (λ) is expressed as:

$$\alpha(\lambda) = \sin^{-1}(\sin(\alpha_0) + 2(\lambda - \lambda_0)/d) \tag{9.12}$$

where d is the groove spacing. Insofar as $\lambda - \lambda_0$ is much smaller than d, $\alpha(\lambda)$ can be approximated as α_0 . For example, when 10-fs pulses at $\lambda_0 = 40$ nm are diffracted by a TDCM with gratings of 550 line/mm, $2(\lambda - \lambda_0)/d$ is 1.3×10^{-4} at λ giving half maximum of the spectrum. This value is negligible for a grazing incident angle of around 80° . In general, because the lower order harmonics are characterized by a more severe angular dispersion, a deviation of $2(\lambda - \lambda_0)/d$ might not be ignored. In other words, the grating with lower dispersion is preferable for the compensation of the pulse-front tilt.

9.4.2 Experimental Demonstration of a Time-Delay Compensated Monochromator

9.4.2.1 Design of a Time-Delay Compensated Monochromator

The first TDCM was demonstrated by Nugent-Glandorf et al. and was applied to the studies of time-resolved photoelectron spectroscopy of bromine molecules [14–22]. Nugent-Glandorf et al. constructed the system using the combination of a spherical grating and a toroidal grating. However, the use of a spherical grating in the grazing incident angle introduces high degree of astigmatism. Therefore, a significant distortion of the output beam profile becomes inevitable, and the throughput at the central slit becomes lower. The maximum photon number on the target was 3×10^9 photons/s, obtained for the pulse duration of 182 fs at a repetition rate of 1 kHz.

Poletto et al. have constructed a TDCM employing the conical mount of plane gratings, as shown in Fig. 9.6 [23]. Toroidal mirrors were used for the collimation and focusing of the beam. Although the relatively complicated optical configuration appears to be difficult to construct, the throughput of TDCM was 18 %, which made it quite efficient when compared with the TDCM that employs a pair of toroidal gratings (which will be described below). The energy and the duration of the pulse were 1.3×10^9 photons/s and 8 fs, respectively, obtained at a repetition rate of 1 kHz [24].

Ito et al. were motivated to construct and evaluate the original design proposed by Villoresi, because the simplicity of the original design still offers more practical advantages [25]. They employed a pair of toroidal gratings (HORIBA Jobin Yvon, 54000910) whose radii of curvature were 1 and 104.09 mm in the horizontal and vertical directions, respectively. Accordingly, the deviation angle was 142°. The groove density was 550 lines/mm, and the grooves had a variable pitch. The distances

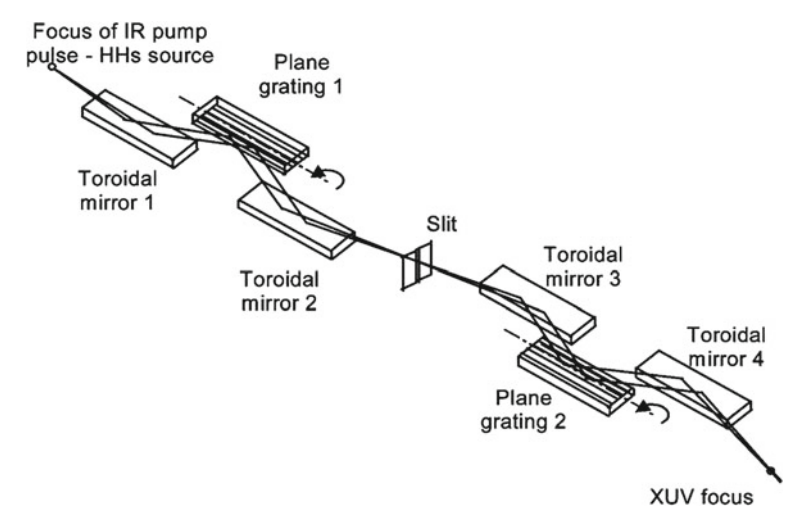


Fig. 9.6 Time-delay compensated monochromator employing the conical mount of diffraction gratings [23]

from the center of the grating to the entrance and the exit foci were 319.9 and 319.5 mm, respectively. The spectral dispersion was 2.07 and 2.22 nm/mm at 48.75 and 82.5 nm, respectively. The toroidal gratings were mounted on the rotational stages and were installed such that the emitting point of high harmonics coincided with the source point of the first toroidal grating. The slit that selected one harmonic order was placed at the image point of the first grating. The second grating, which compensated for the pulse-front tilt, was placed symmetrically with respect to the slit. A harmonic order was chosen by rotating the stage accessible from the outside of the vacuum chamber. The harmonic separator was very compact: the total optical path length from the emitting point of high harmonics to the focusing point was 1.28 m. The maximum photon flux was 4.2×10^9 photons/s at the 21st harmonic, at a repetition rate of 1 kHz. Based on the diffraction efficiency of the gratings, the throughput was estimated to be 2.6%.

9.4.2.2 Characterization of a Time-Delay Compensated Monochromator

In this subsection, we describe two features of the output pulses from the TDCM that employs toroidal gratings: (1) the size of the focus spots and (2) the pulse duration for selected high harmonics [25]. The experimental setup is shown in Fig. 9.7. High harmonics were generated by focusing Ti:sapphire (TiS) laser pulses into a pulsed argon gas jet with a mirror whose focal length was 50 cm. The TiS laser system delivered 800- μ J, 30-fs pulses at a repetition rate of 1 kHz. The laser pulse was separated in two pulses using a beam splitter: 600- μ J pulses were used for the generation of high harmonics, and the remaining pulses were for the probe that was used in the

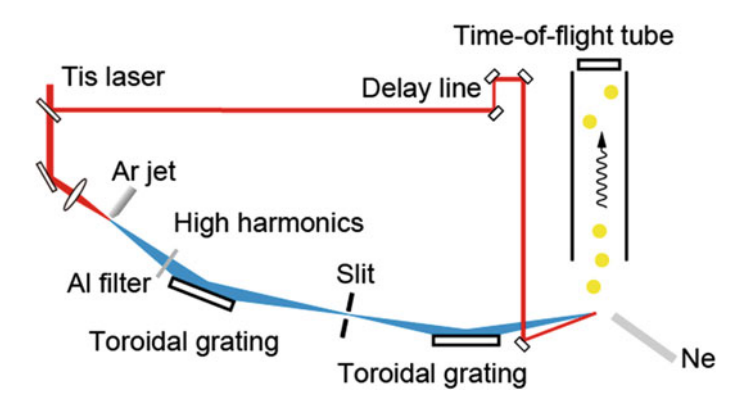


Fig. 9.7 Experimental setup for the spatial and temporal characterization of the time-delay compensated monochromator [25]

temporal characterization. For the generation of high harmonics, the spot size of the laser beam was $68\,\mu m$ and the peak intensity was 5.5×10^{14} W/cm². The selected harmonic order was monitored using a photoelectron spectrometer. To visualize the XUV photons, we employed a Ce:YAG crystal to convert them to visible photons whose wavelength was around 500 nm. The luminescence from the Ce:YAG crystal inserted at the focal point was imaged using a CCD camera. The temporal durations of the selected harmonic pulses were measured by observing the temporal evolution of the sideband peaks in the photoelectron spectra of Ne; these peaks were caused by the two-photon free-to-free transition under the simultaneous irradiation of both XUV and fundamental photons. The peak intensity of a probe pulse was 1.3×10^{11} W/cm², which is weak enough not to cause the ponderomotive shift in the photoelectron spectra. After passing through a time-of-flight tube, the photoelectrons were detected by a multichannel plate (MCP) and then counted.

Figure 9.8 shows the beam profiles of the 17th high harmonic. When both gratings were set to the 0th order reflection, the output beam, shown in Fig. 9.8a, had a nearly circular profile with a diameter of $58\pm3~\mu m$. When the first grating was set to the 1st order diffraction, the beam profile of the 17th harmonic, shown in Fig. 9.8b, became oval-shaped because of the diffraction. As shown in Fig. 9.8c, an almost full compensation for the spectral dispersion of the harmonic was achieved by directing the second grating at the 1st order. The beam diameter at the focus was $58\pm3~\mu m$, which assured a good focusing ability of the TDCM. At the same time, the circular profile of the beam suggests that the divergence of the output beam, predicted by 9.12, might be negligible and that the pulse-front tilt was almost cancelled out by the second grating. This is the first spatial characterization of a TDCM.

The temporal profiles were characterized as follows: When only the first grating was set to the first order, the cross-correlation measurement of high harmonic pulses with the fundamental laser pulses through the two-photon free-to-free transition yielded of 230 ± 10 fs for the pulse duration of the 23rd harmonic pulses

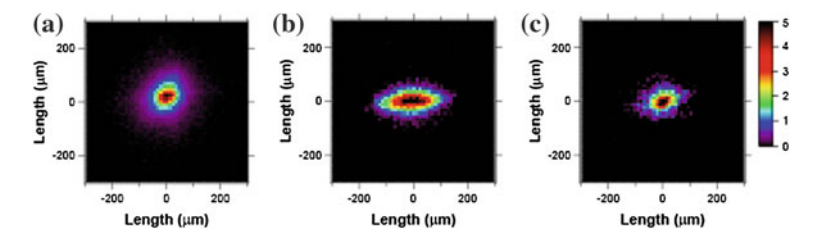


Fig. 9.8 Beam profiles of the 17th harmonic at the exit of the time-delay compensated monochromator. **a** A pair of gratings was set to the 0th order. **b** The first grating was set to the 1st order. **c** Both gratings were set to the 1st order [25]

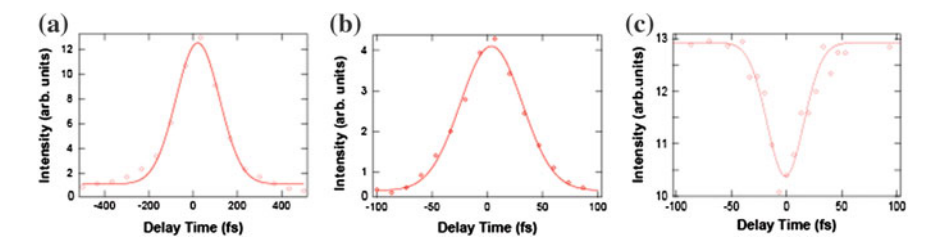


Fig. 9.9 Temporal cross-correlation functions of the 23rd harmonic pulses with the fundamental laser pulses: **a** with only the first grating set to the 1st order, **b** with both gratings set to the 1st order, and **c** with both gratings set to the 0th order. The corresponding pulse durations after the deconvolution are 230 ± 10 , 59 ± 2 , and 25 ± 5 fs. The *solid lines* are the results of a fit to a Gaussian function [25]

Table 9.1 Pulse durations of selected high harmonics

Harmonic order	Photon energy (eV)	Pulse duration (fs)
17	26.5	96 ± 3
19	29.6	80 ± 3
21	32.8	47 ± 2
23	35.9	59 ± 2

(Fig. 9.9a). The compensation produced by the pulse-front tilt was confirmed by setting the second grating to the 1st order. Figure 9.9b shows the cross-correlation and the pulse duration obtained after the compensation was 59 ± 2 fs. Pulse-front-tilt compensation can clearly be seen. For the high harmonic pulses, from the 17th to the 23rd harmonics, we measured the pulse durations and tabulated them in Table 9.1. The shortest pulse duration measured in this case was 47 ± 2 fs when the 21st harmonic was selected. Because the photon number for the 23rd harmonic pulses was 3.0×10^6 photons/pulse, the peak intensity at the focus was $11 \, \text{MW/cm}^2$.

To examine the extent of the recompression by the TDCM, we measured the original pulse duration of the 23rd harmonic, by setting both gratings to the 0th order reflection and then observing the intensity of the photoelectron peak through

one-photon absorption of the 23rd harmonic photons with delay time. The main, rather than the sideband, photoelectron peak was noted here by one-photon transition, because the contribution of the sideband peak was indistinguishable from that of the neighboring peaks (21st or 25th). The main peak was reduced to produce the sidebands under the simultaneous irradiation by the laser pulses. The cross-correlation trace is shown in Fig. 9.9c. The pulse duration was 25 ± 5 fs, which is less than half of the recompressed pulse. Therefore, as shown in Fig. 9.9b, the pulse-front tilt was still present after the TDCM.

The broadening of the pulse, from 25 to 59 fs, corresponds to a 10- μ m difference in the optical path length within the beam. One possible origin of this effect can be attributed to small displacements of the gratings and the slit from an ideal position, because a 10- μ m difference in the optical path is equivalent to the change of 286 grooves in the irradiation area on the grating. Because the angle of incidence is around 71° , only a 170- μ m (286-groove) change in the spot size will result in the broadening of a pulse to 59 fs. This can easily be caused by the misalignment of the angle of incidence or by the misalignment of the focal length.

9.4.2.3 Temporal Optimization of a Time-Delay Compensated Monochromator

The pulse duration was found not to be compressed completely. Thus, in this subsection, we pursued the pulse compression in the TDCM that employed toroidal gratings [11]. As discussed in the previous subsection, the incomplete compression may arise from the unequally illuminated areas on two gratings. In our system, both the focus and the emitting point of the high harmonics were fixed. Thus, when the incident angle to the second grating deviated from the planned angle, the diffraction angle of the second grating became different from that of the first grating. This resulted in different illuminated areas on the gratings. Here, the incident angle to the second grating can be adjusted by simultaneously displacing the slit's position in the Fourier plane of the gratings and by rotating the first grating.

First, the pulse stretch of the 21st harmonic in the TDCM system was estimated by a numerical simulation, using the given parameters of the toroidal grating. Figure 9.10 shows the calculated pulse stretch that arises from unequal irradiation areas on the gratings, as a function of the slit's position. The irradiated areas of both gratings become equal at the origin, and the pulse stretch becomes about 100 fs with 5-mm displacement of the slit. Therefore, the pulse duration could be compressed by shifting the slit position by several millimeters. A similar pulse stretch, resulting from the misalignment of the gratings in the TDCM, was also numerically predicted in a TDCM that employed the conical mount [26]. The pulse stretch estimated in [26] was about five times smaller than that obtained in the present case. This is because the groove density of the assumed grating was about five times lower than that of the toroidal grating used in this TDCM.

The displacement of the slit by several millimeters was found to prolong the durations of the separated harmonic pulses. In other words, pulse compression could

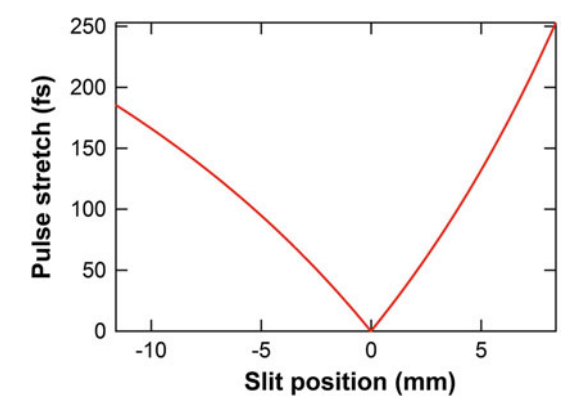


Fig. 9.10 Pulse stretch as a function of the slit's position, determining the incident angle to the second grating [11]

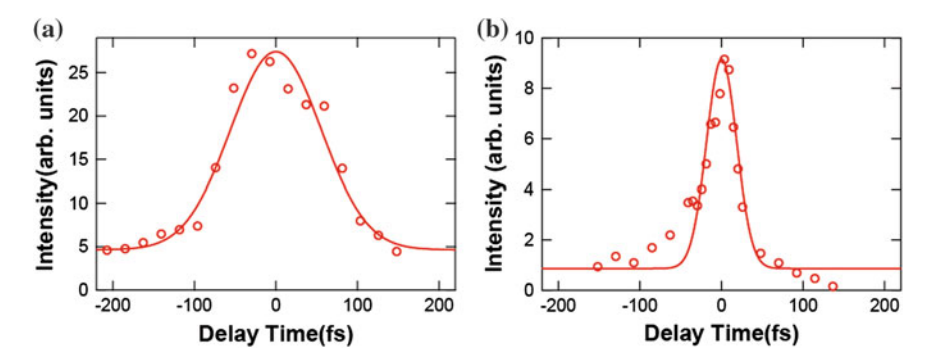
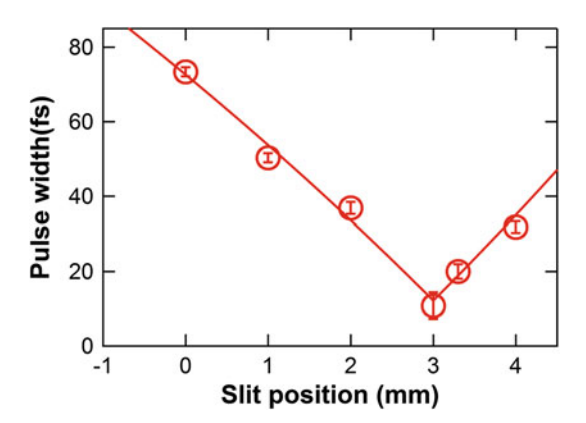


Fig. 9.11 Cross-correlation between the 21st harmonic and fundamental pulses at slit positions of: **a** 0 mm, and **b** 3 mm. The *solid lines* are the results of fits to Gaussian functions [11]

be achieved by moving the slit's position along the Fourier plane of the gratings. We measured the pulse duration of the 21st harmonic as a function of the slit's position for pulse compression. Figure 9.11a, b shows the cross-correlation between the 21st harmonic and the fundamental pulses at slit positions of 0 and 3 mm, respectively. Here, the origin of the slit's position was defined as the slit position at the start of the experiment. The temporal width of the cross correlation was smaller for higher values of slit's position. For a selected harmonic pulse, the pulse duration was obtained by the deconvolution of a high harmonic pulse from the cross-correlation, by assuming the harmonic and fundamental pulses to be described by the Gaussian functions. Figure 9.12 shows that the pulse duration was compressed down to 11 ± 3 fs when the slit was located at 3 mm relative to its initial position. Further shifts increased the pulse duration. The solid line in Fig. 9.12 is the calculated pulse stretch, shifted by 11 fs and by 3 mm in the vertical and horizontal directions, respectively. The experimentally measured pulse duration was explained very well without reference

Fig. 9.12 Pulse duration of the 21st harmonic pulse as a function of slit's position. The *solid line* is the numerically calculated pulse stretch, shifted by the measured shortest pulse duration [11]



to free parameters. Therefore, the deviation of the incident angle to the second grating from the optimal value is the most important parameter in the construction of the TDCM. To reduce the pulse broadening to within $\pm 10\%$ of the optimum, the slit position should be determined to an accuracy of $0.1\,\mathrm{mm}$.

For the 21st harmonic, the shortest compressed pulse duration was $11\pm3\,\mathrm{fs}$. As a consistency check, we calculated the pulse profile of the 21st harmonic from the single atom response, assuming the strong-field approximation [27]. When the pulse duration of the driving laser was 30 fs, the pulse duration of the output harmonic pulse was 15 fs; this calculated result was almost consistent with the experimental results.

Very recently, the application of this TDCM to time-resolved photoelectron spectroscopy of gas-phase 1,3-butadiene molecules was reported in [28], where the ultrafast relaxation from the doubly excited state 2^1A_g and the corresponding recovery of the ground state 1^1A_g were observed simultaneously. This result demonstrates that the developed TDCM light source delivers enough photons for time-resolved spectroscopy. The TDCM is one of the key optical devices for XUV light sources.

9.4.3 Future Applications

It has been proposed that the TDCM that employs the conical mount of gratings can be used as a pulse compressor of the XUV and soft X-ray pulses [29, 30]. Because the conical mount assures high throughput of a TDCM, the idea of an "XUV attosecond compressor" (XAC) appears to be attractive, and suggests a new application of a TDCM.

The pulse stretcher used in a femtosecond laser amplifier system consists of a grating pair and a telescope, and yields both positive and negative phase dispersions of optical pulses when the grating distance is varied. The design of the TDCM that employs the conical mount is similar to the pulse stretcher in that the TDCM also

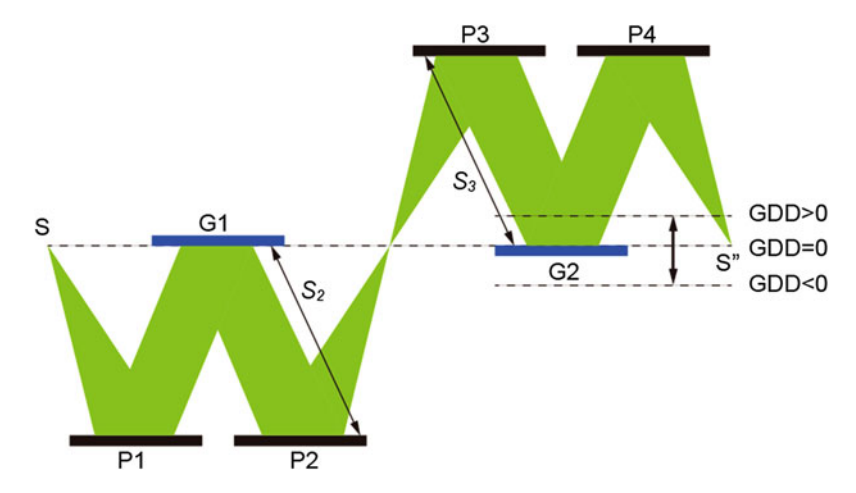


Fig. 9.13 Schematic of a XUV attosecond compressor. P1, P2, P3, and P4 are parabolic mirrors and G1 and G2 are plane gratings. Group-delay dispersion (GDD) changes with the arm length S_3

has a pair of gratings, which provides a chromatic optical path length. The idea of a XUV pulse compressor based on a TDCM was proposed in [29]. Figure 9.13 shows the schematic of the XUV pulse compressor. S and S" in Fig. 9.13 are the light source and the focus of the output, respectively. P1, P2, P3, and P4 are parabolic mirrors for collimation or for focusing, and G1 and G2 are plane gratings. For the TDCM operation, the optical path length S_2 between G1 and P2 should be identical to the optical path length S_3 between G2 and P3. However, the parallel displacement of G2 provides the optical pulses with the group delay dispersion (GDD), for which the sign changes with the direction of the displacement: For $S_3 < S_2$, GDD becomes positive and vice versa. The numerical calculation, performed for a range of energies from 50 to 100 eV, using the gratings with a groove density of 200 lines/mm, predicts a GDD on the order of 10^3 as⁻², which is comparable to GDD given by an intrinsic chirp that comes from the generation mechanism of the attosecond pulse generation [31]. Although the phase compensation using a thin metal filter has already been demonstrated [32], the advantages of a XAC are the tunability of the GDD, the center wavelength, and the total throughput of the photon flux. A XUV attosecond compressor is a promising optical system for attosecond time-resolved spectroscopy.

9.5 Conclusions

A time-delay compensated monochromator (TDCM), which selects a single harmonic with the pulse duration preserved, was described, along with the fundamentals of the optical gratings, for the XUV and soft X-ray light. A beam line combining a high harmonic light source and a TDCM delivers to the target ultrashort XUV photons

on the order of 10^9 – 10^{10} photons/s at a repetition rate of 1 kHz, which is comparable to the radiation coming from a small synchrotron facility. Recent developments in laser technology enable generating the femtosecond laser pulses at higher repetition rate, thus increasing the XUV photon flux. In addition, because of its widely tunable photon energy, a device consisting of a high harmonic beam line with a TDCM would become useful for XUV spectroscopy in the near future.

References

- M. Born, E. Wolf, *Principles of Optics*, 7th edn. (Cambridge University Press, Cambridge, 1999)
- 2. J.-C. Diels, R. Wolfgang, *Ultrashort Laser Pulse Phenomena, Optics and Photonics Series*, 2nd edn. (Academic Press, San Diego, 2006)
- 3. J.A.R. Samson, D.L. Ederer, *Vacuum Ultraviolet Spectroscopy* (Academic Press, San Diego, 2000)
- A. McPherson, G. Gibson, H. Iara, H. Johann, T.S. Luk, I.A. McIntyre, K. Boyer, C.K. Rodes, J. Opt. Soc. Am. B 4, 595 (1987)
- M. Ferray, A. L'Huillier, X.F. Li, L.A. Lompre, G. Mainfray, C. Manus, J. Phys. B 21, L31 (1988)
- 6. P.B. Corkum, Phys. Rev. Lett. 71, 1994 (1993)
- 7. T. Popmintchev et al., Science **336**, 1287 (2012)
- E. Goulielmakis, M. Schultze, M. Hofstetter, V.S. Yakovlev, J. Gagnon, M. Uiberacker, A.L. Aquila, E.M. Gullikson, D.T. Attwood, R. Kienberger, F. Krausz, U. Kleineberg, Science 320, 1614 (2008)
- 9. T. Sekikawa, A. Kosuge, T. Kanai, S. Watanabe, Nature **432**, 605 (2004)
- 10. K. Zhao, Q. Zhang, M. Chini, Y. Wu, X. Wang, Z. Chang, Opt. Lett. 37, 3891 (2012)
- 11. H. Igarashi, A. Makida, M. Ito, T. Sekikawa, Opt. Express **20**, 3725 (2012)
- 12. T. Ishikawa et al., Nat. Photon 6, 540 (2012)
- 13. R. Haight, J.A. Silberman, M.I. Lilie, Rev. Sci. Instrum. 59, 1941 (1988)
- 14. L. Nugent-Glandorf, M. Scheer, D.A. Samuels, V.M. Bierbaum, S.R. Leone, Rev. Sci. Instrum. 73, 1875 (2002)
- 15. P. Villoresi, Appl. Opt. 38, 6040 (1999)
- 16. E.D. Palik, Handbook of Optical Constants of Solids (Academic Press Inc., San Diego, 1985)
- 17. M. Neviere, D. Maystre, W.R. Hunter, J. Opt. Soc. Am. 68, 1106 (1978)
- 18. W. Werner, Appl. Opt. 16, 2078 (1977)
- 19. W. Werner, H. Visser, Appl. Opt. 20, 487 (1981)
- 20. L. Poletto, F. Frassetto, Appl. Opt. 49, 5465 (2010)
- F. Frassetto, C. Cacho, C.A. Froud, I.C.E. Turcu, P. Villoresi, W.A. Bryan, E. Springate, L. Poletto, Opt. Express 19, 19169 (2011)
- L. Nugent-Glandorf, M. Scheer, D.A. Samuels, A.M. Mulhisen, E.R. Grant, X. Yang, V.M. Bierbaum, S.R. Leone, Phys. Rev. Lett. 87, 193002 (2001)
- 23. L. Poletto, P. Villoresi, E. Benedetti, F. Ferrari, S. Stagira, G. Sansone, M. Nisoli, Opt. Lett. 32, 2897 (2007)
- L. Poletto, P. Villoresi, E. Benedetti, F. Ferrari, S. Stagira, G. Sansone, M. Nisoli, Opt. Lett. 33, 140 (2008)
- 25. M. Ito, Y. Kataoka, T. Okamoto, M. Yamashita, T. Sekikawa, Opt. Express 18, 6071 (2010)
- 26. L. Poletto, Appl. Opt. 48, 4526 (2009)
- M. Lewenstein, P. Balcou, M.Y. Ivanov, A. L'Huillier, P.B. Corkum, Phys. Rev. A 49, 2117 (1994)

- A. Makida, H. Igarashi, T. Fujiwara, T. Sekikawa, Y. Harabuchi, T. Taketsugu, J. Phys. Chem. Lett. 5, 1760 (2014)
- 29. F. Frassetto, P. Villoresi, L. Poletto, Opt. Express 16, 6652 (2008)
- 30. M. Mero, F. Frassetto, P. Villoresi, L. Poletto, K. Varj_E, Opt. Express 19, 23420 (2011)
- Y. Mairesse, A. de Bohan, L.J. Fransinski, H. Merdji, L.C. Dinu, P. Monchicourt, P. Breger, M. Kovacev, R. Taieb, B. Carre, H.G. Muller, P. Agostini, P. Salieres, Science 302, 1540 (2003)
- R. López-Martens, K. Varju, P. Johnsson, J. Mauritsson, Y. Mairesse, P. Salieres, M. Gaarde, K.J. Schafer, A. Persson, S. Svanberg, C.-G. Wahlstrom, A. L'Huillier, Phys. Rev. Lett. 94, 033001 (2005)

Index

A Above threshold ionization, 123 Absorption, 152 Active optic, 36 Angular dispersion, 179 Antireflection layers, 159 Aperiodic multilayer, 165, 166 Atomic force microscope (AFM), 140 Attochirp, 164 Attosecond pulses, 41, 53, 54, 59, 116, 121,	D Damage threshold, 9, 162 Density modulation (electrons), 81 Difference frequency generation, 44 Diffractionless beam, 72 Direct seeding (free-electron laser), 101 Double optical gating, 57 Double slit experiment, 10, 32 Dual-band multilayer, 161
163, 168 Attosecond streaking, 118 Autocorrelation, 126	E Echo enabled harmonic generation, 86 Efficiency, 66 Elastic emission machining (EEM), 138 Electron streaking, 128, 129
B Beam position monitor, 25 Beam shaping, 72 1,3-butadiene, 190	Ellipsoidal, 36 Energy modulation (electrons), 81 European-XFEL, 137, 138, 145 EUV lithography, 162 Extended shear angle difference method (ESAD), 140
C Capillary, 71 Carrier envelope phase, 42, 45 Carrier envelope phase stabilization, 46 Ce:YAG, 186 Coherent diffraction imaging, 6 Coherent spontaneous emission, 89 Computer aided polishing (CAP), 138 Conical mount, 180	F FERMI, 23, 137 FLASH, 2, 137, 141, 142, 147 Fluorescent screen, 27, 30, 37 Fresnel coefficient, 152 FROG-CRAB technique, 116, 118, 121, 122 FROG technique, 118
Coulomb explosion, 125 CRAB technique, 117 Cross-correlation, 131, 132 Cutoff, 64	Gas absorber, 25 Gas absorption, 5 Gas filled attenuator, 14
© Springer-Verlag Berlin Heidelberg 2015 F. Canova and L. Poletto (eds.), <i>Optical Technologies Extreme-Ultraviolet and Soft X-ray Coherent Sources</i> in Optical Sciences 197, DOI 10.1007/978-3-662-474	s, Springer Series

196 Index

Gas monitor detector, 5, 11	Mirrors, 137
Genetic algorithm, 72	Mo/Si multilayers, 156
Gouy phase, 52	Multilayer mirror, 6, 126
Gratings, 137, 175	
Grazing incidence, 3, 5, 155	
Group delay dispersion, 121, 164	N
	Nanometer optical component measuring machine (NOM), 140
H	Nonlinear intensity autocorrelation, 126
Hartmann sensor, 10, 37	Normal incidence, 152, 153, 155
Helical undulator, 97	
HHG seeding (FEL), 98	
High-density carbon coating, 6	0
High gain harmonic generation, 24, 84	Off-axis parabola, 6
High-order harmonics, 41, 47, 87, 97, 176	Optical cavity, 82
High stability mirrors, 162	Optical parametric amplifier, 43, 86
	Optical parametric chirped pulse amplifica-
T	tion, 42, 44
I Intensity monitor 11, 25	
Intensity monitor, 11, 25 Interferometric gating, 58	P
Interferometry, 140	Periodic multilayer, 153
Ion beam figuring (IBF), 138	Phase matching, 52, 66, 93
Ion chamber, 27	coherence, 66
	Photodiode, 27
	Photoionization, 27, 118
J	Photoionization spectrometer, 12
Jitter (FEL), 130	Photon analysis delivery and reduction sys-
	tem (PADReS), 25
	Physical vapor deposition, 154
K	Plane grating monochromator, 6
Kilohertz amplified laser systems, 73	Polarization gating, 55, 56
Kirkpatrick-Baez, 6, 8, 36	Power spectral density, 139
	Pulse compression, 42
•	Pulse-front tilt, 176, 182
L	
Laser-assisted photoelectric effect, 128	0
Light interferometer (WLI), 140	Q
Linac Coherent Light Source (LCLS), 145, 147	Quasi Phase Matching (QPM), 69
Littrow blaze condition, 179	n.
Long path trajectories (HHs), 93	R
Long trace profiler (LTP), 140	RABBIT technique, 120
Loose focusing, 67, 72	Raman spectrometer, 7
	Reflectance, 177 Rotating shutter, 15
M	Roughness (interface), 153
Mach Zehnder, 126	Rowland circle, 180
Mach-Zehnder autocorrelator, 16	Rowland Chele, 100
Magnetron sputtering, 154	
Maréchal criterion, 140	S
Metal foil filter, 15	Sagittal focus, 180
Metrology, 138	Seeded free-electron laser, 84
Microjoule, 68	Self amplified spontaneous emission, 2, 82

Index 197

Self-seeding free-electron laser, 86	THz radiation, 5, 18
Shape, 141	Time-delay compensated monochromator
Short path trajectories (HHs), 93	(TDCM), 176
Shot noise, 90, 92	Time-resolved photoelectron spectroscopy,
Single active electron approximation, 116	190
Single-pass free electron laser, 2, 81, 83, 84	Toroidal grating, 183
Slope error, 138–140, 142	Total electron yield, 166
Slowly varying envelope approximation, 93,	Trajectories, 65
117	Transient reflectivity, 131
Spatial coherence, 10	Transverse coherence, 32
Spatial frequencies, 138	Two color, 65
Spatial gating, 58	Two-photon absorption, 124
Spectral gating, 53	Two-photon double ionization, 124
Spectrometer, 13, 27, 30	Two-photon free-to-free transition, 186
SPIDER technique, 123	,
Split-and-delay unit, 15, 35	
Streak camera, 121	U
Streak camera method, 116	Undulator (linear polarized), 80
Strehl factor, 139	Chaulator (micar polarized), 00
Strong field approximation, 92, 116	
Supercontinuum, 43	V
Superradiant regime, 94	•
Surface oxidation, 153	Variable line spacing grating, 11, 25, 27
Surface profilers, 140	
Surface roughness, 139, 140	
Surface slope, 143	W
Switching mirror, 8	Water window, 155
Synchronization, 17, 97, 102	Wavefront, 73
Synchrotron radiation, 80, 154	Wave-front sensor, 9
•	
T	X
Tangential focus, 180	XUV attosecond compressor (XAC), 190,
Temporal gating, 55	191
Three-step semi-classical model, 49, 65, 87	XUV non-linear optics, 123